

ADVANCED OXIDATION OF CHEMICALS OF EMERGING CONCERN:
MODELING AND EXPERIMENTAL SIMULATION

by

Mario Roberto Rojas Cardozo

A Dissertation Submitted to the Faculty of the

DEPARTMENT OF CHEMICAL AND ENVIRONMENTAL ENGINEERING

In Partial Fulfillment of the Requirements
For the Degree of

DOCTOR OF PHILOSOPHY
WITH A MAJOR IN CHEMICAL ENGINEERING

In the Graduate College

THE UNIVERSITY OF ARIZONA

2011

THE UNIVERSITY OF ARIZONA
GRADUATE COLLEGE

As members of the Dissertation Committee, we certify that we have read the dissertation prepared by Mario Roberto Rojas Cardozo entitled Advanced Oxidation of Chemicals of Emerging Concern: Modeling and Experimental Simulation and recommend that it be accepted as fulfilling the dissertation requirement for the Degree of Doctor of Philosophy

A. Eduardo Sáez Date: 07/06/11

Robert G. Arnold Date: 07/06/11

Paul Blowers Date: 07/06/11

Wendell P. Ela Date: 07/06/11

Final approval and acceptance of this dissertation is contingent upon the candidate's submission of the final copies of the dissertation to the Graduate College.

I hereby certify that I have read this dissertation prepared under my direction and recommend that it be accepted as fulfilling the dissertation requirement.

Dissertation Director: A. Eduardo Sáez Date: 07/06/11

STATEMENT BY AUTHOR

This dissertation has been submitted in partial fulfillment of requirements for an advanced degree at the University of Arizona and is deposited in the University Library to be made available to borrowers under rules of the Library.

Brief quotations from this dissertation are allowable without special permission, provided that accurate acknowledgment of source is made. Requests for permission for extended quotation from or reproduction of this manuscript in whole or in part may be granted by the head of the major department or the Dean of the Graduate College when in his or her judgment the proposed use of the material is in the interests of scholarship. In all other instances, however, permission must be obtained from the author.

SIGNED: Mario Roberto Rojas Cardozo

ACKNOWLEDGMENTS

It would be very hard for me to acknowledge here all the people that have played a positive role and contributed to my education during my whole life. However, at this point, I try to remember all these people with a humbling feeling of gratitude, as I approach to finish my doctorate. In this list of people, I would foremost need to include my mother, who has worked exceptionally hard all her life to inspire her children and other people to study, and to value education as one of the most precious fortunes one can possess. I would need to include all those god teachers, who since I was a kid had patience to my curiosity and gave me the tools to one day be able to do research. Those, who believed in me and gave me the strength to continue during the roughest times.

I would specially like to thank my advisor Dr. Eduardo Sáez for giving me the opportunity to do research in his group, and for kindly teaching and mentoring me in many different areas of engineering that were completely new for me. I also want to thank Dr. Robert Arnold for being a mentor, for his motivation and for all these years of prolific long-lasting discussions that have taught me so much. To both of you, I will be always in debt.

I am greatly thankful to all my research team and all the students that over these years help me with the experiments in the lab: Dan, Cary, Fabian, Yan, Fernando and Leah. I have special gratitude to Brian Barbaris, who was always willing to help me develop new experimental skills.

Finally, I want to thanks my wife and friends for making graduate school such a wonderful experience. These years in Tucson would not have been the same without your support: Tomás, Elias, David, Andrea L., Andrea C, Umur, Lucia, Martico, Vicky, Nelson, Armando, Rainier and Mariela. Thank you for your friendship and for all the great moments that we have shared. To all of you: *Gracias Totales!*

DEDICATION

*To my wife Mónica, whose motivation and encouragement over these
years has made this work possible.*

TABLE OF CONTENTS

LIST OF FIGURES	11
LIST OF TABLES	17
ABSTRACT	18
DISSERTATION OVERVIEW	20
CHAPTER 1 INTRODUCTION	24
1.1. Environmental Significance	24
1.2. Conventional Wastewater Treatment	26
1.3. Chemicals of Emerging Concern	28
1.4. Advanced Oxidation Processes: UV/H ₂ O ₂	32
1.5. Fenton's Reaction	38
1.6. Project Objectives	40
1.7. Literature Cited	42
CHAPTER 2 ASSESSMENT OF THE EFFECTIVENESS OF SECONDARY WASTEWATER TREATMENT TECHNOLOGIES TO REMOVE TRACE CHEMICALS OF EMERGING CONCERN	46
2.1. Abstract	46
2.2. Introduction	47
2.3. Previous Work	49
2.4. Methodology	54
2.5. Results and Discussion	62

TABLE OF CONTENT - *Continued*

2.5.1. Conventional Activated Sludge	62
2.5.2. Membrane Bioreactors	69
2.5.3. Factors that Affect Removal Efficiencies	71
2.5.4. Comparison of Biological Treatment Alternatives	77
2.5.5. Effects of Operating Conditions	77
2.6. Concluding Remarks.....	79
2.7. Literature Cited	83
 CHAPTER 3 MODELING OF ADVANCED OXIDATION OF TRACE ORGANIC CONTAMINANTS BY HYDROGEN PEROXIDE PHOTOLYSIS AND FENTON'S REACTION	
3.1. Abstract	89
3.2. Introduction.....	90
3.3. Experimental.....	93
3.3.1. Materials.....	93
3.3.2. UV/H ₂ O ₂ Experiments	93
3.3.3. Fenton's Reaction Experiments	95
3.3.4. Analytical Methods.....	95
3.3.5. Actinometry	96
3.3.6. Iron	96
3.4. Models.....	97
3.4.1. UV/H ₂ O ₂ Model.....	97

TABLE OF CONTENT - *Continued*

3.4.2. Fenton's Reaction Model	109
3.5. Results and Discussion	113
3.5.1. Hydrogen Peroxide Photolysis.....	113
3.5.2. P-Cresol Experiments and Scavenger Effects.....	113
3.5.3. Nonylphenol Experiments.	118
3.5.4. Implications for Reactor Design	124
3.5.5. Fenton's Reaction	127
3.6. Concluding Remarks.....	130
3.7. Literature Cited	132
 CHAPTER 4 ADVANCED OXIDATION OF TRACE ORGANICS IN WATER BY HYDROGEN PEROXIDE SOLAR PHOTOLYSIS.....	 137
4.1. Abstract	137
4.2. Introduction.....	138
4.3. Experimental	141
4.3.1. Materials.	141
4.3.2. Solar UV-H ₂ O ₂ Experiments	142
4.3.3. Wastewater Experiments	143
4.3.4. Analytical	143
4.4. Modeling	144
4.4.1. Solar Spectral Irradiance.....	144
4.4.2. Solar UV/H ₂ O ₂ Model.	150

TABLE OF CONTENT - *Continued*

4.5. Results and Discussion	155
4.5.1. P-Cresol and Fluorescein Experiments.....	155
4.5.2. Wastewater Applications.....	160
4.6. Concluding Remarks.....	164
4.7. Literature Cited	166
 CHAPTER 5 EXPERIMENTAL SIMULATION OF ADVANCED OXIDATION PROCESSES IN FLOW-THROUGH REACTORS	
5.1. Abstract	170
5.2. Introduction.....	171
5.3. Experimental	171
5.3.1. Materials and Analytical Methods	171
5.3.2. Experimental Setup.....	171
5.3.3. Procedure	174
5.4. Modeling	176
5.5. Results and Discussion	177
5.5.1. Monochromatic Reactor (R1)	177
5.5.2. Polychromatic Reactor (R2)	183
5.6. Concluding Remarks.....	190
5.7. Literature Cited	191
 CHAPTER 6 CONCLUSIONS	
 APPENDIX A SUPPLEMENTARY MATERIAL ABOUT CECs REMOVAL	
	195

TABLE OF CONTENT - *Continued*

APPENDIX B SUPPLEMENTARY MATERIAL FOR THE UV/H ₂ O ₂ AND FENTON'S KINETIC MODELS	220
B1. UV/H ₂ O ₂ Model	220
B2. Fenton's Model	223
B3. Giovanni-NASA Data for the Calculation of Solar Spectral Irradiance using SMARTS (Chapter 3).	228
APPENDIX C ADDITIONAL RESEARCH ON FLOW OF NON-NEWTONIAN SLURRIES WITH APPLICATION TO TRANSPORT OF NUCLEAR WASTE.....	230
C.1. Abstract	230
C.2. Introduction	231
C.3. Experimental	233
C.4. Model Description and Modifications.....	237
C.5. Results and Discussion	244
C.6. Conclusions	252
C.7. Acknowledgements	252
C.8. Literature Cited.....	253
C.9. Nomenclature and Acronyms	255

LIST OF FIGURES

Figure 1-1.	Secondary treatment is provided via a combination of pre-treatment steps, primary treatment to remove settleable solids and biological treatment. Solids generated and separated during these processes are stabilized via sludge digestion, dewatered and then disposed of.....	28
Figure 2-1.	Box plots of liquid removal in activated sludge processes for selected pharmaceuticals. In this and subsequent plots, the boxes cover the 25 to 75 percentiles of the data range, the open circles are the median, the horizontal line in the box is the mean, the vertical lines extend between the 10 and 90 percentiles of the data set, and the X marks the whole data range.....	63
Figure 2-2.	Box plots of liquid removal in activated sludge processes for selected antibiotics. Sulfamethoxazole, roxythromycin, norfloxacin and ciprofloxacin exhibit mean removal.....	64
Figure 2-3.	Box plots of liquid removal in activated sludge processes for selected natural and synthetic hormones.....	64
Figure 2-4.	Box plots of liquid removal in activated sludge processes for selected organic wastewater organics.	65
Figure 2-5.	Cumulative probability for selected pharmaceuticals in activated sludge. In these plots, cumulative counts represent the percent of data with liquid-phase removal efficiencies lower than the influent-to-effluent removal specified.	68
Figure 2-6.	Cumulative probability for selected hormones and synthetic musks in activated sludge.....	69
Figure 2-7.	Box plots of liquid removal for selected pharmaceuticals in MBR process.....	70
Figure 2-8.	Box plots of liquid removal for selected antibiotics in MBR process.	70
Figure 2-9.	Box plots of liquid removal for selected natural and synthetic hormones, bisphenol A and nonylphenol in MBR process.....	71

LIST OF FIGURES - *Continued*

- Figure 2-10. (Left) Probability of achieving 75⁺% removal efficiency for selected CECs as a function of octanol-water partition coefficient; (Right) Biodegradable (Ready and inherent biodegradable compounds from Table 2-1) compounds have been eliminated and K_{OW} has been replaced by D_{OW} . Solid line is a visual guide. The Spearman correlation coefficient (ρ) is shown for each data set. 73
- Figure 2-11. Probability of achieving 75⁺% removal efficiency in activated sludge processes vs. BIOWIN 2 (left) and BIOWIN 6 (right) estimation of biodegradation probabilities. Numbers correspond to legend in Figure 2-10. Solid line represents a linear fit. Compounds with $\log D_{ow} > 3.5$ are not considered. 74
- Figure 2-12. (Left): Probability of achieving 75⁺% removal efficiency as a function of biodegradation rate constants as reported by Urase and Kikuta 2005 (47), and Dickenson *et al.*, (48) in activated sludge for selected compounds. Solid line is a visual guide. (Right): Mean Removal for the same compounds as a function of STPWIN total removal prediction using half-lives calculated from the rate constants. Numbers correspond to legend in Figure 2-10. Error bars are plus and minus one standard deviation. Solid line is the 45-degree line. 75
- Figure 2-13. Removal efficiency comparison for conventional activated sludge (CAS), membrane bioreactor (MBR), tricking filters (TF), sequenced batch reactors (SBR) and lagooning (LAG) for selected CECs. Open circles represent the mean and the horizontal bars represent plus and minus one standard deviation. The number of data points is indicated for each case. 76
- Figure 2-14. Removal efficiencies as functions of SRT and HRT for diclofenac and ketoprofen in activated sludge process. 78
- Figure 3-1. Model prediction of average radical concentration vs. time for a nonylphenol degradation experiment (UV/H₂O₂). Comparison between quasi-steady state approximation calculations (QSSA) and full model simulations. Initial conditions: [H₂O₂]₀ =50 mM, [NP]₀=15 μ M, [EtOH]₀=3.4 mM, λ =250 nm. The scavenging effect of ethanol was considered in the calculations. 108

LIST OF FIGURES - *Continued*

Figure 3-2.	Decomposition of (a) <i>p</i> -cresol and (b) hydrogen peroxide for two initial H ₂ O ₂ concentrations (UV/H ₂ O ₂). [PC] ₀ =240 μM, λ=250 nm.	114
Figure 3-3.	Pseudo-first order rate constants for UV/ H ₂ O ₂ oxidation of <i>p</i> -cresol as a function of initial H ₂ O ₂ concentrations. Solid line is the model prediction, obtained from a fit of model results to a first-order decay curve; [PC] ₀ =240-250 μM, λ=250 nm. Error bars represent standard deviations from repeat experiments.....	116
Figure 3-4.	Decomposition of PC with and without an organic scavenger (isopropanol). [PC] ₀ =289 μM, λ=250 nm (UV/H ₂ O ₂).	118
Figure 3-5.	Decomposition of NP for two initial concentrations of hydrogen peroxide; [NP] ₀ =14.0 μM, λ=250 nm (UV/H ₂ O ₂). Ethanol is added to facilitate NP dissolution and its role as a scavenger of hydroxyl radicals is modeled. To generate model results, the rate constant for ·OH/NP reaction was used as an adjustable parameter.	119
Figure 3-6.	Evolution of pH during NP degradation experiments at two initial H ₂ O ₂ concentrations (UV/H ₂ O ₂); [NP] ₀ =14.0 μM, λ=250 nm.....	120
Figure 3-7.	Pseudo-first order rate constant for oxidation of NP as a function of H ₂ O ₂ concentration (UV/H ₂ O ₂). Lines represent model predictions. [NP] ₀ =10-15 μM, [EtOH] ₀ =3.4-4.2 mM. λ=250 nm. The constant pH prediction neglects the CO ₂ produced by NP mineralization.	121
Figure 3-8.	Nonylphenol isomers decomposition in UV/H ₂ O ₂ . [NP] ₀ =14μM, [ethanol] ₀ =3.4 mM. [H ₂ O ₂] ₀ =100 mM, λ=250nm.....	123
Figure 3-9.	Wavelength/intensity effects in the UV/H ₂ O ₂ decomposition of nonylphenol. The light intensities for each wavelength are reported in Table 3-4.	124
Figure 3-10.	Model calculations of design parameters for a batch reactor with I ₀ =1×10 ⁻⁶ ein/mol s, ℓ=5 cm, pH 7; (a) time required to reach 90% destruction of target (1 μM initial concentration) as a function of initial hydrogen peroxide concentration and intrinsic rate constant for the reaction between the target and hydroxyl radicals; (b) optimum process times from (a) and hydrogen peroxide concentration at which they are achieved as a function of the intrinsic rate constant.....	127

LIST OF FIGURES - *Continued*

- Figure 3-11. *p*-Cresol degradation in the Fenton system as a function of (a) pH at fixed $[\text{Fe(III)}]_0 = 0.135$ mM, and (b) iron concentration at fixed pH=2.1; $[\text{PC}]_0=20$ μM ; $[\text{H}_2\text{O}_2]_0 = 10$ mM, 25°C. Solid lines represent model predictions..... 128
- Figure 3-12. Nonylphenol degradation in the Fenton system as a function of (a) pH at fixed $[\text{H}_2\text{O}_2]_0=120$ mM, and (b) H_2O_2 concentration at fixed pH=2.7. In all cases $[\text{Fe(III)}]_0=0.25$ mM, $[\text{NP}]_0=13-20$ μM ; 25 °C. Solid lines represent model predictions. 130
- Figure 4-1. (a) Comparison of the global spectral irradiance at the top of the atmosphere and at ground level in Tucson on July 15, 2010; (b) Comparison of the UV global solar spectral irradiance in Tucson, Arizona, in fall 2009 and summer 2010, obtained with SMARTS. Experiments were performed on the dates shown, which were close to solstices. The figure includes the molar absorption coefficient for hydrogen peroxide.147
- Figure 4-2. (a): Global spectral irradiance and diffusive spectral irradiance in November 18, 2010 in Tucson; (b) Time-dependent total irradiance as a fraction of the maximum (noon) irradiance at ground level in Tucson on November 18, 2010. Polynomial fitting: $0.8024 + 5.4765\text{E}^{-5}x - 3.8069\text{E}^{-9}x^2$ 149
- Figure 4-3. Experimental decomposition of *p*-cresol by solar-catalyzed UV- H_2O_2 as a function of initial hydrogen peroxide concentration. Solid lines represent model predictions. Experiments were carried out on February 19, 2010. 156
- Figure 4-4. pH change during *p*-cresol experimental decomposition by solar-catalyzed UV- H_2O_2 , at different hydrogen peroxide concentrations, and kinetic model performance. Solid lines represent the model. Experiments were carried out on February 19, 2010..... 157
- Figure 4-5. Effect of an organic scavenger (IPOH) on *p*-cresol decomposition by solar-catalyzed UV- H_2O_2 . Solid lines represent model predictions. Experiments were carried out in September 10, 2009. 158

LIST OF FIGURES - *Continued*

- Figure 4-6. Half-lives for *p*-cresol decomposition by solar-catalyzed UV-H₂O₂ as a function of hydrogen peroxide concentration in winter (Feb 2009) and summer (July 2010). Insert: Half-life times for *p*-cresol at a fixed H₂O₂ concentration (10 mM), as a function of total solar irradiation (ground-level). Solid lines represent model predictions. 160
- Figure 4-7. Experimental decomposition of sodium fluorescein dye by solar-catalyzed UV-H₂O₂ as a function of hydrogen peroxide concentration. Solid lines represent model predictions. Experiments were carried out on June 15, 2010. 161
- Figure 4-8. Excitation-emission matrices (EEM) for Ina Road wastewater effluent (05/16/2011) before (a) and after (b) 3 h of solar-catalyzed AOP treatment with 5 mM H₂O₂ in a batch reactor..... 162
- Figure 4-9. Relative intensity of the 435/350 em/ex peak in the fluorescence spectrum for Ina Road wastewater effluent (05/16/2011) as a function of time of solar-catalyzed UV-H₂O₂ treatment and hydrogen peroxide concentration..... 163
- Figure 5-1. Hanovia pilot-scale polychromatic reactor (R2). The medium pressure lamp (2.5 kW) concentrically located at the center of the pipe provides light energy in the UV-visible range..... 172
- Figure 5-2. Schematic representation of the experimental setup for the two reactors, pump and recirculation tank..... 173
- Figure 5-3. Residence time distributions for pulse and step inputs in the large tubular reactor (R2), measured in terms of the time-dependent effluent conductivity. Sodium chloride was the tracer. 174
- Figure 5-4. Hydrogen peroxide conversion in the monochromatic reactor (R1). 178
- Figure 5-5. *p*-Cresol conversion in the monochromatic reactor (R1). Solid line represents the kinetic model, using the lamp intensity as adjustable parameter..... 179
- Figure 5-6. *p*-Cresol oxidation in the monochromatic reactor (R1) at different hydrogen peroxide concentrations. Solid line represents model predictions using the input light intensity determined in the actinometry experiment (Figure 5-5). Legend shows hydrogen peroxide concentration..... 180

LIST OF FIGURES - *Continued*

- Figure 5-7. pH evolution during *p*-Cresol oxidation experiments in the monochromatic reactor (R1) at different hydrogen peroxide concentrations. Solid line represents model predictions. Legend shows hydrogen peroxide concentration..... 181
- Figure 5-8. EEMs for Ina Road wastewater effluent before (above) and after 55 seconds of treatment (below) with a hydrogen peroxide concentration of 5 mM in the monochromatic reactor (R1). Legend shows relative intensity..... 182
- Figure 5-9. Spectra for two different Hanovia medium pressure lamps (3.5 and 5-kW)..... 184
- Figure 5-10. Hydrogen peroxide conversion at different starting concentrations in the polychromatic large reactor (R2). Experimental values were taken at the exit of the treatment reactor. Solid lines represent model calculations using lamp intensity at 255 nm as adjustable parameter (best fit at 19.5 W) and a relative intensity spectrum determined from Figure 5-9..... 185
- Figure 5-11. *p*-Cresol oxidation at pH=6 in the pilot scale reactor system with polychromatic light source (reactor R2). Solid lines represent model predictions. Concentrations are measurements at the exit of the reactor (C_2)..... 186
- Figure 5-12. *p*-Cresol and fluorescein absorption spectrum in the UV range. 187
- Figure 5-13. Fluorescein oxidation at pH=9.8 in the pilot scale reactor system with polychromatic light source (reactor R2). Solid lines represent model predictions..... 188
- Figure 5-14. *p*-Cresol oxidation in the pilot scale reactor system with polychromatic light source (reactor R2). Solid lines represent the hydraulic model predictions considering the reactor as an ideal PFR and the reaction a first-order process. $k=0.71 \text{ min}^{-1}$ 189

LIST OF TABLES

Table 1-1.	Southwest water extraction in 2005 according to USGGS data (2).....	25
Table 1-2.	Colorado River use rights (2).....	25
Table 1-3.	Oxidation potentials of selected chemical oxidants (19).....	34
Table 2-1.	Physical properties, biodegradability data and removal data in conventional activated sludge for selected CECs.....	59
Table 2-2.	Total number of samples in activated sludge, confidence width, and assessment of removal for selected CECs. For criteria on low, medium and high qualifications, see Table 2-3.....	81
Table 2-3.	Summary of confidence level vs. removal efficiency for selected CECs (activated sludge processes).....	82
Table 3-1.	Elementary reactions in aqueous UV/H ₂ O ₂ photolysis in the presence of CO ₂ . Kinetic and equilibrium constants are at 25°C. Reactions E1 to E4 are considered to equilibrate instantaneously.	98
Table 3-2.	Elementary reactions in the Fe(III)-catalyzed decomposition of H ₂ O ₂ (25°C; ionic strength: 0.1 M). Values are taken from De Laat and Le; Fe(III) represents the sum of Fe ³⁺ , Fe(OH) ₂ ⁺ and Fe ₂ (OH) ₂ ⁴⁺ , while Fe(II) represents the sum of Fe ²⁺ and FeOH ⁺	110
Table 3-3.	Additional reactions for the Fe(III)/H ₂ O ₂ system in the presence of sulfate (25°C; ionic strength: 0.1 M). Values form De Laat and Le.	111
Table 3-4.	Carbon tetrachloride (CT) decomposition zeroth-order rate constant in actinometry experiments (k _λ) and resultant wavelength-dependent UV source intensity (I ₀)	114
Table 4-1.	Input parameters used to model the UV solar spectral irradiance (SMARTS) at the University of Arizona in Tucson, AZ	146

ABSTRACT

Every year, new trace chemicals are detected in natural waters as well as treated wastewater effluents all over the world. Public health and environmental concerns have driven the development of new technologies to treat water and eliminate chemicals that may pose risk to humans and wildlife. This work presents a detailed statistical analysis on the removal of some of the most widely occurring chemicals of emerging concern in wastewater based on information available in the literature. Results show that existing water treatment processes only partially eliminate most of these contaminants. Advanced oxidation processes (AOPs) are some of the technologies that have shown the most promising results for the removal of recalcitrant organics in water. Hydrogen peroxide photolysis (UV/H₂O₂) and Fenton's reaction are some examples of AOPs that use hydroxyl radicals to oxidize organics.

The kinetics of UV/H₂O₂ and Fenton's reaction were studied from the experimental and mathematical points of view. Comprehensive models with no adjustable parameters successfully accounted for radical initiation via photolysis of H₂O₂ or radical initiation via Fenton's mechanism; reaction of organic targets such as p-cresol and nonylphenol with hydroxyl radicals; and recombination mechanisms, as well as changes in solution pH due to evolution of carbon dioxide because of target mineralization. The presence of radical scavengers was successfully handled by the models, suggesting that they can be generalized to the treatment of complex matrices.

The UV/H₂O₂ model was also extended to solar catalyzed applications. Using an atmospheric solar irradiation model (SMART) and data from the Giovanni-NASA online database, ground-level solar spectral irradiance were obtained and used as model inputs. The kinetic model provided an excellent fit to experimental results obtained with p-cresol and fluorescein targets using no fitted parameters.

The UV/H₂O₂ process was also studied in commercial flow-through UV reactors with monochromatic and polychromatic light sources. Organic targets of interest such as p-cresol can be degraded effectively in these reactors at relatively low peroxide concentrations. Results with wastewater effluents suggest that these commercial reactors can be used for AOP tertiary treatment as a way to reduce dissolved organic matter and eliminate potential harmful chemicals present in the water.

DISSERTATION OVERVIEW

This dissertation work is divided in six chapters and three appendices with supplementary and supporting material. A brief description of the content of each of the section is given below.

Chapter 1. Introduction.

This chapter presents a general introduction on the topic of trace organic contaminants in natural waters and wastewater, and the motivation to perform the research work. A brief background is presented to illustrate the problem, its context and the importance of advanced oxidation processes as a relatively new technology to clean water. Also, the objectives of the research project are highlighted here.

Chapter 2. Assessment of the Effectiveness of Secondary Wastewater Treatment Technologies to Remove Trace Chemicals of Emerging Concern.

A critical review on the effectiveness of current wastewater treatment technologies is presented through a detailed statistical analysis of the literature data from the last ten years. Treatment-dependent attenuations during conventional wastewater treatment are examined in depth for forty chemicals of emerging concern frequently detected in wastewater effluent. Biological treatment processes contributing to the review included conventional activated sludge, membrane bioreactors, trickling filters, sequencing batch reactors and lagoons. The results of the review include physical characteristics and biodegradability data that are potential determinants of removal mechanisms, so that the

efficiency of conventional treatment for management of a great many compounds that have not been widely monitored can be anticipated.

Chapter 3. Modeling of Advanced Oxidation of Trace Organic Contaminants by Hydrogen Peroxide Photolysis and Fenton's Reaction.

This chapter presents the study of the photolysis of hydrogen peroxide and Fenton's reaction to oxidize different trace organic compounds such as nonylphenol (NP) and p-cresol (PC) in aqueous solution. Bench-scale experiments were performed at different wavelengths and different dosages of hydrogen peroxide (H_2O_2). The objective was to measure rates of the target destruction as a function of hydrogen peroxide concentration, UV irradiation, and the presence of scavenger compounds.

Comprehensive kinetic models with no adjustable parameters were used for both UV/ H_2O_2 and Fenton's processes to predict the kinetics of oxidation of the targets under different experimental conditions. An optimization of the process in batch reactors using the model as a predictive tool is presented for the removal rates of trace organic with different second-order rate constants of reaction with hydroxyl radicals.

Chapter 4. Advanced Oxidation of Trace Organics in Water by Hydrogen Peroxide Solar Photolysis.

This chapter presents a novel exploration of the UV/ H_2O_2 process catalyzed by solar irradiation. The kinetics of oxidation of p-cresol and fluorescein were investigated using solar light as UV irradiation source in homogeneous batch reactors under different

experimental conditions. The UV/H₂O₂ kinetic model, previously developed for monochromatic light, was extended to solar polychromatic UV irradiance (280-400 nm). The model requires the input of the global ground-level solar spectral irradiance distribution in 5-nm bandwidths, and accounts for the changes in absorbance and light intensity in the whole UV-range, assuming a constant quantum yield for the hydrogen peroxide photolysis. The solar spectral irradiance for the specific experimental dates have been computed using the SMARTS model that takes into account optical depth, ozone and water vapor content in the atmosphere, which have been obtained from the Giovanni-NASA online database. The model was successfully applied to predict the kinetics of degradation of p-cresol and fluorescein.

Chapter 5. Experimental Simulation of Advanced Oxidation Processes in Flow-Through Reactors.

The application of UV/H₂O₂ in continuous-flow reactors, primarily designed for disinfection purposes, is evaluated in this chapter. Two reactors, the first using monochromatic light (low pressure lamp) and with the second using polychromatic light (medium pressure lamp) were employed to study the oxidation of p-cresol and fluorescein. The AOP kinetic model was combined with the hydraulics of the reactor with successful results for the monochromatic lamp reactor in the prediction of oxidation rates. The effectiveness of the process to treat real wastewater effluents and to evaluate the scavenging effect of wastewater was also explored in this section.

Chapter 6. Conclusions.

The environmental impact of the conducted research and main conclusions from this dissertation are highlighted in this chapter.

Appendix A. Supplementary Material about CECs Removal

Appendix A includes information about CECs classification and CECs literature that support results presented in Chapter 2.

Appendix B. Supplementary Material for the UV/H₂O₂ and Fenton's Kinetic Models

Appendix B includes information about the kinetic models to support material for the results and discussion presented in Chapter 3 and 4.

Appendix C. Additional Research on Flow of Non-Newtonian Slurries with Application to Transport of Nuclear Waste

This appendix includes a manuscript prepared for publication that is associated with independent research carried out in collaboration with Pacific Northwest National Laboratory (PNNL) Mathematical models were developed to predict pressure drops and solids concentration distributions in flows of non-Newtonian slurries through pipes. The main novelty of the approach was the extension of previous models to deal with high-density and large particle size solids.

CHAPTER 1

INTRODUCTION

1.1. Environmental Significance

During the last decade there has been an increasing worldwide concern on the effects that human activities have on available water resources. The importance of this goes beyond the scope of specific research interests as the sustainable use of our natural resources, especially water resources, will determine our ability to survive and to prosper.

Each watershed in the United States has an estimated average renewable water supply. This is basically rainfall less evaporation plus imports (via rivers and canals) and minus exports. This is a crude upper limit of water that can be consumed sustainably in the same region. The United States Geological Survey keeps these data for watersheds in the United States (1). The Colorado River Basin is the most stressed watershed in the US, since the region is consuming more water than is provided annually. The difference must be made up by “mining” ground water—taking more water out of the ground than nature replenishes (Tables 1-1 and 1-2).

In Arizona, as well as other inland semi-arid regions worldwide, one of the primary underutilized water resources is reclaimed wastewater. Research is required to maximally utilize these resources appropriately and safely. Water demand in the Southwest will outstrip water supply in the near future. Throughout the Southwest of the US, groundwater supplies 35 percent of water use, and the Colorado River supplies another

18 percent; however in Arizona, groundwater plus the Colorado River amount to 90 percent of total water use (2.3 trillions of gallons per year). Both sources are being used at a rate that cannot be sustained (2). For illustration, the rate of groundwater withdrawal in Arizona is roughly 1.0 trillion of gallons per year. Unfortunately, the regional rate of groundwater replenishment is about two thirds of that amount. An overdraft of 358-billion of gallons per year will persist despite the full utilization of regional rights to Colorado River water that is itself of impaired quality (2). At the same time, the region is reusing little of the wastewater effluent that is produced in the State. In the case of the US Southwest, wastewater effluent is mostly recharged into local aquifers due to the absence of natural courses of water.

Table 1-1. Southwest water extraction in 2005 according to USGGS data (2).

Water Use	Southwest	Arizona	California	Nevada	New Mexico	Utah
Total water use (MAF ¹)	55.6	7.0	36.8	2.7	3.7	5.4
Total groundwater use (MAF)	19.4	3.4	12.0	1.1	1.9	1.0
Groundwater share of the total use for each region (%)	35	49	33	41	50	18

¹ Millions of acre ft

Table 1-2. Colorado River use rights (2).

Water Use	Southwest	Arizona	California	Nevada	New Mexico	Utah
Colorado River use rights (MAF)	10.1	2.9	4.4	0.3	0.9	1.7
Colorado supply as a share of total use for each region (%)	18	41	12	11	23	31

Even though wastewater treatment processes are efficient in improving the quality of the treated water, one aspect of current technologies is that they only partially remove certain trace contaminants that as a result, end in the streams of natural waters (3,4). The U.S. Environmental Protection Agency (EPA) regulates more than 90 specific contaminants in public drinking water supplies. Natural waters affected by the effluent of wastewater treatment plants contain, in general, additional synthetic chemicals that may impact aquatic life and that have potential effects on human health (4). In particular, concern has grown in the last few years over the presence of pharmaceuticals, personal care products, natural and synthetic hormones, and pesticides in wastewater effluents. Some of these chemicals are endocrine disrupting compounds (EDCs) and their effect on fish and wildlife has been widely documented (5).

1.2. Conventional Wastewater Treatment

The persistence of problems related to fecal contamination of water arose from our use of surface waters as both sources of potable water and conduits for the removal of waste. In parts of the United States and elsewhere, cities are strung out along rivers that both supply water and serve as a discharge point for treated wastewater. To protect in-stream water uses such as fishing and swimming, and downstream communities that also depend on the river as a potable water source, wastewater is treated before it is discharged.

With the exception of a handful of large cities that discharge treated wastewater to the ocean, all municipal wastewaters must receive a minimum of secondary treatment before treatment plant effluents can be released back to the environment. Secondary treatment

consists of a combination of three treatment stages (Figure 1-1): (i) preliminary treatment to remove material that might damage mechanical equipment in the wastewater treatment plant—large objects, hair, gravel, grit and so forth, (ii) primary treatment to remove solids capable of settling—those with settling velocities large enough to remove them via sedimentation during quiescent periods of a few hours, and (iii) some form of biological treatment to remove additional solids and biodegradable organics. Together these processes comprise secondary treatment, which is quantified by the percentage removal of suspended solids and biochemical oxygen demand across the treatment plant. The most common form of biological treatment is called activated sludge. Other important biological treatments are membrane bioreactor (MBR) and tricking filters (6).

The distinguishing features of activated sludge treatment are the provision of supplemental oxygen and the separation and recycle of microorganisms to the bioreactor to accelerate the microbially-mediated oxidation of organic material in the treatment plant. Wastewater treated in this way is usually chlorinated to kill pathogens and then dechlorinated to protect wildlife before it is discharged into the environment.

In many communities, only secondary treatment is provided before the treated wastewater is discharged. In others, additional treatments, collectively called “tertiary treatment” are practiced to protect the effluent receiving waters (lakes and streams).

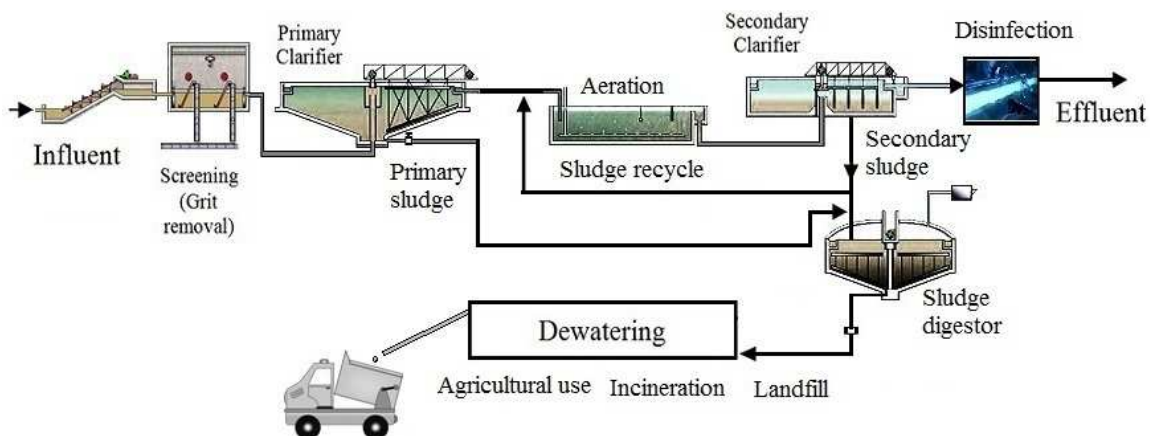


Figure 1-1. Secondary treatment is provided via a combination of pre-treatment steps, primary treatment and biological treatment. Solids generated and separated during these processes are stabilized via sludge digestion, dewatered and then disposed of.

There are many types of tertiary treatment processes, but the most common ones used are for nutrient removal (nitrogen or phosphorus) to avoid in-stream stimulation of algal growth and eventual depletion of dissolved oxygen. Other tertiary treatments are designed to remove or destroy residual organics or trace organics that escape secondary treatment (6,7). These include adsorption of residual organics on activated carbon and advanced oxidation processes. Such additional treatments become important in situations where water reuse is anticipated.

1.3. Chemicals of Emerging Concern

The development of new analytical techniques and equipment have allowed the detection of new organic contaminants in natural waters and at the different stages of wastewater treatment processes. Nevertheless, there are still gaps and limitations regarding the reliability of these measurements, which continue to be a challenge for chemists and

engineers. As a consequence, there is an expanding database in the literature regarding the presence of these compounds in surface waters and, to a lesser degree, their respective fates during wastewater treatment. Trace organics that are unregulated for which there is uncertainty as to possible impact on ecosystem and human health of long-term exposures have been denominated as “chemicals of emerging concern” (CECs).

The EPA and the Water Environment Research Foundation (WERF) have reviewed CECs in wastewater and their WWTP removal efficiencies. The EPA measured CECs throughout nine WWTPs (8). The CECs sampled included pharmaceuticals and personal care products, steroids and hormones, alkylphenols and alkylphenol ethoxylates, polybrominated diphenyl ethers (PBDEs) and pesticides. A large fraction of the compounds were present in the inlet and outlet of multiple WWTPs. However, the objective of the study was not to assess compound-specific removal efficiencies, and the authors cautioned that the data gathered were insufficient for that purpose.

More recently, EPA (9) summarized influent-to-effluent removals for the same classes of CECs plus polynuclear aromatic hydrocarbons, plasticizers and flame retardants other than PBDEs. A total of 246 compounds were surveyed using 88 references spanning the period 2003-2008, and a database with removal efficiencies was compiled. A detailed analysis was presented for a subset of 16 compounds. The results of this study confirm that most of emerging contaminants assessed are only partially removed during conventional biological treatment processes.

Miege *et al.* (10) in 2009, compiled a database for occurrence and removal of 183 personal care products and pharmaceuticals (PPCPs), based on 117 publications. In general, it was found that PPCPs have a frequency of occurrence in the influent and effluent of wastewater treatment plants above 90% for most of the compounds included in the study. In terms of removal, hormones show the highest removal efficiencies (70-99 %) while other drugs such as carbamazepine (<10%), clofibric acid diclofenac (<25%) seem to be persistent through activated sludge processes. The authors also explored the efficiency of different secondary treatment processes, finding activated sludge with nitrogen removal and membrane bioreactors as the most promising technologies to destroy PPCPs.

Although wastewater treatment plants or municipalities do not generally require companies to request permission to discharge trace organic contaminants into the waste stream, in the case of pharmaceuticals, the Food and Drug Administration (FDA) does require drug manufacturers to calculate an Estimated Introduction Concentration (EIC) for new pharmaceuticals under its National Environmental Policy Act of 1969 obligations (11).

The EIC calculation is based on the estimated annual usage for the active ingredient distributed uniformly throughout the US according to population and wastewater generation rates, without accounting for the drug's metabolism in either the human body or wastewater treatment processes. Revisions to the FDA's regulatory process enacted in June 1997 created categorical exemptions from the general requirements for full

Environmental Assessments of a drug's potential impact when the EIC yielded concentrations less than one part per billion (11). Despite these regulatory efforts, wastewater treatment plants (WWTPs) represent a major disposal route for many emerging contaminants (12,13). Waste load estimations are loosely supported by difficult-to-make correlations between human pharmaceutical loads in raw wastewater with local sales figures for the same products (3). However, based on the EIC formula, Arcand-Hoy *et al.* (14) estimated the concentrations of 17β -estradiol (E2), 17α -ethinyl estradiol (EE2) and total conjugated estrogens is on the order of 2-40 ng/L in raw domestic sewage. These estimations are in good agreement with observed concentrations of these compounds in raw wastewater samples (12,15).

The most commonly cited ecological impacts from wastewater CECs result from disruption of endocrine system function among continuously exposed aquatic life (5,16). For that reason, WWTP removal of estrogens and estrogen mimics has been a common research focus (15). The compounds most frequently identified as endocrine disrupting compounds (EDCs) in wastewater include natural hormones (17β -estradiol) and their related metabolites (estrone and estriol). Estrogen mimics include 17α -ethinylestradiol (EE2, an oral contraceptive) and the alkylphenol polyethoxylates (APEs; a class of surfactants) and their derivatives, of which nonylphenol (NP) and octylphenol (OP) are the most important (15).

The widespread presence of APEs in United States surface waters (17) suggests that they may contribute to intersex characteristics (mild hermaphroditism) that are now frequently

observed in natural water fish affected by the discharge of treated municipal wastewater. The estrogenic potencies of APEs are several orders of magnitude below those of natural estrogens and birth control agents like EE2 (15). Nevertheless, the concentration of these compounds in the environment can be orders of magnitude greater than those of the hormones.

1.4. Advanced Oxidation Processes: UV/H₂O₂

The presence of trace organic contaminants in wastewater has become a widely observed phenomenon, driving many researchers to focus their efforts on identifying treatment processes that have the best removal efficiency (12). This approach will presumably elucidate commonalities among highly performing systems and provide insight into the most efficient removal mechanisms. Activated carbon, membrane bioreactors, ozone, ultraviolet radiation, filtration and advanced oxidation processes have all, on different conditions, exhibited high removal efficiencies for diverse trace organic contaminants (12,18).

Advanced Oxidation Processes (AOPs) involve specific chemical reactions in which oxidation of organic contaminants occurs primarily through reactions with oxidants such as hydroxyl radicals ($\bullet\text{OH}$) (19). The suitability of AOPs for pollutant degradation was recognized in the early 1970s and much research and development work has been undertaken to commercialize some of these processes. They are particularly useful for cleaning biologically toxic or non-biodegradable materials such as aromatics, pharmaceutical, endocrine disrupting chemicals, pesticides, petroleum constituents, and

volatile organic compounds in wastewater. Among different available AOPs producing hydroxyl radicals, a combination of a strong oxidizing agent (e.g. hydrogen peroxide) with a catalyst (e.g. transition metal ions) and/or irradiation (e.g. ultraviolet light) seem to be the most widely available technologies for tertiary wastewater treatment (19).

Chemical oxidation is defined as the transfer of one or more electrons from an electron donor (reductant) to an electron acceptor (oxidant), which has a higher affinity for electrons. These electron transfers result in the chemical transformation of both the oxidant and the reductant, in some cases producing chemical species with an odd number of valence electrons. These species, known as radicals, tend to be highly unstable and, are therefore, highly reactive because one of their electrons is unpaired. Oxidation reactions that produce radicals tend to be followed by additional oxidation reactions between the radical oxidants and other reactants until thermodynamically stable oxidation products are formed. The ability of an oxidant to initiate chemical reactions is measured in terms of its oxidation potential (Table 1-3). The hydroxyl radical is one of the most potent oxidizing agents known in nature.

Klaraviroti *et al.*, in 2009 (20), reviewed the uses of advanced oxidation processes to eliminate pharmaceuticals from water and wastewater. In their assessment they found that, from the current available literature on AOPs, 32% is devoted to study the application of heterogeneous catalysis such as UV-titanium dioxide, 30% is focused on ozonation; 13% on Fenton's and photo-Fenton's processes, and 12% on UV/H₂O₂

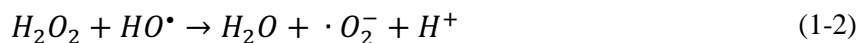
process. The remaining 13% is divided between technologies with less applications such as sonolysis, wet air oxidation and electrolysis (20).

Table 1-3. Oxidation potentials of selected chemical oxidants (19).

Compound	Oxidation Potential (V)
Hydroxyl Radical ($\bullet\text{OH}$)	2.8
Sulfate Radical ($\text{SO}_4^{\bullet-}$)	2.6
Ozone (O_3)	1.5
Hydrogen Peroxide (H_2O_2)	1.8
Permanganate	1.7
Chlorine Dioxide	1.5
Chlorine	1.4
Oxygen	1.2
Bromine	1.1
Iodine	0.76

Among all AOPs, two processes have gained more attention in recent years for their application to destroy trace organic contaminants: UV/ H_2O_2 and Fenton's reaction. UV/ H_2O_2 is a photo-catalyzed process that relies on the peroxide absorption of UV light to react and produce hydroxyl radicals (equation 1-1). This homogeneous process has the advantage that it does not require the recovery or extraction of a catalyst from the water and can be applied at near-neutral pHs. The main disadvantage is, that given the low molar absorption coefficient of hydrogen peroxide in the UV range ($19.6 \text{ M}^{-1}\text{cm}^{-1}$ at 254 nm), in order to be effective, relatively high concentrations of peroxide need to be used to absorb the maximum amount of light possible (21). However, excesses of hydrogen

peroxide slows down the process due to its scavenging effect on hydroxyl radicals (equation 1-2).



The quantum yield of the photolysis of H_2O_2 by 254 nm light in a 0.1 N perchloric acid solution is found to be 1.00 at 25°C and it is independent of concentration and light intensity over the range of 2×10^{-5} to 0.1 M and 4.5×10^{-7} to 5×10^{-4} Ein $L^{-1}min^{-1}$ (22). The hydroxyl radical produced in this reaction will react with the organic target. The target may be also directly degraded by direct UV irradiation. Both contributions to the overall oxidation of the target (T) yield the following kinetic equation (21)

$$\frac{d[T]}{dt} = -k_{OH,T}[T][\bullet OH] - \phi_T I_o f_T (1 - e^{-2.303A}) \quad (1-3)$$

where $k_{OH,T}$ is the second-order intrinsic rate constant of reaction between the hydroxyl radicals and the target ($M^{-1}s^{-1}$); ϕ_T is the quantum yield of the direct photolysis of the target, usually determined empirically from experimental data; I_o represents the light intensity at the selected wavelength in Ein $L^{-1}min^{-1}$; and f_T is the fraction of light absorbed by the target, which is given by

$$f_T = \frac{\epsilon_T [PC] L}{A} \quad (1-4)$$

where ϵ_T is the molar absorption coefficient of the target and L is the effective path length of the reactor. The total absorbance is expressed as follows

$$A = (\epsilon_T [T] + \epsilon_{H_2O_2} [H_2O_2]) L \quad (1-5)$$

Alkalinity can adversely affect the UV/H₂O₂ process. Inorganic carbon species, bicarbonate and carbonate ions are natural scavengers of hydroxyl radicals and, therefore, are expected to affect the rate of reaction of the target with the hydroxyl radical (21),



In the presence of carbonate and bicarbonate ions, some of the hydroxyl radicals react to form carbonate radicals (CO₃^{•-}) via reactions 1-6 and 1-7 (23). The kinetics and mechanism of carbonate radical reactions with organic compounds is still poorly understood; however, there are sufficient data to suggest that these radicals may react more selectively with organic compounds than hydroxyl radicals, and that their intrinsic rate constants are generally much lower than those observed with •OH (24).

Because of the effectiveness of ultraviolet (UV) radiation for disinfecting drinking water, many water utilities will be installing UV capability in the coming years. As interest in

UV radiation technology for disinfection of microbial contaminants increases, water utilities that are also concerned with treating chemical contaminants of emerging concern have begun looking into the application of AOPs using UV in combination with hydrogen peroxide (25).

Previous work has contributed to the development of a kinetic model for the UV/H₂O₂ process over the past two decades. Glaze *et al.* in 1995 (26), proposed a kinetic model containing the most important elements of the UV/H₂O₂ photolysis to predict the time-dependent concentration of a halogenated target. They used a quasi-steady-state assumption (QSSA) to account for all system free radicals concentrations. This model did not account for carbon dioxide (CO₂) evolution/pH change and neglected the role of all radical scavenging species except for H₂O₂. The modeling approach of Stefan *et al.* (27) was similar, but it was assumed that the target compound (acetone) was transformed to oxalic and formic acids and then to CO₂, resulting in a steady decline in pH.

Subsequently, Crittenden *et al.* (28) modeled the same chemical mechanism without reliance on a quasi-steady-state assumption for radical concentrations ($\dot{\text{O}}\text{H}$, $\text{O}_2^{\dot{-}}$, and $\text{CO}_3^{\dot{-}}$). Their work showed that the QSSA tends to under-predict hydroxyl radical concentrations and therefore the target rates of decomposition. Furthermore, their model included radical scavenging reactions that were previously neglected. Their experiments included the presence of a phosphate buffer and it was assumed that the halogenated targets were oxidized to carbon dioxide and mineral acids so that pH effects could be anticipated by using the charge balance of the solution at every step of the integration.

Song *et al.* (29) developed a model based on earlier efforts that accounts for time-dependent radical concentrations, pH changes due to product formation of carbon dioxide and mineral acids, radical scavenging by H_2O_2 and surrogates of natural organic matter; and known radical/radical extinction reactions. Their resulting model is in agreement with their experimental data for rate of decomposition of alachlor, pH changes, and hydrogen peroxide oxidation.

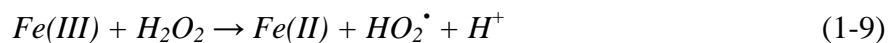
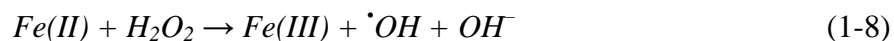
All previous models assume that concentrations of all species in the reactor are uniform. However, light enters the reactor through a surface and is absorbed (mostly by H_2O_2) as it penetrates the reactive mixture. Since light intensity decays with distance from the source, the rate of production of hydroxyl radicals is not uniform in the reactor even if the hydrogen peroxide concentration is uniform. When most of the incident light is absorbed, uniform concentrations would require a mixing regime that can overcome the non-uniformity of the light intensity and local radical generation.

1.5. Fenton's Reaction

Fenton's oxidation is a homogeneous process that is performed in the presence of ferrous and ferric ions with hydrogen peroxide. It is considered to be a metal-catalyzed oxidation reaction, in which iron acts as the catalyst. In addition, Fenton's oxidation is relatively faster than many others AOPs such as ozonation, UV/ TiO_2 or UV/ H_2O_2 (20).

In Fenton's reaction, the generation of hydroxyl radicals relies on the cycle of Fe(II) and Fe(III) due to their reaction with H_2O_2 at low pHs. The oxidation of Fe(II) produces the

hydroxyl radicals capable of reacting with the target organics presents in the water (equations 1-8). However, reduction of Fe(III) to Fe(II) limits the overall rate of radical production under most circumstances (equation 1-9); this makes iron speciation a strong determinant of Fenton's kinetics (30).



Solution pH is a critical parameter in Fenton's reaction since it determines iron speciation in ferric ions and hydroxylated forms ($FeOH^{2+}$, $Fe(OH)_2^+$, $Fe_2(OH)_2^{4+}$). Moreover, Fe(III) solubility limits the process for its application only at $pH < 3$ (20). Furthermore, the process is sensitive to the presence of other ions such as chloride and sulfate that can also produce iron complexes that limit the availability of Fe(II) species and therefore, the rate of production of hydroxyl radicals (31). Even though Fenton's oxidation has limitations for its application to treat large volumes of water, the process can be effective for other environmental applications. For instance Fenton's reaction has proven to be an effective way to regenerate activated carbon by the elimination of the chemicals adsorbed on the pores of the granular material (32).

1.6. Project Objectives

This dissertation has a general objective to investigate and quantify the UV/H₂O₂ AOP for the treatment of natural waters and wastewater effluents to eliminate trace organic species of emerging concern. To emphasize the relevance of the research, this work has included a comprehensive statistical analysis of the scientific literature from the last decade that provides evidence of the limitations of current wastewater technologies for destroying these chemicals releases from industrial and residential activities.

The project combined laboratory bench-scale experimentation, pilot-scale experiments and first principles mathematical modeling to evaluate the effectiveness of artificial and natural UV-catalyzed AOPs to treat different matrices of water.

The specific objectives of the research included:

- To investigate the effects of intensity and nature of the UV source (monochromatic and polychromatic) on the kinetics of trace organics degradation by UV/H₂O₂ AOP.
- To evaluate the effect of hydrogen peroxide concentration on the efficiency of target decomposition.
- To develop a comprehensive kinetic model, and validate it with experimental data for predicting the degradation of organic targets under different experimental conditions.
- To quantify the scavenging effects of different organics on the kinetics of oxidation of trace organic contaminants.

- To extend the kinetic model for its application to polychromatic light from both a solar source and from artificial lamps.
- To use the kinetic model to establish the optimal experimental conditions to obtain the maximum removal efficiency for different families of trace organics with the minimum use of light power and hydrogen peroxide concentration.
- To explore the effectiveness of advanced oxidation processes to destroy natural organic matter from real wastewater effluents in continuous-flow pilot-scale experiments.

1.7. Literature Cited

- (1) USGS. National Water Summary 1983-Hydrologic Events and Issues: U.S. Geological Survey Water-Supply Paper 2250, 1984.
- (2) Ackerman, F.; Stanton, E.E. The Last Drop: Climate Change and the Southwest Water Crisis. Stockholm Environment Institute. February 2011.
- (3) Halling-Sorensen, B.; Nielsen, N.; Lanzky, P.F.; Ingerslev, F.; Holten Lützheft, H.C.; Jergensen, S.E. Occurrence, Fate and Effects of Pharmaceutical Substances in the Environment - A Review. *Chemosphere* **1998**, 36, 357.
- (4) Heberer, T.; Reddersen, K.; Mechlinski, A. From Municipal Sewage to Drinking Water: Fate and Removal of Pharmaceutical Residues in the Aquatic Environment in Urban Areas. *Water Sci. Technol.* **2002**, 46, 81.
- (5) Kidd, K.A.; Planchfield, P.J.; Mils, K.H.; Palace, V.P.; Evans, R.E.; Lazorchak, J.M.; Flick, R.W. Collapse of a Fish Population After Exposure to a Synthetic Estrogen. *Proc. Nat. Acad. Sci.* **2007**, 104, 8897.
- (6) Crittenden, J.C.; Trussell, R.R.; Hand, D.W.; Howe, K.J.; Tchobanoglos, G. Water Treatment: Principles and Design (MWH). Second Edition. Wiley, New York, NY, 2005.
- (7) Tchobanoglos, G.; Bourton, F.; Stensel, D. Wastewater Engineering Treatment and Reuse (Metcalf & Eddy Inc). Fourth Edition. McGraw Hill, New Jersey, NJ, 2003.
- (8) US EPA. Occurrence of Contaminants of Emerging Concern in Wastewater From Nine Publicly Owned Treatments Works. EPA-821-R-09-009. *Environmental Protection Agency*, Washington DC, 2009.
- (9) US EPA. Treating Contaminants of Emerging Concern: A Literature Review Database. EPA-820-R-10-002. *Environmental Protection Agency*, Washington DC, 2010.

- (10) Miege, C.; Choubert, J.M.; Ribeiro, L.; Eusebe, M.; Coquery, M. Fate of Pharmaceuticals and Personal Care Products in Wastewater Treatment Plants – Conception of a Database and First Results. *Environ Pollution* **2009**, *157*, 1721.
- (11) CDER. Guidance for Industry: Environmental Assessment of Human Drug and Biologics Applications. CMC 6, Revision 1. Center for Biologics Evaluation and Research, Center for Drug Evaluation and Research, Food and Drug Administration, *US Department of Health and Human Services*, Washington, D.C, 1998.
- (12) Khanal, S.K.; Xie, B.; Thompson, M.L.; Sung, S.; Ong, S.K.; Van Leeuwen J.H. Fate, Transport and Biodegradation of Natural Estrogens in the Environment and Engineered Systems. *Environ. Sci. Technol.* **2006**, *40*, 6537.
- (13) Zhao, Z.; Knowlton K.F.; Love, N.G. Hormones in waste from concentrated animal feeding operations, in Aga D.S. (ed), *Fate of Pharmaceuticals in the Environment and in Water Treatment Systems*, CRC Press, New York, NY, 2008.
- (14) Arcand-Hoy, L.D.; Nimrod, A.C.; Benson, W.H. Endocrine-Modulating Substances in the Environment: Estrogenic Effects of Pharmaceutical Products. *Intl. J. Toxicol.* **1998**, *17*, 139.
- (15) Teske, S.S.; Arnold, R.G.; Removal of Natural and Xeno-Estrogens During Conventional Wastewater Treatment. *Rev. Environ. Sci. Biotechnol.* **2008**, *7*, 107.
- (16) Taylor, A.A.; Jobling, S.; Nolan, M.; Tyler, C.R.; van Aerle, R.; Brighty, G. Spatial Survey of the Extent of Sexual Disruption in Wild Roach in English and Welsh Rivers. Science Report P6-018/SR. The Environment Agency, Bristol, UK, 2005
- (17) Kolpin, D.W.; Furlong, E.T.; Meyer, M.T.; Thurman, E.M.; Zaugg, S.D.; Barber, L.B.; Buxton, H.T.; Pharmaceuticals, Hormones, and Other Organic Wastewater Contaminants in U.S. Streams, 1999–2000: A National Reconnaissance. *Environ. Sci. Technol.* **2002**, *36*, 1202.
- (18) Carballa, M.; Fink, G.; Omil, F.; Lema, J.M.; Ternes, T. Determination of the Solid-Water Distribution Coefficient (KD) for Pharmaceuticals, Estrogens and Musk Fragrances in Digested Sludge. *Water Res.* **2008**, *2*, 287.

- (19) Dorfman, L.M.; Adams, G.E. Reactivity of the Hydroxyl Radical in Aqueous Solutions, National Standard Reference System. Monograph NSRDS-NBS 46. *National Bureau of Standards*, Washington DC, 1973.
- (20) Klavarioti, M., Mantzavinos, D.; Kassinos, D. Removal of Residual Pharmaceuticals from Aqueous Systems by Advanced Oxidation Processes. *Env. Intl.* **2009**, *35*, 402.
- (21) Tuhkanen T. UV/H₂O₂ processes, in Parsons, S. (ed), *Advanced Oxidation Processes for Water and Wastewater Treatment*. IWA Publishing, London, UK, 2004.
- (22) Baxendale, J.H.; Wilson, J.A. Photolysis of Hydrogen Peroxide at High Light Intensities. *Trans. Faraday Soc.* **1957**, *53*, 344.
- (23) Buxton, G.V.; Greenstock, C.L.; Helman, W.P.; Ross, A.B. Critical-Review of Rate Constants for Reactions of Hydrated Electrons, Hydrogen-Atoms and Hydroxyl Radicals in Aqueous-Solution. *J. Phys. Chem. Ref. Data* **1988**, *17*, 513.
- (24) Chen, S.; Hoffman, M.Z. Rate Constant for the Reaction of Carbonate Radicals with Compounds of Biochemical Interest in Neutral Aqueous Solution. *Rad. Res.* **1973**, *56*, 40.
- (25) Rosenfeldt, E.J.; Linden, K.G. The R_{OH,UV} Concept to Characterize and the Model UV/H₂O₂ Process in Natural Waters. *Environ. Sci. Technol.* **2007**, *41*, 2548.
- (26) Glaze, W.H.; Lay, Y.; Kang, J.W. Advanced Oxidation Processes - A Kinetic Model for the Oxidation of 1,2-Dibromo-3-Chloropropane in Water by the Combination of Hydrogen-Peroxide and UV-Radiation. *Ind. Eng. Chem. Res.* **1995**, *34*, 2314.
- (27) Stefan, M.I.; Hoy, A.R.; Bolton, J.R. Kinetics and Mechanism of the Degradation and Mineralization of Acetone in Dilute Aqueous Solution Sensitized by the UV Photolysis of Hydrogen Peroxide. *Environ. Sci. Technol.* **1996**, *30*, 2382.
- (28) Crittenden, J.C.; Hu, S.; Hand, D.W.; Green, S.A. A Kinetic Model for H₂O₂/UV Process in a Completely Mixed Batch Reactor. *Water Res.* **1999**, *33*, 2315.

- (29) Song, W.; Ravindran, V.; Pirbazari, M. Process Optimization Using a Kinetic Model for the Ultraviolet Radiation-Hydrogen Peroxide Decomposition of Natural and Synthetic Organic Compounds in Groundwater. *Chem. Eng. Sci.* **2008**, *63*, 3249.
- (30) De Laat, J.; Gallard, H. Catalytic Decomposition of Hydrogen Peroxide by Fe(III) in Homogeneous Aqueous Solution: Mechanism and Kinetic Modeling. *Environ. Sci. Technol.* **1999**, *33*, 2726.
- (31) De Laat, J.; Le, T.G. Kinetics and Modeling of the Fe(III)/H₂O₂ System in the Presence of Sulfate in Acidic Aqueous Solutions. *Environ. Sci. Technol.* **2005**, *39*, 1811.
- (32) De Las Casas, C.L.; Bishop, K.G. Bercik, L.M.; Johnson, M.; Potzler, M.; Ela, W.P.; Sáez, A.E.; Huling, G.G.; Arnold, R.G. In-Place Regeneration of Granular Activated Carbon Using Fenton's Reagents, *Innovative Approaches for the Remediation of Subsurface-Contaminated Hazardous Waste Sites: Bridging Flask and Field Scales*; ACS Symposium Series, **2006**, *940*, 43.

*CHAPTER 2

ASSESSMENT OF THE EFFECTIVENESS OF SECONDARY WASTEWATER TREATMENT TECHNOLOGIES TO REMOVE TRACE CHEMICALS OF EMERGING CONCERN

2.1. Abstract

This work presents the results of a literature review and statistical analysis of removals of chemicals of emerging concern (CECs) during conventional wastewater treatment. Process-dependent attenuations are examined for the 42 most frequently measured and reported CECs. Biological treatment processes included in the review are conventional activated sludge, membrane bioreactors, trickling filters, sequencing batch reactors and lagoons. Also summarized are compound-specific physical characteristics and biodegradability data that are potential determinants of removal. As anticipated, results of the statistical analysis point to biodegradability and hydrophobicity as the most important contributing factors for removal.

* A modified version of this chapter has been submitted for publication in *Critical Reviews in Environmental Science and Technology*.

2.2. Introduction

Trace organic chemicals in effluents from conventional wastewater treatment plants include pharmaceuticals, personal care products, endocrine disrupting compounds, and other household and personal use organics (1). When discharged to surface waters, trace organics in treated municipal wastewater can affect aquatic ecosystem health. Endocrine disrupting compounds are particularly well studied in this regard (2). There is a well-developed body of knowledge regarding methods for measuring trace organics at part-per-trillion concentrations, leading to a rapidly expanding database regarding the presence of these compounds in surface waters and, to a lesser degree, their respective fates during municipal wastewater treatment. Trace organics that remain unregulated at the federal level and which have uncertain impacts on ecosystem or human health due to chronic exposures are herein collectively called “chemicals of emerging concern” (CECs).

Relatively little is known regarding the attenuation of most CECs following their release into the environment. However, several noteworthy ecological effects have been linked to aqueous-phase CECs, particularly among continuously exposed fish (2). Environmental and especially human health effects of CEC exposures are particularly difficult to study, due in part to the simultaneous presence of multiple CECs in waters affected by municipal effluent discharges. Uncertainties regarding chemical toxicity encourage adoption of precautionary strategies relative to wastewater treatment and water reuse. The informational and regulatory void in this area interferes with water supply planning,

particularly in water-short areas such as the American Southwest, where water reuse is frequently required to satisfy water supply sustainability objectives (3).

Although wastewater treatment plants (WWTPs) were not specifically designed to remove CECs, physicochemical and biological processes that are part of current technologies contribute, with various degrees of success, to CEC removal during wastewater treatment. In a general sense, it is important to attribute the removal of CECs from wastewater to physical partitioning among liquid, gas and solid phases vis-a-vis biochemical transformation. Volatile CECs might be stripped into a gas phase contacting the wastewater in aerobic reactors. Similarly, hydrophobic CECs might partition to the sludge phase and leave the plant with the residual biosolids. Alternatively, biochemical transformation might destroy CECs or even produce potentially deleterious reaction by-products.

This study summarizes data for removal of CECs during conventional municipal wastewater treatment. The importance of this topic stems in part from expansion of water reuse practices and the potential cost of advanced water or wastewater treatment processes, should conventional treatment methods fail to meet public or environmental health objectives. We have arbitrarily confined our search to peer reviewed publications and agency reports from the last ten years. Older data appear if included in recent literature reviews. CECs selected for review include pharmaceuticals, personal care products, natural and synthetic hormones, alkylphenols and alkylphenol ethoxylates, pesticides, synthetic musks, perfluorinated surfactants and plastic-manufacture additives

(e.g. plasticizers). The study includes information from full-scale plants, pilot-scale studies and laboratory experiments on removal efficiencies for CECs. A total of 422 references that include reports from professional organizations and government agencies, peer-reviewed publications and literature reviews were surveyed. Forty-two compounds provided an adequate data set for statistical analysis of removal efficiency.

2.3. Previous Work

Over the last ten years, interest in the occurrence, fate and transport of CECs in the environment has increased substantially, as reflected by numerous surveys of natural water bodies, drinking water sources and wastewater treatment facilities. A subset of these works addresses aqueous-phase removal efficiencies of CECs in WWTPs. In the context of this work, aqueous-phase removal is defined based on the difference between total influent and effluent concentrations of respective compounds. In this section, we will summarize recent attempts to review and analyze the effectiveness of WWTPs for CEC management and generalize, if possible, on removals of specific families of compounds.

The US Environmental Protection Agency (EPA) and the Water Environment Research Foundation (WERF) have reviewed CEC incidence in wastewater and the removal efficiency in WWTP (4,5). Particularly, the EPA measured CECs throughout nine WWTPs (4). Chemicals included pharmaceuticals and personal care products, steroids and hormones, alkylphenols and alkylphenol ethoxylates, bisphenol A (BPA),

polybrominated diphenyl ethers (PBDEs) and pesticides. The EPA also has summarized influent-to-effluent removals for the same classes of CECs plus polynuclear aromatic hydrocarbons, plasticizers, and flame retardants other than PBDEs (5). More than 200 chemicals were initially surveyed, and 16 of those were selected based on the available literature. A detailed analysis was presented based on a database with removal efficiencies compiled. The objective of that work was similar to our own, but here we considered additional sources of information, expanded the reporting period, included a greater number of compounds in our survey, developed statistics from reported removals when sufficient data were available and used the weight of available evidence to make general statements regarding (i) the utility of conventional wastewater treatment for CEC management and (ii) the state of the engineering art or knowledge base in this area.

Stephenson and Oppenheimer (6) (WERF report) surveyed WWTP removal efficiencies for 20 pharmaceuticals and personal care products (PPCPs) to assess the effect of solids retention time (SRT) on removal efficiencies. SRT ranged from 0.5 to 30 days at the six WWTPs studied. Although data on occurrence and removal were scattered, specific conclusions could be reached regarding relative, compound-specific removal efficiencies. For example, galaxolide was widely observed in the waters tested, and its removal efficiency was generally low. In yet another survey, PPCPs were included in the more general category of household chemicals (7). Twenty-six representative compounds were selected, of which twenty were present in all wastewater samples analyzed. These included all the PPCPs surveyed. Compound-specific removals during conventional activated sludge and MBR processes varied greatly.

The reviews of Halling-Sorensen *et al.* (8) and Heberer *et al.* (9) covered the occurrence, fate and effects of pharmaceuticals in the environment, illustrating the limits of conventional treatment for attenuation of pharmaceuticals and the widespread presence of these compounds in both natural and drinking waters. Also, Jones *et al.* (2005) reviewed the occurrence and behavior of pharmaceuticals in different wastewater treatment processes. Subsequent monitoring studies efforts have shown that PPCPs are present in secondary effluents from WWTPs throughout the world —Clara *et al.* (10), Lindqvist *et al.* (11), Tauxe-Wuersch *et al.* (12), Yu *et al.* (13), Lishman *et al.* (14), Santos *et al.* (15), Jones *et al.* (16), Ying *et al.* (17), Sui *et al.* (18), Sim *et al.* (19) — among others.

A recent study (20) covering the occurrence and removal of 184 PPCPs at WWTPs found that the frequency with which those compounds were present at or above their respective quantification limits in influent and effluent was >90% for the majority of the compounds considered, including pharmaceuticals and personal care products.

One of the most documented impacts of wastewater CECs involve disruption of endocrine system function among continuously exposed aquatic life (2,21). For that reason, WWTP removal of estrogens and endocrine disruptors compounds (ECDs) has been a common research focus (22) Some of the most widespread ECDs in wastewater include natural estrogens (17β -estradiol, estrone and Estriol, 17α -ethynylestradiol, an oral contraceptive), alkylphenol polyethoxylates (APEs) and their derivatives.

The widespread presence of APEs in United States surface waters (1) suggests that they may contribute to intersex characteristics (mild hermaphroditism) that are now frequently observed in natural waters affected by the discharge of treated municipal wastewater. The estrogenic potencies of APEs are several orders of magnitude below those of natural estrogens and birth control agents like EE2, however, the concentration of these compounds in the environment can be orders of magnitude greater than those of the hormones (22). Petrovic *et al.* (23) studied the occurrence of APEs and both natural and synthetic steroids in wastewater treatment facilities, sludge samples, river water and sediments in Spain, concluding that “NP, estriol, and estrone, detected in water could be responsible for the increased VTG [vitellogenin] observed in male carp” in two rivers studied, thereby providing a link between wastewater effluent and endocrine disruption in fish. Cespedes *et al.* (24) found that relatively short chain APEs partition readily on organic-rich particulate matter such as sludges produced during wastewater treatment, while longer chain nonylphenol ethoxylates are relatively stable in the aqueous phase and therefore are present at higher concentrations in treated wastewater. Removal efficiencies for APEs varied from 37 to 90%, depending on the treatment process employed. The *Alkylphenol Ethoxylates Research Council* has reviewed APE removals during full-scale wastewater treatment and bench-scale simulations (25). Their scope included removal by both biological treatments (activated sludge, membrane bioreactor) and physicochemical processes such as nanofiltration, microfiltration and advanced oxidation.

Despite their importance in agricultural settings and their potential health effects (26), data regarding the removal of pesticides in conventional WWTPs are surprisingly sparse.

Use of lagoons and constructed wetlands for management of pesticides is relatively common, however. In this context, Braskerud and Haarstad (27) reviewed the relationship between retention time and pesticide removal in constructed wetlands. Factors contributing to pesticide removal included compound hydrophobicity (adsorption on organic matter) and biodegradability (for the nitrogen-rich pesticides).

Synthetic musk fragrances are commonly used in the cosmetic, detergent and perfume industries. They reach $\mu\text{g/L}$ -level concentrations in municipal wastewater (28). These chemicals are usually classified as nitro-aromatics (NMs) or polycyclic musks (PCMs). The use of NMs is declining due to recent concerns regarding their toxicity to humans. However, PCM use has increased. NMs such as musk ketone and musk xylene, and PCMs such as galaxolide (HHCB) and tonalide[®] (AHTN), represent more than 12% and 85% (respectively) of the total global consumption of synthetic musks (28,29).

Perfluorinated compounds (PFCs) such as perfluorooctanesulfonate (PFOS) and perfluorooctanoic acid (PFOA) are recalcitrant in the environment. Their main sources in natural waters are thought to be WWTP effluents and urban runoff (30). PFOS and PFOA are ubiquitous in United States municipal wastewaters. Reported concentrations in WWTP effluents range from 5.3-130 ng/L for PFOS to 2.5-58 ng/L for PFOA (31). It has been suggested that biodegradation of precursor compounds such as fluorotelomer sulfonates or fluorotelomer alcohols produce PFOS and PFOA during wastewater treatment (32). There is no evidence that PFOS and PFOA transformations are encouraged by specific conventional wastewater treatment processes or manipulation of

operational conditions. PFOS can be removed from water via adsorption on activated carbon (33).

The manufacture, use and disposal of plastics inevitably release a great variety of chemicals into the environment. Among the chemicals used to produce plastics, plasticizers such as di-(2-ethylhexyl) phthalate (DEHP) and di-(2-ethylhexyl) adipate (DEHA) are among the most commonly found ones in natural waters and municipal wastewaters (34). Plasticizers are also used in the production of paints, glues, lubricants, pharmaceuticals, cosmetics, and pesticides. Most plasticizers are not chemically bound within the cross-linked polymer product, allowing them to escape into the environment during manufacture, product use, and following product disposal. WWTP effluent and urban runoff are major environmental sources of phthalates.

2.4. Methodology

CECs were selected for review based on the *Review of Chemicals of Emerging Concern and Analysis of Environmental Exposures in the Great Lakes Basin*, submitted to the International Joint Commission (35). This list, which includes more than 300 compounds, was the starting point in our search for removal data regarding the performances of conventional wastewater treatment processes.

Our survey of CEC removal information was arbitrarily constrained by publication date (2000-2010) and treatment process selection—activated sludge, membrane bioreactors, sequencing batch reactors and lagoons. The Science Citation Index was the primary

source for peer-reviewed articles. References from, and citations to, the articles discovered initially were also surveyed. Additionally, reports from national and international agencies were scrutinized for data or general information about removal of CECs. These agencies or institutes include: the United States Environmental Protection Agency (USEPA), Water Environment Federation (WEF), Water Environment Research Foundation (WERF), United States Geological Survey (USGS), National Water Research Institute (NWRI), Minnesota Pollution Control Agency (MPCA), American Water Works Association (AWWA), Cooperative Research Centres (CRC Australia), European Commission Environment and Environment Canada. About 800 documents dealing with removal of organics in WWTPs and related processes were obtained and screened for information. Sources that survived an initial screening step contained both (i) influent-to-effluent removal data for one or more CECs, and (ii) descriptions of treatment processes and operating conditions. Documents based solely on the occurrence of CECs were not further considered.

Aqueous-phase removals were calculated based on concentrations in influent wastewater and secondary effluent using,

$$R (\%) = \frac{C_{influent} - C_{effluent}}{C_{influent}} \times 100 \quad (2-1)$$

A database was developed to compile and organize CEC removal data. When sufficient information was available, database entries included (i) contemporary treatment performance data such as removal efficiencies for TOC, BOD or COD, and (ii) both

influent-to-effluent and overall compound removals. The latter accounted for contaminant mass fluxes in biosolids as well as effluent. The database also contains compound-specific ready biodegradability data, and physical properties such as Henry's law (H) as a measure of volatility, and octanol-water (K_{ow}) partitioning constant as a measure of hydrophobicity.

Experimental values were obtained from the EPI SuitesTM 4.1 software and database (<http://www.epa.gov/opptintr/exposure/pubs/episuite.htm>). When empirical values were not available, EPI Suites was employed to predict partition constants using KOWINTM and HENRYWINTM (Bond Contribution model). For acids, octanol-water partition coefficients at pH 7 (D_{ow}), were calculated for compounds using the following expression,

$$D_{ow} = K_{ow} \frac{1 + 10^{-pKa}}{1 + 10^{pH-pKa}} \quad (2-2)$$

Equation (2-2) reflects an assumption that the ionized species does not partition into the octanol phase at either the pH for which D_{ow} is estimated (usually pH 7), or at pH 0, which is the reference value for K_{ow} .

Biodegradability information was obtained using two QSAR models, BIOWINTM 2 and 6, from EPI Suites. Both models predict the compound-specific probability of biodegradation based on the suite of functional groups that contribute to compound structure and the anticipated biodegradability of each functional group present.

Functional group biodegradabilities are determined from software databases. BIOWIN 2 uses a Syracuse Research Corporation database for that purpose (36), whereas BIOWIN 6 predictions are based on the OECD301C test, using data from the Chemicals Evaluation and Research Institute Japan (CERIJ) database (37). In addition, the STPWIN model, also from EPI Suites, was used to predict removal efficiencies in wastewater treatment plants for comparison to results obtained using the statistical approaches described here. STPWIN is a version of the Sewage Treatment Plant (STP) Model originally developed by Mackay and coworkers at the University of Toronto (38). The model predicts the fates of organic chemicals during conventional wastewater treatment with activated sludge. Removal mechanisms considered include evaporation, biochemical degradation and sorption to sludge. The most critical and often uncertain variable is the biodegradation rate and its dependence on biomass concentration (STPWIN Model). Therefore, empirical biodegradation rates in activated sludge were used, when available, as inputs for STPWIN. The treatment conditions and operational parameters used were defaults provided by the software.

To assist in data analysis, box-plots and cumulative probability curves were developed using OriginLab™ 8.0 software to represent distributions of compound-specific removal data (See details about box-plot characteristics in Appendix A). Only compounds for which sufficient activated sludge performance data are available ($n > 8$) were analyzed in this way. When sources reported more than one observation from a single facility, the average of these values was taken as a singular data point. When documents reported a range of removals, end values of the range were taken as data points to represent worst-

case performance variability. In all, 42 compounds satisfied criteria for statistical analysis. Chemical structures for these compounds are provided (Table A-1, Appendix A), and relevant compound-specific properties are summarized (Table 2-1). When possible, removals during activated sludge, membrane bioreactor, trickling filter, sequencing batch reactor and lagoon treatments are compared. Compound-specific references and a list of all the references included in the database for the forty-two CECs are provided in Appendix A.

As an measure of statistical confidence, the width of the 95% confidence interval for mean removal estimates was calculated as follows (39),

$$95\% \text{ CI width}(\%) = 2t \frac{S}{\sqrt{N}} \quad (2-3)$$

where t is the t -distribution value for the 95% confidence interval, S is the standard deviation, and N is the total number of independent removal measurements. We recognize that chemical-specific removal data were not always normally distributed, a condition on which the relevance of Eq. (2-3) normally rests. Nevertheless, confidence intervals for the population mean, so calculated, provide a relative indication of the reliabilities with which compound-specific removals arising during conventional wastewater treatment can be anticipated based on the weight of existing evidence.

Table 2-1. Physical properties, biodegradability data and removal data in conventional activated sludge for selected CECs.

CEC	CAS #	Biodegradability BIOWIN 2	Log K _{ow}	H (atm- m ³ /mole)	pK _a	Lab Test Removal Range % (# studies)	Pilot Plant Removal Range % (# studies)	Full Scale Removal Range % (# studies)
17 α -ethynyl estradiol (EE2)	57-63-6	Not Ready Biodegradable	3.67	7.94E-12 ^b	10.33 ^c	39-100 (n=9)	59-100 (n=9)	47-100 (n=18)
17 β -estradiol (E2)	50-28-2	Ready Biodegradable	4.01	3.64E-11 ^b	10.33 ^c	20-100 (n=11)	36.3-100 (n=7)	10-100 (n=44)
Acetaminophen	103-90-2	Ready Biodegradable	0.46	6.42E-13 ^b	9.46 ^c	91-100 (n=7)	20-99.9 (n=3)	98.4-100 (n=6)
Atrazine	1912-24-9	Not Ready Biodegradable	2.61	4.47E-09 ^b	3.2 ^c	25 (n=1)	-	22.7-95 (n=4)
Benzophenone	119-61-9	Ready Biodegradable	3.18	1.94E-06 ^b	-	95 (n=1)	-	62-99 (n=4)
Bezafibrate	41859-67-0	Inherently Biodegradable	4.25 ^a	2.12E-15 ^b	3.61	-	80.8-99 (n=2)	15-99 (n=12)
Bisphenol A	80-05-7	Inherently Biodegradable	3.32	9.16E-12 ^b	9.78 ^c	28-99 (n=5)	71.3 (n=1)	23-99 (n=23)
Caffeine	58-08-2	Inherently Biodegradable	-0.07	3.58E-11	-0.92 ^c	94-100 (n=1)	68-100 (n=3)	40-99 (n=20)
Carbamazepine	298-46-4	Inherently Biodegradable	2.45	1.08E-10	15.96	0-99 (n=14)	0-99 (n=9)	0-99 (n=39)
Ciprofloxacin	85721-33-1	Not Ready Biodegradable	0.28	5.09E-19 ^b	6.09	4-100 (n=5)	-	0-100 (n=15)
Clofibric acid	882-09-7	Not Ready Biodegradable	2.57	2.19E-08 ^b	2.84	16-75 (n=5)	1-30 (n=4)	15-99.6 (n=12)
Di (2-ethylhexyl) adipate (DEHA)	103-23-1	Ready Biodegradable	8.12 ^a	4.34E-07	-	-	-	80-99 (n=2)
Di (2-ethylhexyl) phthalate (DEHP)	117-81-7	Ready Biodegradable	7.6	2.70E-07	-	-	8.54 (n=1)	60-99 (n=8)
Diclofenac	15307-86-5	Not Ready Biodegradable	4.51	4.73E-12 ^b	4.0 ^c	0-58 (n=13)	0-75 (n=11)	0-98 (n=340)
Erythromycin	114-07-8	Not Ready Biodegradable	3.06	5.42E-29 ^b	8.88	2-89 (n=7)	35.4 (n=1)	0-100 (n=19)
Estriol (E3)	50-27-1	Ready Biodegradable	2.45	1.33E-12 ^b	-	91-99 (n=3)	0-80 (n=2)	16-100 (n=19)
Estrone (E1)	53-16-7	Not Ready Biodegradable	3.13	3.80E-10 ^b	10.33 ^c	20-100 (n=8)	52-100 (n=8)	0-100 (n=43)

Table 2-1. *Continued.*

CEC	CAS #	Biodegradability BIOWIN 2	Log KOW	H (atm- m ³ /mole)	pKa	Lab Test Removal Range % (# studies)	Pilot Plant Removal Range % (# studies)	Full Scale Removal Range % (# studies)
Galaxolide (HHCB)	1222-05-5	Not Ready Biodegradable	5.9	1.32E-04 ^b	-	0-92 (n=2)	0-86 (n=2)	40-99 (n=13)
Gemfibrozil	25812-30-0	Ready Biodegradable	4.77 ^a	1.19E-08 ^b	4.42 ^c	50-96 (n=4)	-	0-99 (n=15)
Ibuprofen	15687-27-1	Ready Biodegradable	3.97	1.50E-07	4.88 ^c	74-100 (n=11)	41-99 (n=12)	15.5-99 (n=38)
Indomethacin	53-86-1	Inherently Biodegradable	4.27	3.13E-14 ^b	4.50	23.4-100 (n=2)	-	0-98 (n=4)
Ketoprofen	22071-15-4	Ready Biodegradable	3.12	2.12E-11 ^b	4.45	30-98 (n=8)	10-97 (n=3)	11.2-100 (n=20)
Musk ketone	81-14-1	Not Ready Biodegradable	4.3	4.80E-10 ^b	-	-	-	53-85 (n=5)
N,N-diethyl- toluamide (DEET)	134-62-3	Ready Biodegradable	2.18	2.08E-08 ^a	-	-	-	0-91 (n=5)
Naproxen	22204-53-1	Ready Biodegradable	3.18	3.39E-10 ^b	4.19 ^c	50-100 (n=10)	55-93.3 (n=8)	43-99.6 (n=28)
Nonylphenol	25154-52-3	Ready Biodegradable	5.76	3.40E-05	10.3	28-99 (n=6)	74-96 (n=5)	24-100 (n=39)
Nonylphenol diethoxylate (NP2EO)	20427-84-3	Ready Biodegradable	5.20 ^a	2.56E-09 ^b	-	3.76-99 (n=8)	46-95 (n=6)	0-99 (n=21)
Nonylphenol monoethoxylate (NP1EO)	104-35-8	Ready Biodegradable	5.58 ^a	1.65E-07 ^b	-	20-98 (n=2)	-	41-97 (n=12)
Norfloracin	70458-96-7	Ready Biodegradable	-1.03	8.70E-19 ^b	-	-	50-64.6 (n=2)	0-99 (n=20)
Octylphenol	1806-26-4	Ready Biodegradable	5.5 ^a	4.50E-06 ^b	9.9	0	-	0-48 (n=7)
Perfluorooctanoic acid (PFOA)	335-67-1	Not Ready Biodegradable	4.81 ^a	9.08E-02 ^b	2.5**	0.93 (n=1)	-	0-42 (n=8)
Perfluorooctyl sulfonate (PFOS)	1763-23-1	Not Ready Biodegradable	-1.08*	1.10E-02 ^b	-3.3†	0	-	

Table 2-1. Continued.

CEC	CAS #	Biodegradability BIOWIN 2	Log KOW	H (atm- m ³ /mole)	pKa	Lab Test Removal Range % (# studies)	Pilot Plant Removal Range % (# studies)	Full Scale Removal Range % (# studies)
Pyrene	0129-00-0	Not Ready Biodegradable	4.88	1.19E-05	-	51-95 (n=4)	-	56-68 (n=1)
Ranitidine	66357-35-5	Not Ready Biodegradable	0.27	3.42E-15 ^b	2.7	-	24.7 (n=1)	31.2-98 (n=8)
Sulfamerazine	127-79-7	Not Ready Biodegradable	0.14	1.75E-10 ^b	7.4	100 (n=1)	-	0-75 (n=4)
Sulfamethoxazole	723-46-6	Not Ready Biodegradable	0.89	9.56E-13 ^b	6.16 ^c	30-96 (n=6)	73.8-99 (n=4)	17-96 (n=32)
Testosterone	58-22-0	Not Ready Biodegradable	3.32	3.53E-09 ^b	19.38 ^c	-	100 (n=1)	69-100 (n=4)
Tetracycline	60-54-8	Not Ready Biodegradable	-1.3	4.66E-24 ^b	3.3	37-89 (n=5)	79-89 (n=1)	0-100 (n=12)
Tonalide (AHTN)	1506-02-1	Not Ready Biodegradable	5.7	1.39E-04	-	50 (n=1)	60-85 (n=2)	6-98 (n=13)
Triclosan	3380-34-5	Not Ready Biodegradable	4.76	4.99E-09 ^b	8.1	10-94 (n=5)	0-97 (n=2)	0-99 (n=22)
Trimethoprim	738-70-5	Ready Biodegradable	0.91	2.39E-14 ^b	7.16 ^c	11-74 (n=3)	0-40.4 (n=2)	0-100 (n=26)

Biodegradability predictions are estimations made with BIOWIN™ 2 (EPI Suite™); classification: ready biodegradable corresponds to >60% degradation in Ready test, inherently biodegradable corresponds to degradation between 40 and 60% and not Ready biodegradable corresponds to <40% degradation.

Values of K_{ow} , pK_a and Henry's law constants were taken from EPI Suite™ database, except for (a) K_{ow} values calculated by simulations with KOWWIN™, and (b) Henry's law constants calculated by simulation with HENRYWIN™ (bond contribution model), both from EPI Suites™; (c) pK_a obtained from Stevens-Garmon *et al.* (42).

* K_{ow} for PFOS obtained from Beach *et al.* (43); ** pK_a for PFOA obtained from Prevedouros *et al.* (44); † pK_a for PFOS obtained from Brooke *et al.* (45).

2.5. Results and Discussion

2.5.1. Conventional Activated Sludge

About half of the articles and reports reviewed here contain data regarding WWTP removal efficiencies of pharmaceuticals, making them the most thoroughly studied class of CECs. Twenty of the 42 compounds judged to provide an adequate database for statistical summaries are pharmaceuticals. Box plot summaries of influent-to-effluent removals of prescription and non-prescription drugs during full- and pilot-scale activated sludge treatment of municipal wastewater are provided (Figures 2-1 and 2-2). Caffeine and acetaminophen (Figure 2-1) are effectively removed in most conventional wastewater treatment plants. Both were removed with near 100% efficiency in well over half the treatment plants in the survey. Influent-to-effluent removals of carbamazepine and diclofenac, on the other hand, were generally poor. Roughly half the plants in the survey exhibited <50% removal of diclofenac. Half the plants removed <20% of the influent carbamazepine. Both caffeine and acetaminophen are biodegradable (Table 2-1), perhaps accounting for the efficient removal of these compounds. Removal efficiencies of diclofenac, clofibric acid and indomethacin, among others, were highly variable, suggesting that design or operating conditions are important determinants of reported removals. Coefficients of variation (the ratio of the standard deviation to the mean) for these compounds all exceed 0.5, which suggest that the data are highly scattered.

Reported removals of antibiotics during activated sludge treatment of wastewater were also highly plant specific and perhaps sensitive to plant operating conditions (Figure 2-2). The only antibiotic with a mean removal value higher than 70% is tetracycline, while sulfamerazine and trimethoprim have values below 50%. The highest coefficients of variation were obtained for sulfamerazine and erythromycin (0.75 and 0.62, respectively), while norfloxacin and tetracycline data produced values lower than 0.4. A more detailed analysis is warranted to establish operating conditions that promote CEC removal.

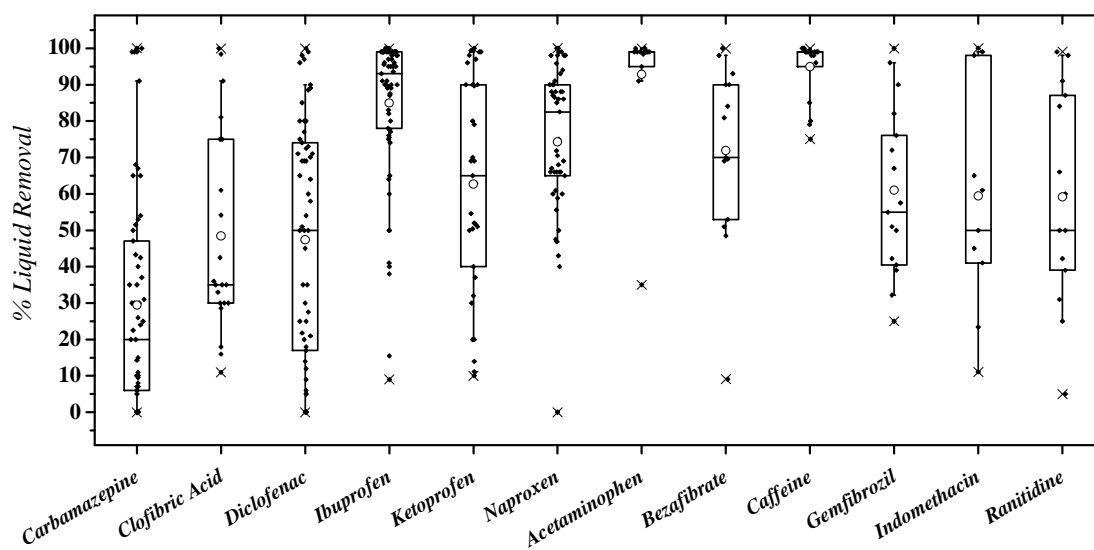


Figure 2-1. Box plots of liquid removal in activated sludge processes for selected pharmaceuticals. In this and subsequent plots, the boxes cover the 25 to 75 percentiles of the data range, the open circles are the median, the horizontal line in the box is the mean, the vertical lines extend between the 10 and 90 percentiles of the data set, and the X marks the whole data range. Scattered symbols represent the data.

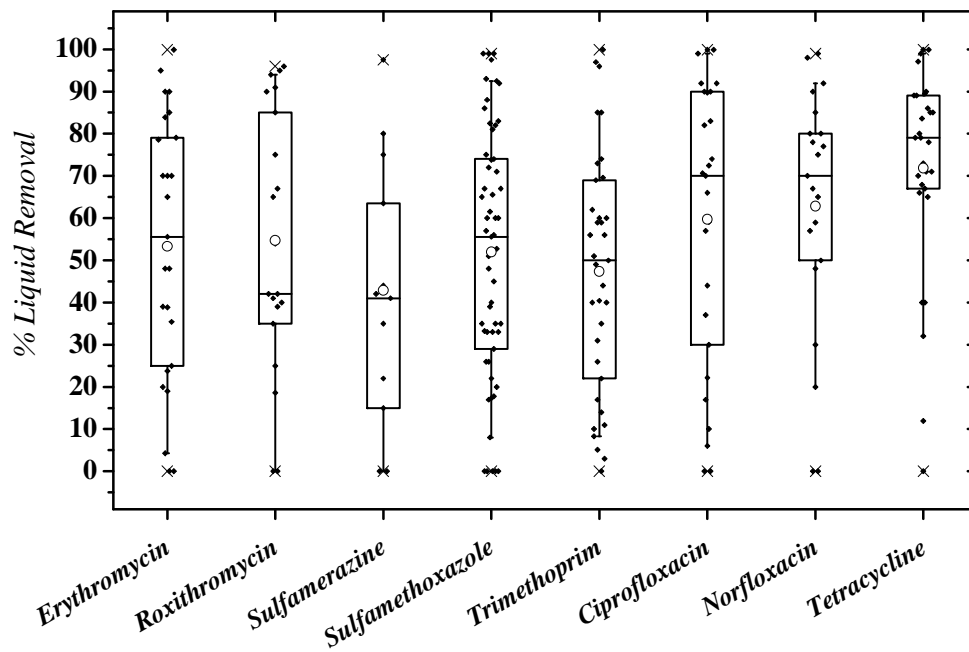


Figure 2-2. Box plots of liquid removal in activated sludge processes for selected antibiotics. Sulfamethoxazole, roxythromycin, norfloxacin and ciprofloxacin exhibit mean removal.

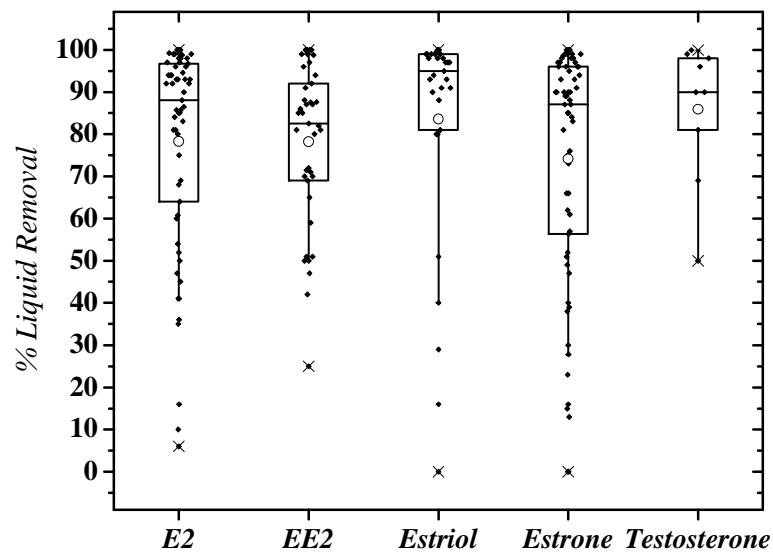


Figure 2-3. Box plots of liquid removal in activated sludge processes for selected natural and synthetic hormones.

Removals of estrogens and estrogen mimics were generally high. Median removal efficiencies were uniformly greater than 75% (Figure 2-3). The greatest degree of scattering was exhibited by estrone—coefficient of variation equal to 0.37. Nevertheless, estrogen-dependent ecological effects are frequently observed among fish populations that are continuously exposed to treated wastewater. Despite relatively high removal efficiencies, human hormones probably contribute significantly to estrogenic activity in wastewater effluent. Estrone is approximately 30% as potent an estrogen as EE2 (22). EE2 produces devastating effects on fish populations at exposure levels of a few ng/L (2).

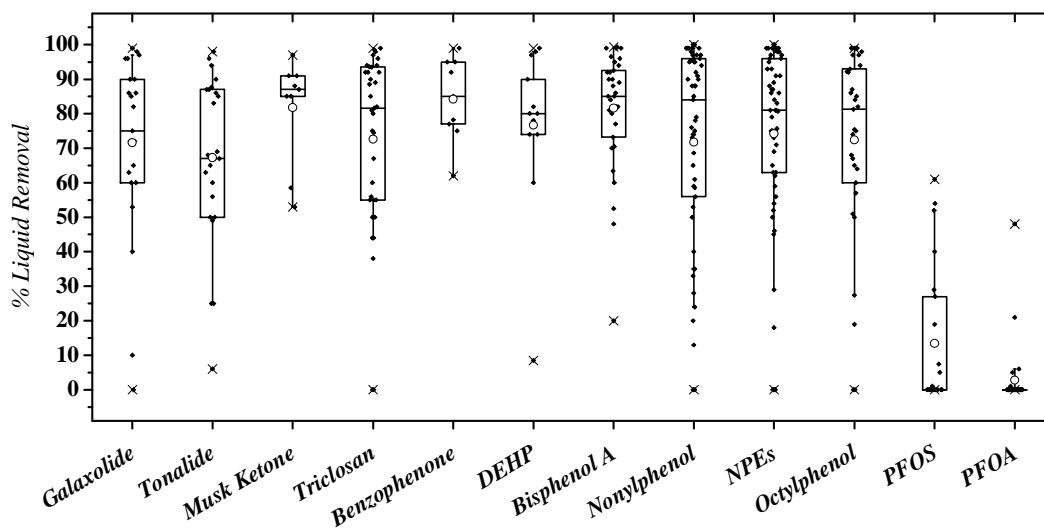


Figure 2-4. Box plots of liquid removal in activated sludge processes for selected organic wastewater organics.

The box-plots representing removal efficiencies of selected synthetic musks, triclosan, PCP, benzophenone, (a UV blocker in plastics), and DEHP (a plasticizer) indicate that polycyclic musks such as AHTN and HHCB are removed with medium to high efficiencies—mean values above 65% (Figure 2-4). Musk ketone, a nitro-musk, was

readily removed (>90%). All the musks are classified as non biodegradable (Table 2-1, 40,41). However, they are relatively hydrophobic; so that observed removals could result from adsorption to sludge. Similarly, triclosan, which is also categorized as not Ready-biodegradable, shows relatively high removals (median removal > 80% and $\geq 90\%$ removal in more than 25% of plants). Triclosan remains a potential concern, however, since it is frequently present at $\mu\text{g/L}$ levels in raw sewage. In addition, triclosan is hydrophobic ($\log D_{ow} = 4.73$) and may be concentrated in sludges produced during wastewater treatment, providing another avenue for introduction into the environment when biosolids are disposed of via land application.

The plastics additives benzophenone and DEHP exhibit relatively high removal efficiencies, although based on limited sampling. Removal efficiencies of bisphenol A (BPA), a precursor monomer of polycarbonate plastic and epoxy resins; alkylphenols and alkylphenol ethoxylates follow similar patterns (Figure 2-4). All have median removals from 80-85%, and near total removal is achieved in a few treatment plants. However, only the 1, 2 ethoxylates were included in this summary, and the simultaneous production of APs and short-chain APEs from longer-chain precursors during wastewater treatment makes data interpretation difficult. Here, negative removals, which were sometimes observed as a consequence of experimental or analytical limitations, are shown as zero-efficiencies, which may slightly distort the summaries for these compounds.

The perfluorinated compounds PFOS and PFOA were poorly removed during conventional wastewater treatment. The median removal of PFOA was near zero. This

was expected since the compounds are non-biodegradable and hydrophilic ($\log D_{ow} = -9.3$ and -5.9 for PFOA and PFOS, respectively).

A subset of the CEC data was used to produce cumulative probability distribution functions (Figures 2-5 and 2-6). In these plots, cumulative counts represent the percent of data with aqueous-phase removal efficiencies lower than the influent-to-effluent removal specified. Using caffeine as an example (Figure 2-5), removal efficiencies were $< 75\%$ for only 10% of the WWTPs in the survey. Compounds that are readily removed via activated sludge processes such as caffeine, acetaminophen and ibuprofen exhibit cumulative removal patterns with upward concavity. Those that are poorly removed such as carbamazepine and clofibrac acid show a downward concavity.

Results can be interpreted also in terms of removal probability: the probability of removing $\geq 75\%$ of the influent caffeine during conventional secondary treatment was $> 90\%$, whereas the probability of removing $\geq 75\%$ of the influent carbamazepine using the same processes was $< 10\%$. When removals of specific CECs among the plants in the survey were widely, and more or less uniformly, distributed across the entire range of efficiencies, e.g. diclofenac and many of the antibiotics, resultant cumulative probability functions tend toward the 45-degree line. In a sense, these are the most interesting compounds in the summary, since their removals during conventional wastewater treatment may be highly sensitive to operational conditions. Compounds in this category are ketoprofen, diclofenac, erythromycin, roxithromycin, sulfamethoxazole, trimethoprim, gemfibrozil and, to some extent, clofibrac acid (Figure 2-5).

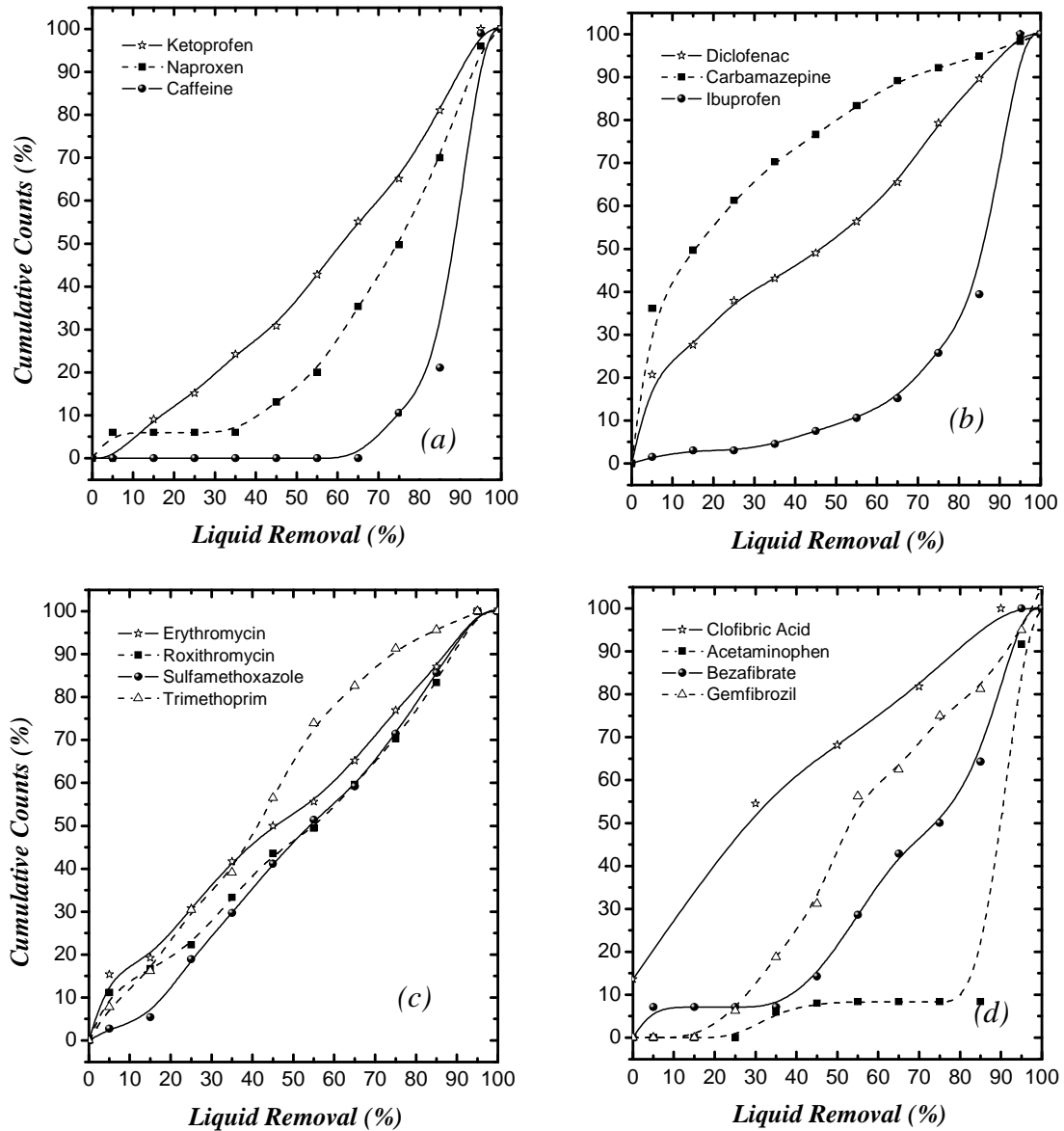


Figure 2-5. Cumulative probability for selected pharmaceuticals in activated sludge. In these plots, cumulative counts represent the percent of data with liquid-phase removal efficiencies lower than the influent-to-effluent removal specified.

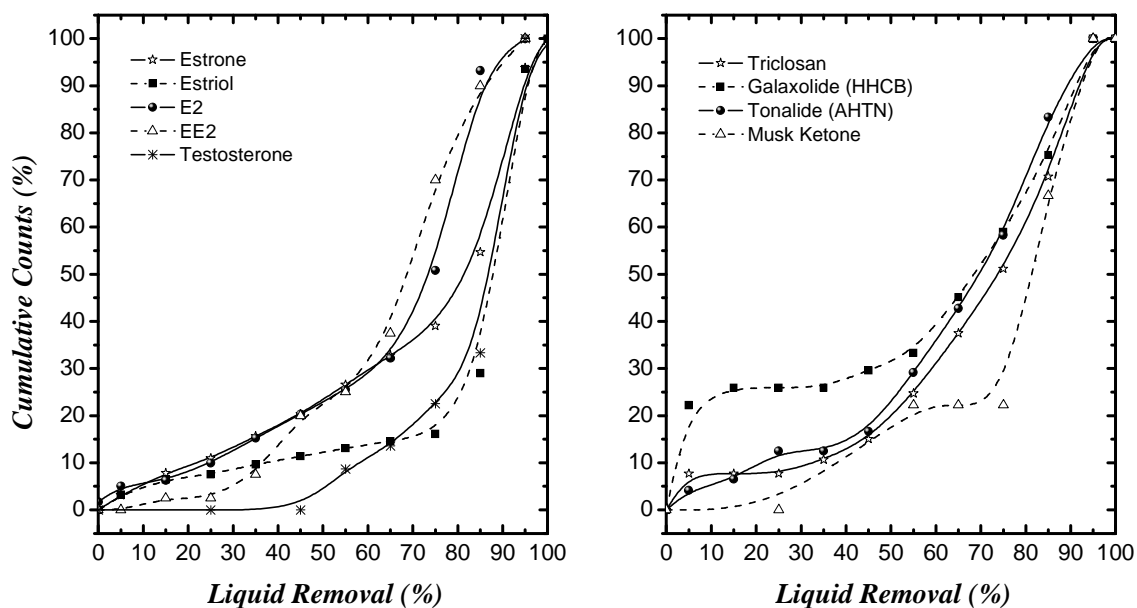


Figure 2-6. Cumulative probability for selected hormones and synthetic musks in activated sludge.

2.5.2. Membrane Bioreactors

As the large-scale deployment of MBR technology is relatively limited, there are fewer data with which to analyze CEC removal efficiencies. Data summaries (Figures 2-7 to 2-9) suggest that median CEC removals in MBRs are comparable to removal efficiencies in more conventional biological treatment processes. While MBR efficiencies are modestly higher for clofibric acid and naproxen, median removals were slightly lower for acetaminophen, diclofenac; ibuprofen and ketoprofen (compare Figures 2-1 and 2-7). MBR removal of carbamazepine (Figure 2-8) was lower but less erratic than in the comparison data set (Figure 2-1).

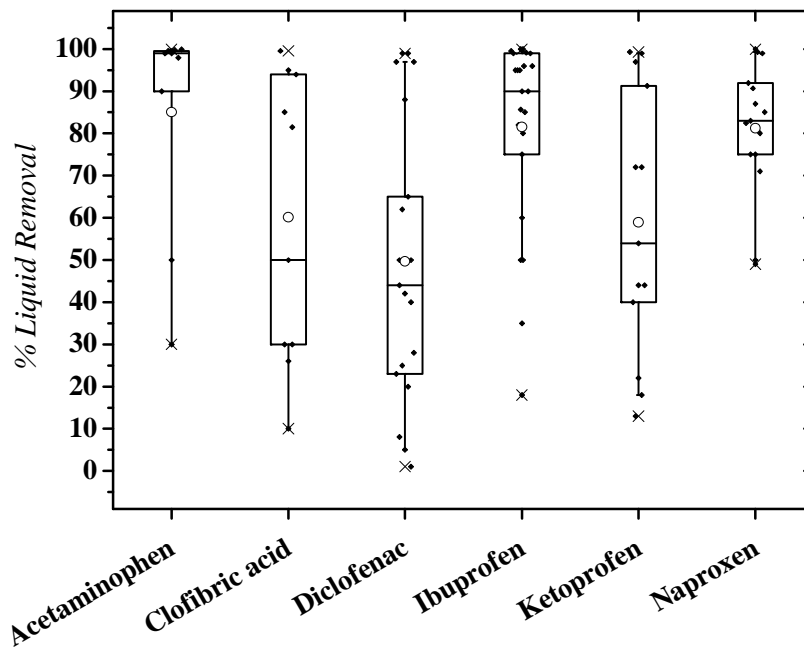


Figure 2-7. Box plots of liquid removal for selected pharmaceuticals in MBR process.

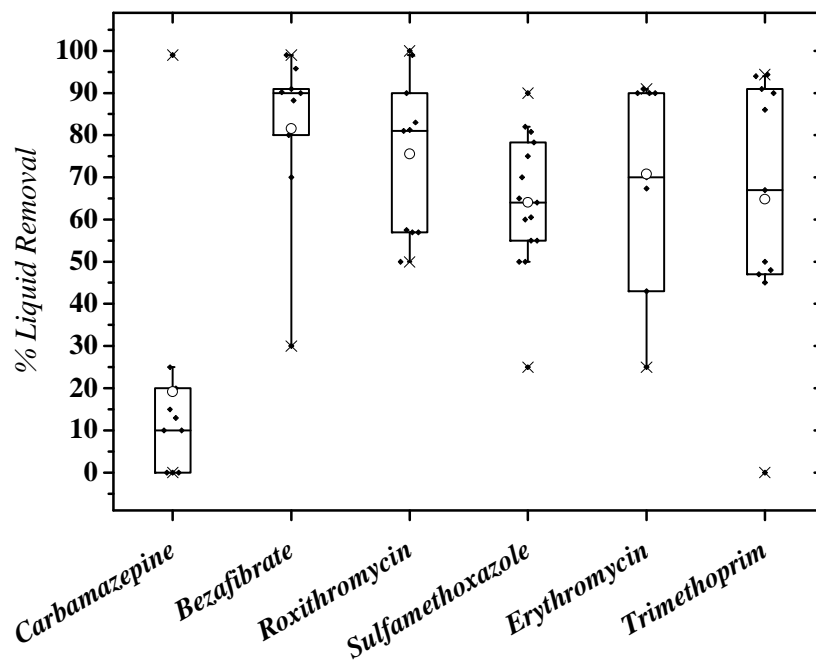


Figure 2-8. Box plots of liquid removal for selected antibiotics in MBR process.

For the antibiotics and bezafibrate, median performances in the MBR were slightly better than those obtained in other activated sludge reactors (Figures 2-8, 2-1 and 2-2). Again, MBR data are noticeably less scattered. The estrogenic compounds analyzed—BPA, *p*-nonylphenol, and the natural and metabolized hormones—were all efficiently removed in both reactor types (median removals > 80%, Figures 2-3, 2-4 and 2-9).

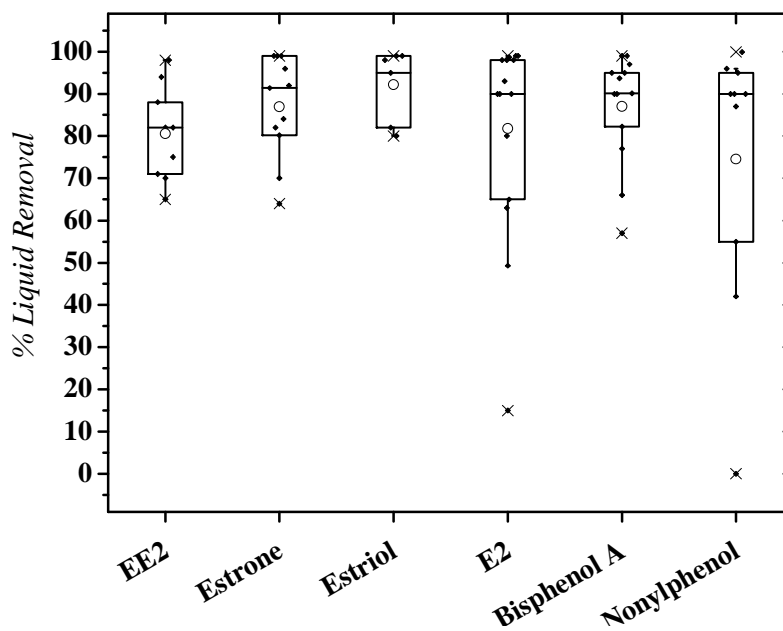


Figure 2-9. Box plots of liquid removal for selected natural and synthetic hormones, bisphenol A and nonylphenol in MBR process.

2.5.3. Factors that Affect Removal Efficiencies

It is frequently held that equilibrium partitioning of organic chemicals between liquid and solid phases is governed by proportionality between the aqueous-phase concentration and concentration in organic material that contributes to the solid phase. The constant of

proportionality is determined by compound-specific relative affinities for the aqueous and solid phases and is frequently represented in terms of the octanol/water partition coefficient (K_{ow}). Using these relationships, it is possible to rationalize the sorptive removal of CECs during conventional wastewater treatments. Even when this model breaks down, it is likely that compound hydrophobicity is directly related to abiotic removal efficiency. For persistent and recalcitrant compounds, it is possible that partitioning into organic solids is the primary determinant of through-plant removal efficiency.

To test these ideas, the compound-specific probability of observing >75% removal in facilities represented in this survey was plotted as a function of $\log K_{ow}$ (Figure 2-10). When all 42 compounds represented statistically were included, there was no obvious trend. However, when the biodegradable compounds (per BIOWIN 2, i.e. acetaminophen, estriol, caffeine nonylphenol, etc.) are excluded and K_{ow} is replaced by D_{ow} (from equation 2-2), the correlation between hydrophobicity and removal efficiency is improved.

In order to quantify the degree of correlation between the removal probability and hydrophobicity, Spearman correlation coefficients (46) were calculated for the Figure 2-10 data. The Spearman coefficient is a numerical measure of the degree to which two random variables are correlated. It varies from -1 to 1 . Positive values arise when the two variables are directly related, while negative values indicate inverse correlation. Values close to $+1$ or -1 indicate that the two variables are highly correlated. Clearly, the

relationship between the probability of 75⁺% removal and D_{ow} is strengthened when biodegradable compounds are not considered, suggesting that partitioning to solid sludge is a major contributor to removal of hydrophobic compounds, as expected when biodegradation is minimal.

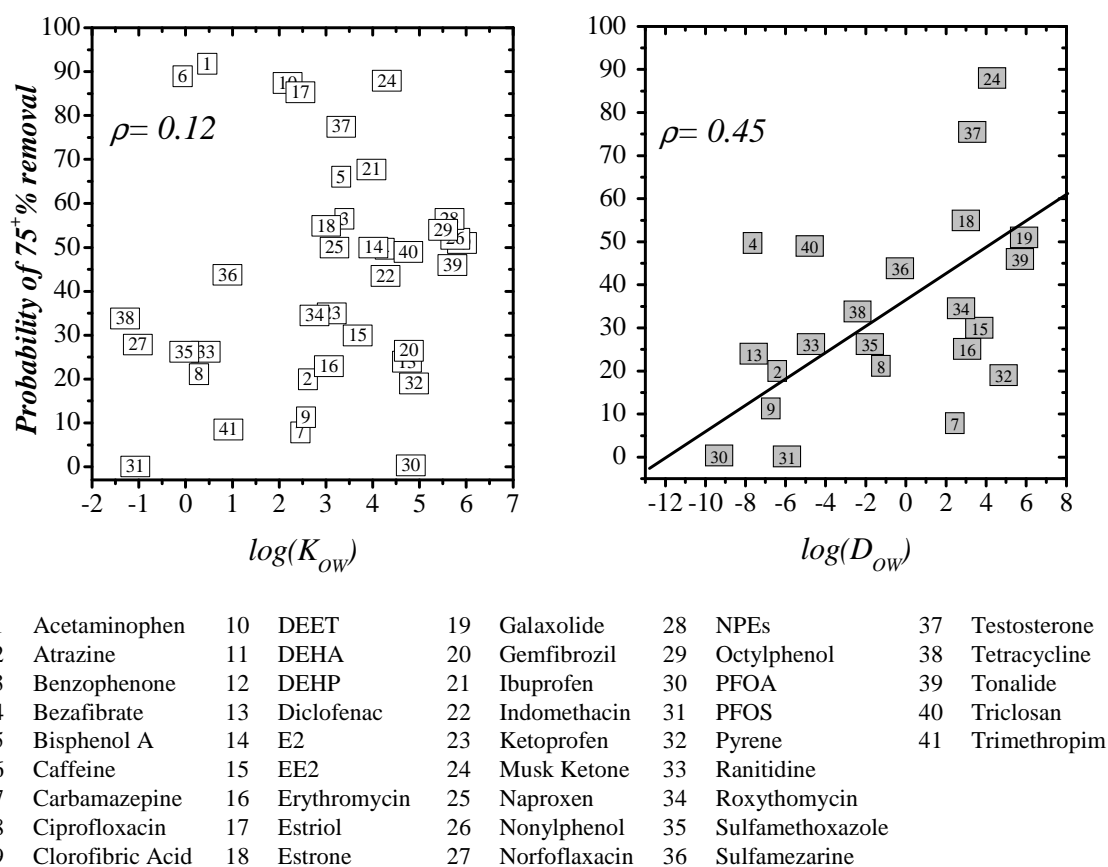


Figure 2-10. (Left) Probability of achieving 75⁺% removal efficiency for selected CECs as a function of octanol-water partition coefficient; (Right) Biodegradable (Ready and inherent biodegradable compounds from Table 2-1) compounds have been eliminated and K_{ow} has been replaced by D_{ow} . Solid line is a visual guide. The Spearman correlation coefficient (ρ) is shown for each data set.

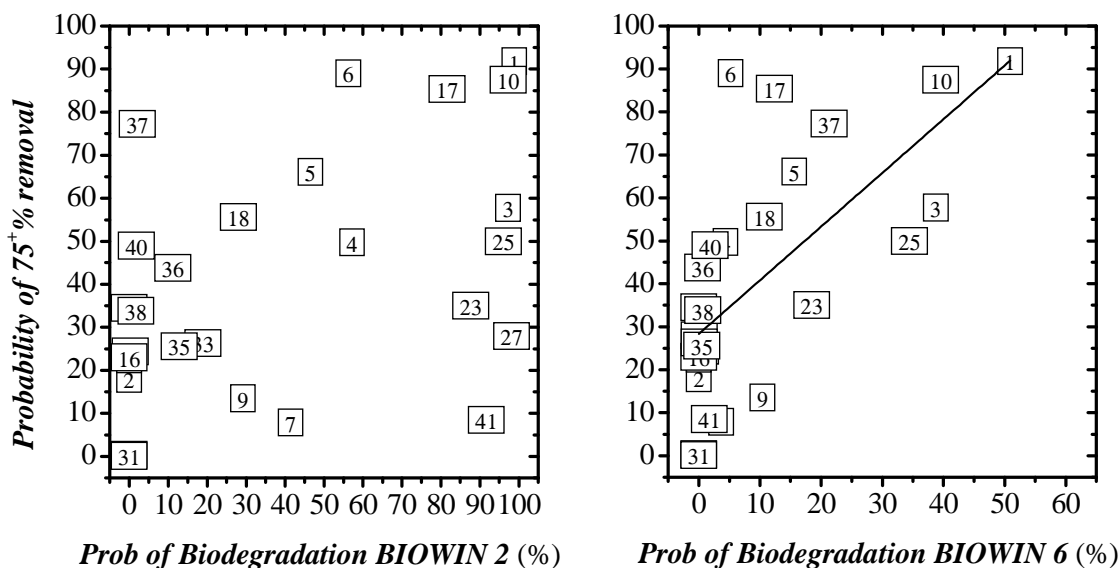


Figure 2-11. Probability of achieving 75+% removal efficiency in activated sludge processes vs. BIOWIN 2 (left) and BIOWIN 6 (right) estimation of biodegradation probabilities. Numbers correspond to legend in Figure 2-10. Solid line represents a linear fit. Compounds with log D_{ow} > 3.5 are not considered.

A similar analysis was carried out to investigate the importance of method selection for estimation of compound biodegradability. There is no single, comprehensive database with which to quantify the biodegradability of CECs during wastewater treatment, in part due to unavoidable differences between biochemical conditions in tests and working bioreactors. A comparison was performed using BIOWIN 2 and BIOWIN 6 predictions. Results are summarized for compounds with log D_{ow} < 3.5 (Figure 2-11) avoiding situations in which removal is dominated by compound hydrophobicity and physical partitioning with sludge. BIOWIN 2 results were poorly related to the probabilities of removal obtained in this work. On the other hand, the dependence of removal efficiency on biodegradation probabilities calculated with BIOWIN 6 is evident despite residual

error. To refine the analysis, we selected a group of 17 compounds for which first-order rate constants of laboratory-scale biodegradation (k_{bio}) with activated sludge have been reported (47,48) (Figure 2-12 left). Correlation between removal efficiency and the biodegradation rate constant is clear.

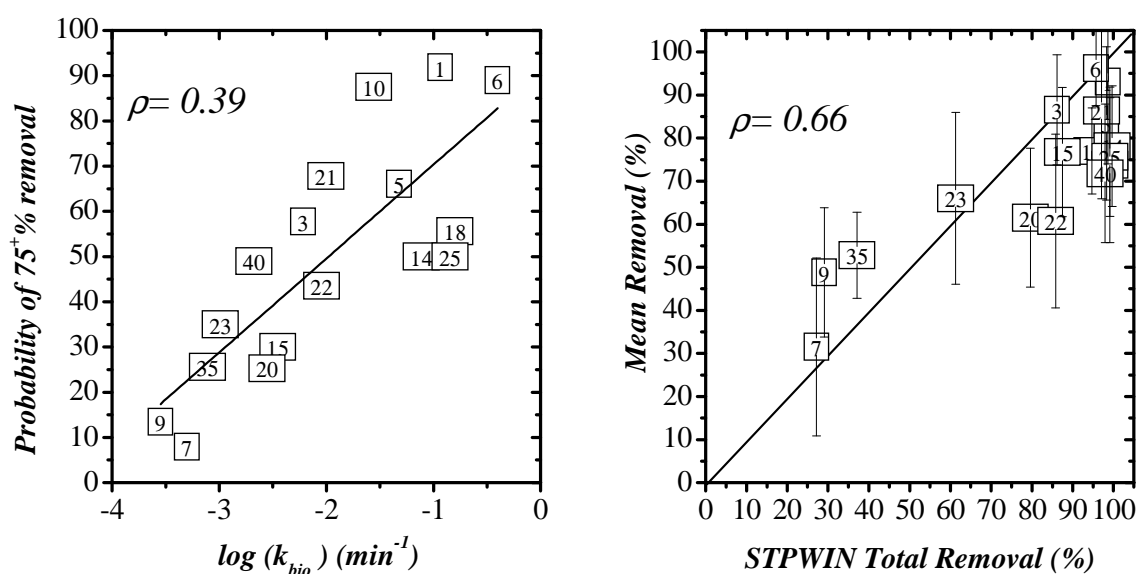


Figure 2-12. (Left): Probability of achieving 75+% removal efficiency as a function of biodegradation rate constants as reported by Urase and Kikuta 2005 (47), and Dickenson *et al.*, (48) in activated sludge for selected compounds. Solid line is a visual guide. (Right): Mean Removal for the same compounds as a function of STPWIN total removal prediction using half-lives calculated from the rate constants. Numbers correspond to legend in Figure 2-10. Error bars are plus and minus one standard deviation. Solid line is the 45-degree line.

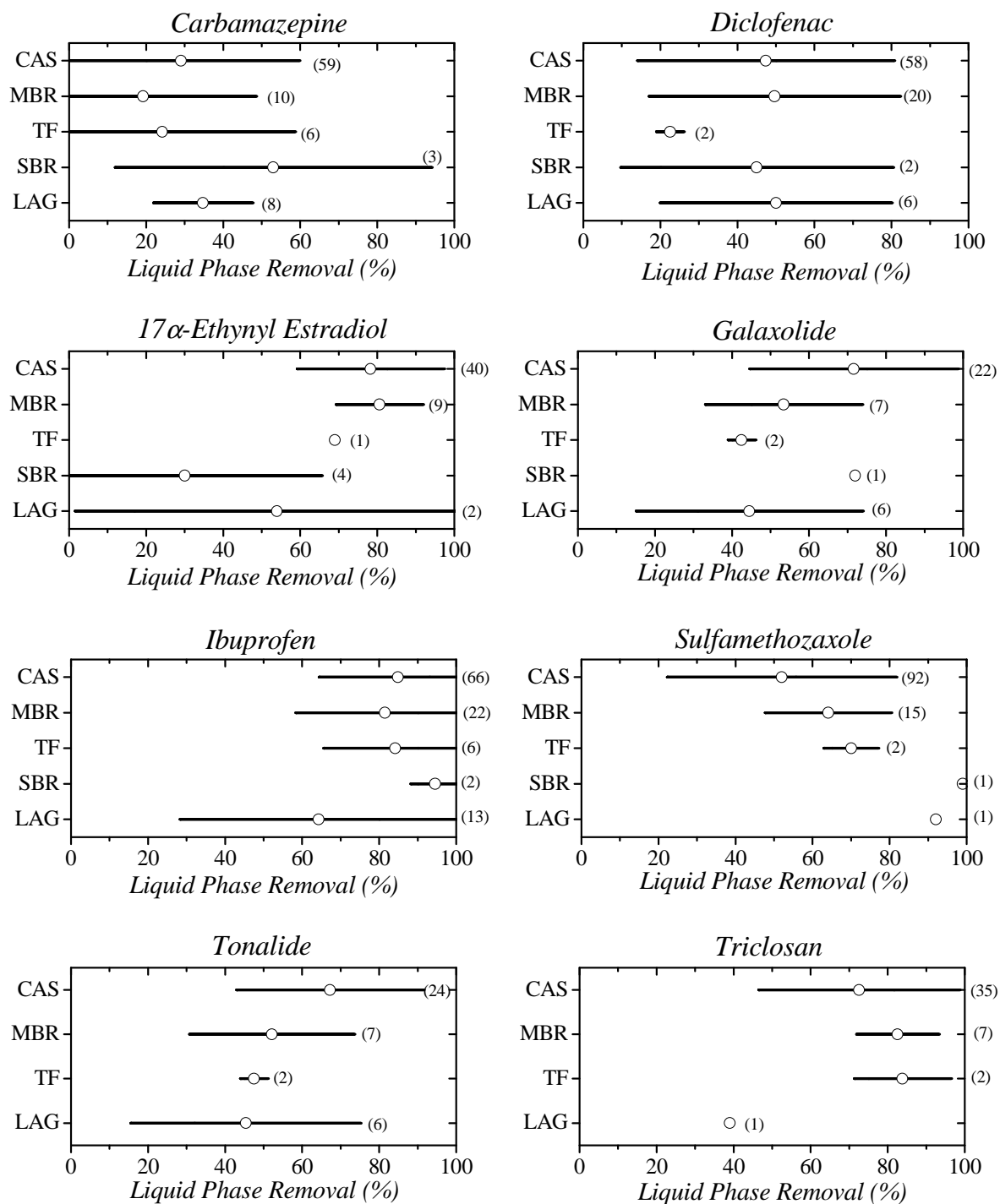


Figure 2-13. Removal efficiency comparison for conventional activated sludge (CAS), membrane bioreactor (MBR), tricking filters (TF), sequenced batch reactors (SBR) and lagooning (LAG) for selected CECs. Open circles represent the mean and the horizontal bars represent plus and minus one standard deviation. The number of data points is indicated for each case.

The same rate constants were used in the STPWIN model to predict through-plant, compound-specific removals during wastewater treatment. Figure 2-12 (right) compares the mean removal obtained in this work to the total removal predicted by STPWIN. The qualitative results and Spearman correlation coefficient suggest that STPWIN adequately simulates the fate of the selected compounds during activated sludge treatment when empirical biodegradation rates are used as model inputs.

2.5.4. Comparison of Biological Treatment Alternatives

The limited number of studies available did not support extensive statistical analyses of other biological processes. Removal efficiencies for a subset of eight CECs are used to compare CEC removals observed in WWTPs using membrane bioreactors (MBR), trickling filters (TF), sequenced batch reactors (SBR) and lagoons with results from conventional activated sludge (Figure 2-13). Compound-specific removal efficiencies tend to be similar for all processes. For example, ibuprofen exhibits high removal efficiencies in all five processes, whereas the removal of diclofenac was modest in four of the five processes compared and low in trickling filters.

2.5.5. Effects of Operating Conditions

Solids retention time (SRT) and hydraulic retention time (HRT) were used to assess the effects of operational conditions on compound-specific removal efficiencies during conventional wastewater treatment (activated sludge). Among the 42 compounds studied, only 10 chemicals (all of them pharmaceuticals), offered sufficient data to pursue these

relationships. Figure 2-14 illustrates the dependence of removal on SRT and HRT for diclofenac and ketoprofen. No strong trend is apparent, although diclofenac removal was modestly dependent on HRT, as was ketoprofen treatment on SRT, based on Spearman correlation coefficients. For the rest of the CECs studied (results not shown) compound removals were poorly related to both SRT and HRT.

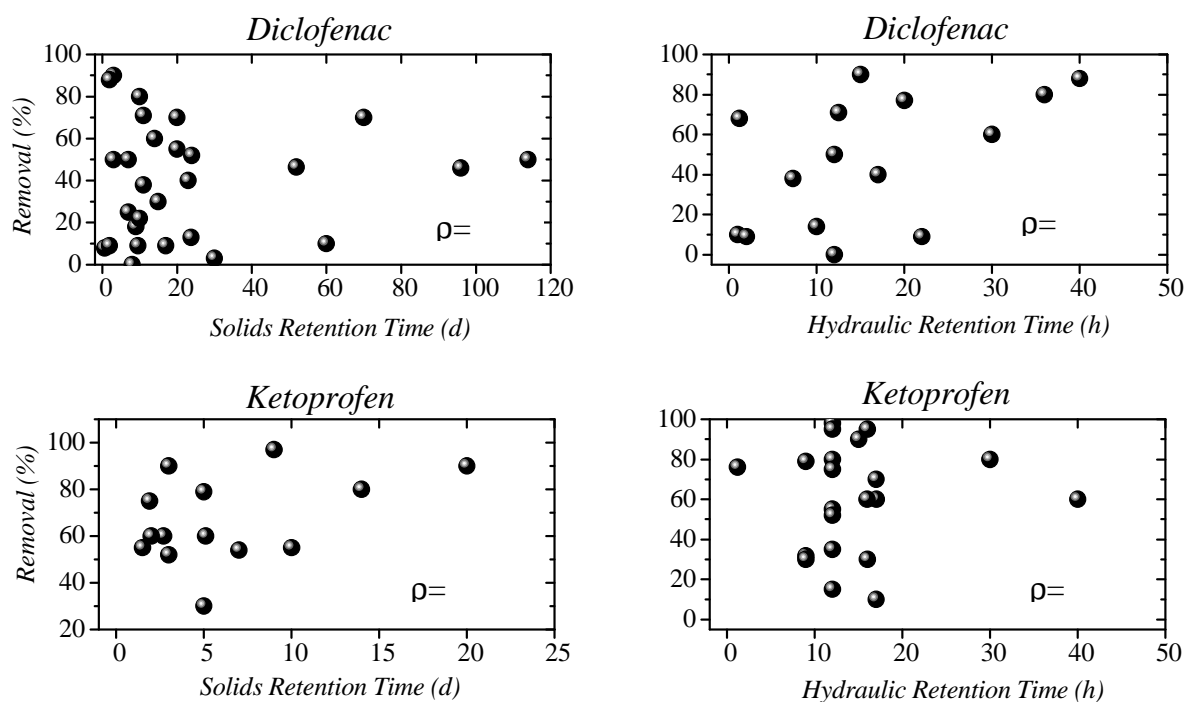


Figure 2-14. Removal efficiencies as functions of SRT and HRT for diclofenac and ketoprofen in activated sludge process.

2.6. Concluding Remarks

Overall, the analysis indicates that biodegradability is the most important contributor to CEC removal during conventional secondary treatment processes. The role of hydrophobicity and physical partitioning is apparent among compounds that are poorly biodegraded. Compound- and process-specific data are generally scattered. Factors contributing to the scatter may include variation in operating conditions or analytical inaccuracies. Statistical confidence in the results was addressed using the confidence interval for the estimated mean removal efficiency, calculated from equation (3). Table 2-2 includes those results, along with the probability of 75% removal efficiency for selected CECs. Based on Table 2-2 statistics, CECs were assigned positions in a matrix (Table 2-3) that reflects both removal efficiency and statistical confidence (weight of evidence). CI widths representing high, medium and low confidence levels were chosen to distribute compounds more or less equally among the three confidence levels.

Compounds for which the width of the 95% CI for mean removal was <15% were arbitrarily assigned a high degree of confidence—that is, average removal during conventional wastewater treatment can be anticipated with reasonable certainty. It is noteworthy perhaps that this category includes compounds that are both efficiently removed (e.g., caffeine) and poorly removed (e.g., carbamazepine). Those in the latter group are not expected to be removed by conventional processes and, as such, are candidates for tertiary removal technologies such as advanced oxidation, activated carbon or membrane treatment. Parallel reasoning suggests that more study is necessary to

understand the mechanisms of removal or operating conditions that promote removal of compounds in the low-confidence row of the matrix. For those compounds, e.g. atrazine and DEET, operational conditions during conventional treatment appear to be exceptionally important to treatment efficiency.

Data limitations do not allow us to reach firm conclusions regarding comparative effectiveness of alternative treatment technologies. Limited results indicate that compound-specific removal efficiencies amongst the various processes analyzed are similar (Figure 2-13). It seems that large-scale investment in MBR technology for management of CECs in wastewater effluent is not yet warranted.

Table 2-2. Total number of samples in activated sludge, confidence width, and assessment of removal for selected CECs. For criteria on low, medium and high qualifications, see Table 2-3.

CEC	Total # samples	Prob. 75%+ Removal	Removal Efficiency in Activated Sludge	CI width (%)	Confidence in Assessment
Acetaminophen	11	92	High	25	Medium
Atrazine	10	20	Low	36	Low
Benzophenone	10	58	Medium	18	Medium
Bezafibrate	12	50	Medium	33	Low
Bisphenol A	32	66	Medium	13	High
Caffeine	16	89	High	9	High
Carbamazepine	60	8	Low	15	High
Ciprofloxacin	26	23	Low	27	Low
Clofibrac acid	22	13	Low	22	Medium
DEET	10	88	High	29	Low
DEHA	10	90	High	33	Low
DEHP	10	42	Medium	38	Low
Diclofenac	59	24	Low	16	Medium
E2	57	50	Medium	13	High
EE2	39	30	Low	12	High
Erythromycin	28	23	Low	24	Medium
Estriol	28	85	High	22	Medium
Estrone	64	56	Medium	14	High
Galaxolide (HHCB)	22	51	Medium	24	Medium
Gemfibrozil	14	25	Low	27	Low
Ibuprofen	66	68	High	10	High
Indomethacin	10	44	Medium	58	Low
Ketoprofen	34	35	Medium	21	Medium
Musk Ketone	10	88	High	22	Medium
Naproxen	69	50	Medium	11	High
Nonylphenol	54	52	Medium	14	High
Norfloxacin	21	28	Medium	27	Low
NPEs	58	57	Medium	15	High
Octylphenol	32	54	Medium	20	Medium
PFOA	29	0	Low	7	High
PFOS	23	0	Low	21	Medium
Pyrene	10	19	Low	29	Low
Ranitidine	14	26	Low	34	Low
Roxythromycin	18	29	Low	30	Low

Table 2-2. Continued

CEC	Total # samples	Prob. 75%+ Removal	Removal Efficiency in Activated Sludge	CI width (%)	Confidence in Assessment
Sulfamerazine	11	26	Low	44	Low
Sulfamethoxazole	55	44	Medium	14	High
Testosterone	29	77	High	24	Medium
Tetracycline	24	34	Medium	19	Medium
Tonalide (AHTN)	34	46	Medium	21	Medium
Triclosan	35	49	Medium	18	Medium
Trimethoprim	35	9	Low	19	Medium

Removal efficiency levels in activated sludge were determined as follows: high corresponds to CECs with >75% probability of 75%+ removal, medium corresponds to CECs with 25-75% probability of 75%+ removal, low corresponds to CECs with <25% probability of 75%+ removal. Confidence in assessment was judged as follows: high means that CI width<15%; medium corresponds to compounds with CI width between 15 and 25%, and low corresponds to compounds for which CI width obtained is >25%.

Table 2-3. Summary of confidence level vs. removal efficiency for selected CECs (activated sludge processes).

Confidence level	Low removal efficiency (<33% probability of 75%+ removal)	Medium removal efficiency (34–66% probability of 75%+ removal)	High removal efficiency (>67% probability of 75%+ removal)
Low (CI width \geq 25%)	Atrazine, Ciprofloxacin, Gemfibrozil, Ranitidine, Pyrene, Roxythromycin, Sulfamerazine	Bezafibrate, Indomethacin, Norfloxacin	DEHP, DEET, DEHA
Medium (15% \leq CI width<25%)	Erythromycin, Trimethoprim, Diclofenac	PFOS, Benzophenone, acid, Ketoprofen, Tetracycline, Triclosan	Clofibric acid, Galaxolide, Octylphenol, Tonalide, Musk, Testosterone
High (CI width<15%)	Carbamazepine, EE2, PFOA	Bisphenol A, Naproxen, NP1EO, Sulfamethoxazole	Estrone, E2, Nonylphenol, NP2EO, Caffeine, Ibuprofen

2.7. Literature Cited

- (1) Kolpin, D.W.; Furlong, E.T.; Meyer, M.T.; Thurman, E.M.; Zaugg, S.D.; Barber, L.B.; Buxton, H.T.; Pharmaceuticals, Hormones, and Other Organic Wastewater Contaminants in U.S. Streams, 1999–2000: A National Reconnaissance. *Environ. Sci. Technol.* **2002**, *36*, 1202.
- (2) Kidd, K.A.; Planchfield, P.J.; Mils, K.H.; Palace, V.P.; Evans, R.E.; Lazorchak, J.M.; Flick, R.W. Collapse of a Fish Population After Exposure to a Synthetic Estrogen. *Proc. Nat. Acad. Sci.* **2007**, *104*, 8897.
- (3) Ackerman, F.; Stanton, E.E. The Last Drop: Climate Change and the Southwest Water Crisis. Stockholm Environment Institute. February 2011.
- (4) US EPA. Occurrence of Contaminants of Emerging Concern in Wastewater From Nine Publicly Owned Treatments Works. EPA-821-R-09-009. *Environmental Protection Agency*, Washington DC, 2009.
- (5) US EPA. Treating Contaminants of Emerging Concern: A Literature Review Database. EPA-820-R-10-002. *Environmental Protection Agency*, Washington DC, 2010.
- (6) Stephenson, R.; Oppenheimer, J. Fate of Pharmaceutical and Personal Care Products through Municipal Wastewater Treatment Processes. *WERF-03-CTS-22UR*. IWA Publishing, London, UK, 2007.
- (7) Drewes, J.E.; Dickenson, E.R.V.; Snyder, S. Contributions of Household Chemicals to Sewage and Their Relevance to Municipal Wastewater Systems and the Environment. *WERF-03-CTS-21UR*. IWA Publishing, London, UK, 2009.
- (8) Halling-Sorensen, B.; Nielsen, N.; Lanzky, P.F.; Ingerslev, F.; Holten Lützhøft, H.C.; Jørgensen, S.E. Occurrence, Fate and Effects of Pharmaceutical Substances in the Environment - A Review. *Chemosphere* **1998**, *36*, 357.

- (9) Heberer, T.H.; Reddersen, K.; Mechlinski, A. From Municipal Sewage to Drinking Water: Fate and Removal of Pharmaceutical Residues in the Aquatic Environment in Urban Areas, *Water Sci. Technol.* **2002**, *46*, 81.
- (10) Clara, M.; Strenn, B.; Gans, O.; Martinez, E.; Kreuzinger, N.; Kroiss, H. Removal of Selected Pharmaceuticals, Fragrances and Endocrine Disrupting Compounds in a Membrane Bioreactor and Conventional Wastewater Treatment Plants. *Water Res.* **2005**, *39*, 4797.
- (11) Lindqvist, N.; Tuhkanen, T.; Kronberg, L. Occurrence of Acidic Pharmaceuticals in Raw and Treated Sewages and in Receiving Waters. *Water Res.* **2005**, *39*, 2219.
- (12) Tauxe-Wuersch, A.; De Alencastro, L.F.; Grandjean, D.; Tarradellas, J. Occurrence of Several Acidic Drugs in Sewage Treatment Plants in Switzerland and Risk Assessment. *Water Res.* **2005**, *39*, 1761.
- (13) Yu, T.; Lin, A.Y.; Lateef, S.K.; Lin, C.; Yang, P. Removal of Antibiotics and Non-Steroidal Anti-Inflammatory Drugs by Extended Sludge Age Biological Process. *Chemosphere* **2009**, *77*, 175.
- (14) Lishman, L.; Smyth, S.A.; Sarafin, K.; Kleywegt, S.; Toito, J.; Peart, T.; Lee, B.; Servos, M.; Beland, M.; Seto, P. Occurrence and Reductions of Pharmaceuticals and Personal Care Products and Estrogens by Municipal Wastewater Treatment Plants in Ontario, Canada. *Sci. Total Environ.* **2006**, *367*, 544.
- (15) Santos, J.L.; Aparicio, I.; Callejón, M.; Alonso, E. Occurrence of Pharmaceutically Active Compounds During 1-Year Period in Wastewaters From Four Wastewater Treatment Plants in Seville (Spain). *J. Hazardous Mat.* **2009**, *164*, 1509.
- (16) Jones, O.A.H.; Voulvoulis, N.; Lester, J.N. The Occurrence and Removal of Selected Pharmaceutical Compounds in a Sewage Treatment Works Utilising Activated Sludge Treatment. *Environ. Pollution* **2007**, *145*, 738.
- (17) Ying, G.G.; Kookana, R.; Kumar, A. Fate of Estrogens and Xenoestrogens in Four Sewage Treatment Plants with Different Technologies. *Environ. Toxicol. Chem.* **2008**, *27*, 87.

- (18) Sui, Q.; Huang, J.; Deng, S.; Yu, G.; Fan, Q. Occurrence and Removal of Pharmaceuticals, Caffeine and DEET in Wastewater Treatment Plants of Beijing, China. *Water Res.* **2010**, *44*, 417.
- (19) Sim, W.; Lee, J.; Oh, J. Occurrence and Fate of Pharmaceuticals in Wastewater Treatment Plants and Rivers in Korea. *Environ. Pollution* **2010**, *158*, 1938.
- (20) Miege, C.; Choubert, J.M.; Ribeiro, L.; Eusebe, M.; Coquery, M. Fate of Pharmaceuticals and Personal Care Products in Wastewater Treatment Plants – Conception of a Database and First Results. *Environ Pollution* **2009**, *157*, 1721.
- (21) Taylor, A.A.; Jobling, S.; Nolan, M.; Tyler, C.R.; van Aerle, R.; Brighty, G. Spatial Survey of the Extent of Sexual Disruption in Wild Roach in English and Welsh Rivers. Science Report P6-018/SR. The Environment Agency, Bristol, UK, 2005
- (22) Teske, S.S.; Arnold, R.G.; Removal of Natural and Xeno-Estrogens During Conventional Wastewater Treatment. *Rev. Environ. Sci. Biotechnol.* **2008**, *7*, 107.
- (23) Petrovic, M.; Sole, M.; Lopez De Alda, M.A.; Barcelo, D. Endocrine Disruptors in Sewage Treatment Plants, Receiving Waters, and Sediments: Integration of Chemical Analysis and Biological Effects on Feral Carp. *Environ. Toxicol. Chem.* **2002**, *21*, 2146.
- (24) Cespedes, R.; Lacorte, S.; Ginebreda, A.; Barcelo, D. Occurrence and Fate of Alkylphenols and Alkylphenol Ethoxylates in Sewage Treatment Plants and Impact on Receiving Waters Along the Ter River (Catalonia, NE Spain). *Environ. Pollution* **2008**, *153*, 384.
- (25) Melcer, H.; Klečka, G.; Monteith, H.; Staples, C. Wastewater Treatment of Alkylphenols and Their Ethoxylates: A State of the Science Review. *Alkylphenols & Ethoxylates Research Council, Water Environment Federation*, Alexandria, VA, 2007.
- (26) Müller, K.; Magesan, G.N.; Bolan, N.S. A Critical Review of the Influence of Effluent Irrigation on the Fate of Pesticides in Soil. *Agriculture Ecosys. Environ.* **2007**, *120*, 93.

- (27) Braskerud, B.C.; Haarstad, K. Screening the Retention of Thirteen Pesticides in a Small Constructed Wetland. *Water Sci. Technol.* **2003**, *48*, 267.
- (28) Lee, I.S.; Lee, S.H. Occurrence and Fate of Synthetic Musk Compounds in Water Environment. *Water Res.* **2010**, *44*, 214.
- (29) Heberer, T. Occurrence, Fate and Assessment of Polycyclic Musk Residues in the Aquatic Environment of Urban Areas – A Review. *Acta Hydrochim. Hydrobiol.* **2002**, *30*, 227.
- (30) Murakami, M.; Shinohara, H.; Takada, H. Evaluation of Wastewater and Street Runoff as Sources of Perfluorinated Surfactants (PFSS) Over Water. *Chemosphere* **2009**, *74*, 487.
- (31) Schultz, M.M.; Higgins, C.P.; Huset, C.A.; Luthy, R.G.; Barofsky, D.F.; Field, J.A. Fluorochemical Mass Flows in a Municipal Wastewater Treatment Facility. *Environ. Sci. Technol.* **2006b**, *40*, 7350.
- (32) Schultz, M.M.; Barofsky, D.F.; Field, J.A. Quantitative Determination of Fluorinated Alkyl Substances by Large-Volume-Injection Liquid Chromatography Tandem Mass Spectrometry – Characterization of Municipal Wastewaters. *Environ. Sci. Technol.* **2006a**, *40*, 289.
- (33) Senevirathna, S.T.; Tanaka, S.; Fujii, S.; Kunacheva, C.; Harada, H.; Shivakoti, B.R.; Okamoto, R. A Comparative Study of Adsorption of Perfluorooctane Sulfonate (PFOS) onto Granular Activated Carbon, Ion-Exchange Polymers and Non-Ion-Exchange Polymers. *Chemosphere* **2010**, *80*, 647.
- (34) Roslev, P.; Vorkamp, K.; Aarup, J.; Frederiksen, K.; Nielsen, P.H. Degradation of Phthalate Esters in an Activated Sludge Wastewater Treatment Plant. *Water Research* **2007**, *41*, 969.
- (35) Klečka, G.; Persoon, C.; Currie, R. Chemicals of Emerging Concern in the Great Lakes Basin: An Analysis of Environmental Exposures. *Rev Environ. Contam. Toxicol.* **2010**, *207*, 1.

- (36) Howard, P.H.; Boethling, R.S.; Stiteler, W.M.; Meylan, W.M.; Hueber, A.E.; Beauman, J.A.; Larosche, M.E. Predictive Model for Aerobic Biodegradability Developed from a File of Evaluated Biodegradation Data. *Environ. Toxicol. Chem.* **1992**, *11*, 593.
- (37) Tunkel, J.; Howard, P.H.; Boethling, R.S.; Stiteler, W.; Loonen, H. Predicting Ready Biodegradability in the Japanese Ministry of International Trade and Industry Test. *Environ. Toxicol. Chem.* **2000**, *19*, 2478.
- (38) Clark, B.; Henry, J.G.; Mackay, D. Fugacity Analysis and Model of Organic Chemical Fate in a Sewage Treatment Plant. *Environ. Sci. Technol.* **1995**, *29*, 1488.
- (39) MacBean, E.A.; Rovers, F.A. Statistical Procedures for Analysis of Environmental Monitoring Data & Risk Assessment. Prentice Hall PTR, Upper Saddle River, NJ, 1998.
- (40) Balk, F.; Ford, R.A. Environmental Risk Assessment for the Polycyclic Musk AHTN and HHCB in the EU: Fate and Exposure Assessment. *Toxicol Letters* **1999**, *111*, 57.
- (41) Tas, J.W.; Balk, F.; Ford, R.A.; Van de Plassche, E.J. Environmental Risk Assessment of Musk Ketone and Musk Xylene in the Netherlands in Accordance with the EU-TGD. *Chemosphere* **1997**, *35*, 2973.
- (42) Stevens-Garmon, J.; Drewes, J.E.; Khan, S.J.; McDonald, J.A. Sorption of Emerging Trace Organic Compounds onto Wastewater Sludge Solids. *Water Research* **2011**, *45*, 3417.
- (43) Beach, S.A.; Newsted, J.L.; Coady, K.; Giesy, J.P. (2006) Ecotoxicological Evaluation of Perfluorooctanesulfonate (PFOS). *Rev. Environ. Contam. Toxicol.* **2006**, *186*, 133.
- (44) Prevedouros, K.; Cousins, I.T.; Buck, R.C.; Korzeniowski, S.H. Sources, Fate and Transport of Perfluorocarboxylates. *Environmental Science and Technology* **2006**, *40*, 32.

- (45) Brooke, D.; Footitt, A.; Nwaogu, T.A. Environmental Risk Evaluation Report: Perfluorooctanesulphonate (PFOS). Reseach Contractor: Building Research Establishment Ltd, Risk and Policy Analysts Ltd, 2006.
- (46) Myers, J.L.; Well, A.D. Research Design and Statistical Analysis (2nd ed). Lawrence Erlbaum 2003, pp. 508.
- (47) Urase, T.; Kikuta, T. Separate Estimation of Adsorption and Degradation of Pharmaceutical Substances and Estrogens in the Activated Sludge Process. *Water Research* **2005**, *39*, 1289.
- (48) Dickenson, E.R.V.; Drewes, J.E.; Stevens-Garmon, J.; Khan, S.; McDonald, J. Evaluation of QSPR techniques for wastewater treatment processes. *WERF – U2R07*. IWA Publishing, London, UK, 2010.

*CHAPTER 3
MODELING OF ADVANCED OXIDATION OF TRACE ORGANIC
CONTAMINANTS BY HYDROGEN PEROXIDE PHOTOLYSIS AND FENTON'S
REACTION

3.1. Abstract

The kinetics of nonylphenol and p-cresol destruction via hydrogen peroxide photolysis and Fenton's reaction was investigated under a variety of operating conditions in homogeneous, laboratory-scale batch reactor experiments. Models with no adjustable parameters successfully accounted for radical initiation via photolysis of H_2O_2 , or radical initiation via Fenton's mechanism, reaction of organic targets with hydroxyl radical, and radical scavenging and recombination mechanisms, as well as changes in solution pH due to evolution of carbon dioxide because of target mineralization. Simulations of the UV/ H_2O_2 and Fenton-based models can be used to anticipate the kinetics of advanced oxidation involving any target compound for which there is a known apparent second-order rate constant for reaction with hydroxyl radical. The presence of radical scavengers was successfully treated by the model, suggesting that the model can be generalized to the treatment of complex matrices.

*A modified version of this chapter was published in Critical Industrial Engineering Chemistry Research 2010, 49, 11331-11343.

3.2. Introduction

Common to advanced oxidation processes (AOP) is the physical-chemical enhancement of hydroxyl radical production in water (1). Advanced oxidation processes include Fenton's reaction, irradiation of photo-catalysts such as titanium dioxide with ultraviolet (UV) light, ozonation, sonolysis, and UV photolysis of hydrogen peroxide, among others. Each process has certain limitations. Fenton's reaction, for example, performs well at $\text{pH} \leq 3.0$, where Fe(III) solubility is assured (2,3) Solid-phase TiO_2 must be immobilized or recovered from treated water to increase process practicality. Photolysis of hydrogen peroxide consumes aqueous-phase H_2O_2 for radical production and can be readily applied for the destruction of micro-pollutants in water or wastewater in a variety of sanitary engineering applications (4).

There have been noteworthy explorations of AOPs for the destruction of low molecular weight aromatics, including nonylphenol (NP) and *p*-cresol (PC). Nonylphenol is present in municipal wastewater as a consequence of the use of nonylphenol polyethoxylates, a group of nonionic surfactants, in detergents, emulsifiers, and wetting/de-foaming agents (5). Nonylphenol is a weak estrogenic contaminant in many surface waters that receive treated municipal wastewater. Although NP is 10^4 to 10^5 times less estrogenic than 17β -estradiol (6) its concentrations in surface waters can be orders of magnitude higher than those of natural and synthetic hormones. Furthermore, in many surface waters NP is present in combination with other endocrine disrupting compounds, so that overall biological effects are difficult to anticipate (7) *p*-Cresol is prevalent in wastewaters

originating from refineries, petrochemicals, polymeric resins, pharmaceuticals, coal conversion plants and various chemical industries (8). Similarities in chemical structure and reactivity with hydroxyl radical suggest that steps governing AOP-driven destruction of NP, PC, and similar aromatic targets are the same.

Neamtu and Frimmel (5) explored the decomposition of NP by UV light in the presence and absence of hydrogen peroxide, qualitatively establishing the effects of pH, bulk organic matter, presence of Fe(III) and H₂O₂ concentration on reaction rate. Under specific conditions, phenol and 1,4-dihydroxybenzene were recognizable reaction intermediates. The pseudo-first-order rate constant for NP disappearance increased with increasing pH, perhaps as a consequence of greater reactivity between hydroxyl radical and NP in its basic form. A rigorous kinetic model was not developed.

Chen *et al* (7) applied UV/H₂O₂ treatment to destroy a variety of phenolic and steroidal estrogens in water. Again, degradation was pseudo-first-order in the concentration of the target. The presence of bulk organics decreased the rates of oxidation of the target contaminants, suggesting that these compounds acted as radical scavengers. Other studies focused on UV/TiO₂ (9) and a magnetic photo-catalyst (to assist in catalyst recovery) for alkylphenol destruction (10). Ning *et al.* (11,12) studied the oxidation of NP and octylphenol via ozonation. The second-order rate constant for direct reaction of O₃ and nonylphenol was $(3.9 \pm 0.1) \times 10^4 \text{ M}^{-1} \text{ s}^{-1}$. Based on an assumed quasi-steady concentration for hydroxyl radical, they estimated the second-order rate constant for the NP/OH radical

reaction at $(1.1\pm 0.2)\times 10^{10} \text{ M}^{-1}\text{s}^{-1}$. The value is similar to those reported for the reaction of OH radicals with other phenolic compounds, including *p*-cresol ($1.2\times 10^{10} \text{ M}^{-1}\text{s}^{-1}$) (13)

As a class, phenolic compounds tend to be soluble in water, weakly adsorbed on inorganic solids and persistent in the environment. Previous studies have illustrated the utility of ozonation, photocatalytic oxidation, and the Fenton process to degrade *p*-cresol. Zheng *et al.* (14) described the comparative kinetics of cresol isomer oxidation via ozone/H₂O₂ in the presence and absence of iron. Others investigated the mechanisms of heterogeneous photocatalytic, e.g. UV/TiO₂ (15), and Fenton-motivated oxidations of cresol isomers (16) Fenton-based oxidation produced carbon dioxide and several low-molecular-weight organic acids, including acetic and oxalic acids. Flox *et al.* (8) explored an AOP variant, photoelectro-Fenton oxidation of aqueous-phase cresol in a continuous-flow reactor. Cresol transformation was well described by pseudo-first-order kinetics. Process intermediates included carboxylic acids and methylhydroquinone.

In this work, we extend previous efforts to characterize the mechanism and kinetics of UV/H₂O₂ oxidation and Fenton's reaction to decompose aqueous-phase nonylphenol and *p*-cresol. Using monochromatic light, we examined the dependence of transformation kinetics on wavelength in the range $230 \text{ nm} \leq \lambda \leq 270 \text{ nm}$ and the concentrations of well known hydroxyl radical scavengers (isopropanol or ethanol). The second-order rate constant for reaction of NP with hydroxyl radical was estimated from a kinetic model. Agreement between experimental results and AOP simulations accounting for light intensity/attenuation, pH, hydrogen peroxide levels and concentrations of other radical

scavengers was excellent using models with formulations similar to previous efforts (17-21)

3.3. Experimental

3.3.1. Materials

All chemicals were from commercial sources and used without further purification, including nonylphenol (Aldrich, technical grade: ring and chain isomer mixture), extra-pure *p*-cresol (Acros, 99%+), isopropanol (OmniSolv, GC/HPLC grade), and hydrogen peroxide (Acros, 50 wt%). *n*-Heptane served as a solvent for the GC/MS analysis. All solutions were prepared using a (Millipore Q) water purification system (resistivity > 18 M Ω cm⁻¹). Hydrogen peroxide doses ranged from 25 to 250 mM. Acetone (Fisher, HPLC grade) and carbon tetrachloride (Acros, 99.8%) were used for actinometry. In Fenton-based experiments, ferric sulfate (Fe₂(SO₄)₃·6H₂O) (Sigma-Aldrich), was the source of Fe(III), and sulfuric acid (EM Science) was added as necessary to establish the initial pH. Glassware was routinely washed with water and a 2% soak solution, rinsed several times with deionized water and baked overnight at 500°C prior to use.

3.3.2. UV/H₂O₂ Experiments

The experimental setup consisted of a 20-mL cylindrical glass reactor (length: 4 cm) that was covered with a quartz window and stirred continuously using a 1-cm glass-coated stir bar. Light was provided from a 1000 W xenon-arc lamp with f/4 ellipsoidal reflector (Photon Technology International, A-6000). A water filter removed infrared light ahead

of the reactor. A grating blaze/manual monochromator was used to select the wavelength of influent light (varied between 230 and 270 nm) and bandwidth (10 nm) for experiments. A mirror reflected the beam vertically downward through a collimating lens before entering the reactor from the top surface. Water temperature was maintained at 25°C using a cooling bath (Nestlab low T bath, ULT-80).

Stock solutions of PC, NP and H₂O₂ were prepared on day of use. To overcome low NP solubility in water, 25 µM at 25°C (5), a concentrated stock solution (50 mM) was prepared in ethanol. Aqueous-phase solutions of NP, 10 to 25 µM, were then obtained by adding measured volumes from the ethanol stock solution. Solutions of *p*-cresol were prepared in water due to its relatively high aqueous-phase solubility, 23 g/L at 25°C (22). Hydrogen peroxide was added to produce initial concentrations from 25 to 250 mM. The resulting solution was then stirred for 15 minutes before experiments were initiated by irradiation of the reactor with UV light. Liquid samples (50 µL) were withdrawn from the reactor at 2-3 hour intervals and added to 1 mL of *n*-heptane to quench radical reactions and extract organic targets. Independent experiments showed that NP extraction was essentially complete (results not shown). For PC, a constant partition coefficient of 0.55 between water/heptane was measured over the range of concentrations studied and used to calculate pre-extraction aqueous-phase PC concentrations. The duration of each experiment was around 24 hours.

3.3.3. Fenton's Reaction Experiments

Reactors consisted of 200-mL amber glass vials. Chemicals in the reaction mixtures were added in the following order: pre-prepared PC or NP solutions as described above, H₂SO₄ to control the solution pH, Fe₂(SO₄)₃, then H₂O₂ to initiate the reaction. Reactors were filled to near capacity and placed in an Orbit Shaker Bath with temperature control at 25°C.

3.3.4. Analytical Methods

Both PC and NP were analyzed by GC/MS (Agilent 6890N Series with 5963 MS) with a quadrupole mass analyzer and auto-injector. Electron impact ionization was at 70 eV. The carrier gas was helium at 22 cm/s. Source and interface temperatures were 200 °C and 250 °C. The HP-5 MS column (30 m × 0.25 mm ID) contained a 0.25-μm fused silica film.

For PC measurements, the initial oven temperature (100 °C) was maintained for 1 min, after which the temperature was ramped to 150 °C at 10 °C/min. The injector had a split ratio of 1:50, and the injection volume was 2 μL.

The NP samples provided a series of isomer peaks in the GC/MS chromatograms. Single ion mode (SIM) (m/z 135) was used for quantification purposes, following the protocol of Azevedo *et al.* (23). The oven temperature was held at 60 °C for 1 min, and then ramped to 170 °C at 10 °C/min and from 170 to 220 °C at 5 °C/min. The injector

temperature was 100 °C, splitless mode, and the injection volume was 5 µL. The detection limit using this method was ~1 µM.

In a subset of experiments, H₂O₂ concentration was measured using a modified peroxytitanic (colorimetric) method (24). One-hundred µL samples and 50 µL of a titanium sulfate solution were added to 5 mL of deionized water to quench the AOP reaction. Color (A_{407}) was measured by a spectrophotometer (Hitachi U-2000, Hitachi Corp). Samples were diluted as necessary to maintain absorbance values within the range of the standards.

3.3.5. Actinometry

A chemical actinometer based on that of Li *et al.* (25) was used to measure light intensity from the UV source. The actinometer is based on the dehalogenation of carbon tetrachloride to chloroform by a light-activated series of reactions involving acetone and isopropanol. A 5.7 M isopropanol solution was purged with argon for > 30 min to eliminate dissolved oxygen, after which the reactor was amended with acetone and CCl₄. The resultant solution (200 mL) was stirred for 30 minutes and then exposed to the UV source. Samples were withdrawn and analyzed for CCl₄ and CHCl₃ at 20-min intervals for 5 hr. Conversion to light intensity was as described by Li *et al.* (25).

3.3.6. Iron

The total soluble iron concentration was measured by the *o*-phenanthroline method (26) in which Fe(III) is reduced to the Fe(II) via reaction with excess hydroxylamine, then

reacted with 1,10-phenanthroline at pH 3.2 to 3.3. The iron/*o*-phenanthroline complex produces an orange-red color that was measured spectrophotometrically, $\lambda = 510$ nm (extinction coefficient: $11,000 \text{ M}^{-1}\text{cm}^{-1}$) using a Hitachi U-2000 double beamed spectrophotometer.

3.4. Models

3.4.1. UV/H₂O₂ Model

The generalized mechanism of UV/H₂O₂ photolysis includes an initiation step that produces hydroxyl radicals ($\cdot\text{OH}$), which react with the target compound. Propagation steps scavenge $\cdot\text{OH}$, producing other active radicals ($\text{O}_2^{\cdot-}$ and $\text{CO}_3^{\cdot-}$, Table 3-1).

Glaze *et al.* (33) proposed a kinetic model containing the most important elements of UV/H₂O₂ photolysis to predict the time-dependent concentration of a halogenated target. They used a quasi-steady-state assumption (QSSA) to calculate the time-dependent concentrations of free radicals. Their model did not account for CO₂ evolution/pH change and neglected the role of all radical scavenging species except H₂O₂. Stefan *et al.*(17) took a similar approach, but assumed that the target compound (in their case acetone) was transformed to oxalic and formic acids and then to CO₂.

Table 3-1. Elementary reactions in aqueous UV/H₂O₂ photolysis in the presence of CO₂. Kinetic and equilibrium constants are at 25 °C. Reactions E1 to E4 are considered to equilibrate instantaneously.

No.	Reaction	Rate constant, k (M ⁻¹ s ⁻¹) or equilibrium constant, K	Reference
R1	$\text{H}_2\text{O}_2 + h\nu \rightarrow 2\text{HO}\cdot$	$\phi=0.5$ (primary quantum yield)	27
R2	$\cdot\text{OH} + \text{H}_2\text{O}_2 \rightarrow \text{O}_2\cdot^- + \text{H}_2\text{O} + \text{H}^+$	$k_2 = 2.7 \times 10^7$	13
R3	$\cdot\text{OH} + \text{HO}_2^- \rightarrow \text{O}_2\cdot^- + \text{H}_2\text{O}$	$k_3 = 7.5 \times 10^9$	13
R4	$\cdot\text{OH} + \text{HCO}_3^- \rightarrow \text{CO}_3\cdot^- + \text{H}_2\text{O}$	$k_4 = 8.5 \times 10^6$	13
R5	$\cdot\text{OH} + \text{CO}_3^{2-} \rightarrow \text{CO}_3\cdot^- + \text{OH}^-$	$k_5 = 3.9 \times 10^8$	13
R6	$\cdot\text{OH} + \text{HO}_2\cdot \rightarrow \text{O}_2 + \text{H}_2\text{O}$	$k_6 = 6.6 \times 10^9$	13
R7	$\cdot\text{OH} + \text{O}_2\cdot^- \rightarrow \text{O}_2 + \text{OH}^-$	$k_7 = 8.0 \times 10^9$	13
R8	$\cdot\text{OH} + \cdot\text{OH} \rightarrow \text{H}_2\text{O}_2$	$k_8 = 5.5 \times 10^9$	13
R9	$\cdot\text{OH} + \text{CO}_3\cdot^- \rightarrow \text{Products}$	$k_9 = 3.0 \times 10^9$	28
R10	$\text{O}_2\cdot^- + \text{H}_2\text{O}_2 \rightarrow \cdot\text{OH} + \text{O}_2 + \text{OH}^-$	$k_{10} = 1.3 \times 10^{-1}$	29
R11	$\text{O}_2\cdot^- + \text{CO}_3\cdot^- \rightarrow \text{O}_2 + \text{CO}_3^{2-}$	$k_{11} = 6.5 \times 10^8$	30
R12	$\text{O}_2\cdot^- + \text{HO}_2\cdot + \text{H}_2\text{O} \rightarrow \text{H}_2\text{O}_2 + \text{O}_2 + \text{OH}^-$	$k_{12} = 9.7 \times 10^7$	13
R13	$\text{HO}_2\cdot + \text{HO}_2\cdot \rightarrow \text{H}_2\text{O}_2 + \text{O}_2$	$k_{13} = 8.6 \times 10^5$	31
R14	$\text{HO}_2\cdot + \text{H}_2\text{O}_2 \rightarrow \cdot\text{OH} + \text{O}_2 + \text{H}_2\text{O}$	$k_{14} = 3.7$	29
R15	$\text{CO}_3\cdot^- + \text{H}_2\text{O}_2 \rightarrow \text{HCO}_3^- + \text{O}_2\cdot^- + \text{H}^+$	$k_{15} = 8.0 \times 10^5$	32
R16	$\text{CO}_3\cdot^- + \text{HO}_2^- \rightarrow \text{HCO}_3^- + \text{O}_2\cdot^-$	$k_{16} = 3.0 \times 10^7$	32
R17	$\text{CO}_3\cdot^- + \text{CO}_3\cdot^- \rightarrow 2\text{CO}_3^{2-}$	$k_{17} = 2.0 \times 10^7$	32
R18	$\text{PC} + \cdot\text{OH} \rightarrow \text{Products}$	$k_{\text{PC}} = 1.2 \times 10^{10}$	13
R19	$\text{NP} + \cdot\text{OH} \rightarrow \text{Products}$	$k_{\text{NP}} = 1.33 \times 10^{10}$	This work
R20	$\text{C}_3\text{H}_8\text{O} + \cdot\text{OH} \rightarrow \text{Products}$	$k_{\text{IPOH}} = 1.9 \times 10^9$	13
R21	$\text{C}_2\text{H}_6\text{O} + \cdot\text{OH} \rightarrow \text{Products}$	$k_{\text{EtOH}} = 1.9 \times 10^9$	13
E1	$\text{H}_2\text{O}_2 \leftrightarrow \text{HO}_2^- + \text{H}^+$	$K_{a1} = 10^{-11.60}$	19
E2	$\text{HO}_2\cdot \leftrightarrow \text{O}_2\cdot^- + \text{H}^+$	$K_{a2} = 10^{-4.86}$	19
E3	$\text{H}_2\text{CO}_3 \leftrightarrow \text{HCO}_3^- + \text{H}^+$	$K_{a3} = 10^{-6.30}$	19
E4	$\text{HCO}_3^- \leftrightarrow \text{CO}_3^{2-} + \text{H}^+$	$K_{a4} = 10^{-10.36}$	19

Subsequently, Crittenden *et al.* (18) modeled UV/H₂O₂ AOP without reliance on a quasi-steady-state assumption for radical concentrations ($\cdot\text{OH}$, $\text{O}_2\cdot^-$ and $\text{CO}_3\cdot^-$). Their work showed that the QSSA tends to under-predict hydroxyl radical concentrations in some cases and therefore the rates of target compound decomposition. Furthermore, their model included radical scavenging reactions. Experiments were done in a phosphate buffer. It was assumed that the halogenated targets were oxidized to carbon dioxide and mineral acids and pH changes were predicted as a function of reaction progress.

The model of Song *et al.* (19) accounted for time-dependent radical ($\cdot\text{OH}$, $\text{O}_2\cdot^-$ and $\text{CO}_3\cdot^-$) concentrations, pH changes due to product formation (CO_2 and other acids), and radical scavenging by H_2O_2 and natural organic matter. Its application to alachlor oxidation accounted well for the disappearance of the halogenated target and for the time dependence of bulk solution pH.

Previous models assume that concentrations of all species in the reactor are uniform. However, light enters the reactor through a surface and is absorbed (mostly by H_2O_2) as it penetrates the reactive mixture. Since light intensity decays with distance from the source, the rate of production of hydroxyl radicals (R1, Table 3-1) is not uniform in the reactor even if the hydrogen peroxide concentration is uniform. In the experiments reported in this work, most of the incident light is absorbed. Hence, uniform concentrations would require a mixing regime that can overcome the non-uniformity of the light intensity and local radical generation. However, the fast kinetics of some of the

reactions (Table 3-1) suggests that mixing might not be fast enough to make all concentrations uniform. To explore this point, consider the laminar-flow convective-diffusion equation applied to a dilute chemical species i in the reaction mixture,

$$\frac{\partial c_i}{\partial t} + \mathbf{v} \cdot \nabla c_i = D_i \nabla^2 c_i + R_i \quad (3-1)$$

where c_i is species molar concentration, \mathbf{v} is the fluid velocity vector, D_i is the diffusivity of species i in the reactive mixture, and R_i is the net rate of generation of species i by chemical reaction.

Formally, c_i is uniform whenever the convective and/or diffusive transport mechanisms are fast enough with respect to the local reaction rate; that is, when the second and third terms in equation (3-1) are much larger than the reaction rate term. Here, we will consider that the mixing regime in the reactor is such that convection prevails over diffusion. The magnitude of the convective term can be roughly estimated as

$$\mathbf{v} \cdot \nabla c_i = O\left(\frac{v_0 c_{i0}}{\ell}\right) \quad (3-2)$$

where v_0 and c_{i0} are representative fluid velocity and species i concentration, respectively, and ℓ is a characteristic length over which the concentration changes appreciably. A constraint that will ensure rapid mixing and uniform concentration can be derived by comparing convection and reaction terms in equation (3-1); that is, if

$$\frac{v_0 c_{i0}}{\ell R_{i0}} \gg 1 \quad (3-3)$$

species i can be considered well mixed in the reactor. In equation (3), R_{i0} is a representative reaction rate.

Our batch reactor is a 20-mL cylindrical glass vial with light entering the reactor through the top. The reactor depth is 4 cm. To quantify the dimensionless parameter in equation (3-3) for $\cdot\text{OH}$ and H_2O_2 , we take $\ell = 4$ cm and a representative velocity $v = 1$ cm/s. We will assume that reaction R2 (Table 3-1) is the most important contribution to the rate of disappearance of the two species (this is consistent with model calculations). Hence, we can state

$$R_{i0} = k_2 c_{P0} c_{R0}, \quad i = P, R \quad (3-4)$$

where the indices P and R denote hydrogen peroxide and hydroxyl radical, respectively. In our experiments, the order of magnitude of the concentrations is $c_P = 10^{-2}$ M, $c_R = 10^{-15}$ M. The dimensionless parameter in equation (3-3) is calculated for each species to be

$$\left(\frac{v_0 c_{i0}}{\ell R_{i0}} \right)_P = 9 \times 10^6 \quad (3-5)$$

$$\left(\frac{v_0 c_{i0}}{\ell R_{i0}} \right)_R = 9 \times 10^{-7} \quad (3-6)$$

For the conditions considered, this calculation shows that hydrogen peroxide will be well mixed in the reactor, but the hydroxyl radical will not be mixed at all, and a hydroxyl radical concentration profile will exist at all times. We expect that this will be the case in most batch reactors; that is, radical concentrations will not be uniform but will vary along the direction of light attenuation.

In principle, the spatial variability of radical concentrations needs to be considered in a mathematical model of the advanced oxidation process. Therefore, an overall kinetic equation can be obtained only by averaging equation (3-1) over the reactor volume, V . Consider the volume average operator applied to species concentration,

$$\langle c_i \rangle = \frac{1}{V} \int_V c_i dV \quad (3-7)$$

Now consider the volume average of equation (3-1). Use of the divergence theorem for a batch reactor (no entrances and exits) leads to

$$\frac{1}{V} \int_V \mathbf{v} \cdot \nabla c_i dV = \frac{1}{V} \int_V \nabla \cdot (\mathbf{v} c_i) dV = \frac{1}{V} \int_A \mathbf{n} \cdot \mathbf{v} c_i dA = 0 \quad (3-8)$$

$$\frac{1}{V} \int_V D \nabla^2 c_i dV = \frac{D}{V} \int_A \mathbf{n} \cdot \nabla c_i dA = 0 \quad (3-9)$$

where A is the surface area of the reactor and \mathbf{n} is a unit vector normal to the reactor surface. Note that both convective and diffusive fluxes are zero everywhere on A . The volume average of equation (3-1) becomes

$$\frac{d \langle c_i \rangle}{dt} = \langle R_i \rangle \quad (3-10)$$

In principle, this equation must be applied to all species that participate in the reaction system (Table 3-1).

In what follows, we will present the equations that constitute our model for the specific case in which the target compound is *p*-cresol (PC) and no radical scavengers other than H_2O_2 are present. The rate of reaction R1 (Table 3-1), expressed as disappearance of H_2O_2 , is given by

$$R_{P1} = -\phi_{\text{H}_2\text{O}_2} f_{\text{H}_2\text{O}_2} I \quad (3-11)$$

where $\phi_{\text{H}_2\text{O}_2}$ is the primary quantum yield for photo-catalytic decomposition of hydrogen peroxide, assumed to be 0.5 in the wavelength range of the experiments, 230-270 nm (19), I is the specific light intensity (moles of photons per unit time and reactor volume), and $f_{\text{H}_2\text{O}_2}$ is the fraction of total light attenuation that is absorbed by hydrogen peroxide. Here, we will assume that only H_2O_2 and the target (PC) absorb photons, so that $f_{\text{H}_2\text{O}_2} + f_{\text{PC}} = 1$. According to Lambert-Beer's law, the specific intensity at a given point in the reactor is given by

$$I = I_0 e^{-2.303A_z} \quad (3-12)$$

where I_0 is the specific intensity at the top of the reactor, and the total absorbance is given by

$$A_z = (\epsilon_{PC}[PC] + \epsilon_{H_2O_2}[H_2O_2])z \quad (3-13)$$

where ϵ_{PC} and $\epsilon_{H_2O_2}$ are wavelength-dependent molar extinction coefficients for *p*-cresol and hydrogen peroxide, respectively, and z is the distance measured downwards within the reactive mixture from the top surface, where light enters the reactor. Molar extinction coefficients were obtained from UV absorption spectra at the wavelengths of interest (Table 3-4). Note that

$$f_{PC} = \frac{\epsilon_{PC}z[PC]}{A_z} \quad (3-14)$$

$$f_{H_2O_2} = \frac{\epsilon_{H_2O_2}z[H_2O_2]}{A_z} \quad (3-15)$$

The above equations are based on the assumption that concentrations of PC and H_2O_2 are uniform in the reactor, which is consistent with the order of magnitude analysis presented above. Additionally, it is assumed that none of the incident light is reflected from the reactor base back into solution.

The volume averaging of equation (3-11) involves integration with respect to z which yields, after mathematical manipulation,

$$\langle R_{p1} \rangle = -\phi_{H_2O_2} I_0 f_{H_2O_2} (1 - e^{-2.303A}) \quad (3-16)$$

where $A = A_z(z = \ell)$.

Rate equations based on equation (3-10) were derived for all relevant chemical species listed in Table 3-1. For example, balances for PC and H_2O_2 are

$$\frac{d[PC]}{dt} = -k_{PC}[PC] \langle [\cdot OH] \rangle - \phi_{PC} I_0 f_{PC} (1 - e^{-2.303A}) \quad (3-17)$$

$$\begin{aligned} \frac{d[H_2O_2]}{dt} = & -\phi_{H_2O_2} I_0 f_{H_2O_2} (1 - e^{-2.303A}) - k_2[H_2O_2] \langle [\cdot OH] \rangle - k_3[HO_2^-] \langle [\cdot OH] \rangle \\ & - k_{10}[H_2O_2] \langle [O_2^{\cdot -}] \rangle - k_{14}[H_2O_2] \langle [HO_2^{\cdot}] \rangle - k_{15}[H_2O_2] \langle [CO_3^{\cdot -}] \rangle \\ & - k_{16} \langle [CO_3^{\cdot -}] \rangle \langle [HO_2^-] \rangle + k_8 \langle [\cdot OH] \rangle^2 + k_{12} \langle [HO_2^{\cdot}] \rangle \langle [O_2^{\cdot -}] \rangle + k_{13} \langle [HO_2^{\cdot}] \rangle^2 \end{aligned} \quad (3-18)$$

where ϕ_{PC} is the quantum yield for the decomposition of PC by direct photolysis. This direct photolysis reaction is included here for completeness, but our results showed that it is negligible in our experiments. In these equations, square brackets denote point concentrations, which are also average concentrations for non-radical species but not so for the radicals (e.g. $\langle [\cdot OH] \rangle$ denotes the average concentration of hydroxyl radical in the reactor.) Since H_2O_2 and HO_2^- are at equilibrium (R19, Table 3-1), equation (3-18) is the sum of the balances for the two species, and it considers the HO_2^- concentration to be

negligible with respect to $[H_2O_2]$, which is a good assumption in the pH range of our experiments. Similar equations were developed for net rates of reaction of free radicals ($\cdot OH$, $O_2\cdot^-/HO_2\cdot^-$ and $CO_3\cdot^-$); radical scavengers isopropanol (R20) or ethanol (R21), when present, and carbonate species.

A total carbonate balance was based on the assumption of a closed system (no exchange with atmospheric CO_2) and complete mineralization of the target (18,19) since no intermediates were detected by GC/MS under all the reaction conditions explored,

$$\begin{aligned} \frac{d[TotalCO_3]}{dt} = & -k_4 \langle [\cdot OH] \rangle [HCO_3^-] - k_5 \langle [\cdot OH] \rangle [CO_3^{2-}] + k_{11} \langle [O_2\cdot^-] [CO_3\cdot^-] \rangle \\ & + k_{15} \langle [CO_3\cdot^-] \rangle [H_2O_2] + k_{16} \langle [CO_3\cdot^-] \rangle [HO_2^-] + N \left(-\frac{d[PC]}{dt} \right) \end{aligned} \quad (3-19)$$

where

$$[TotalCO_3] = [H_2CO_3^*] + [CO_3^{2-}] + [HCO_3^-] \quad (3-20)$$

(i.e. total carbonate species concentration excluding radicals, which is also uniform in the reactor.)

In equation (3-19), N is the number of carbon atoms present in the molecular structure of the target (7 for PC and 15 for NP). A charge balance was used to calculate the bulk solution pH at each time step in the simulation, and the concentrations of carbonate and

bicarbonate ions were calculated based on carbonate equilibria, the solution pH and total carbonate, so that the hydrogen ion concentration was the only unknown.

A complete formulation of all the model equations is provided in Appendix B.

In the formulation presented, dependent variables include the average concentration of all radicals. The equations cannot be solved in the present form, owing to existence of terms involving radical/radical reactions. For example, the term that represents reaction R12 in equation (3-16) contains the factor $\langle [HO_2^{\cdot-}][O_2^{\cdot-}] \rangle$. Closure could be obtained if approximations of the type $\langle [HO_2^{\cdot-}][O_2^{\cdot-}] \rangle \approx \langle [HO_2^{\cdot-}] \rangle \langle [O_2^{\cdot-}] \rangle$ were valid. In this case, our formulation would be very similar to that of previous models (18,19) However, these approximations are not valid in the range of conditions explored in this and previous works whenever there is significant light attenuation, since this leads to steep concentration profiles of radical species. On the other hand, detailed calculations using our model with the approximation stated above (results not shown) indicate that the contributions of all radical/radical reactions to the kinetic expressions are negligible over the range of experimental conditions employed in this work. Hence, our model neglects these reactions, which provides closure to the formulation.

The overall approach produced a stiff system of ordinary differential equations governing the rates of formation or disappearance of PC, H_2O_2 , $\cdot OH$, $O_2^{\cdot-}$, $HO_2^{\cdot-}$, $CO_3^{\cdot-}$, TotCO₃ and scavengers, when present, plus algebraic equations ($[HCO_3^-]$ as a function of

[TotCO₃] and pH; and the charge balance). Details are provided in Appendix B. A numerical solution was found at each time step using the stiff differential equations solver ODE15s MATLAB subroutine (Gear's method). The relative tolerance was 10⁻⁸ while the absolute tolerances for concentrations of all species were set four orders of magnitude below their respective values.

Figure 3-1 shows calculated radical concentrations for a sample simulation, illustrating the unsteady nature of radical concentrations during the 24-hour course of individual experiments. Comparison is made with the radical concentrations calculated under the QSSA. Note that the concentrations of primary radicals differ significantly from those calculated under the QSSA for the case therein.

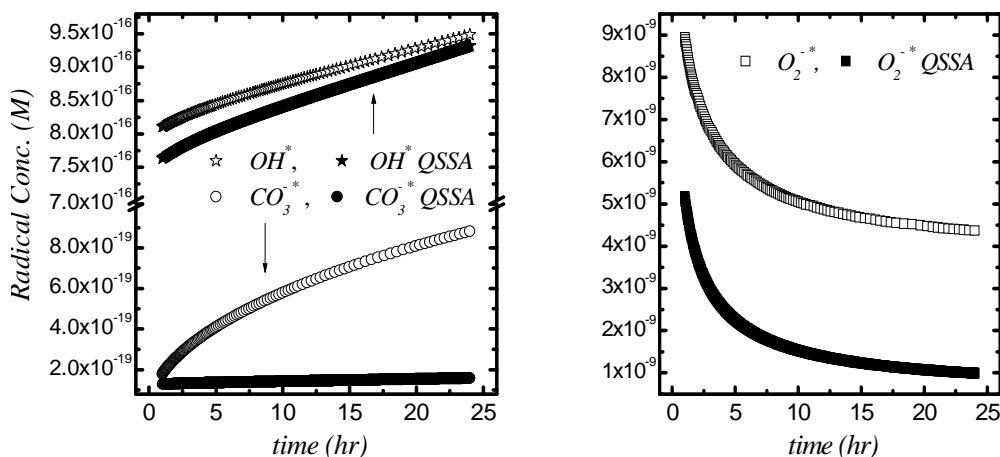


Figure 3-1. Model prediction of average radical concentration vs. time for a nonylphenol degradation experiment (UV/H₂O₂). Comparison between quasi-steady state approximation calculations (QSSA) and full model simulations. Initial conditions: [H₂O₂]₀=50 mM, [NP]₀=15 μM, [EtOH]₀=3.4 mM, λ=250 nm. The scavenging effect of ethanol was considered in the calculations.

Even though superoxide and carbonate radicals can be ignored as a potential source of reactions with the target, given their low reactivity, their presence and effect on the process is nevertheless relevant, since they participate in important scavenging reactions (Table 3-1) that affect the hydroxyl radical concentration. Moreover, special attention should be paid to the scavenging effects of carbonate and bicarbonate ions when they are present at significant concentrations or, as here, when they are produced in significant quantities by the continuous evolution of carbon dioxide.

3.4.2. Fenton's Reaction Model

The Fenton's reaction kinetic model is based on the Fe(III)/H₂O₂ system model of De Laat *et al.* (20,21) (Table 3-2). The model describes the decomposition of hydrogen peroxide by iron in a homogeneous aqueous solution, taking into account the rapid formation and rate limiting reduction of Fe(III)-hydroperoxo complexes (Fe^(III)(HO₂)²⁺ and Fe^(III)(OH)(HO₂)⁺). Successive reactions with hydrogen peroxide cycle iron between Fe(II) and Fe(III), generating two radical species ($\cdot\text{OH}$, and $\text{HO}_2\cdot^-/\text{O}_2\cdot^-$) per cycle. The objective here was to show the effect of operational parameters such as pH and initial concentrations of H₂O₂ and iron on the degradation of trace organic contaminants, and to investigate if target degradation by reaction with hydroxyl radicals, using the same reaction rate constants as in the H₂O₂ photolysis process, can be used to predict Fenton's reaction target degradation profiles.

Table 3-2. Elementary reactions in the Fe(III)-catalyzed decomposition of H₂O₂ (25°C; ionic strength: 0.1 M). Values are taken from De Laat and Le; Fe(III) represents the sum of Fe³⁺, Fe(OH)₂⁺ and Fe₂(OH)₂⁴⁺, while Fe(II) represents the sum of Fe²⁺ and FeOH⁺.

No.	Reaction	Rate constant, k (s ⁻¹ , M ⁻¹ s ⁻¹) or equilibrium constant, K
FE1	Fe ³⁺ + H ₂ O ↔ FeOH ²⁺ + H ⁺	K ₁ = 2.34 × 10 ⁻³
FE2	Fe ³⁺ + 2H ₂ O ↔ Fe(OH) ₂ ⁺ + 2H ⁺	K ₂ = 4.68 × 10 ⁻⁷
FE3	2Fe ³⁺ + 2H ₂ O ↔ Fe ₂ (OH) ₂ ⁴⁺ + 2H ⁺	K ₃ = 1.12 × 10 ⁻³
FE4	Fe ²⁺ + H ₂ O ↔ FeOH ⁺ + H ⁺	k ₄ = 1.9 × 10 ¹⁰ , k ₋₄ = 1.0 × 10 ¹⁰
FE5	HO ₂ • ↔ O ₂ • ⁻ + H ⁺	k ₅ = 1.58 × 10 ⁵ , k ₋₅ = 1.0 × 10 ¹⁰
FE6	Fe ³⁺ + H ₂ O ₂ ↔ Fe(HO ₂) ²⁺ + H ⁺	K _{1a} = 3.1 × 10 ⁻³
FE7	FeOH ²⁺ + H ₂ O ₂ ↔ Fe(OH)(HO ₂) ⁺ + H ⁺	K _{1b} = 2.0 × 10 ⁻⁴
F8	Fe ²⁺ + H ₂ O ₂ → Fe ³⁺ + •OH + OH ⁻	k ₈ = 55
F9	FeOH ⁺ + H ₂ O ₂ → Fe ³⁺ + •OH + 2OH ⁻	k ₉ = 5.9 × 10 ⁶
F10	Fe(HO ₂) ²⁺ → Fe ²⁺ + HO ₂ •	k ₁₀ = 2.3 × 10 ⁻³
F11	Fe(OH)(HO ₂) ⁺ → Fe ²⁺ + HO ₂ • + OH ⁻	k ₁₁ = 2.3 × 10 ⁻³
F12	Fe ²⁺ + •OH → Fe ³⁺ + OH ⁻	k ₁₂ = 2.7 × 10 ⁸
F13	FeOH ⁺ + •OH → Fe ³⁺ + 2OH ⁻	k ₁₃ = 2.7 × 10 ⁸
F14	Fe(II) + HO ₂ • → Fe ³⁺ + HO ₂ ⁻	k ₁₄ = 1.2 × 10 ⁶
F15	Fe(II) + O ₂ • ⁻ → Fe ³⁺ + O ₂ ²⁻	k ₁₅ = 1.0 × 10 ⁷
F16	Fe(III) + HO ₂ • → Fe ²⁺ + O ₂ + H ⁺	k ₁₆ = 2.0 × 10 ⁴
F17	Fe(III) + O ₂ • ⁻ → Fe ²⁺ + O ₂	k ₁₇ = 5.0 × 10 ⁷
F18	•OH + H ₂ O ₂ → O ₂ • ⁻ + H ₂ O + H ⁺	k ₁₈ = 3.3 × 10 ⁷
F19	•OH + HO ₂ • → O ₂ + H ₂ O	k ₁₉ = 7.1 × 10 ⁹
F20	•OH + O ₂ • ⁻ → O ₂ + OH ⁻	k ₂₀ = 1.0 × 10 ¹⁰
F21	•OH + •OH → H ₂ O ₂	k ₂₁ = 5.2 × 10 ⁹
F22	HO ₂ • + H ₂ O ₂ → •OH + O ₂ + H ₂ O	k ₂₂ = 0.5
F23	HO ₂ • + HO ₂ • → H ₂ O ₂ + O ₂	k ₂₃ = 8.6 × 10 ⁵
F24	O ₂ • ⁻ + HO ₂ • + H ₂ O → H ₂ O ₂ + O ₂ + OH ⁻	k ₂₄ = 9.7 × 10 ⁷

Table 3-3. Additional reactions for the Fe(III)/H₂O₂ system in the presence of sulfate (25°C; ionic strength: 0.1 M). Values form De Laat and Le.

No.	Reaction	Rate constant, k (s ⁻¹ , M ⁻¹ s ⁻¹) or equilibrium constant, K
FE25	$\text{SO}_4^{2-} + \text{H}^+ \leftrightarrow \text{HSO}_4^-$	$K_{25} = 34.7$
FE26	$\text{Fe}^{3+} + \text{SO}_4^{2-} \leftrightarrow \text{FeSO}_4^+$	$K_{26} = 389$
FE27	$\text{Fe}^{3+} + 2 \text{SO}_4^{2-} \leftrightarrow \text{Fe}(\text{SO}_4)_2^-$	$K_{27} = 4.47 \times 10^3$
F28	$\text{Fe}^{2+} + \text{SO}_4^{2-} \leftrightarrow \text{FeSO}_4$	$k_{28} = 2.29 \times 10^{11}$, $k_{-28} = 1.0 \times 10^{10}$
F29	$\text{HSO}_4^- + \cdot\text{OH} \rightarrow \text{SO}_4^{\cdot-} + \text{H}_2\text{O}$	$k_{29} = 3.5 \times 10^5$
F30	$\text{FeSO}_4 + \text{H}_2\text{O}_2 \rightarrow \text{Fe}^{3+} + \text{SO}_4^{2-} + \cdot\text{OH} + \text{OH}^-$	$k_{30} = 78$
F31	$\text{FeSO}_4 + \cdot\text{OH} \rightarrow \text{Fe}^{3+} + \text{SO}_4^{2-} + \text{OH}^-$	$k_{31} = 2.7 \times 10^8$
F32	$\text{FeSO}_4 + \text{HO}_2\cdot \rightarrow \text{Fe}^{3+} + \text{SO}_4^{2-} + \text{HO}_2^-$	$k_{32} = 1.2 \times 10^6$
F33	$\text{FeSO}_4 + \text{O}_2^{\cdot-} \rightarrow \text{Fe}^{3+} + \text{SO}_4^{2-} + \text{O}_2^{2-}$	$k_{33} = 5.0 \times 10^8$
F34	$\text{Fe}^{2+} + \text{SO}_4^{\cdot-} \rightarrow \text{Fe}^{3+} + \text{SO}_4^{2-}$	$k_{34} = 3.0 \times 10^8$
F35	$\text{FeOH}^+ + \text{SO}_4^{\cdot-} \rightarrow \text{Fe}^{3+} + \text{SO}_4^{2-}$	$k_{35} = 3.0 \times 10^8$
F36	$\text{FeSO}_4 + \text{SO}_4^{\cdot-} \rightarrow \text{Fe}^{3+} + 2 \text{SO}_4^{2-}$	$k_{36} = 3.0 \times 10^8$
F37	$\text{FeSO}_4^+ + \text{HO}_2\cdot \rightarrow \text{Fe}^{2+} + \text{SO}_4^{2-} + \text{O}_2 + \text{H}^+$	$k_{37} = 1.0 \times 10^3$
F38	$\text{FeSO}_4^+ + \text{O}_2^{\cdot-} \rightarrow \text{Fe}^{2+} + \text{SO}_4^{2-} + \text{O}_2$	$k_{38} = 1.0 \times 10^3$
F39	$\text{Fe}(\text{SO}_4)_2^- + \text{HO}_2\cdot \rightarrow \text{Fe}^{2+} + 2 \text{SO}_4^{2-} + \text{O}_2 + \text{H}^+$	$k_{39} = 1.0 \times 10^3$
F40	$\text{Fe}(\text{SO}_4)_2^- + \text{O}_2^{\cdot-} \rightarrow \text{Fe}^{2+} + \text{SO}_4^{2-} + \text{O}_2$	$k_{40} = 1.0 \times 10^3$

Kinetic expressions were obtained for all species (Tables 3-2 and 3-3), and a kinetic model was set up in MATLAB (per above), to calculate time-dependent concentrations of iron species, scavengers, radicals, hydrogen peroxide and organic targets. Special attention was paid to reactions involving sulfate (Table 3-3) because of its addition with iron and for pH control. Concentrations of all species were uniform in the reactor.

The use of low pHs had several important effects on the Fenton-based simulation. First, the buffering effect of low pH made it unnecessary to consider time-dependent pH changes and consequent changes in Fe speciation. Second, because $\text{pH} \ll \text{pK}_{\text{a}3}$ (Table 3-1), CO_2 production does not need to be considered since the scavenging species carbonate and bicarbonate ions can be neglected.

Rate expressions for concentrations of organic targets, ethanol (if present), H_2O_2 , $\cdot\text{OH}$, $\text{HO}_2\cdot^-$, $\text{O}_2\cdot^-$, Fe^{2+} , FeOH^+ , Fe(III) , FeSO_4 and $\text{SO}_4\cdot^-$ were obtained. Here, Fe(III) denotes the sum of all species in which iron has an oxidation state of +3. Algebraic expressions were available for total Fe(III) and total sulfate based on known chemical additions, so that

$$[\text{Fe(III)}] = [\text{Fe}^{3+}] + [\text{FeOH}^{2+}] + [\text{Fe}(\text{OH})_2^+] + 2[\text{Fe}_2(\text{OH})_2^{4+}] \quad (3-21)$$

$$+ [\text{Fe}(\text{HO}_2)^{2+}] + [\text{Fe}(\text{OH})(\text{HO}_2)^+]$$

$$[\text{TotSO}_4] = [\text{HSO}_4^-] + [\text{SO}_4^{2-}] + [\text{FeSO}_4^+] + 2[\text{Fe}(\text{SO}_4)_2^-] \quad (3-22)$$

$$+ [\text{FeSO}_4] + [\text{SO}_4\cdot^-]$$

in which all species can be expressed as functions of Fe^{3+} and SO_4^{2-} using appropriate equilibrium relations from Tables 3-2 and 3-3. This yields a system of ordinary differential equations and algebraic equations. Details are provided in the Appendix B. Ionic strength corrections were made using the Davies equation (34).

The QSSA was again avoided, and the stiff system of nonlinear differential-algebraic equations was solved numerically using the Gear method (ODE15S in MATLAB). The program provided time-dependent chemical trajectories for comparison with experimental results.

3.5. Results and Discussion

3.5.1. Hydrogen Peroxide Photolysis

Preliminary experiments established the wavelength-dependent lamp intensity in 10-nm bandwidth intervals from 230 to 270 nm (Table 3-4) using CCl_4 actinometry. The reported zeroth-order rate constant of carbon tetrachloride degradation (k_λ) and the known quantum yield of the process (25) supported calculation of the lamp intensity in each 10-nm bandwidth tested. Lamp irradiances at 230 and 250 nm were significantly lower than at 270 nm. Wavelength-dependent differences in irradiance were used to rationalize differences in observed reaction rates in subsequent monochromatic light experiments (below).

3.5.2. P-Cresol Experiments and Scavenger Effects.

The kinetics of PC destruction at initial hydrogen peroxide concentrations of 25 and 150 mM indicated that a higher specific rate of PC transformation was achieved at the lower peroxide level (Figure 3-2a). Direct photolysis did not contribute materially to overall reaction rate since no appreciable changes in PC concentrations were measured in the absence of H_2O_2 (control curve in Figure 3-2a).

Table 3-4. Carbon tetrachloride (CT) decomposition zeroth-order rate constant in actinometry experiments (k_λ) and resultant wavelength-dependent UV source intensity (I_0). Intensity was calculated based on a quantum yield of $\phi = 156$ mol/ein. (25) In the actinometry experiments, the wavelength range width was 10 nm, centered on the reported value. Molar extinction coefficients were measured from UV absorption spectra at the specified wavelength.

Wavelength (nm)	k_λ (M/s)	I_0 (ein L ⁻¹ s ⁻¹)	$\epsilon_{\text{H}_2\text{O}_2}$ (M ⁻¹ cm ⁻¹)	ϵ_{NP} (M ⁻¹ cm ⁻¹)	ϵ_{PC} (M ⁻¹ cm ⁻¹)
230	3.917×10^{-7}	2.636×10^{-9}	50.7	4333	-
250	9.033×10^{-7}	5.790×10^{-9}	17.1	1600	115.0
270	1.435×10^{-6}	9.199×10^{-9}	9.2	2533	-

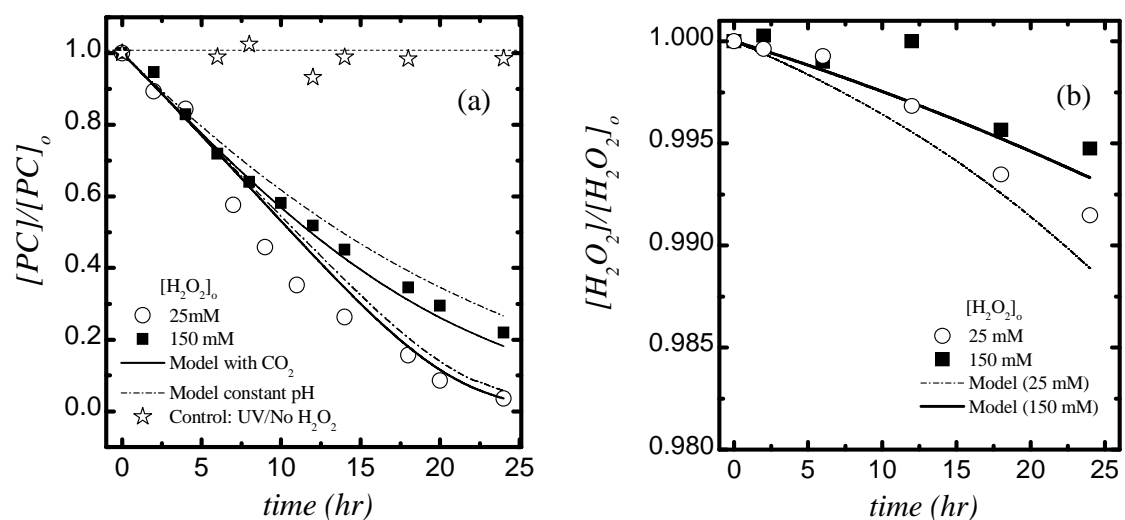


Figure 3-2. Decomposition of (a) p-cresol and (b) hydrogen peroxide for two initial H_2O_2 concentrations (UV/ H_2O_2). $[\text{PC}]_0 = 240 \mu\text{M}$, $\lambda = 250$ nm.

Two modeling approaches were used to simulate process kinetics. In the first, the evolution of CO_2 from PC mineralization and the consequent change in solution pH were neglected (constant pH lines in Figure 2a). In the second, the complete model was used. When target mineralization/pH effects were considered, agreement between model and

experiment improved. The solution pH decreased with time (see Figure 3-6 and discussion below for similar results). It is emphasized that model results were achieved with no fitting parameters. All necessary rate constants were obtained from preliminary experiments or published data (Table 3-1).

The inverse relationship between hydrogen peroxide concentration and specific rate of reaction can be understood on the basis of reactivity between hydroxyl radical and hydrogen peroxide (R2, Table 3-1). Although the second-order rate constant for the $\cdot\text{OH}/\text{H}_2\text{O}_2$ reaction is more than two orders of magnitude lower than that of the $\cdot\text{OH}/\text{PC}$ (R18, Table 3-1), the initial concentration of hydrogen peroxide was at least two orders of magnitude higher than that of PC. Furthermore, PC decreased by 80-95% during the 24-hour experiments, while the H_2O_2 varied only slightly (Figure 3-2b), increasing the fraction of hydroxyl radicals consumed by reaction with hydrogen peroxide over the course of each experiment. Increasing H_2O_2 concentration from 25 to 150 mM lowered the near-steady concentration of hydroxyl radicals from 2.30×10^{-15} M to 1.78×10^{-15} M (model prediction at 10 hours), due to the increase in hydrogen peroxide scavenging over hydroxyl radicals, reducing the pseudo-first-order rate constant for PC disappearance proportionately.

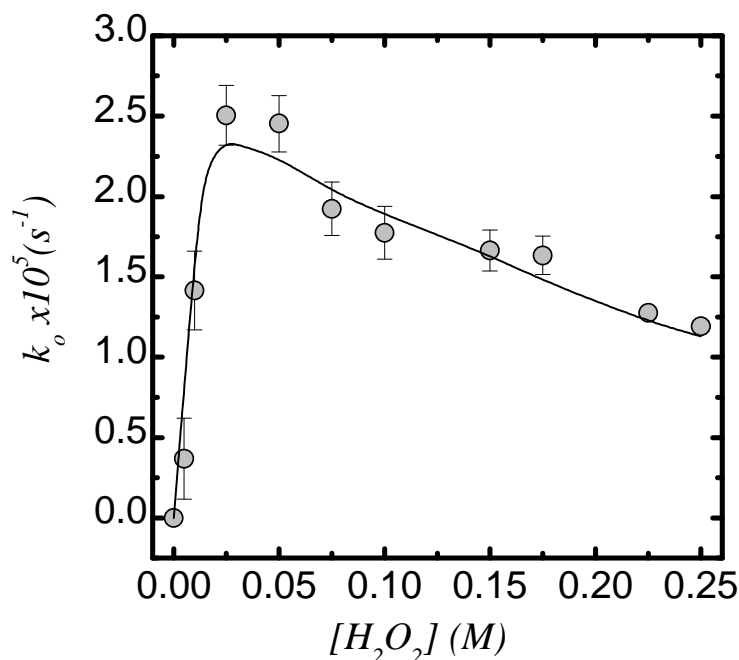


Figure 3-3. Pseudo-first order rate constants for UV/ H₂O₂ oxidation of *p*-cresol as a function of initial H₂O₂ concentrations. Solid line is the model prediction, obtained from a fit of model results to a first-order decay curve; [PC]₀=240-250 μM, λ=250 nm. Error bars represent standard deviations from repeat experiments. The coefficient of variation among rate constant estimates was 9-12% across the entire range of hydrogen peroxide concentrations examined.

Experimental and modeling results for PC degradation at all H₂O₂ concentrations tested (Figure 3-3) reflect the fact that hydrogen peroxide competes with the target compound for hydroxyl radicals. Pseudo-first order rate constants for PC degradation were estimated from fits of log-concentration vs. time curves (experiment and model results), resulting in the points and continuous curve shown. Use of a pseudo-first order rate constant to represent the overall rate of reaction is not completely adequate mainly due to the dependence of hydroxyl radical concentration on time. Furthermore, the overall process involves changes in pH and other species concentrations (e.g., carbonate ion) that affect the rate of consumption of radicals and the target over time. Therefore, it is expected that

there will be deviations from first order kinetics (Figure 3-2, for example). Nevertheless, pseudo-first-order rate constants provide a means to compare the effects of peroxide dosages in the system and offer a convenient way to compare model predictions to experimental observations. Over the entire range of H₂O₂ concentration studied (5 to 250 mM), model predictions are in good agreement with experimental observations. The rate increased up to a H₂O₂ concentration of about 25 mM, after which additional H₂O₂ slowed the disappearance of PC due to the activity of hydrogen peroxide as a hydroxyl radical scavenger. The results support model validity and suggest that no major contributor to the overall reaction mechanism has been omitted. The validated model can be used to anticipate the effects of scavenging reactions on contaminant transformation and to calculate intrinsic rate constants for reactions of hydroxyl radicals with other targets from experimental data.

Addition of 10 mM isopropanol, a hydroxyl radical scavenger (R20, Table 3-1), significantly reduced the PC oxidation rate (Figure 3-4). The pseudo-first-order rate constant for PC disappearance dropped from $1.23 \times 10^{-5} \text{ s}^{-1}$ to $3.96 \times 10^{-6} \text{ s}^{-1}$, reflecting a lower concentration of hydroxyl radicals. The published second-order rate constant for the reaction of isopropanol with hydroxyl radical (Table 3-1) was used to model PC disappearance. Results suggest that the effect of any radical scavenger for which there is a known reaction rate constant can be rationally treated in the overall UV/peroxide AOP model.

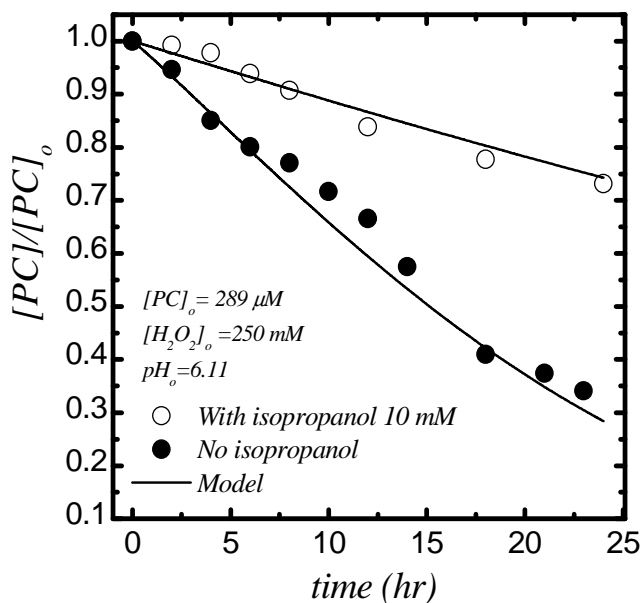


Figure 3-4. Decomposition of PC with and without an organic scavenger (isopropanol).
 $[PC]_0 = 289 \mu\text{M}$, $\lambda = 250 \text{ nm}$ (UV/ H_2O_2).

3.5.3. Nonylphenol Experiments.

Batch experiments and the validated kinetic model were used to estimate the second-order rate constant for reaction of hydroxyl radical with NP. Incorporation of a scavenging reaction between hydroxyl radical and ethanol was necessary due to the limited aqueous-phase solubility of NP and the consequent introduction of ethanol with NP. Experimental data on NP degradation was fitted to the model, using the intrinsic rate constant for the second-order $\cdot\text{OH}/\text{NP}$ reaction as the only adjustable parameter. Results yielded a rate constant of $(1.33 \pm 0.14) \times 10^{10} \text{ M}^{-1}\text{s}^{-1}$ at 25°C . Model and experiment were in agreement at hydrogen peroxide concentrations of 25 mM and 100 mM (Figure 3-5). The fitted second-order rate constant is slightly higher than that of Ning *et al.* (12) ($1.1 \times 10^{10} \text{ M}^{-1}\text{s}^{-1}$), derived from ozonation experiments.

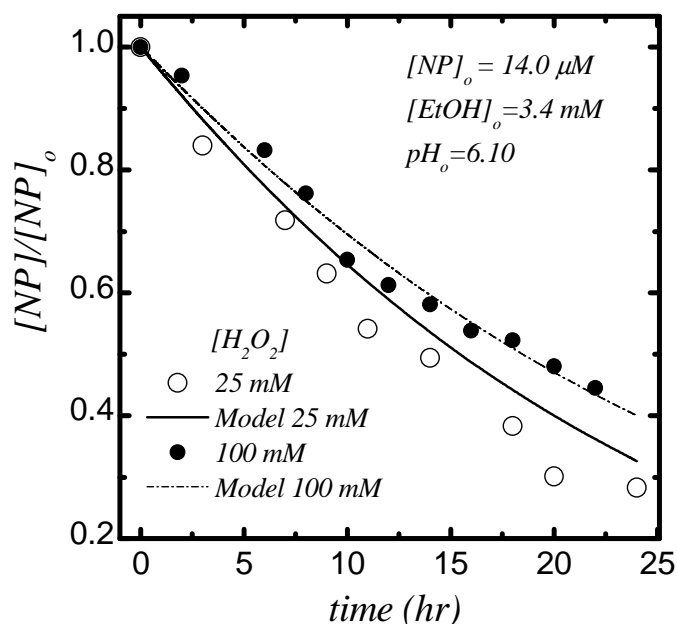


Figure 3-5. Decomposition of NP for two initial concentrations of hydrogen peroxide; $[NP]_0=14.0 \mu M$, $\lambda=250 \text{ nm}$ (UV/H₂O₂). Ethanol is added to facilitate NP dissolution and its role as a scavenger of hydroxyl radicals is modeled. To generate model results, the rate constant for $\cdot OH/NP$ reaction was used as an adjustable parameter.

Previous works have noted the importance of pH changes when AOPs result in carbon dioxide evolution (18,19). In our experiments, a significant drop in pH was observed over the 24-hour period of reaction. To model pH change, it was assumed that the target (PC or NP) and scavenger (when present) were completely mineralized. The model was capable of predicting the pH drop adequately (Figure 3-6), although it slightly overpredicts reaction-dependent pH variation during the initial stages of the experiments with NP and underpredicts pH variation in the latter stages. This would occur if NP were mineralized via sequential steps in which metastable organic intermediates were produced and later oxidized to CO₂. The formation/oxidation of intermediates would affect NP oxidation kinetics if hydroxyl radicals are consumed via reaction with

intermediates. Because H_2O_2 provides a relatively large sink for hydroxyl radicals, however, intermediates must accumulate to fairly large concentrations before their effects are likely to be appreciable. The procedures used to extract and measure NP and PC did not reveal the presence of known intermediates of free radical attack, such as alkylbenzoquinones, alkylhydroquinones, or carboxylic acids such as acetic, oxalic, formic and maleic acids.

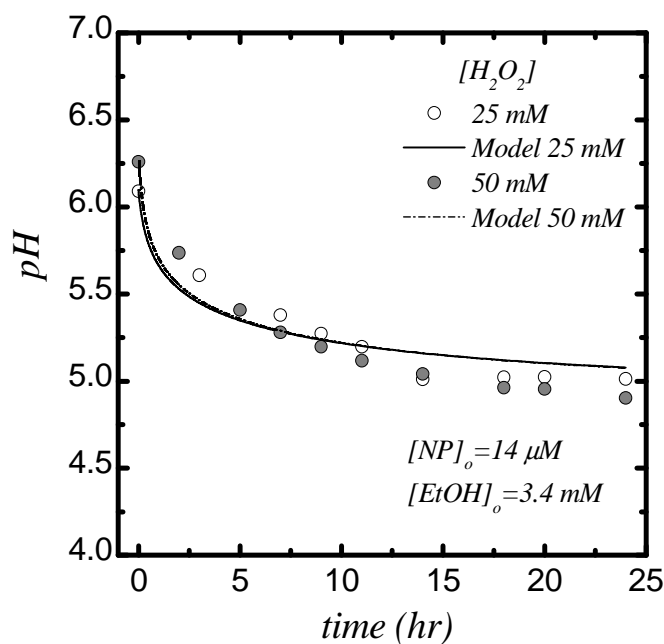


Figure 3-6. Evolution of pH during NP degradation experiments at two initial H_2O_2 concentrations (UV/ H_2O_2); $[\text{NP}]_0 = 14.0 \mu\text{M}$, $\lambda = 250 \text{ nm}$.

The significance of CO_2 evolution and pH variation to model outcome and accuracy is evident (Figures 3-2 and 3-7). Values of the pseudo-first-order rate constants for NP oxidation increased up to 35% when CO_2 evolution was included in the oxidation

mechanism, and fits to kinetic observations were greatly improved at H_2O_2 concentrations from 25-200 mM (Figure 3-7).

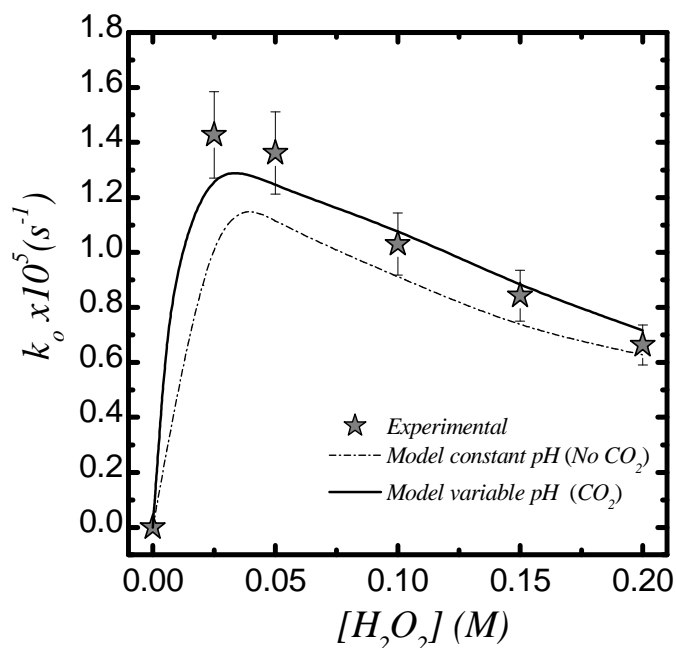


Figure 3-7. Pseudo-first order rate constant for oxidation of NP as a function of H_2O_2 concentration (UV/ H_2O_2). Lines represent model predictions. $[\text{NP}]_0=10\text{-}15\ \mu\text{M}$, $[\text{EtOH}]_0=3.4\text{-}4.2\ \text{mM}$. $\lambda=250\ \text{nm}$. The constant pH prediction neglects the CO_2 produced by NP mineralization.

Hydrogen ions are produced by the reaction of H_2O_2 with hydroxyl and carbonate radicals (R2 and R15, Table 3-1). In addition, several reactions produce OH^- . The contribution of these reactions to pH change in model simulations was small. Instead, differences in model predictions based on carbon dioxide evolution arise primarily from the pH dependence of carbonate species distribution (reactions E4 and E5, Table 3-1) and increased total carbonate concentration in the charge balance. Observed pH variation (in the range $5 < \text{pH} < 6$) should have lowered the concentrations of free radical scavenger bicarbonate and carbonate ions, allowing the rate of NP oxidation to increase. However,

the increase in total carbonate decreased the steady hydroxyl radical concentration (R4 and R5, Table 3-1), offsetting the pH effect, and slowed the decomposition of NP.

It is well known that commercial preparations of NP consist of as many as 10 isomers with different patterns of alkyl chain branching (35,36). Several isomers elute as distinguishable, albeit overlapping, peaks using the chromatographic procedures employed here. Nevertheless, no effort was made to identify specific isomers, and NP concentration/removals are reported as the sum of all detectable isomers. This approach was justified by experimental observations in which UV/peroxide treatment extinguished all NP peaks proportionately (Figure 3-8), suggesting that the NP phenolic ring is the site for initial free radical attack. Such speculation is supported by similarities in second-order reaction rate constants for p-cresol, nonylphenol and other simple aromatics ($1.2\text{--}1.3 \times 10^{10} \text{ M}^{-1}\text{s}^{-1}$). Hence, kinetic results based on oxidation of PC or other simple aromatics selected for analytical convenience may be representative of the entire class of compounds.

Differences in the oxidation kinetics of NP at incident light wavelengths of 230, 250 and 270 nm and variable light intensities (Table 3-4) were well accounted for in the model (Figure 3-9), suggesting that there is no wavelength dependence of UV/peroxide quantum yield ($\phi_{H_2O_2}$) in the range 230-270 nm and perhaps beyond, as suggested elsewhere (37). In this case, there is a compromise between the loss in absorption of light by the hydrogen peroxide as the wavelength increases and the fact that the total irradiance increased with wavelength (Table 3-4). Model calculations reported in Figure 3-9 were

obtained using the intrinsic rate constant fitted to previous data (Figure 3-5), without adjustable parameters.

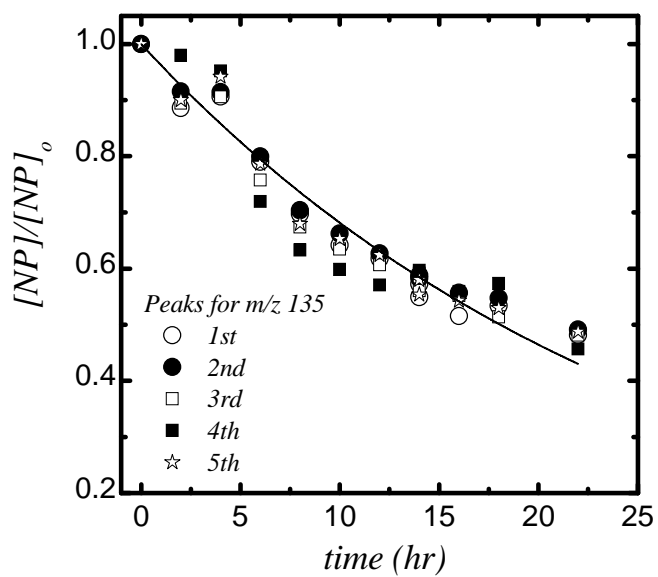


Figure 3-8. Nonylphenol isomers decomposition in UV/H₂O₂. [NP]₀=14μM, [ethanol]₀=3.4 mM. [H₂O₂]₀=100 mM, λ=250nm.

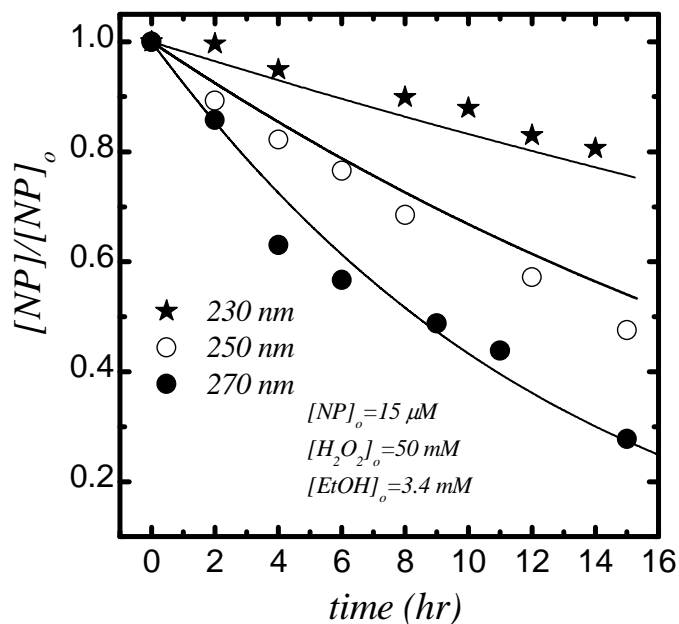


Figure 3-9. Wavelength/intensity effects in the UV/H₂O₂ decomposition of nonylphenol. The light intensities for each wavelength are reported in Table 3-4.

3.5.4. Implications for Reactor Design

The model used in this work to quantify UV/H₂O₂ AOP is sufficiently robust to represent the degradation kinetics of organic contaminants over a wide range of conditions. Because the model can handle accurately radical scavenger pathways, it is likely a good predictive tool for the treatment of complex matrices containing multiple targets, as long as the hydroxyl radical oxidation rates are known for each target, and complete mineralization is anticipated. Evidently, design of a large-scale reactor using practical UV-light sources will necessitate an integrated analysis over the intensity spectrum. In addition, mixing should be evaluated, keeping in mind the existence of radical concentration gradients induced by light intensity gradients, which potentially can make treatment of radical/radical reactions more relevant. Under the conditions explored in this

work, radical/radical reactions were negligible, so that their inclusion in the model was not necessary.

In practical design situations, the H_2O_2 dosage, the UV-light intensity spectrum and the intrinsic rate constant for reaction of the target compound and hydroxyl radicals will be the most important parameters in the determination of the reactor's residence time and, eventually, process cost and feasibility. The model developed in this work could be adapted to the reactor type used, and model calculations could be used to predict the target's rate of decomposition for cost analysis and eventual process optimization.

To illustrate aspects of design optimization, consider the behavior of a batch reactor similar to that used in our experiments, which will treat an organic target with initial concentration $c_0=1 \mu\text{M}$. Additional input parameters are: light intensity, $I_0=1\times 10^{-6} \text{ Ein/mol s}$ (typical of pilot-scale UV disinfection units), light path length $\ell=5 \text{ cm}$, constant pH of 7. Figure 3-10a shows the expected dependence of the time required for 90% destruction of the target ($t_{90\%}$) as a function of initial hydrogen peroxide concentration and the intrinsic second-order reaction rate constant between the target and hydroxyl radicals (k_T). As expected, there is a minimum in process time with hydrogen peroxide concentration, which reflects the behavior leading to maxima in Figures 3-3 and 3-7. It is interesting to note that low values of k_T (e.g. $1\times 10^7 \text{ M}^{-1}\text{s}^{-1}$ in Figure 3-10a) require such long process times that, at relatively low H_2O_2 concentrations, the H_2O_2 is itself completely consumed, and 90% conversion of the target is never achieved. In this case the $t_{90\%}$ vs. $[\text{H}_2\text{O}_2]_0$ curve exhibits a vertical asymptote.

The minimum process time ($t_{90\%,m}$) is plotted as a function of k_T , along with the H_2O_2 concentration at which the minimum occurs, in Figure 3-10b. These would be the optimum design parameters for the light intensity, initial target concentration and reactor configuration selected. Note that the relation between process time and k_T is practically a straight line in the log-log representation. The optimum H_2O_2 concentration is between 0.5 and 2 mM for most of the practical range of k_T values, but it increases abruptly for $k_T < 2 \times 10^7 \text{ M}^{-1}\text{s}^{-1}$ due to significant hydrogen peroxide consumption at longer process times. Trace contaminants of interest are located in Figure 3-10b based on reported k_T values. It is clear that, for $k_T > 3 \times 10^7 \text{ M}^{-1}\text{s}^{-1}$, application of this technology is feasible to destroy these compounds, since the required optimum process times do not exceed 2 min, and hydrogen peroxide doses are between 0.5 and 2 mM. On the other hand, more recalcitrant compounds, such as perfluorooctane sulfonate (PFOS) and perfluorooctanoate (PFOA) ($k_T < 10^6 \text{ M}^{-1}\text{s}^{-1}$) (38) clearly fall outside the range in which this process can be carried out with practical effectiveness for the light intensity level considered.

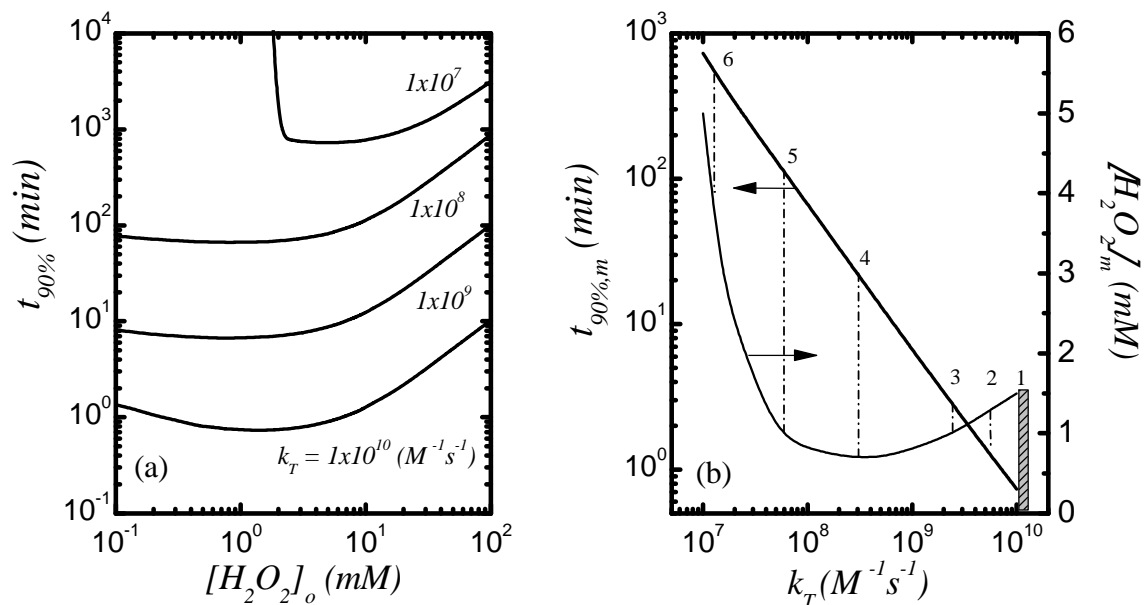


Figure 3-10. Model calculations of design parameters for a batch reactor with $I_0=1 \times 10^{-6}$ ein/mol s, $\ell=5$ cm, pH 7; (a) time required to reach 90% destruction of target (1 μ M initial concentration) as a function of initial hydrogen peroxide concentration and intrinsic rate constant for the reaction between the target and hydroxyl radicals; (b) optimum process times from (a) and hydrogen peroxide concentration at which they are achieved as a function of the intrinsic rate constant. Parameters for several trace contaminants of interest are indicated: 1– phenolic compounds (e.g. NP and PC, this work) and other endocrine disruptors (bisphenol A, 17 α -ethinyl estradiol, 17 β -estradiol) (39); 2 – trichloroethylene (40), 3 – Atrazine (41), 4 – NDMA (42), 5 – trichloroacetic acid (43), 6 – difluoroacetic acid (43).

3.5.5. Fenton's Reaction

Fenton-based oxidations of PC and NP were carried out in aqueous solution at pH ≤ 2.7 in the presence of sulfate ion, a hydroxyl radical scavenger. Process simulation followed the same approach used for the UV/H₂O₂ AOP, with kinetic rate and equilibrium constants reported by De Laat and Le (21), taking into account the oxidation of trace organics and the influence of ethanol addition (NP experiments) on AOP kinetics. Conditions for the Fenton-based experiments were selected to illustrate the importance of solution pH, total

iron concentration, initial hydrogen peroxide concentration, total sulfate and ethanol concentrations and solution ionic strength to reaction kinetics.

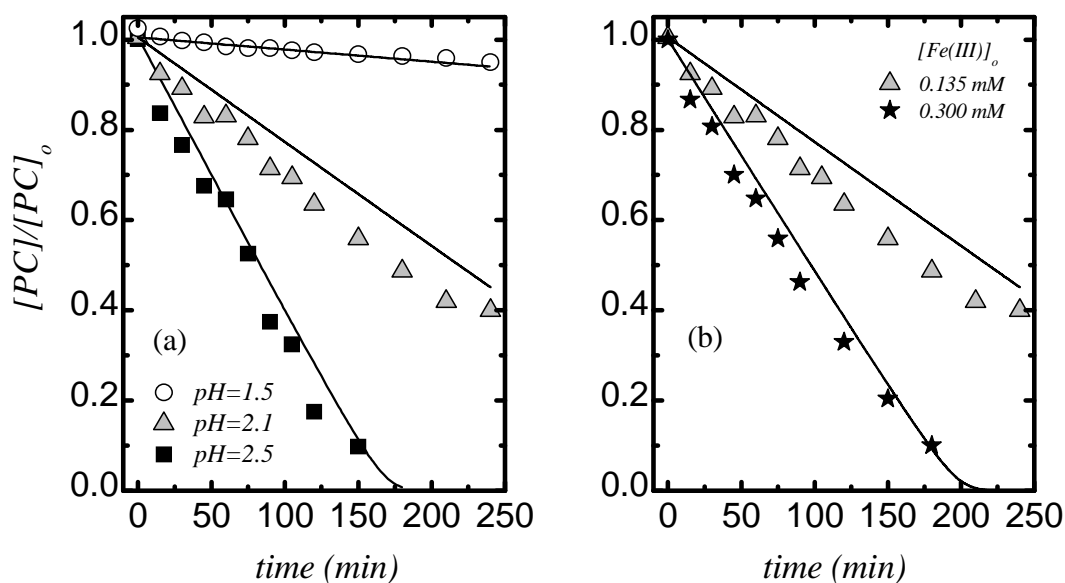


Figure 3-11. *p*-Cresol degradation in the Fenton system as a function of (a) pH at fixed $[Fe(III)]_0 = 0.135 \text{ mM}$, and (b) iron concentration at fixed pH=2.1; $[PC]_0=20 \text{ }\mu\text{M}$; $[H_2O_2]_0=10 \text{ mM}$, 25°C. Solid lines represent model predictions.

Oxidation kinetics of PC became faster with increasing pH in the range 1.5–2.7 due to (i) the effect of pH on Fe(III)/H₂O₂ complexation (Table 3-2), and (ii) decreased total sulfate concentration at higher pH. The model and observations were in reasonable agreement for PC oxidation (Figure 3-11a) over the range of pH and total iron concentrations tested. The intrinsic rate constant used for the PC/•OH reaction was $1.2 \times 10^{10} \text{ M}^{-1}\text{s}^{-1}$, following the results obtained for the UV/H₂O₂ process. Solution pH was essentially constant

during the course of each experiment. The model also accurately predicts the effect of changes in the total iron concentration (Figure 3-11b).

The oxidation of nonylphenol was similarly affected by variation in pH (Figure 3-12a). Experimental data were well represented by the model in the Fenton-based simulations. The rate constant for the NP/ \cdot OH reaction used in the simulations was $1.33 \times 10^{10} \text{ M}^{-1} \text{ s}^{-1}$, as determined by the H_2O_2 photolysis experiments. The model responded well to changes in the initial H_2O_2 concentration and presence/concentration of ethanol and sulfate. In the range of hydrogen peroxide concentrations provided, there was a direct relationship between the initial concentration of H_2O_2 and NP removal kinetics (Figure 3-12b). Relatively low concentrations of iron effectively catalyze H_2O_2 decomposition, radical generation and NP degradation, reactions that were well described in the modeling exercise. Model results (not shown) indicate that sulfate effects were due to changes in complexation of Fe(III) species by sulfate, as opposed to radical scavenging by sulfate ion, an observation offered previously by De Laat and Le (21).

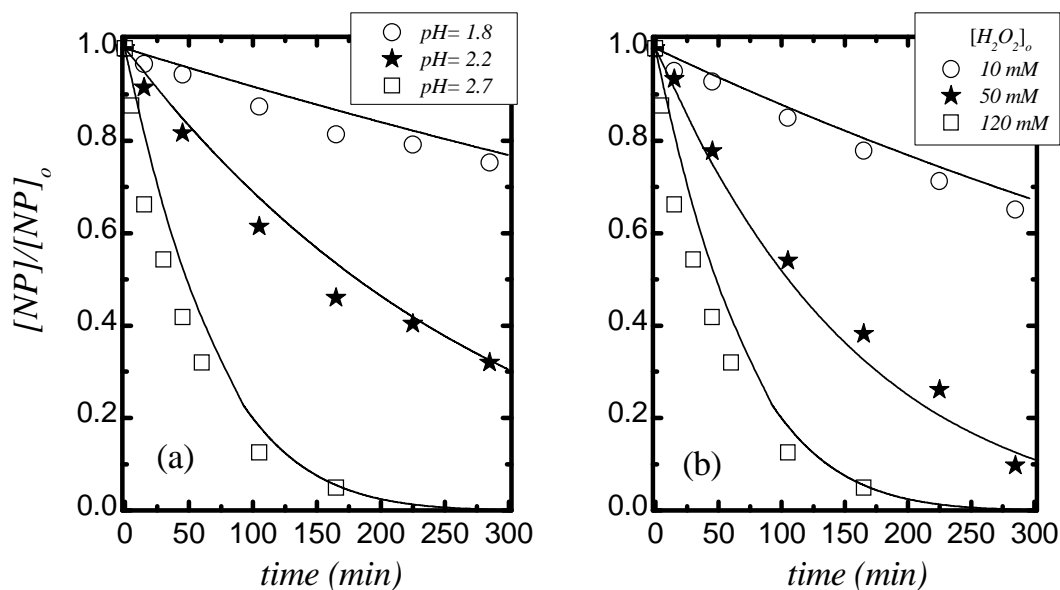


Figure 3-12. Nonylphenol degradation in the Fenton system as a function of (a) pH at fixed $[H_2O_2]_0=120$ mM, and (b) H_2O_2 concentration at fixed pH=2.7. In all cases $[Fe(III)]_0=0.25$ mM, $[NP]_0=13-20$ μ M; 25 °C. Solid lines represent model predictions.

3.6. Concluding Remarks

A comprehensive kinetic model was successfully used to simulate the destruction of two alkylphenol contaminants: *p*-cresol and nonylphenol. The rate constant for reaction between nonylphenol and hydroxyl radicals was estimated at $(1.33 \pm 0.14) \times 10^{10} \text{ M}^{-1} \text{ s}^{-1}$ from UV/ H_2O_2 photolysis experiments, a value close to those of structurally similar alkylphenols, including *p*-cresol (12). Excess hydrogen peroxide (>25 mM) decreased the rate of PC decomposition due to radical scavenging, as predicted.

The effect of organic decomposition on solution pH was successfully modeled by assuming that organic targets were mineralized and resultant carbonate species were distributed to satisfy equilibrium requirements. Resultant pH changes proved to be

important determinants of reaction kinetics. The model readily accounts for the effects of radical scavengers, ethanol and isopropanol on rates of NP and PC oxidation both for UV/H₂O₂ photolysis and Fenton's treatment.

3.7. Literature Cited

- (1) Von Sonntag, C. Advanced Oxidation Processes: Mechanistic Aspects. *Water Sci. Technol.* **2008**, 58, 1015.
- (2) Pignatello, J.J.; Oliveros, E.; MacKay, A. Advanced Oxidation Processes for Organic Contaminant Destruction Based on the Fenton Reaction and Related Chemistry. *Crit. Rev. Environ. Sci. Technol.* **2006**, 36, 1.
- (3) De Las Casas, C.L.; Bishop, K.G. Bercik, L.M.; Johnson, M.; Potzler, M.; Ela, W.P.; Sáez, A.E.; Huling, G.G.; Arnold, R.G. In-Place Regeneration of Granular Activated Carbon Using Fenton's Reagents, *Innovative Approaches for the Remediation of Subsurface-Contaminated Hazardous Waste Sites: Bridging Flask and Field Scales*; ACS Symposium Series, 940, 43, 2006.
- (4) Tuhkanen, T.A. UV/H₂O₂ Processes, *Advanced Oxidation Processes for Water and Wastewater Treatment*, Parsons, S. (ed.) IWA Publishing: London, 2004.
- (5) Neamtu, M.; Frimmel, F.H. Photodegradation of Endocrine Disrupting Chemical Nonylphenol by Simulated Solar UV-irradiation. *Sci. Total Environ.* **2006**, 369, 295.
- (6) Teske, S.; Arnold, R.G. Removal of Natural and Xeno-Estrogens during Conventional Wastewater Treatment. *Rev. Environ. Sci. Biotechnol.* **2008**, 7, 107.
- (7) Chen, P.J.; Rosenfeldt, E.J.; Kullman, S.W.; Hinton, D.E.; Linden, K.G. Biological Assessments of a Mixture of Endocrine Disruptors at Environmentally Relevant Concentrations in Water Following UV/H₂O₂ Oxidation. *Sci. Total Environ.* **2007**, 376, 18.
- (8) Flox, C.; Cabot, P.L.; Centellas, F.; Garrido, J.A.; Rodriguez, R.M.; Arias, C.; Brillas, E. Solar Photoelectro-Fenton Degradation of Cresols Using a Flow Reactor with a Boron-Doped Diamond Anode. *Appl. Catal. B* **2007**, 75, 17.
- (9) Pelizetti, E.; Minero, C.; Maurino, V.; Sclafani, A.; Hidaka, H. Photocatalytic Degradation of Nonylphenol Ethoxylated Surfactants. *Environ. Sci. Technol.* **1989**, 23, 1380.

- (10) Kurinobu, S.; Tsurusaki, K.; Natui, Y.; Kimata, M.; Hasegawa, M. Decomposition of Pollutants in Wastewater Using Magnetic Photocatalyst Particles. *J. Magn. Magn. Mater.* **2007**, *310*, E1025.
- (11) Ning, B.; Graham, N.J.D.; Zhang, Y.P. Degradation of Octylphenol and Nonylphenol by Ozone - Part I: Direct Reaction. *Chemosphere* **2007**, *68*, 1163.
- (12) Ning, B.; Graham, N.J.D.; Zhang, Y.P. Degradation of Octylphenol and Nonylphenol by Ozone - Part II: Indirect Reaction. *Chemosphere* **2007**, *68*, 1173.
- (13) Buxton, G.V.; Greenstock, C.L.; Helman, W.P.; Ross, A.B. Critical-Review of Rate Constants for Reactions of Hydrated Electrons, Hydrogen-Atoms and Hydroxyl Radicals in Aqueous-Solution. *J. Phys. Chem. Ref. Data* **1988**, *17*, 513.
- (14) Zheng, Y.; Hill, D.O.; Kuo, C.H. Destruction of Cresols by Chemical Oxidation. *J. Hazard. Mater.* **1993**, *34*, 245.
- (15) Wang, K.H.; Hsieh, Y.H.; Chen, L.J. The Heterogeneous Photocatalytic Degradation, Intermediates and Mineralization for the Aqueous Solution of Cresols and Nitrophenols. *J. Hazard. Mater.* **1998**, *59*, 251.
- (16) Kavitha, V.; Palanivelu, K. Destruction of Cresols by Fenton Oxidation Process. *Water Res.* **2005**, *39*, 3062.
- (17) Stefan, M.I.; Hoy, A.R.; Bolton, J.R. Kinetics and Mechanism of the Degradation and Mineralization of Acetone in Dilute Aqueous Solution Sensitized by the UV Photolysis of Hydrogen Peroxide. *Environ. Sci. Technol.* **1996**, *30*, 2382.
- (18) Crittenden, J.C.; Hu, S.; Hand, D.W.; Green, S.A. A Kinetic Model for H₂O₂/UV Process in a Completely Mixed Batch Reactor. *Water Res.* **1999**, *33*, 2315.
- (19) Song, W.; Ravindran, V.; Pirbazari, M. Process Optimization Using a Kinetic Model for the Ultraviolet Radiation-Hydrogen Peroxide Decomposition of Natural and Synthetic Organic Compounds in Groundwater. *Chem. Eng. Sci.* **2008**, *63*, 3249.

- (20) De Laat, J.; Gallard, H. Catalytic Decomposition of Hydrogen Peroxide by Fe(III) in Homogeneous Aqueous Solution: Mechanism and Kinetic Modeling. *Environ. Sci. Technol.* **1999**, *33*, 2726.
- (21) De Laat, J.; Le, T.G. Kinetics and Modeling of the Fe(III)/H₂O₂ System in the Presence of Sulfate in Acidic Aqueous Solutions. *Environ. Sci. Technol.* **2005**, *39*, 1811.
- (22) Dean J.A., *Lange's Handbook of Chemistry*. Fifteenth edition; McGraw-Hill: New York, 1999.
- (23) Azevedo, D.D.; Lacorte, S.; Barcelo, P.V.; Barcelo, D. Occurrence of Nonylphenol and Bisphenol-A in Surface Waters from Portugal. *J. Brazilian Chem. Soc.* **2001**, *12*, 532.
- (24) Boltz, D.; Holwell, J. *Colorimetric Determination of Nonmetals*. Second Edition; John Wiley and Sons: New York, 1978.
- (25) Li, H.; Betterton, E.A.; Arnold, R.G.; Ela, W.P.; Barbaris, B.; Grachane, C. Convenient New Chemical Actinometer Based on Aqueous Acetone, 2-Propanol, and Carbon Tetrachloride. *Environ. Sci. Technol.* **2005**, *39*, 2262.
- (26) Tamura, H.; Goto, K.; Yotsuyan, T.; Nagayama, M. Spectrophotometric Determination of Iron(II) with 1,10-Phenanthroline in Presence of Large Amounts of Iron(III). *Talanta* **1974**, *21*, 314.
- (27) Baxendale, J.H.; Wilson, J.A. The Photolysis of Hydrogen Peroxide at High Light Intensities. *Trans. Faraday Soc.* **1957**, *53*, 344.
- (28) Holcman, J.; Bjergbakke, E.; Sehested, K. The Importance of Radical-Radical Reactions in Pulse Radiolysis of Aqueous Carbonate/Bicarbonate. *Proc. Tihany Symp. Radiat. Chem.* **1987**, *6*, 429.
- (29) Bielski, B.H.J.; Cabelli, D.E.; Arudi, R.L.; Ross, A.B. Reactivity of HO₂/O₂ Radicals in Aqueous-Solution. *J. Phys. Chem. Ref. Data* **1985**, *14*, 1041.

- (30) Eriksen, T.E.; Lind, J.; Merenyi, G. On the Acid-Base Equilibrium of the Carbonate Radical. *Radiat. Phys. Chem.* **1985**, *26*, 197.
- (31) Weinstein, J.; Bielski, B.H.J. Kinetics of the Interaction of HO₂ and O₂⁻ Radicals with Hydrogen-Peroxide - Haber-Weiss Reaction. *J. Am. Chem. Soc.* **1979**, *101*, 58.
- (32) Neta, P.; Huie, R.E.; Ross, A.B. Rate Constants for Reactions of Inorganic Radicals in Aqueous-Solution. *J. Phys. Chem. Ref. Data* **1988**, *17*, 1027.
- (33) Glaze, W.H.; Lay, Y.; Kang, J.W. Advanced Oxidation Processes - a Kinetic Model for the Oxidation of 1,2-Dibromo-3-Chloropropane in Water by the Combination of Hydrogen-Peroxide and UV-Radiation. *Ind. Eng. Chem. Res.* **1995**, *34*, 2314.
- (34) Stumm, W.; Morgan, J.J. *Aquatic Chemistry: An Introduction Emphasizing Chemical Equilibria in Natural Waters*. Second ed. John Wiley & Sons: New York, 1981.
- (35) Thiele, B.; Heinke, V.; Kleist, E.; Guenther, K. Contribution to the Structural Elucidation of 10 Isomers of Technical p-nonylphenol. *Environ. Sci. Technol.* **2004**, *38*, 3405.
- (36) Moeder, M.; Martin, C.; Harynyuk, J.; Gorecki, T.; Vinken, R.; Corvini, P.F.X. Identification of Isomeric 4-Nonylphenol Structures by Gas Chromatography-Tandem Mass Spectrometry Combined with Cluster Analysis. *J. Chromatogr. A* **2006**, *1102*, 2455.
- (37) Goldstein, S.; Aschengrau, D.; Diamant, Y.; Rabani, J. Photolysis of Aqueous H₂O₂: Quantum Yield and Applications for Polychromatic UV Actinometry in Photoreactors. *Environ. Sci. Technol.* **2007**, *41*, 7486.
- (38) Vecitis, C.D.; Park, H.; Cheng, J.; Mader, B.T.; Hoffmann, M.R. Kinetics and Mechanism of the Sonolytic Conversion of the Aqueous Perfluorinated Surfactants, Perfluorooctanoate (PFOA), and Perfluorooctane Sulfonate (PFOS) into Inorganic Products. *J. Phys. Chem. A* **2008**, *112*, 4261.

- (39) Rosenfeldt, E.J.; Linden, K.G. Degradation of Endocrine Disrupting Chemicals Bisphenol A, Ethinyl Estradiol, and Estradiol during UV Photolysis and Advanced Oxidation Processes. *Environ. Sci. Technol.* **2004**, *38*, 5476.
- (40) Buxton, G.V.; Greenstock, C.L.; Helman, W.P.; Ross, A.B. Critical Review of Rate Constants for Reactions of Hydrated Electrons, Hydrogen Atoms and Hydroxyl Radicals (.OH/.O-) in Aqueous Solution. *J. Phys. Chem. Ref. Data* **1988**, *17*, 514.
- (41) Balci, B.; Oturan, N.; Cherrier, R.; Oturan, M.A. Degradation of Atrazine in Aqueous Medium by Electrocatalytically Generated Hydroxyl Radicals. A Kinetic and Mechanistic Study. *Water Res.* **2009**, *43*, 1924.
- (42) Wink, D.A.; Wink, C.B.; Nims, R.W.; Ford, P.C. Oxidizing Intermediates Generated in the Fenton Reagent: Kinetic Arguments Against the Intermediacy of the Hydroxyl Radical. *Environ. Health Perspect.* **1994**, *102*, 11.
- (43) Maruthamuthu, P.; Padmaja, S.; Huie, R.E. Rate Constants for Some Reactions of Free Radicals with Haloacetates in Aqueous Solution. *Int. J. Chem. Kinet.* **1995**, *27*, 605.

*CHAPTER 4

ADVANCED OXIDATION OF TRACE ORGANICS IN WATER BY HYDROGEN PEROXIDE SOLAR PHOTOLYSIS

4.1. Abstract

The kinetics of solar-UV/H₂O₂ advanced oxidation for destruction of p-cresol and fluorescein was investigated under a variety of operating conditions in homogeneous, laboratory-scale batch reactor experiments. A kinetic model, previously developed for monochromatic light, was adapted for use with solar UV irradiance. Using (i) computed ground-level solar spectral irradiance for the date and time of the experiments, and (ii) wavelength-dependent light attenuation in the reaction mixture as model inputs, the kinetic model represents experimental data without adjustable parameters. Model output included the time-dependent pH arising from complete mineralization of p-cresol or fluorescein. Observed radical scavenging effects were correctly predicted by the kinetic model. Contaminant transformation was also measured in a municipal secondary wastewater effluent matrix. Here, 2-D fluorescence spectroscopy was used as a measure of the time-dependent bulk organic characteristics in treated wastewater. Results indicated that solar-UV/H₂O₂ advanced oxidation is capable of eliminating or drastically reducing the concentrations of organic constituents that remain in conventionally treated municipal wastewater effluent, including both bulk and trace organics.

*A modified version of this chapter has been submitted for publication in *Industrial & Engineering Chemistry Research*.

4.2. Introduction

Modern analytical procedures allow for measurement of trace organic compounds in chemically complex media such as municipal wastewater effluent at parts-per-trillion concentrations. The revelations provided by such measurements raise concern about the potential health and ecosystem impact of treated waters, and motivate efforts to further purify waters that were previously considered clean (1-3). Many trace organics that reach municipal wastewater through human use are only partially removed during conventional wastewater treatment processes, so that advanced treatment processes are sometimes called upon to polish wastewater effluent, particularly when effluent is likely to be reused. However, advanced treatment methods such as reverse osmosis or advanced oxidation processes (AOP) are economically and energetically intensive, requiring investment of capital, engineering and operational resources that are sometimes claimed to be cost inefficient (4) As water stress increases in high-growth, water short areas, water managers are forced to include waters of impaired quality, including reclaimed wastewater, in their respective water resources portfolios. Relatively low cost, energy efficient treatments to improve reclaimed water quality are of great interest in areas where the cost of water renovation is otherwise prohibitive.

Advanced oxidation processes are used for disinfection and to polish waters containing trace organic pollutants. Common to this class of processes is the formation of highly reactive chemical radicals that react indiscriminately with residual organics in wastewater effluent, including many compounds that resist transformation during conventional biochemical processes. Most AOPs are based on the production of hydroxyl radicals

($\cdot\text{OH}$), which are among the strongest chemical oxidants known and react at relatively high rates with many organic contaminants (4,5) Among the methods used to generate such radicals is the hydrolysis of hydrogen peroxide by ultraviolet light.

Ultraviolet irradiation may induce direct photolysis of certain organic compounds. Doll and Frimmel (6) studied the kinetics of direct photodegradation of pharmaceuticals such as carbamazepine, clofibric acid and iomeprol in water, when exposed to a solar UV simulator equipped with atmospheric attenuation filters. The irradiation source, a 1000-W medium pressure xenon lamp, and a set of optical filters mimicked solar irradiation in the 300-500-nm range. Their results showed that pharmaceutical photodegradation follows pseudo-first order kinetics, and that these chemicals could be degraded in natural waters using real sunlight. Successive studies of the same group have shown similar results for other organic targets such as nonylphenol and octylphenol, exploring also the degradation by advanced oxidation in the presence of hydrogen peroxide (UV/H₂O₂) and by photo-Fenton's reactions (UV/H₂O₂/Fe) (7,8).

Since the provision of ultraviolet light energy is an important determinant of overall AOP economics, solar irradiance in the ultraviolet range should not be overlooked. The typical solar UV-flux at ground-level is 20-30 W/m², or 0.2-0.3 moles photons/m²hr in the 300-400-nm range that is suitable for use in photocatalytic reactors (9) Despite its obvious potential, there has been little commercial development or industrial use of solar photocatalysis for wastewater treatment. A brief review of related research follows.

Solar photo-Fenton is among the AOPs that have been considered for the destruction of aqueous-phase pesticides (10), pharmaceuticals (11) and other emerging contaminants (12). The technology uniformly suffers from the need to lower pH in order to maintain adequate levels of soluble Fe(III).

Irradiance of titanium dioxide leading to hydroxyl radical generation has also been explored. Solid-phase titanium dioxide must be immobilized or recovered from treated water in order to increase cost efficiency. Notable examples of solar photocatalyzed applications at the engineering scale for water treatment include a tubular fix-bed photoreactor that was developed to treat ground water contaminated with fuels such as benzene, toluene and xylene (13). The system was packed with titanium dioxide supported on silica gel. Pretreatment was necessary to prevent fouling of the catalyst. Even on cloudy days the unit destroyed >99% of the contaminants (>2 mg/L influent concentration) in less than 7 minutes. Dillert *et al.* (14) used a similar type of photoreactor to polish biologically pretreated industrial wastewater from Volkswagen factories in Wolfsburg, Germany and Taubaté, Brazil. The pilot plant consisted of twelve double-skin sheet reactors (DSSR) made of Plexiglas. The reactor operated in a recycled batch mode and was used to treat up to 1300 L/hr. The TiO₂ photocatalyst was suspended during the process and recovered by settling during non-daylight hours. In another application, the SOLARDETOX Project in Almería, Spain, was based on a commercial solar detoxification system using compound parabolic collector technology (CPC) with either a titanium dioxide slurry or a photo-Fenton process (15).

Solar-UV/H₂O₂ advanced oxidation is not limited by either pH or solids recovery requirements. Its primary disadvantages arise from low light absorption by hydrogen peroxide in the solar UV range. In this work, we explore the use of solar-UV/H₂O₂ to oxidize organic contaminants in water. A kinetic model, previously developed for monochromatic light, was adapted for use with the ground-level solar spectral irradiance calculated using a spectral atmospheric model (SMARTS). Organic targets included *p*-cresol, a common phenolic contaminant present in wastewater as a result of industrial activities (16) and fluorescein, selected for analytical convenience, reactivity with hydroxyl radical and because the compound is directly photolyzed in visible light. Solar-UV/H₂O₂ was then used to oxidize residual (bulk) organics in conventionally treated wastewater, using fluorescence 2-D spectroscopy to follow the transformation of organics.

4.3. Experimental

4.3.1. Materials.

All chemicals were obtained from commercial sources and used without further purification, including *p*-cresol (Acros, >99%), fluorescein (J.T. Baker), isopropanol (OmniSolv, GC/HPLC grade), and hydrogen peroxide (Acros, 50 wt%). *n*-Heptane was the solvent for GC/MS analyses. All solutions were prepared using a Milli-Q water (resistivity >18 MΩ cm⁻¹). Glassware was routinely washed and baked overnight at 500 °C prior to use.

4.3.2. Solar UV-H₂O₂ Experiments

Experiments were conducted in cylindrical (12-cm diameter, 500-mL) glass reactors that were open to the atmosphere and stirred continuously using a 2-cm glass-coated stir bar. Reactor sides and base were covered with aluminum foil. Experiments were performed between 10 am and 2 pm to take advantage of peak solar irradiation. Temperature was controlled (21-25°C) by a water bath. Light-free (organic target with H₂O₂ kept in the dark), peroxide-free (direct solar photolysis) and light/peroxide-free experimental controls were included in the experimental design. All experiments were performed on cloudless days.

Stock solutions of *p*-cresol or fluorescein and H₂O₂ were prepared on the day of use. Hydrogen peroxide was added at initial concentrations from 0 to 150 mM. Resulting solutions were stirred for 15 min before experiments were initiated by exposing the reactor to the sun.

For *p*-cresol experiments, liquid samples (50 μL) were withdrawn from the reactor at 30-min intervals and added to 1 mL of *n*-heptane to quench radical reactions prior to measurement of *p*-cresol by gas chromatography. Separate experiments determined a water/heptane partition coefficient $K_{WH}=0.55$, defined as the ratio of molar concentrations of *p*-cresol in both phases. For fluorescein experiments, 2-mL aliquots were periodically withdrawn to measure fluorescein concentration via UV absorbance. Solution pH was measured in liquid samples.

4.3.3. Wastewater Experiments

Chlorinated/dechlorinated wastewater effluent was obtained from the Ina Road Water Pollution Control Facility in Tucson, AZ. The facility provides conventional secondary treatment (pure oxygen activated sludge). Built in 1977, Ina Road Plant is a 37.5 million gallon per day (MGD) plant. After the treatment process, based on convectional activated sludge, the wastewater is disinfected, with most of it released to the Santa Cruz River; a small amount of effluent is reused at the Arthur Pack golf course and for on-site irrigation (17). In the experiments, effluent was used without filtration. Hydrogen peroxide was added and experiments were initiated via exposure to sunlight. Solution pH and UV₂₅₄ absorbance were monitored throughout each experiment. Time-dependent bulk organic characteristics of the treated wastewater were determined by 2-D fluorescence.

4.3.4. Analytical

p-Cresol was analyzed by GC/MS (Agilent 6890N Series—5963 MS) with a quadrupole mass analyzer and auto-injector. Electron impact ionization was at 70 eV. The carrier gas was helium at 22 cm/s. Source and interface temperatures were 200 °C and 250 °C. The HP-5 MS column (30 m × 0.25 mm ID) contained a 0.25- μ m fused silica film. The initial oven temperature (100 °C) was maintained for 1 min, after which temperature was ramped to 150 °C at 10 °C/min. The injector had a split ratio of 1:50, and the injection volume was 2 μ L.

The fluorescein concentration was measured using UV spectroscopy at 490 nm wavelength. Since fluorescein absorbance is a function of pH, generation of pH-specific calibration curves were performed.

Excitation-Emission matrices (EEM) for wastewater experiments were obtained using a Perkin Elmer Model LS-55B Luminescence Spectrometer. The excitation range was 200-450 nm and the emission range was 300-600 nm. Both excitation and emission slits were set at 5 nm. The scan speed used to generate 2-D fluorescence maps was 400 nm/min.

The hydrogen peroxide concentration was measured using a modified peroxytitanic (colorimetric) method (18). One-hundred μL samples and 50 μL of a saturated titanium sulfate aqueous solution were added to 5 mL of deionized water to quench the AOP reactions. Color (A_{407}) was measured in a spectrophotometer (Hitachi U-2000, Hitachi Corp). Samples were diluted as necessary to maintain absorbance values within the range of the standards.

4.4. Modeling

4.4.1. Solar Spectral Irradiance

The SMARTS (*Simple Model of the Atmospheric Radiative Transfer of Sunshine*) software package was used to calculate solar spectral irradiance. Calculations are based on a spectral model of solar irradiation (version 2.9.5 was used in this work) (19). The program, which is available from the National Renewable Energy Laboratory (NREL), computes the ground-level solar spectral irradiance by representing the atmosphere as a

one-layer medium that attenuates extraterrestrial solar irradiance via scattering and absorption mechanisms (20). The optical depth at $\lambda=550$ nm (turbidity measurement), and the atmospheric ozone and water vapor contents are needed to compute the solar spectral irradiance, as well as the extraterrestrial solar spectrum. These parameters were available for the dates of each solar experiment from NASA—Giovanni online applications (AQUA/AIRS and MODIS). Table 4-1 summarizes the data and input parameters used in the SMARTS calculations. The extraterrestrial spectrum used was obtained from Gueymard (21). The atmospheric concentration of carbon dioxide employed for the calculations was 370 ppm, and the reference solar constant was 1366.1 W/m² (21).

The spectral irradiance calculated at ground level in Tucson, Arizona, on July 15, 2010, and the corresponding extraterrestrial spectral irradiance (Figure 4-1a) indicate that energy at wavelengths $\lambda < 300$ nm is almost completely absorbed by the atmosphere (22). Irradiance is significantly attenuated during passage through the atmosphere at all wavelengths $\lambda < 400$ nm.

Seasonal changes on the total solar irradiance and consequences for solar UV/H₂O₂ AOP kinetics were considered. The ground-level global irradiance close to the winter solstice (December 7, 2009) was less than half of the total spectral irradiance close to the summer solstice (July 10, 2010; Figure 4-1b).

Table 4-1. Input parameters used to model the UV solar spectral irradiance (SMARTS) at the University of Arizona in Tucson, AZ.

Parameters	Dates of Experiments										
	2009					2010					
	09/10	10/17	12/07	01/29	02/19	03/03	05/24	06/15	07/15	10/08	11/18
Water Vapor ^a (cm)	3.12	1.84	0.55	1.33	0.80	0.88	0.40	1.25	4.21	1.79	0.54
Turbidity ^b	0.172	0.125	0.120	0.183	0.145	0.142	0.192	0.234	0.280	0.107	0.096
Ozone ^c (DU)	288	266	254	420	334	322	354	326	276	292	276
Aerosol Mode	Urban SRA IAMAP mode. Atmosphere: US Standard 1976. Gaseous absorption: light pollution.										
Albedo	Concrete slab. Fixed parameter.										
Site Pressure	1019 mb										
Altitude	0.728 km. Height above ground: 12 m. Fixed parameters for all calculations.										
Solar Geometry	32.22 N+, -110.92 W-, -7 GST										

^aPrecipitable water, values obtained from MODIS; ^bAerosol Optical Depth given at 550 nm (MODIS), ^cOzone content obtained from AQUA/AIRS satellite data (NASA); DU: Dobson units.

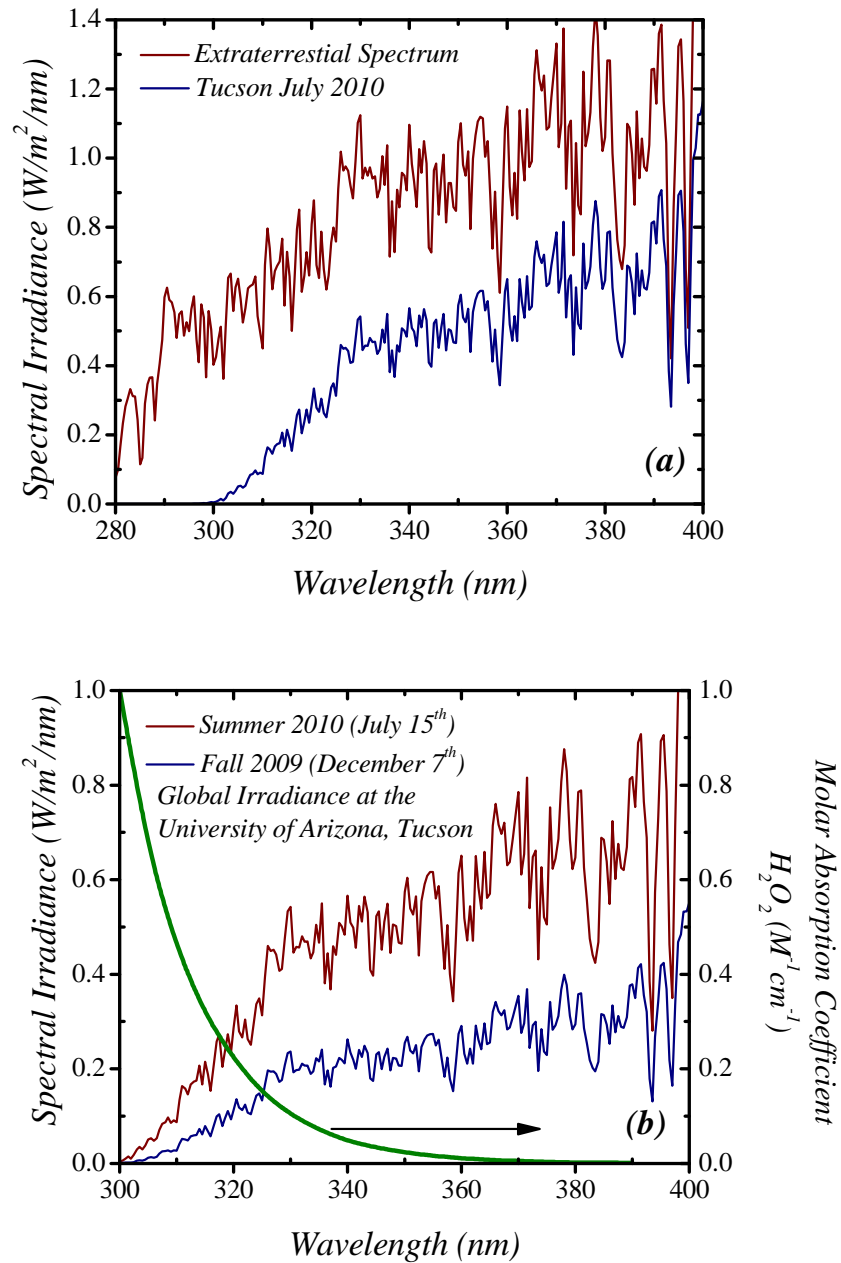


Figure 4-1. (a) Comparison of the global spectral irradiance at the top of the atmosphere and at ground level in Tucson on July 15, 2010; (b) Comparison of the UV global solar spectral irradiance in Tucson, Arizona, in fall 2009 and summer 2010, obtained with SMARTS. Experiments were performed on the dates shown, which were close to solstices. The figure includes the molar absorption coefficient for hydrogen peroxide.

The molar absorptivity of hydrogen peroxide is included in Figure 4-1b, since UV absorbance by hydrogen peroxide is the critical first step in UV/H₂O₂ AOP; the product of the wavelength-dependent irradiance and H₂O₂ absorbance is proportional to the contribution of each discrete wavelength interval to the rate of hydroxyl radical generation. It is easy to see, for example, that wavelengths above 400 nm do not contribute to hydroxyl radical production due to the lack of light absorbance by hydrogen peroxide in that wavelength range. Absorption of light at $\lambda=400$ nm was less than 0.05% over a 4.5-cm path length at the highest concentrations of H₂O₂ used here.

In all kinetic simulations, the global spectral irradiance at ground level was used to estimate the wavelength-dependent irradiance entering the AOP reactors. Global irradiance consists of the superposition of direct or beam irradiance and diffusive irradiance. The direct irradiance provides most of the energy available on the ground from the solar spectrum (23). Diffuse irradiance results from the interaction of solar radiation with suspended particles, gas molecules and aerosols in the atmosphere. The scattering by aerosols is limited to short wavelengths of less than 1000 nm (23). As a result, the contribution of diffuse irradiance to the global irradiance in the infrared range and above is low, but in the UV range, diffuse irradiance provides a substantial fraction of the global irradiance at ground level (Figure 4-2a).

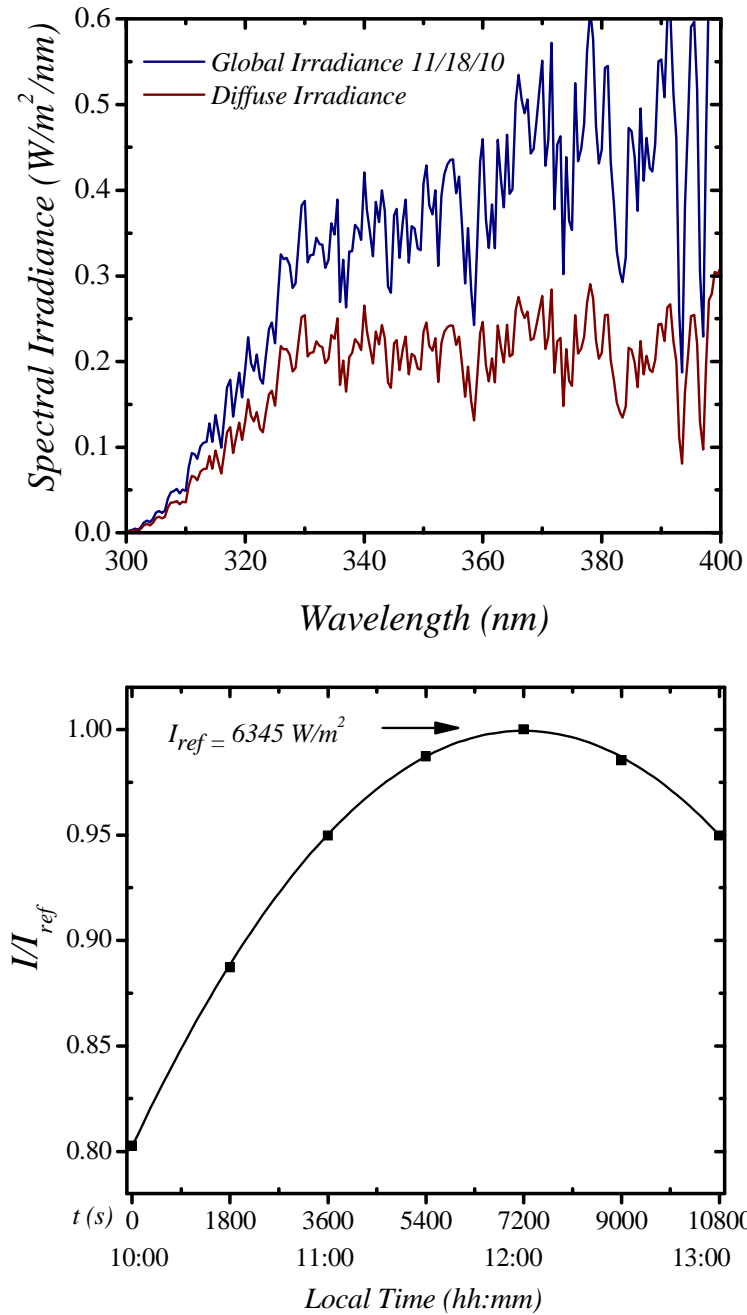


Figure 4-2. (a): Global spectral irradiance and diffusive spectral irradiance in November 18, 2010 in Tucson; (b) Time-dependent total irradiance as a fraction of the maximum (noon) irradiance at ground level in Tucson on November 18, 2010. Polynomial fitting: $0.8024 + 5.4765\text{E}^{-5}x - 3.8069\text{E}^{-9}x^2$.

Not surprisingly, ground-level solar irradiance is sensitive to the time of day. All experiments were conducted between 10 am and 2 pm to maximize solar exposure. Nevertheless, ground-level solar irradiance varied by up to 20% during that period (Figure 4-2b). To model such variations in intensity, a second-order polynomial was fitted to the normalized total irradiance and used as a time-dependent correction factor for incident radiation in each discrete bandwidth element.

4.4.2. Solar UV/H₂O₂ Model.

The mechanism of UV/H₂O₂ advanced oxidation and the corresponding kinetic model have been described previously (16,24). The mechanism involves the generation of hydroxyl radicals by photolysis of hydrogen peroxide, reaction of these radicals with the target compounds and radical scavengers (including hydrogen peroxide itself), generation of other active radical species ($O_2^{\cdot-}$ and $CO_3^{\cdot-}$), and radical-radical recombination reactions.

A summary of all the reactions that were considered in this work is presented in Table 3-1 (Chapter 3). Previous models were valid for monochromatic light sources and were applied to numerous target compounds (16,24,25). The main novelty of the approach used in this work is the extension of the model to polychromatic light, which will find applications not only in the treatment of solar photolysis as is done here but to reactors that use polychromatic light sources.

In a previous work (16) we argued that, in a batch reactor with mechanical agitation, it is a good assumption to consider that all non-radical species are well mixed so that they can be represented by a single molar concentration. However, the rates of formation and decomposition of radicals are much faster than mass transfer rates. As a consequence, radical concentrations will vary with position in the direction of light attenuation. This implies that, rigorously, an overall kinetic model can only be established from a point equation that is then averaged over the reactor volume. This is the approach employed in what follows.

The volume-averaged kinetic equation for the decomposition of an organic target (T) takes into account its reaction with hydroxyl radicals, as well as direct photolysis (16).

$$\frac{d[T]}{dt} = -k_T[T]\langle[\cdot OH]\rangle - \phi_T \int_{\lambda_1}^{\lambda_2} Q_\lambda f_{\lambda-T} (1 - e^{-2.303A_\lambda}) d\lambda \quad (4-1)$$

In this equation, square brackets denote point molar concentrations and angular brackets denote volume averages. The target molar concentration, $[T]$, is considered uniform whereas the hydroxyl radical concentration is a volume average, $\langle[\cdot OH]\rangle$. The first term on the right hand side of the equation includes the second order reaction rate constant for target decomposition by hydroxyl radicals, k_T . The second term on the right hand side represents the volume-averaged rate of decomposition of the target by direct photolysis. Here, ϕ_T is the quantum yield (mol/E), Q_λ is the specific spectral intensity of light that enters the reactor (that is incident light intensity per unit reactor volume and wavelength,

$\text{E/m}^3\text{nm}$ – see below), $f_{\lambda-T}$ is the fraction of the light intensity that is absorbed by the target (see below), and A_λ is the total spectral absorbance of the target in the reactor (see below). The spectral integral in equation 1 is carried out between wavelength limits that cover all relevant light absorption for the target (λ_1 and λ_2 .)

Although direct photolysis is considered, its contribution to *p*-cresol conversion proved to be negligible under experimental conditions explored in this work (see below). Direct photolysis contributed substantially to the overall decomposition of fluorescein, however, and a quantum yield for this target was determined experimentally.

The specific spectral intensity was calculated from the spectral irradiance from

$$Q_\lambda = \frac{A_R \lambda S_\lambda}{V_R N_a h c} \quad (4-2)$$

Where S_λ is the spectral irradiance ($\text{W/m}^2\text{nm}$), V_R is the reactor volume (m^3), A_R is the surface area of the reactor exposed to incident light (m^2), N_a is Avogadro's number (6.022×10^{23}), h is Planck's constant ($6.626 \times 10^{-34} \text{ kg/m}^2\text{s}$) and c is the speed of light ($299,762,458 \text{ m/s}$).

The total spectral absorbance of the solution is given by

$$A_\lambda = (\epsilon_{\lambda-T}[T] + \epsilon_{\lambda-H_2O_2}[H_2O_2])l \quad (4-3)$$

where $\varepsilon_{\lambda-T}$ and $\varepsilon_{\lambda-H_2O_2}$ are the wavelength-dependent molar extinction coefficients for the target and hydrogen peroxide, respectively (assumed here to be the only light-absorbing species in solution), and l is the path length for light in the reactor. Molar extinction coefficients were obtained from UV absorption spectra at the wavelengths of interest. The fraction of irradiation absorbed by the target is

$$f_{\lambda-T} = \frac{\varepsilon_{\lambda-T}[T] l}{A_{\lambda}} \quad (4-4)$$

The integral in equation (4-1) was evaluated numerically. For this purpose, the spectral irradiance was discretized in 5-nm intervals and the limit wavelengths used were $\lambda_1=300$ nm and $\lambda_2=400$ nm. Solar energy outside this wavelength interval had essentially no effect on radical generation due either to attenuation in the atmosphere or inability to photolyze hydrogen peroxide.

A similar approach was used to represent the reaction rate for hydrogen peroxide.

$$\begin{aligned} \frac{d[H_2O_2]}{dt} = & -\phi_{H_2O_2} \int_{\lambda_1}^{\lambda_2} Q_{\lambda} f_{\lambda-H_2O_2} (1 - e^{-2.303A_{\lambda}}) d\lambda - k_2[H_2O_2]\langle[\cdot OH]\rangle \\ & - k_3[HO_2^-]\langle[\cdot OH]\rangle - k_{10}[H_2O_2]\langle[O_2^- \cdot]\rangle - k_{14}[H_2O_2]\langle[HO_2 \cdot]\rangle \\ & - k_{15}[H_2O_2]\langle[CO_3^- \cdot]\rangle - k_{16}[HO_2^-]\langle[CO_3^- \cdot]\rangle + k_8\langle[\cdot OH]^2\rangle \\ & + k_{12}\langle[HO_2 \cdot][O_2^- \cdot]\rangle + k_{13}\langle[HO_2 \cdot]^2\rangle \end{aligned} \quad (4-5)$$

This equation considers that the quantum yield for hydrogen peroxide photolysis is independent of wavelength in the range $300 < \lambda < 400$ nm, which is consistent with previous kinetic studies (26) HO_2^- is determined from the equilibrium with H_2O_2 (R19, Table 3-1) assuming that $[\text{HO}_2^-] \ll [\text{H}_2\text{O}_2]$, a condition that is met throughout the pH range of our experiments.

Equation (4-5) includes averages of products of radical concentrations that result from radical/radical reactions (R8, 12 and 13). Reaction rates for this type of reaction were verified to be negligible in all cases so that no assumptions were necessary regarding nonlinear averages.

Similar equations were developed for net rates of reaction of free radicals ($\cdot\text{OH}$, $\text{O}_2\cdot^-/\text{HO}_2\cdot^-$ and $\text{CO}_3\cdot^-$); radical scavengers (R20) (when present), and carbonate species. Details of the complete formulation are given in Chapter 3.

The approach presented yielded a stiff system of ordinary differential equations governing the rates of formation or disappearance of the target contaminants, H_2O_2 , $\cdot\text{OH}$, $\text{O}_2\cdot^-$, $\text{HO}_2\cdot^-$, $\text{CO}_3\cdot^-$, total carbonate species and radical scavengers. Algebraic equations (carbonate equilibria and the charge balance) were used to calculate the concentrations of carbonate species and solution pH. Numerical solutions were obtained using the ODE15s MATLAB subroutine (Gear's method). The relative tolerance was set at 10^{-8} , and the

absolute tolerances for concentrations of all species were four orders of magnitude below their respective values (16).

4.5. Results and Discussion

4.5.1. P-Cresol and Fluorescein Experiments.

Results of *p*-cresol degradation experiments are presented in Figure 4-3. These experiments, performed in winter (February 2010) show that, under the experimental conditions explored, *p*-cresol can be almost completely degraded in a few hours at high enough hydrogen peroxide concentrations. At an initial hydrogen peroxide concentration of 10 mM, the half time for *p*-cresol disappearance was 112 min. Direct photolysis (no H₂O₂) did not contribute materially to the observed reaction rate. Kinetic simulations accurately reproduced empirical observations with no fitted constants over the entire range of experimental conditions.

Solution pH can be an important determinant of UV/H₂O₂ process kinetics (16,24,25). To calculate reaction dependent changes in solution pH, it was assumed that AOP treatment results in complete target mineralization (16). The model was able to simulate pH change due to *p*-cresol oxidation over the entire range of initial hydrogen peroxide concentrations (Figure 4-4). However, the model slightly overpredicted pH reduction during the initial stages of each experiment, consistent with the temporary development of metastable, partially oxidized intermediates (16). Eventual compound mineralization is suggested by agreement of model pH predictions with measured values in the latter stages of each experiment. It is doubtful that organic intermediates provide a meaningful

sink for hydroxyl radicals since hydrogen peroxide itself is an important radical scavenger at the concentrations used here. In all cases, measurements indicated no appreciable variation of hydrogen peroxide concentrations (results not shown) during the time of the experiment.

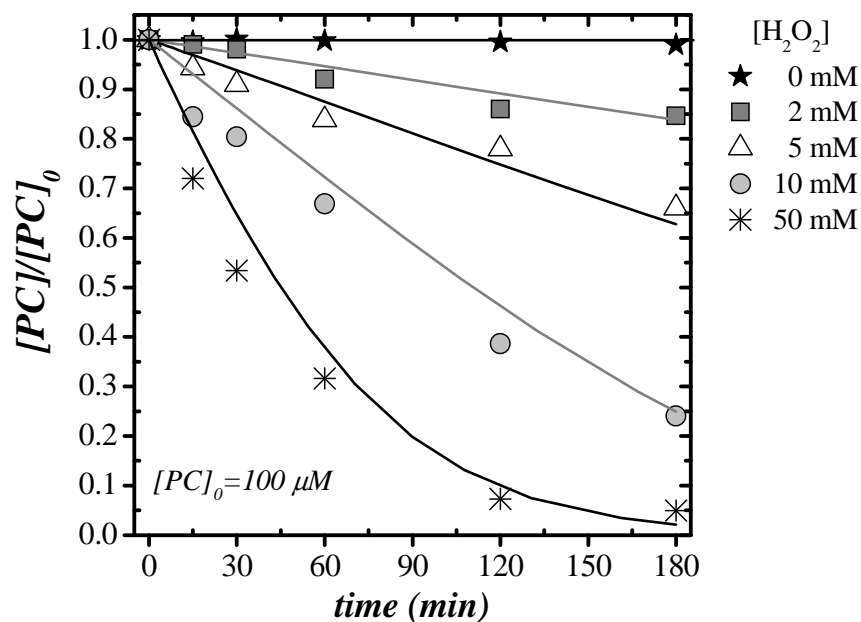


Figure 4-3. Experimental decomposition of *p*-cresol by solar-catalyzed UV-H₂O₂ as a function of initial hydrogen peroxide concentration. Solid lines represent model predictions. Experiments were carried out on February 19, 2010.

Model performance was further tested by adding isopropanol (IPOH), a well characterized hydroxyl radical scavenger, to the reaction mixture. The second-order rate constant for reaction with hydroxyl radical with IPOH is about an order of magnitude lower than the reported value for *p*-cresol oxidation (R18 and 20, Table 3-1). The model accurately predicts the scavenging effect of isopropanol (Figure 4-5), suggesting that the simulation can be usefully applied to predict reaction kinetics in all situations for which

the second-order rate constants for the reaction of hydroxyl radicals with trace organic targets and radical scavenging compounds (including hydrogen peroxide) are known.

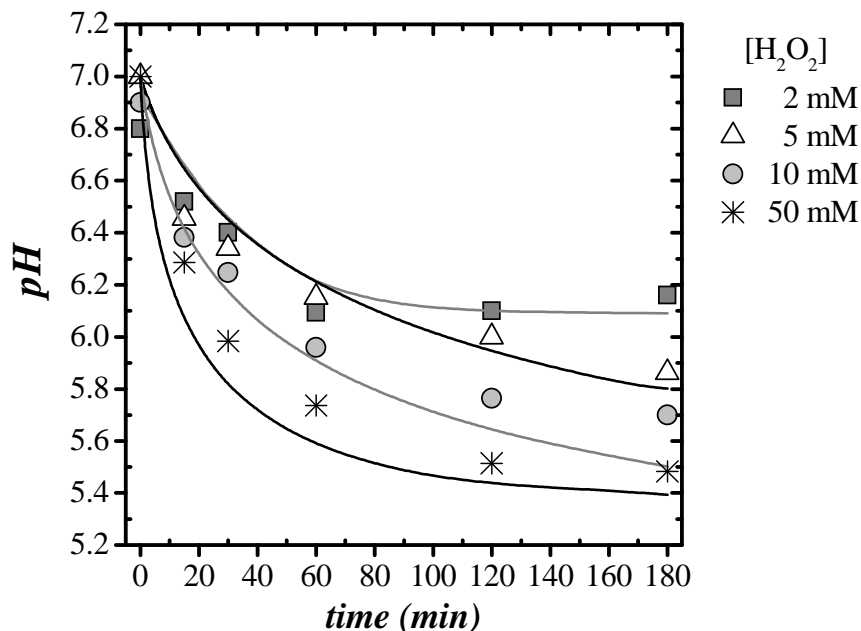


Figure 4-4. pH change during *p*-cresol experimental decomposition by solar-catalyzed UV- H_2O_2 , at different hydrogen peroxide concentrations, and kinetic model performance. Solid lines represent the model. Experiments were carried out on February 19, 2010.

Results also indicate that diurnal and seasonal variations in spectral irradiance can be successfully accounted for in process simulations. Half-lives for *p*-cresol in batch AOP experiments conducted in winter (February) and summer (July) decreased dramatically with increases in hydrogen peroxide concentration up to 50 mM. Not surprisingly, contaminant half-life was inversely related to total irradiance (Figure 4-6).

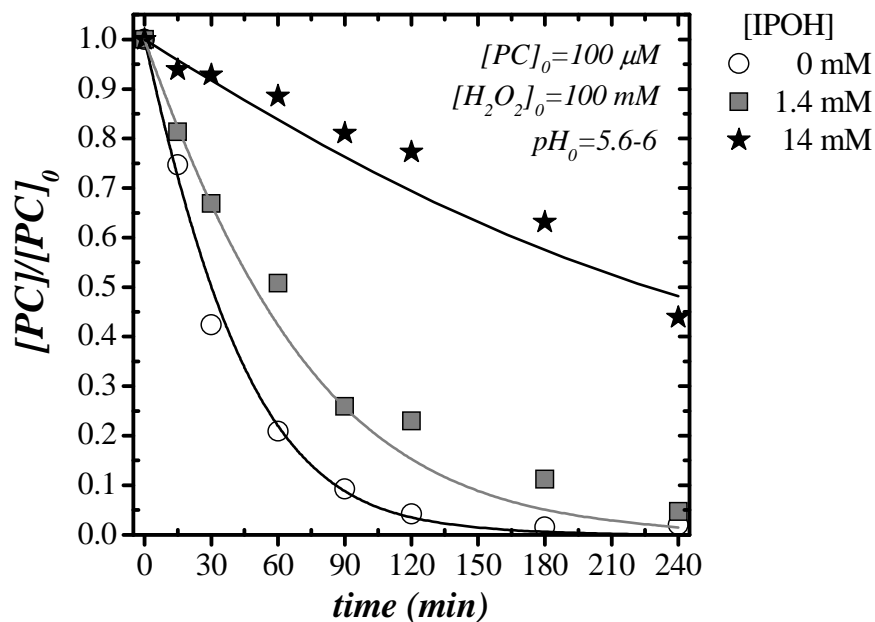


Figure 4-5. Effect of an organic scavenger (IPOH) on *p*-cresol decomposition by solar-catalyzed UV-H₂O₂. Solid lines represent model predictions. Experiments were carried out in September 10, 2009.

Previous work (Chapter 3) showed that high levels of hydrogen peroxide concentrations slowed the rate of UV/peroxide AOP destruction on *p*-cresol because of the scavenging effect of hydrogen peroxide on hydroxyl radicals (R2, Table 3-1). Rate deceleration at very high peroxide concentrations was not observed here, however, because of the relatively small reactor depth (4.5 cm) and limited light path length. A relatively small fraction of the incident irradiance was absorbed in the reactor, even at the higher peroxide concentration (40% absorbed at 300 nm, 1% at 350 nm in 50 mM H₂O₂), so that each H₂O₂ concentration increment increased the net rate of hydroxyl radical production in the reactor, the average hydroxyl radical concentration and the pseudo-first-order rate constant for the disappearance of *p*-cresol. Peroxide- and irradiance-dependent variations

in *p*-cresol concentration conformed to predicted values in model simulations with no adjustable parameters.

At 10 mM H₂O₂, the half-life for *p*-cresol oxidation decreased from 112 min in February 2009 to 71 min in July 2010 as a consequence of increased irradiance. The effect was well anticipated by the simulation. Results corresponding to additional irradiance levels (insert to Figure 4-6) show that the pseudo-first-order rate constant for *p*-cresol disappearance increases approximately in proportion to total irradiance over the range 550-1000 mW/cm². Again, model simulations provided an adequate representation of data with errors below 10% with respect to experimental results.

The fluorescein target provided an additional modeling challenge arising from direct photolysis and fluorescein-dependent light absorbance in the UV range. Maintenance of pH > 9.0 was necessary in these experiments in order to keep fluorescein soluble at all times. The kinetics of fluorescein (FL) degradation in sunlight (Figure 4-7) illustrates the dependence of rate on hydrogen peroxide concentration. Direct photolysis was responsible for disappearance of the target in the peroxide-free experiment. This particular data set was used to fit a fixed quantum yield for fluorescein photolysis (0.0018 mol/Ein in the wavelength range 300-400-nm). This calculated quantum yield was incorporated in the model to predict degradation rates in the presence of hydrogen peroxide (Figure 4-7).

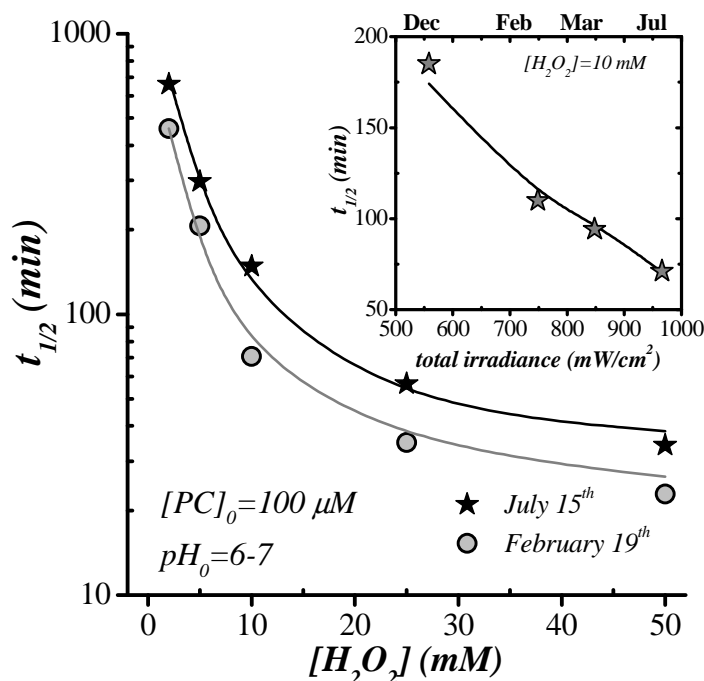


Figure 4-6. Half-lives for *p*-cresol decomposition by solar-catalyzed UV- H_2O_2 as a function of hydrogen peroxide concentration in winter (Feb 2009) and summer (July 2010). Inset: Half-life times for *p*-cresol at a fixed H_2O_2 concentration (10 mM), as a function of total solar irradiation (ground-level). Solid lines represent model predictions.

4.5.2. Wastewater Applications.

Solar-peroxide AOP is potentially a cost effective method for polishing treated wastewater prior to reuse. However, non-productive consumption of hydroxyl radicals with residual (bulk) wastewater organics is likely to have an adverse effect on process efficiency. It is necessary, then, to monitor the fate of bulk organics themselves during UV/peroxide AOP in order to anticipate the time-dependent drag that residual organics will likely exert on AOP applications for management of trace organics. Here, we followed the AOP-dependent destruction of dissolved organic material (DOM) in municipal wastewater effluent using 2-D fluorescence spectroscopy (excitation emission matrices, EEM) as described above. It is recognized that fulvic acids, humic acids and

proteins—primary components of residual DOM in conventionally treated wastewater—are distinct fluorophores (27) Leenheer and Croué (28) and others proposed a classification for EEM peaks, relating them to specific components of DOM, suggesting that fluorescence at 420-480/330-350 and 380-480/250-260 nm (emission/excitation) is associated with humic-like material. Similarly, fluorescence at 300-350/270-280 (em/ex) is related to proteinaceous structures. Consequently, time-dependent excitation/fluorescence contours from EEM may provide a reasonable means to track the fates of several important classes of residual DOM during engineered or natural processes that polish effluent.

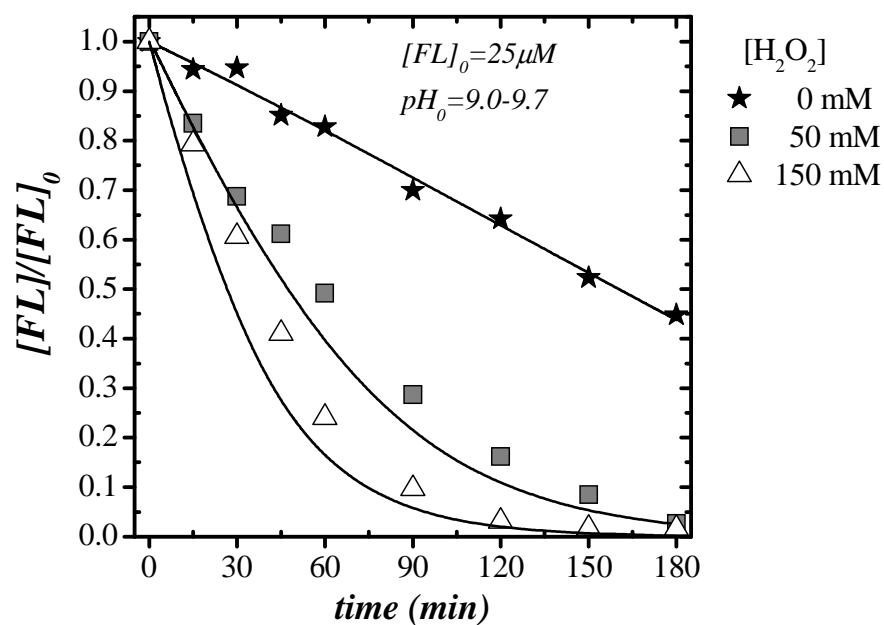


Figure 4-7. Experimental decomposition of sodium fluorescein dye by solar-catalyzed UV- H_2O_2 as a function of hydrogen peroxide concentration. Solid lines represent model predictions. Experiments were carried out on June 15, 2010.

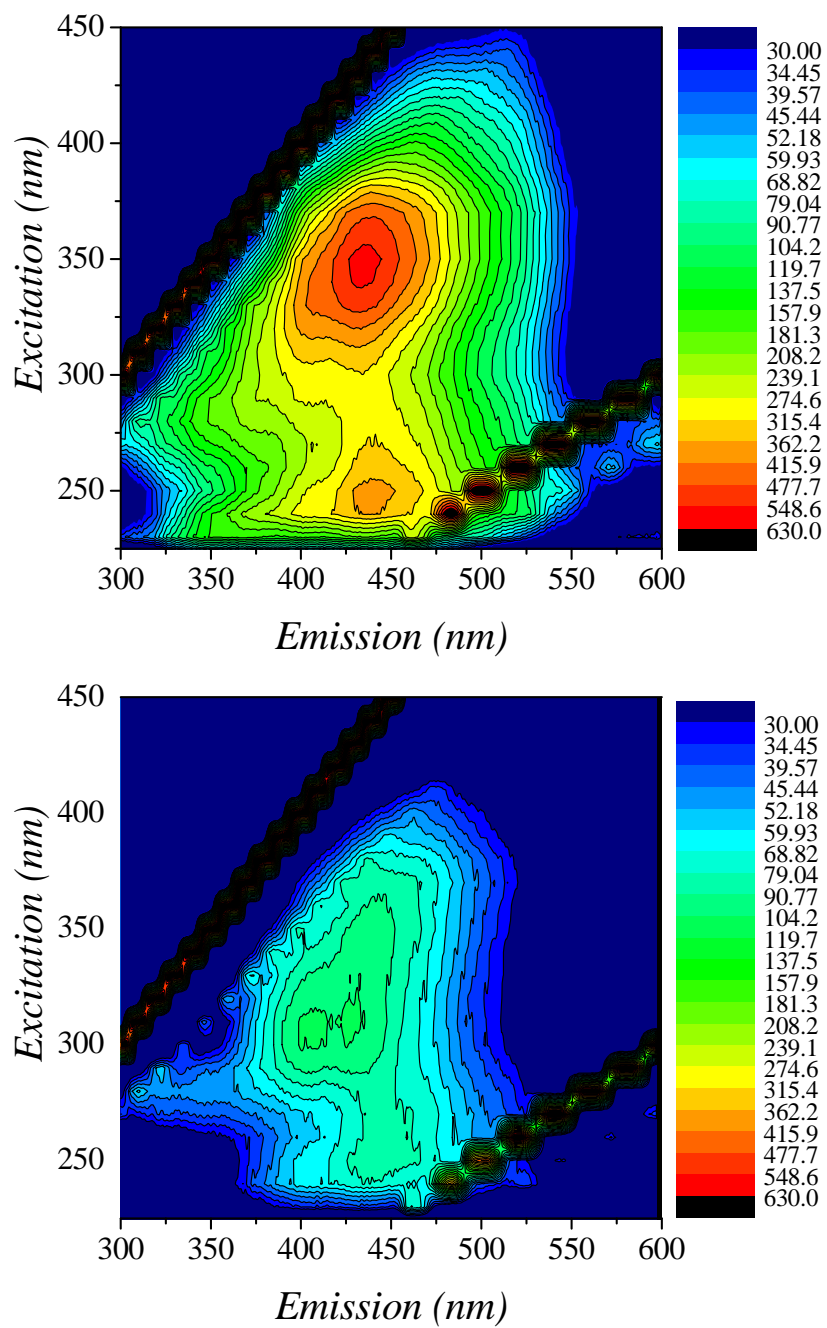


Figure 4-8. Excitation-emission matrices (EEM) for Ina Road wastewater effluent (05/16/2011) before (a) and after (b) 3 h of solar-catalyzed AOP treatment with 5 mM H₂O₂ in a batch reactor.

Solar-UV/peroxide treatment of wastewater effluent clearly lowers the concentrations of residual DOM components (all peaks, Figure 4-8). Here, the peak intensity at 435/350 em/ex (humic substances) was taken as a representative measure of residual DOM in the treated water (3 hr, sunlight, 5 mM initial H₂O₂ concentration). The time-dependent intensity of the 435/350 peak (Figure 4-9) illustrates the effectiveness of solar-UV/peroxide treatment for removal of this organic fraction. The 5 mM H₂O₂ treatment reduced the intensity of the peak by > 80% in three hours. Absent hydrogen peroxide, the peak intensity was reduced by < 20% in a comparable period, presumably due to direct photolysis.

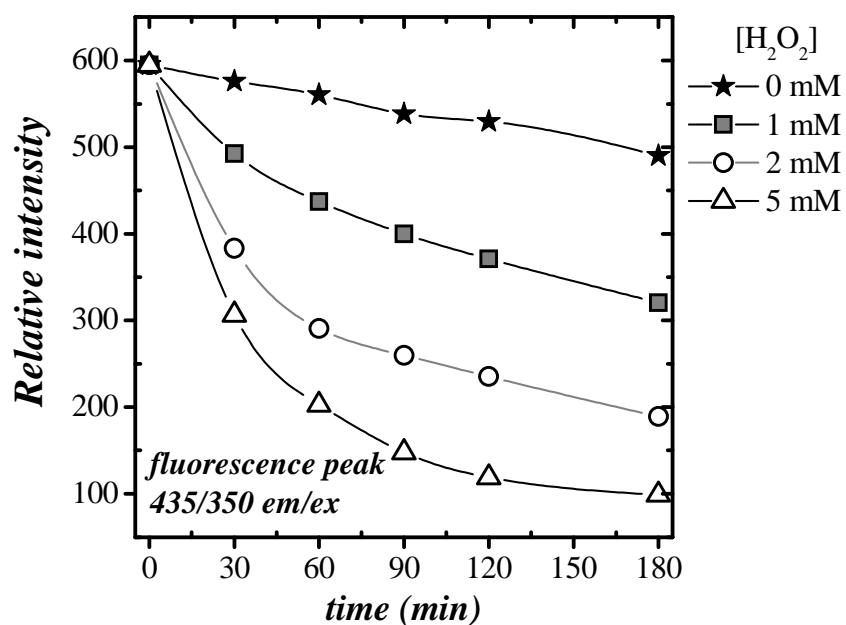


Figure 4-9. Relative intensity of the 435/350 em/ex peak in the fluorescence spectrum for Ina Road wastewater effluent (05/16/2011) as a function of time of solar-catalyzed UV-H₂O₂ treatment and hydrogen peroxide concentration.

These results identify several potentially productive avenues for additional research. Solar-UV/peroxide treatment may be a useful effluent polishing technique, although radical scavenging must be quantified in some way to facilitate reactor design for destruction of trace organic contaminants. If partial oxidation produces organic intermediates and/or by-products, these should be investigated. Radical scavenging by residual organics should be better understood if process modeling is to lead to effective reactor design and selection of operating conditions, particularly if solar-UV is included among a series of treatments designed to restore municipal wastewater for reuse.

4.6. Concluding Remarks

A comprehensive kinetic model with no adjustable parameters and representing the oxidation of organics by solar-catalyzed UV/peroxide AOP in a batch reactor was developed and validated. The model employs solar spectral irradiances in the 300-400 nm range from an atmospheric spectral model (SMARTS) to estimate the irradiance to the reactor. The kinetics of *p*-cresol and fluorescein decompositions were successfully simulated for a wide range of operating conditions, including different hydrogen peroxide concentrations, light intensities and the presence/absence of an organic scavenger. Reaction-dependent changes in pH were adequately modeled by assuming that organic targets were mineralized.

The solar-UV/peroxide process has potential for polishing conventionally treated wastewaters. Decreased intensities in 3D fluorescence maps suggest that DOM in municipal wastewater effluent was substantially reduced during a three-hour exposure to

sunlight. Further research is needed to establish the fates of specific contaminants, establish process kinetics for wastewater applications, and to optimize the process in terms of hydrogen peroxide dosage and reactor configuration.

4.7. Literature Cited

- (1) Halling-Sorensen, B.; Nielsen, N.; Lanzky, P.F.; Ingerslev, F.; Holten Lützhøft, H.C.; Jørgensen, S.E. Occurrence, Fate and Effects of Pharmaceutical Substances in the Environment - A Review. *Chemosphere* **1998**, 36, 357-393.
- (2) Heberer, Th.; Reddersen, K; Mechlinski, A. From Municipal Sewage to Drinking Water: Fate and Removal of Pharmaceutical Residues in the Aquatic Environment in Urban Areas. *Water Sci Technol* **2002**, 46, 81-88.
- (3) Miege, C.; Choubert, J.M.; Ribeiro, L.; Eusebe, M.; Coquery, M. Fate of Pharmaceuticals and Personal Care Products in Wastewater Treatment Plants – Conception of a Database and First Results. *Environ Pollution* **2009**, 15, 1721-1726.
- (4) Malato, S.; Fernández-Ibáñez, P.; Maldonado, M.I.; Blanco, J.; Gernjak, W. Decontamination and Disinfection of Water by Solar Photocatalysis: Recent Overview and Trends. *Catalysis Today* **2009**, 147, 1-59.
- (5) Von Sonntag, C. Advanced Oxidation Processes: Mechanistic Aspects. *Water Sci. Technol.* **2008**, 58, 1015.
- (6) Doll, T.E.; Frimmel, F.H. Fate of Pharmaceuticals—Photodegradation by Simulated Solar UV-Light. *Chemosphere* **2003**, 52, 1757-1769.
- (7) Neamtu, M.; Frimmel, F.H. Photodegradation of Endocrine Disrupting Chemical Nonylphenol by Simulated Solar UV-Irradiation. *Science of the Total Environment* **2006**, 369, 295-306.
- (8) Neamtu, M.; Popa, D-M.; Frimmel, F.H. Simulated Solar UV-Irradiation of Endocrine Disrupting Chemical Octylphenol. *Journal of Hazardous Materials* **2009**, 164, 1561-1567.

- (9) Bahnemann D. Photocatalytic Water Treatment: Solar Energy Applications. *Solar Energy* **2004**, 77, 445-459.
- (10) Shawaqfeh, A.T.; Al Momani F.A. Photocatalytic Treatment of Water Soluble Pesticide by Advanced Oxidation Technologies Using UV Light and Solar Energy. *Solar Energy* **2010**, 84 1157-1165.
- (11) Trovó, A.G.; Nogueira, R.F.P.; Agüera, A.; Fernandez-Alba, A.R.; Sirtori, C.; Malato, S. Degradation of Sulfamethoxazole in Water by Solar Photo-Fenton. Chemical and Toxicological Evaluation. *Water Research* **2009**, 43 3922-3931.
- (12) Klammerth, N.; Malato, S.; Maldonado, M.I.; Agüera, A.; Fernandez-Alba, A.R.; Modified Photo-Fenton for Degradation of Emerging Contaminants in Municipal Wastewater Effluents. *Catalysis Today* **2011**, 161, 241-246.
- (13) Crittenden, J.C., Zhang, Y., Hand, D.W., Perram, D.L., Marchand, E.G. Solar Detoxification of Fuel-Contaminated Groundwater Using Fixed-Bed Photocatalysts. *Water Environ. Res.* **1996**, 68, 270–278.
- (14) Dillert, R., Vollmer, S., Gross, E., Schober, M., Bahnemann, D., Wienefeld, D., Pahlmann, K., Schmedding, T., Arntz, G., Sager, G. Solar-catalytic treatment of an industrial wastewater. *Z. Phys. Chem.* **1999**, 213, 141–147.
- (15) Malato, S.; Blanco, J.; Vidal, A.; Richter, C. Photocatalysis with Solar Energy at a Pilot-Plant Scale: An Overview. *Applied Catalysis B: Environmental* **2002**, 37, 1-15.
- (16) Rojas, M.R.; Pérez, F.; Whitley, D.; Arnold, R.G; Sáez, A.E. Modeling of Advanced Oxidation of Trace Organic Contaminants by Hydrogen Peroxide Photolysis and Fenton's Reaction. *Ind. Eng. Chem. Res.* **2010**, 49, 11331-11343.
- (17) Pima County Wastewater Management Department (PCWWM). The Pima County Effluent Generation and Utilization Report. March 31, **2005**.

- (18) Boltz, D.; Holwell, J. *Colorimetric Determination of Nonmetals*. Second Edition; John Wiley and Sons: New York, **1978**.
- (19) Gueymard, C.A. (1995). SMARTS, A Simple Model of the Atmospheric Radiative Transfer of Sunshine: Algorithms and Performance Assessment. Technical Report No. FSEC-PF-270-95. Cocoa, FL: Florida Solar Energy Center, **1995**.
- (20) Kaskaoutis, D.G.; Kambezidis, H.D. The Role of Aerosol Models of the SMARTS Code in Predicting the Spectral Direct-Beam Irradiance in an Urban Area. *Renewable Energy* **2008**, 33, 1532-1543.
- (21) Gueymard, C. The Sun's Total and Spectral Irradiance for Solar Energy Applications and Solar Radiation Models. *Solar Energy* **2004**, 76, 423-453.
- (22) Gueymard, C.A. Parameterized Transmittance Model for Direct Beam and Circumsolar Spectral Irradiance. *Solar Energy* **2001**, 71, 325-346.
- (23) Brine, D.T.; Iqbal, M. Diffuse and Global Spectral Irradiance Under Cloudless Skies. *Solar Energy* **1983**, 30, 447-453.
- (24) Crittenden, J.C.; Hu, S.; Hand, D.W.; Green, S.A. A Kinetic Model for H₂O₂/UV Process in a Completely Mixed Batch Reactor. *Water Res.* **1999**, 33, 2315.
- (25) Song, W.; Ravindran, V.; Pirbazari, M. Process Optimization Using a Kinetic Model for the Ultraviolet Radiation-Hydrogen Peroxide Decomposition of Natural and Synthetic Organic Compounds in Groundwater. *Chem. Eng. Sci.* **2008**, 63, 3249.
- (26) Goldstein, S.; Aschengrau, D.; Diamant, Y.; Rabani, J. Photolysis of Aqueous H₂O₂: Quantum Yield and Applications for Polychromatic UV Actinometry in Photoreactors. *Environ. Sci. Technol.* **2007**, 41, 7486-7490.

- (27) Saadi, I.; Borisover, M.; Armon, R.; Laor, Y. Monitoring of Effluent DOM Biodegradation Using Fluorescence, UV and DOC Measurements. *Chemosphere* **2006**, 63, 530-539.
- (28) Leenheer, J.A.; Croué, J.-P. Characterizing Dissolved Aquatic Organic Matter. *Environ. Sci. Technol.* **2003**, 37, 19A-26A.

CHAPTER 5

EXPERIMENTAL SIMULATION OF ADVANCED OXIDATION PROCESSES IN FLOW-THROUGH REACTORS

5.1. Abstract

The goals of this project include use of UV/H₂O₂ advanced oxidation in continuous-flow reactors and adaptation of a kinetic model for process simulation and optimization of operating conditions. Simulation of process performance in a continuous flow reactor depends on accurate representations of the light distribution in the reactor, reactor hydrodynamics, and the spectral distribution of light. In this section, the application of AOP in commercial flow-through reactors designed for UV disinfection is evaluated for the treatment of water spiked with trace organic contaminants such as p-cresol and for the treatment of real wastewater effluent from a local wastewater treatment plant. A previously developed kinetic model was adapted for its use in these systems, for both monochromatic and polychromatic light. Results suggest that current technologies available for UV disinfection can be successfully used for the chemical treatment of water contaminated with trace organic contaminants.

5.2. Introduction

Two different cylindrical flow-through reactors, designed primarily for UV disinfection, have been utilized to study the degradation of *p*-cresol and fluorescein via UV/H₂O₂. One reactor was a commercially available residential UV disinfection reactor with a monochromatic light source (low-pressure lamp, $\lambda = 254$ nm). The other was a pilot-scale reactor with a polychromatic light source (medium pressure UV source). In both cases, approximate plug-flow hydrodynamics were observed throughout the experimental range of flow rates. In a subset of experiments, conventionally treated wastewater was the fluid matrix for AOP treatment of the targets.

The model was successfully used to predict the kinetics of target compound disappearance in the bench-scale reactor with monochromatic light source. However, process simulation in the pilot-scale reactor was less successful and will be object of further research.

5.3. Experimental

5.3.1. Materials and Analytical Methods

Experimental materials and methods conformed to procedures described previously (Chapters 3 and 4).

5.3.2. Experimental Setup

The bench-scale reactor (R1) consisted of a 6-cm i.d., 55-cm long stainless steel cylinder that was equipped with a low pressure 16.5-W lamp (Hg, $\lambda = 254$ -nm) located

concentrically in the barrel. The total available volume of the annular region was 1.05 L. The pilot-scale reactor (R2, 20 L, *Hanovia*) was similarly configured, although with larger dimensions —i.d. 15 cm, length 1.5 m, stainless steel with a 2.5-kW medium pressure lamp (xenon/mercury with a wavelength-dependent intensity). Both reactors were equipped with a quartz sleeve to protect the lamp from flowing water and to remove light energy in the range $\lambda < 220$ nm. The reactors and system configurations are provided (Figures 5-1 and 5-2).

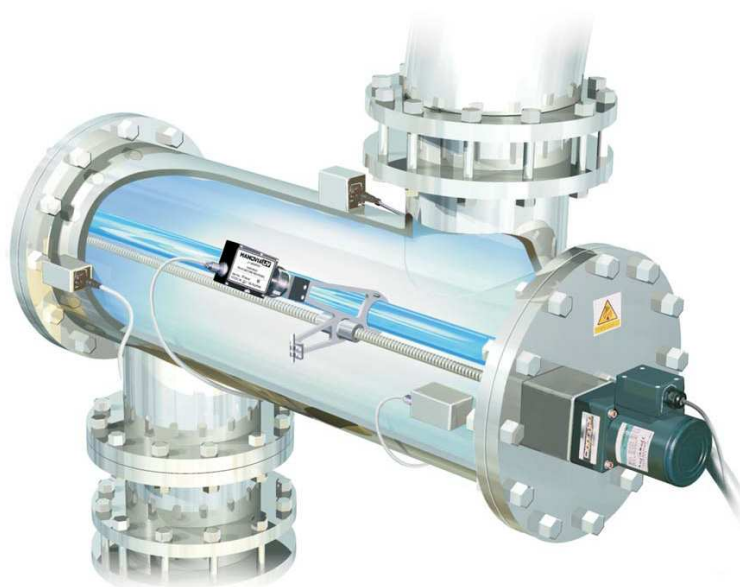


Figure 5-1. Hanovia pilot-scale polychromatic reactor (R2). The medium pressure lamp (2.5 kW) concentrically located at the center of the pipe provides light energy in the UV-visible range.

Water flow to both reactors was provided by a variable speed pump (*Dayton Model 1F976*) with a maximum flow of 23 L/min. The flow rate was fixed to this value when using the larger polychromatic reactor (R2). Flow rate was an independent variable in experiments with the bench-scale reactor (R1, 1-4 L/min). Reactor R1 was operated without recycle. The medium pressure lamp in reactor R2 released considerable heat, so

that a minimum flow was necessary to maintain reactor temperature in the range 18-25°C. To maintain the minimum flow rate without consuming an unacceptable water volume, water was re-circulated to a 120-L tank throughout each experiment with the pilot-scale reactor.

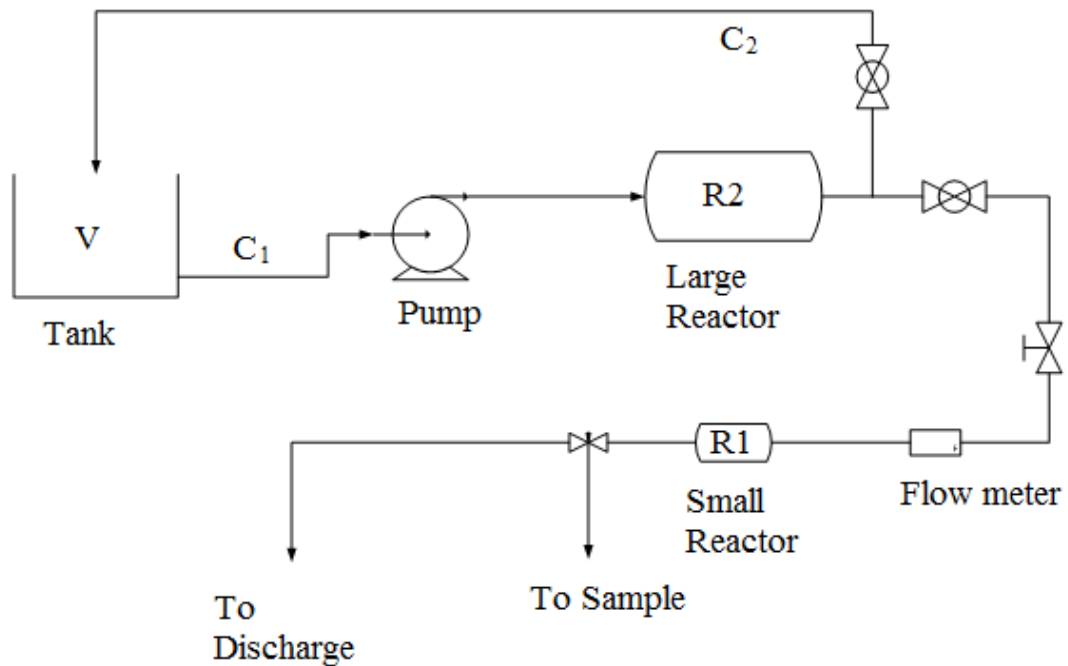


Figure 5-2. Schematic representation of the experimental setup for the two reactors, pump and recirculation tank.

Residence time distributions (RTDs) were measured for reactor R2 using a combination of pulse and step inputs of a salt tracer. Sodium chloride was used as the tracer, and an electrical conductivity meter was connected to the reactor outlet to provide a continuous record of effluent conductivity. RTDs (Figure 5-3) are representative of near-ideal (plug flow) hydrodynamics. However, in the time scale in which the reactions occur in the

polychromatic reactor R2 (55 seconds nominal residence time), there are deviations from the ideal plug flow reactor behavior.

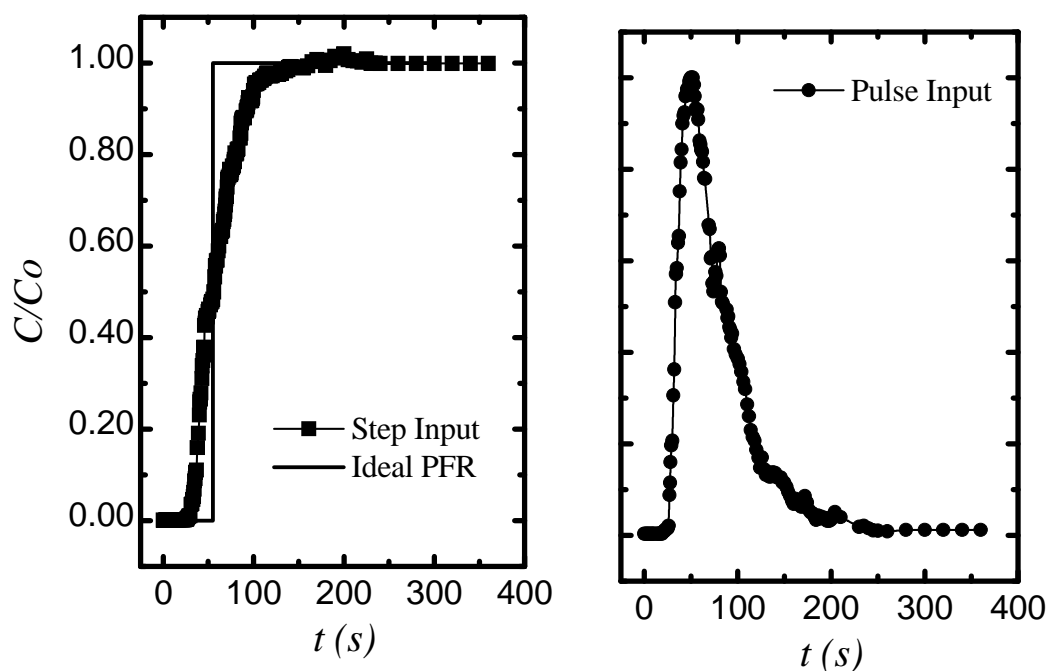


Figure 5-3. Residence time distributions for pulse and step inputs in the large tubular reactor (R2), measured in terms of the time-dependent effluent conductivity. Sodium chloride was the tracer.

5.3.3. Procedure

Solutions of target compounds (p-cresol or fluorescein) were prepared beforehand by diluting a concentrated stock solution in 60-L of water in the feeding tank to achieve the desired concentrations. Recirculation in the system for 10 min proved to be enough to obtain a homogeneous target concentration for each compound. For reactor R1, hydrogen peroxide was added also during this time. After the 10 min, the recirculation was stopped and the lamp turned on. A two minute period of warming was allowed using

a relatively low flow rate (<0.5 L/min); then 5-mL samples were taken at different flow rates. Two minutes between samples was allowed to achieve steady state in the flow. No change in temperature was observed using this reactor. The range of flow rates for turbulent flow in this reactor was estimated using a Reynold's number calculated using the annular flow of the reactor as hydraulic diameter:

$$Re = \frac{\rho D_h V}{\mu} \quad (5-1)$$

Where ρ is the water density (1000 kg/m³); D_h is hydraulic diameter (3.5 cm); V is the annular velocity (flow rate Q divided by annular area= 0.00234 m²); and μ is the water viscosity (1000 kg/m-s²). Using this approach, flow rates above 1-L/min assured turbulent flow regime (Re>2500) in the reactor.

For the polychromatic reactor (recirculation mode), after the 10 min mixing time to dissolve the target, the lamp was turned on, and a 5 min period was given to achieve steady state in the lamp output (manufacturer recommendation). During this time the recirculating solution was exposed to the light and direct photolysis occurred. Then, hydrogen peroxide was added to the tank and the concentration of the target was measured simultaneously in the outlet of the reactor (time zero). 5-mL samples were taken from reactor outlet and, in some experiments, also from tank outlet, every two to five minutes. A spiral chiller connected to a water bath (*Lauda RM-20*) was used to reduce the change in temperature during these experiments. The chiller was submerged in

the feeding tank. However, temperature changes were observed in all experiments (from 75 °F to 85 °F) in 35 minutes.

5.4. Modeling

A kinetic model (Chapter 3) was used to simulate transformation of the target compounds in reactor R1. Inputs to the model included the mean residence and the influent concentrations of the target and hydrogen peroxide. Ideal plug flow reactor hydraulic was used for the calculations. On the other hand, for reactor (R2), an alternative model was created to simulate performance in a recirculating system consisting of a CSTR (mixing tank) and tubular reactor with a residence time distribution given by Figure 5-3. Since reactive radicals that are produced in the tubular reactors are consumed at relatively high rates, no reaction of the organic target or hydrogen peroxide will occur in the holding tank. A mole balance for a chemical species in the mixing tank yields

$$V \frac{dC_{1(t)}}{dt} = Q(C_{2(t)} - C_{1(t)}) \quad (5-2)$$

where V is the mixing tank volume, Q is the volumetric flow rate, C_1 is the species concentration exiting the tank and entering the reactor; and C_2 is the species concentration exiting the reactor and entering the mixing tank. At each step, C_2 was calculated using the kinetic model developed for polychromatic sources (Chapter 4) and C_1 was modeled solving equation 5-2 numerically by Euler's method. The RTD was discretized in ten different residence times (from 35 to 150 s). The tubular reactor was

simulated as a combination of several batch reactors in parallel, each one with its own residence time and volume and with an initial concentration equal to the inlet concentration (C_1). The outlet concentration was calculated with the kinetic model at a time equal to the residence time of each reactor and then the global concentration was calculated as a weight averaged of the contributions of all ten ideal reactors. The time steps for solution of equation 5-2 were 5 s. Note, that for the first residence time, the concentration exiting the reactor (C_1) is constant (initial concentration).

5.5. Results and Discussion

5.5.1. Monochromatic Reactor (R1)

Hydrogen peroxide photolysis provides an adequate actinometer for estimation of light intensity in low pressure lamps if the intensity is high enough to oxidize the peroxide in a time that is observable experimentally (1,2). Using this approach, measurements of hydrogen peroxide in the outlet of the monochromatic reactor were compared to the inlet concentration (1 mM) to calculate H_2O_2 conversion at a variety of flow rates. The calculated conversion was then used to estimate the intensity of the low-pressure lamp (Figure 5-4).

Even at very low initial peroxide concentrations, single-pass peroxide photolysis through the reactor was relatively low due to the short light path-length (1.75-cm) and low lamp intensity (see below). Although a higher peroxide concentration would provide better absorption and more rapid peroxide conversion, concentration differences under reasonable operating conditions proved to be small compared to the initial peroxide

concentration, again leading to error in the estimation of light intensity. Consequently, the conversion of *p*-cresol was used to estimate the quasi-steady concentration of hydroxyl radicals and then the lamp intensity (*p*-cresol actinometry) using a much higher initial hydrogen peroxide concentration (50 mM; Figure 5-5) to absorb essentially all light from the low pressure lamp.

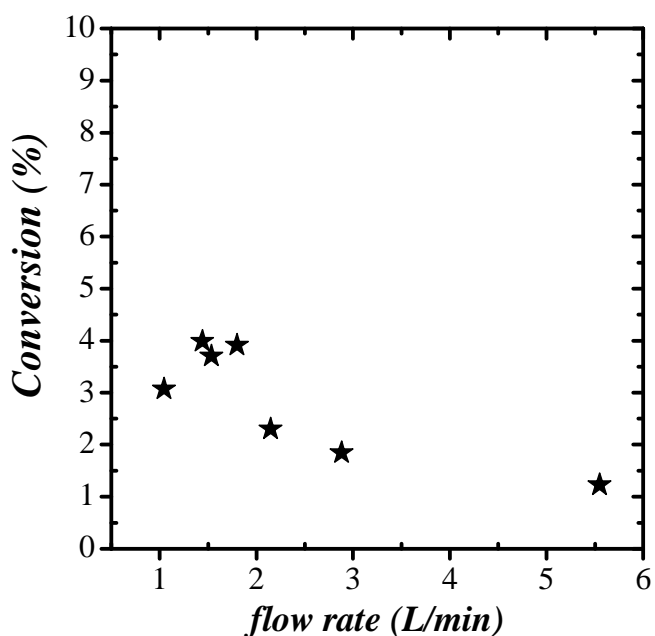


Figure 5-4. Hydrogen peroxide conversion in the monochromatic reactor (R1).

Experimental results in Figure 5-5 were used to estimate the incident light intensity using the kinetic model. Note that the model fit is better at high flow rates (low residence times). This is due to transition from turbulent to laminar flow at low flow rates, which modified the residence time distribution in the reactor due to lack of radial mixing.

Reynolds number calculations using the hydraulic diameter of the annular region in the reactor suggest that flow is no longer turbulent at flow rates < 1 L/min. (See Procedure)

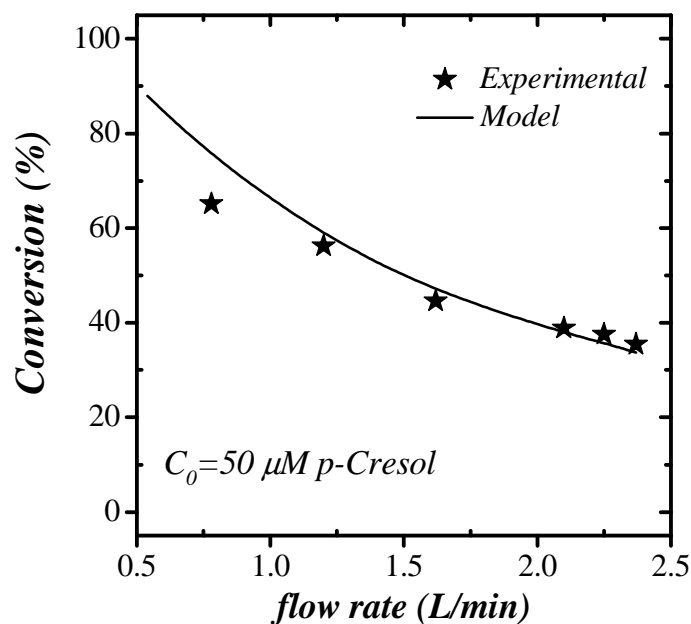


Figure 5-5. *p*-Cresol conversion in the monochromatic reactor (R1). Solid line represents the kinetic model, using the lamp intensity as adjustable parameter.

The light intensity calculated using the model (2.42×10^{-6} Ein/L s) was successfully applied to anticipate *p*-cresol degradation at different hydrogen peroxide concentrations (Figure 5-6). Note that direct photolysis (no peroxide added) does not contribute to the rate of oxidation, as reported previously (Chapters 3 and 4). Changes in pH due to mineralization of the target are also adequately predicted by the model (Figure 5-7).

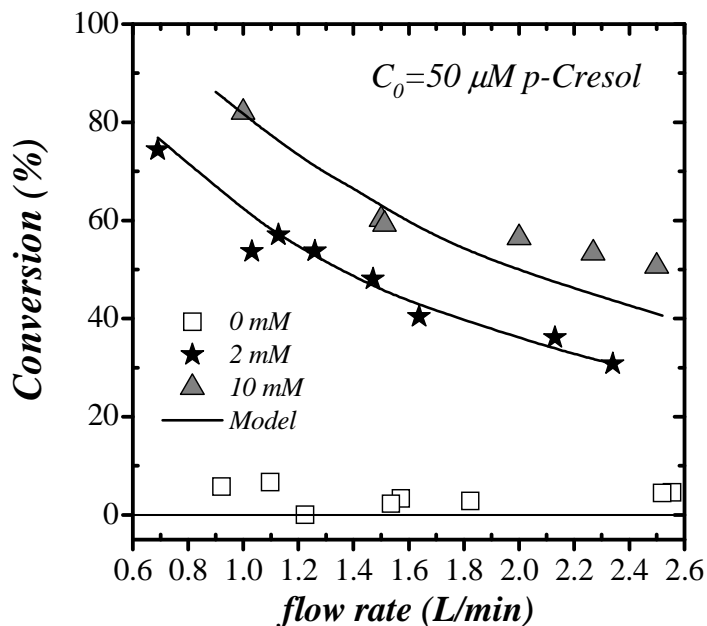


Figure 5-6. *p*-Cresol oxidation in the monochromatic reactor (R1) at different hydrogen peroxide concentrations. Solid line represents model predictions using the input light intensity determined in the actinometry experiment (Figure 5-5). Legend shows hydrogen peroxide concentration.

The monochromatic reactor (R1) was also used in experiments with target organic compounds in a matrix consisting of conventionally treated wastewater effluent from a local wastewater treatment plant (Ina Road, Tucson, AZ- see details in experimental section Chapter 4). Florescence spectroscopy (2-D, EEM) was used to follow the degradation of residual bulk organics in the wastewater matrix (Figure 5-8). Results show that 55 s of treatment with 5 mM hydrogen peroxide reduced the relative intensities of high intensity regions of EEMs by 60% on average.

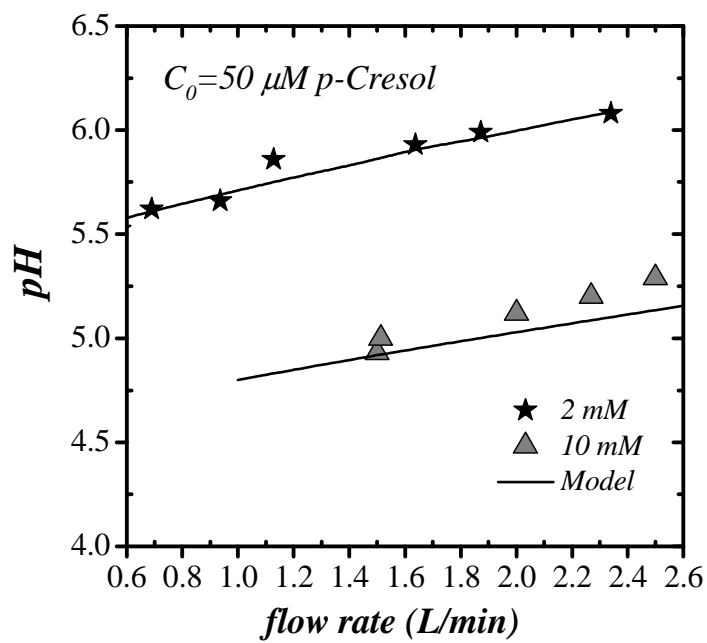


Figure 5-7. pH evolution during p -Cresol oxidation experiments in the monochromatic reactor (R1) at different hydrogen peroxide concentrations. Solid line represents model predictions. Legend shows hydrogen peroxide concentration.

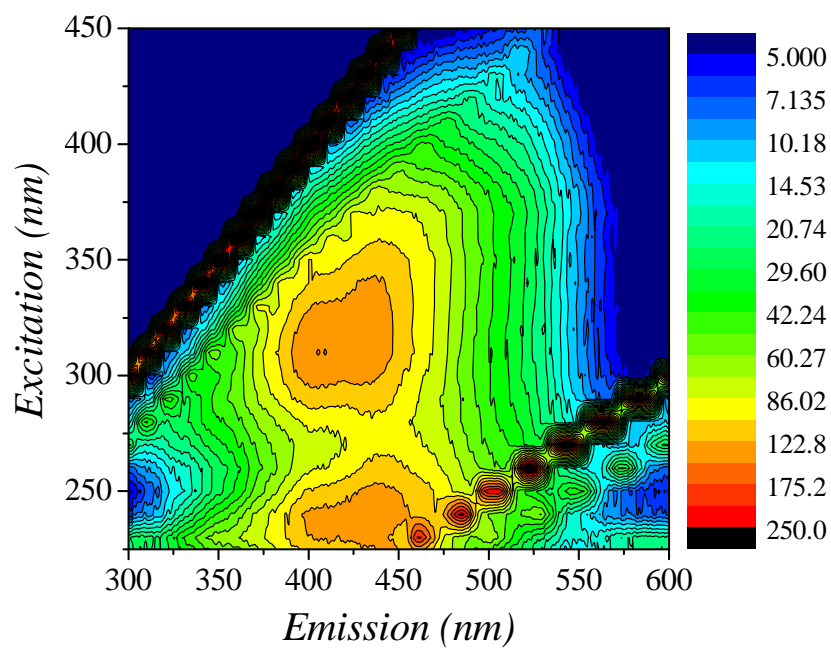
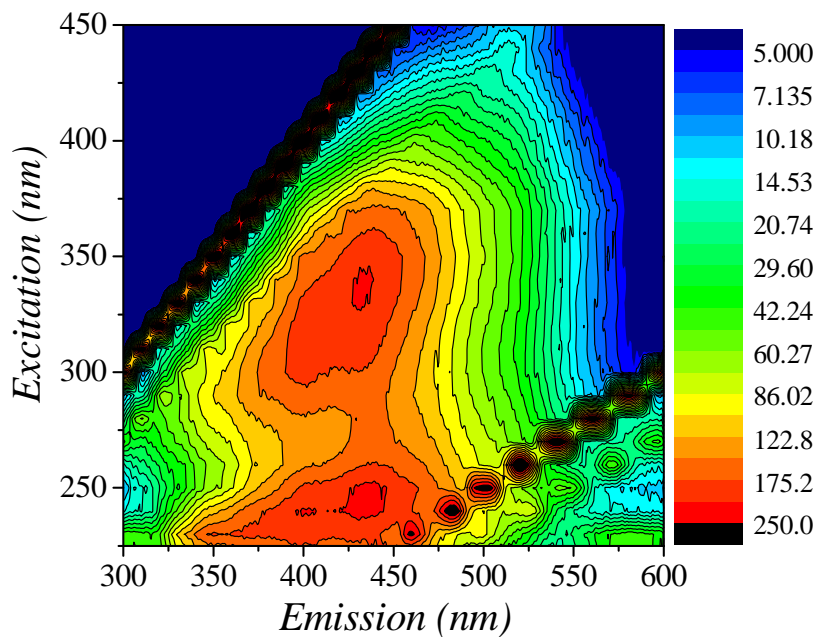


Figure 5-8. EEMs for Ina Road wastewater effluent before (above) and after 55 seconds of treatment (below) with a hydrogen peroxide concentration of 5 mM in the monochromatic reactor (R1). Legend shows relative intensity.

5.5.2. Polychromatic Reactor (R2)

Simulation of the polychromatic reactor performance posed an additional challenge as the spectrum of the lamp was not provided by the manufacturer, and the reactor was operated by recirculating water via the feed (mixing) tank. An alternative spectrum for a medium pressure lamp was obtained from the literature (3) (Figure 5-9). The spectrum was used as a reference to calculate the relative output of the lamp over the 220-340 nm range. According to the manufacturer, the lamp is protected with a quartz sleeve that absorb most of the irradiation at wavelengths below 220 nm. From experience using the solar AOP model, wavelengths from 300-350 nm are relevant to UV-H₂O₂-dependent conversions of the target compounds.

Using methods developed to model solar catalyzed AOP (Chapter 4), the relative intensities in the spectrum were normalized to the total area of the spectrum, and used to calculate a total output of the lamp in the range of wavelengths provided by applying hydrogen peroxide actinometry (Figure 5-10). As described in Chapter 4, the spectrum was discretized in 5 nm bands. The model considers that the quantum yield for hydrogen peroxide photolysis is independent of wavelength in the whole 220-340 nm range, which is consistent with previous studies (3).

Results indicate that hydrogen peroxide oxidation at different initial concentrations can be successfully modeled using a single fitting parameter, the total light intensity in the 220-340 nm range (here, 120 W). All the intensities in the 220-340 nm range can be calculated as they are fractions of this total value in the spectrum.

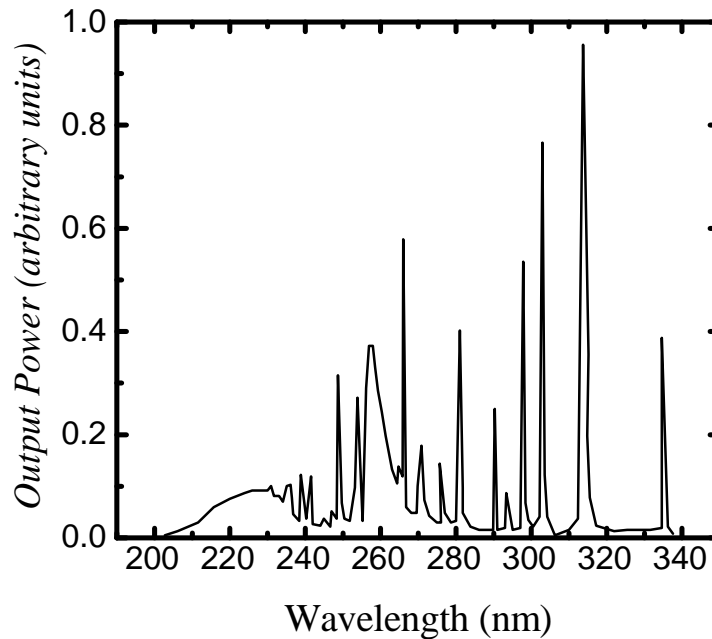


Figure 5-9. Spectrum for a typical mercury medium pressure lamp (3).

As for the solar catalyzed process, the quantum yield for hydrogen peroxide photolysis was assumed constant over the entire UV range (3). The results provided agreement between model simulations for hydrogen peroxide destruction developed on this basis and experimental results (Figure 5-10). Moreover, time-dependent measurements of hydrogen peroxide concentration at the outlet of the mixing tank were in agreement with experimental results (not shown), suggesting that simulations for the recirculating system consisting of ideal reactors in series provided acceptable agreement at all points in the treatment system.

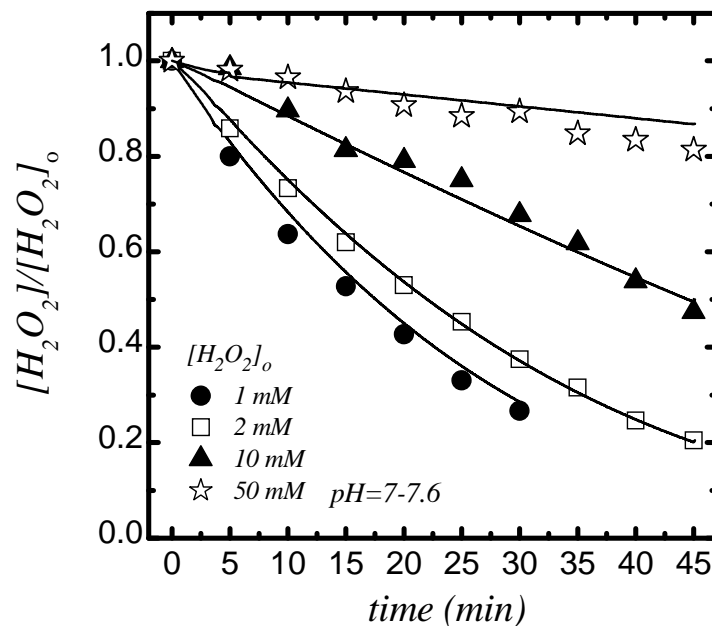


Figure 5-10. Hydrogen peroxide conversion at different starting concentrations in the polychromatic large reactor (R2). Experimental values were taken at the exit of the treatment reactor. Solid lines represent model calculations using total lamp intensity as adjustable parameter (best fit at 120 W) and the relative intensity spectrum shown in Figure 5-9.

Oxidation of *p*-Cresol at various hydrogen peroxide concentrations was used to validate the model developed (Figure 5-11). Direct photolysis of *p*-cresol, evident in experiments with no hydrogen peroxide, proved to be important in the reactor with the medium pressure lamp and was included in subsequent process simulations by fitting a constant quantum yield (0.48 mol/Ein), using the 275-nm band as reference to experimental conversion of *p*-cresol in the absence of hydrogen peroxide. This wavelength band was selected to model *p*-cresol direct photolysis as PC absorption spectrum presents a local maximum around 275-nm (molar absorption coefficient: $\epsilon=3100 \text{ M}^{-1}\text{cm}^{-1}$, see Figure 5-12).

The revised model accounting for direct photolysis significantly overestimated the rate of *p*-cresol removal in the presence of hydrogen peroxide at concentrations ≥ 0.5 mM (Figure 5-11).

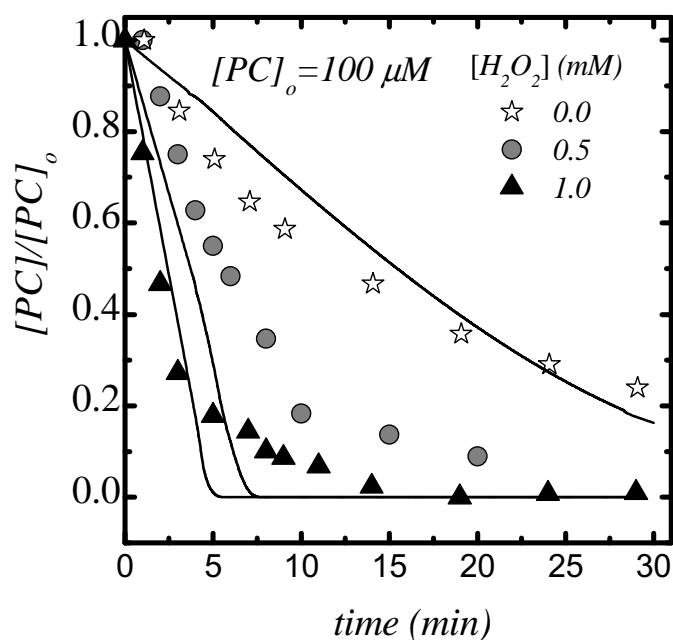


Figure 5-11. *p*-Cresol oxidation at pH=6 in the pilot scale reactor system with polychromatic light source (reactor R2). Solid lines represent model predictions. Concentrations are measurements at the exit of the reactor (C_2).

The model results exhibit two distinct regions during the first two residence times in the reactor: for $0 < t < \tau$, the concentration of *p*-cresol at the reactor exit is approximately constant and equal to the initial concentration while there is no hydrogen peroxide since the H_2O_2 added to the tank at $t=0$ has not reached the reactor exit; $\tau < t < 2\tau$, the H_2O_2 starts reaching the outlet of the reactor at a concentration 1.5 times higher than the nominal concentration, and a discontinuity is observed due to the conversion of the target

compound during the first residence time. During the second residence time, the flow of low target exiting the reactor starts diluting the target concentration in the tank.

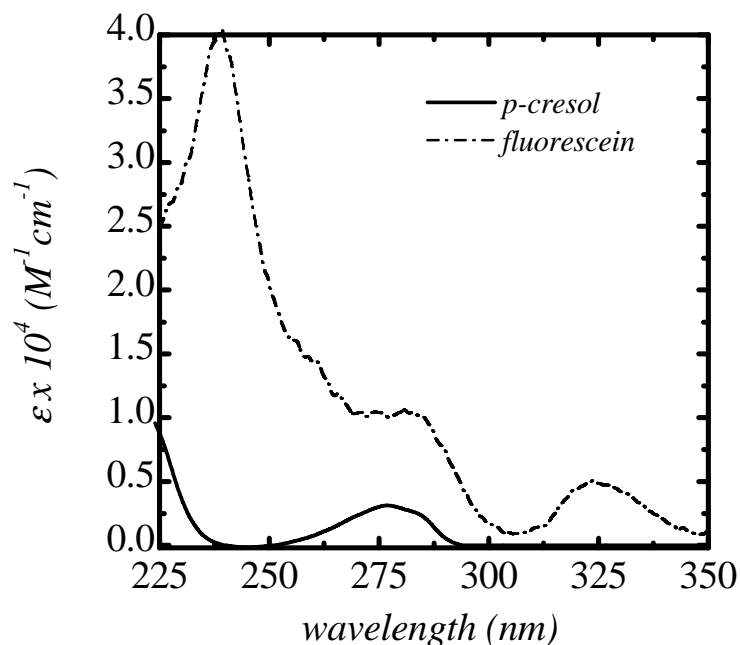


Figure 5-12. *p*-Cresol and fluorescein absorption spectrum in the UV range.

Similar results were obtained when fluorescein was the target compound (Figure 5-13). Fluorescein showed little evidence of direct photolysis (0.029 mol/Ein, using the 240-nm band as a reference) in peroxide-free experiments. Nevertheless, model simulations significantly overpredicted the rates of fluorescein oxidation in the large tubular reactor, suggesting that lamp intensities calculated based on hydrogen peroxide actinometry were in error.

Results obtained with solar-catalyzed AOP (Chapter 3) confirmed that polychromatic light UV/peroxide can be accurately modeled if the light spectrum is well characterized.

At this point, a more accurate and complete spectrum of the xenon-mercury lamp is needed to support process simulation, as the values of intensity obtained with hydrogen peroxide actinometry depend on having the correct spectrum. Unfortunately, the spectrum of light intensities so derived is not useful for simulating the destruction of trace organic targets. Other factors that could lead to potential errors in the calculation of the light intensity are the effects that reflection and refraction of the light on the surfaces of the reactor can have in the distribution of the light (4,5). These effects and deviations from the plug flow reactor behavior have not been considered in this work.

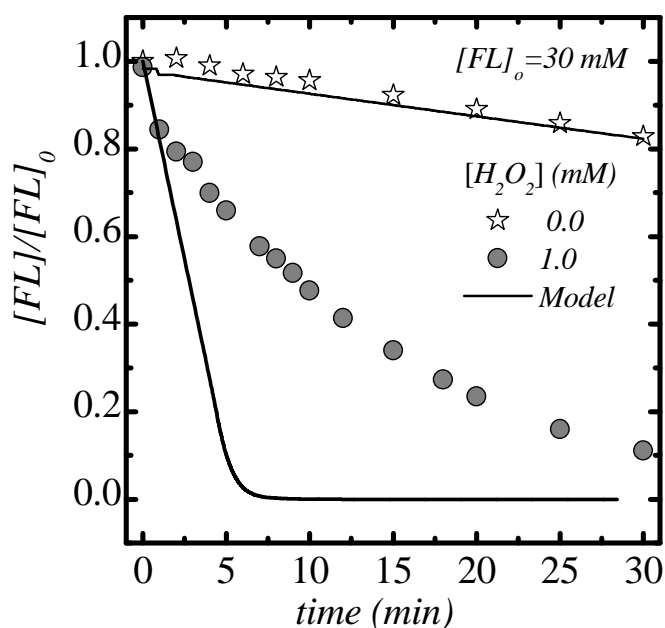


Figure 5-13. Fluorescein oxidation at pH=9.8 in the pilot scale reactor system with polychromatic light source (reactor R2). Solid lines represent model predictions.

If the data are analyzed using just the recirculation model and considering the reaction to be a pseudo-first order process with a rate constant, k , the concentration at the reactor exit would be given by

$$C_{2(t)} = C_{1(t-\tau)} e^{-k\tau} \quad (5-4)$$

The experimental results can be simulated by fitting the pseudo-first order rate constant to data (Figure 5-14), which suggests that process hydrodynamics is well characterized in the model since the concentration in the tank and in the outlet of the reactor can be predicted by using the rate constant as a fitting parameter.

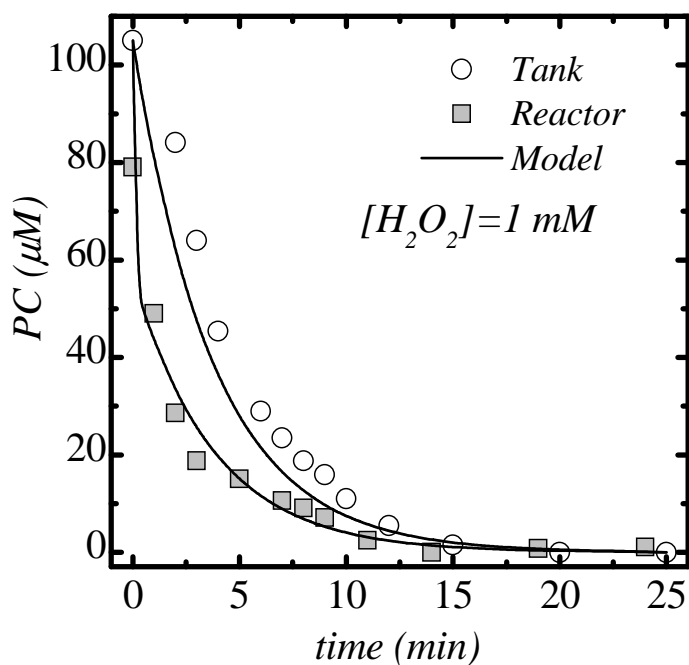


Figure 5-14. *p*-Cresol oxidation in the pilot scale reactor system with polychromatic light source (reactor R2). Solid lines represent the hydraulic model predictions considering the reactor as an ideal PFR and the reaction a first-order process. $k = 0.71 \text{ min}^{-1}$.

5.6. Concluding Remarks

Commercial flow-through reactors designed for UV disinfection can be effectively used for advanced oxidation of trace organic contaminants. Cylindrical reactors operated in a turbulent flow regime were successfully represented as plug-flow reactors for the purpose of process simulation. Agreement between model prediction and experiment was acceptable for hydrogen peroxide and, in the bench-scale reactor, for *p*-cresol disappearance.

2-D fluorescence spectroscopy suggested that residual bulk organics were also effectively oxidized during UV/peroxide AOP. Sixty % reduction of representative EEM peaks was observed during a 55-s residence time using a 16.5 W, low pressure lamp with 5 mM H₂O₂.

Attempts to model process performance in the reactor system with a medium pressure light source achieved mixed success. The disappearance of hydrogen peroxide was adequately modeled using fitted lamp intensity. However, extension of that model for destruction of *p*-cresol and fluorescein, including direct photolysis, was not successful.

5.7. Literature Cited

- (1) Crittenden, J.C.; Hu, S.; Hand, D.W.; Green, S.A. A Kinetic Model for H₂O₂/UV Process in a Completely Mixed Batch Reactor. *Water Res.* **1999**, *33*, 2315.
- (2) Song, W.; Ravindran, V.; Pirbazari, M. Process Optimization Using a Kinetic Model for the Ultraviolet Radiation-Hydrogen Peroxide Decomposition of Natural and Synthetic Organic Compounds in Groundwater. *Chem. Eng. Sci.* **2008**, *63*, 3249.
- (3) Goldstein, S.; Aschengrau, D.; Diamant, Y.; Rabani, J. Photolysis of Aqueous H₂O₂: Quantum Yield and Applications for Polychromatic UV Actinometry in Photoreactors. *Environ. Sci. Technol.* **2007**, *41*, 7486.
- (4) Ho, C.K. Evaluation of Reflection and Refraction in Simulations of Ultraviolet Disinfection Using Discrete Ordinates Radiation Model. *Water Science and Technology* **2009**, *59*, 2421.
- (5) Shanshan, J.; Linden, K.G.; Ducoste, J.; Liu, D. Impact of Lamp Shadowing and Reflection on the fluence Rate Distribution in a Multiple Low-Pressure UV Lamp Array. *Water Research* **2005**, *39*, 2711.

CHAPTER 6

CONCLUSIONS

Analysis of the information available for removal of chemicals of emerging concern during wastewater secondary treatment indicates that biodegradation and adsorption on the biosolids are the most important factors in the removal of trace organics from water. The scarcity of quantitative studies on biodegradability of CECs under typical WWTP bioreactor operating conditions handicaps the application of WWTP performance models for anticipation of CEC removal during conventional wastewater treatment. However, the rapid increase of CEC measurements in the contemporary sanitary literature is sure to remedy that situation within a few years, as will adaptation of laboratory CEC biodegradation measurements for use in field-scale simulations. To be useful, the evolving database on biodegradability of trace organics should be periodically summarized and critically reviewed (as we have attempted) in order to recalibrate efforts to establish and quantify the dominant mechanisms of CEC attenuation, better anticipate compound-specific response to standard WWTP operational variables and performance measures, and refine fate models during wastewater treatment. Based on the results obtained in this work, there remain knowledge gaps, and statistically based conclusions can be reached with acceptable confidence for only a handful of the CECs of potential interest. Low-confidence-level compounds and chemicals included that lack sufficient data for meaningful statistical analysis should be objects of further data collection. The highest priority should be placed on the development of data among mass produced,

relatively toxic chemicals for which physical and biochemical data suggest that removal during conventional wastewater treatment might be low. Such data will either (i) illustrate the general competence of conventional wastewater treatment methods, perhaps after they are better tuned for CEC management, or (ii) motivate investigation and eventual deployment of alternative treatment processes and/or regulatory strategies (e.g., source control) to protect surface waters that are influenced by treated municipal wastewater.

The limitations of wastewater treatment plants in eliminating trace organics justify the application of tertiary treatment technologies such as advanced oxidation processes in many areas in which the water may be reused. Experimental results and mathematical modeling confirm the feasibility of UV/peroxide AOP to destroy trace organics using artificial light sources such as low pressure (monochromatic) and medium pressure lamps (polychromatic) and natural sources (solar irradiance).

Mathematical optimization has shown that chemicals for which the rate of reaction with hydroxyl radicals are relatively low ($<10^8 \text{ M}^{-1}\text{s}^{-1}$) pose a challenge to advanced oxidation technologies because residence times required to remove these contaminants are unpractical from operational point of view. The main limitation of the UV/peroxide process is the need of hydrogen peroxide concentrations high enough to absorb the maximum fraction of light possible in the available path length. Further research is needed to investigate the optimal intensity, hydrogen peroxide concentration and reactor dimensions in terms of operational cost to treat chemicals with different ranges of

reactivity with hydroxyl radicals. Furthermore, the effect of dissolved organic matter needs to be included in the model in order to be able to enable prediction of rates and acceptable times for the treatment of real wastewater. To do this, excitation/emission fluorescence matrices can be used as a surrogate way to measured organic matter scavenging potency.

The development of an AOP kinetic model for polychromatic light applications based on the integration of the light spectrum was successful. Wavelength dependence of light attenuation and photolysis of the hydrogen peroxide was well represented for solar irradiation experiments. Moreover, the novel model can be used to predict the fate of specific target compounds for which the UV spectrum and the intrinsic kinetic constant with hydroxyl radicals are known. Solar spectral atmospheric models proved to be adequate for estimating UV irradiance at different seasonal and atmospheric conditions.

Application of UV/peroxide advanced oxidation in monochromatic and polychromatic UV disinfection reactors demonstrated to be effective to eliminate trace organics and to treat dissolve organic matter in real wastewater effluents. The kinetic model can be effectively used with reactors equipped with low pressure lamps, and for which the hydrodynamics can be well represented by a plug-flow scenario. Polychromatic reactors could not be successfully modeled given the lack of a complete and accurate representation of the lamp spectrum output.

APPENDIX A

SUPPLEMENTARY MATERIAL ABOUT CECs REMOVAL

Table A-1. Chemicals of emerging concern studied and their structures.

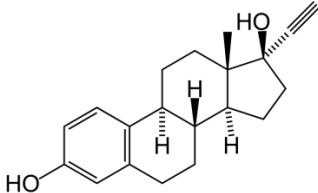
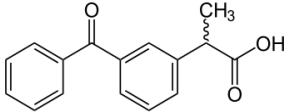
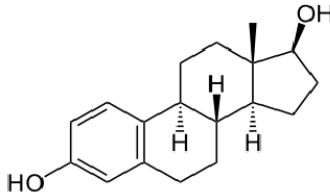
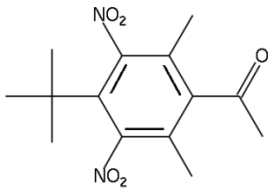
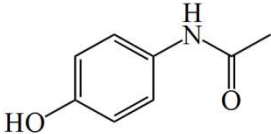
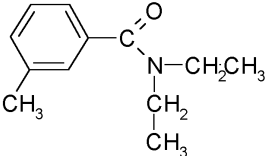
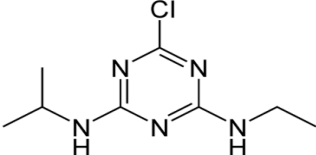
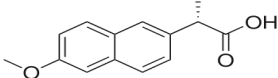
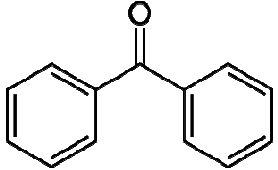
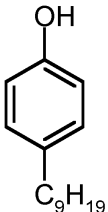
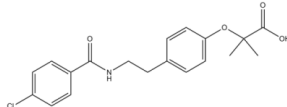
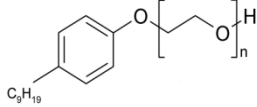
CEC General Class	Structure	CEC General Class	Structure
17α-Ethinyl estradiol (EE2) Hormone		Ketoprofen Pharmaceutical	
17β-Estradiol (E2) Hormone		Musk ketone Synthetic Musk	
Acetaminophen Pharmaceutical		N,N-diethyl-toluamide (DEET) Insect repellent	
Atrazine Pesticide		Naproxen Pharmaceutical	
Benzophenone Plasticizer		Nonylphenol Alkylphenol	
Bezafibrate Pharmaceutical		Nonylphenol diethoxylate (NP1EO) (n=1)	

Table A-1. Continued.

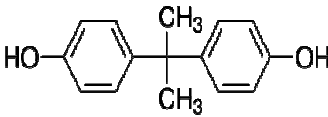
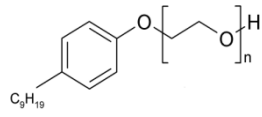
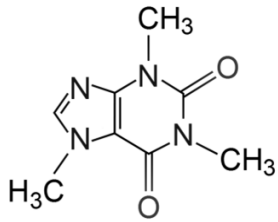
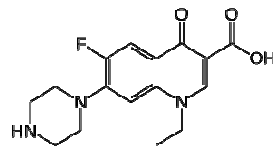
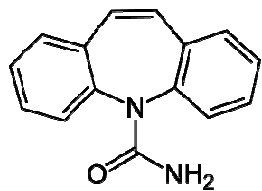
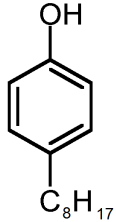
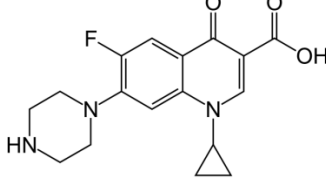
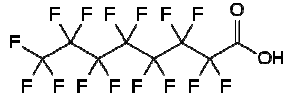
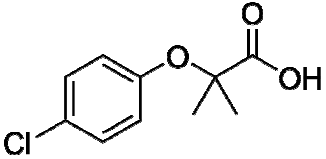
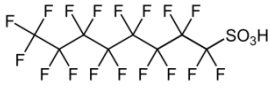
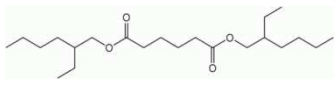
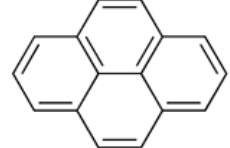
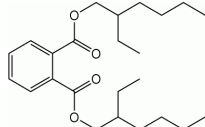
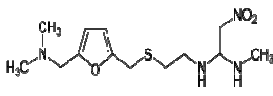
CEC General Class	Structure	CEC General Class	Structure
Bisphenol A Plastic manufacture		Nonylphenol monoethoxylate (NP2EO) (n=2) Alkylphenol Ethoxylates	
Caffeine Pharmaceutical		Norfloracin Pharmaceutical	
Carbamazepine Pharmaceutical		Octylphenol Alkylphenol	
Ciprofloxacin Pharmaceutical		Perfluorooctanoic acid (PFOA) Perfluorinated Surfactant	
Clofibric acid Pharmaceutical		Perfluorooctyl sulfonate (PFOS) Perfluorinated Surfactant	
Di (2-ethylhexyl) adipate (DEHA) Plasticizer		Pyrene Polycyclic Aromatic	
Di (2-ethylhexyl) phthalate (DEHP) Plasticizer		Ranitidine Pharmaceutical	

Table A-1. Continued.

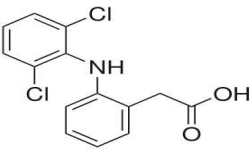
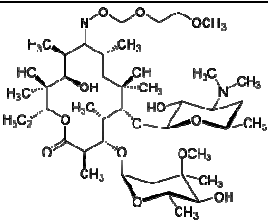
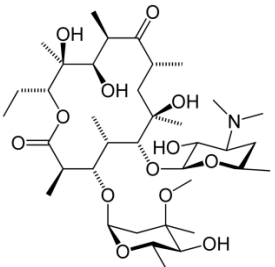
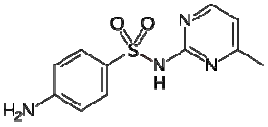
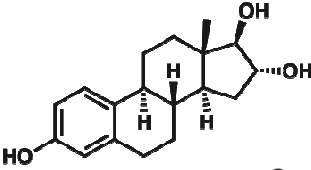
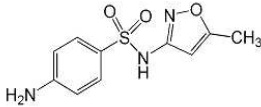
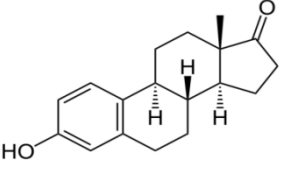
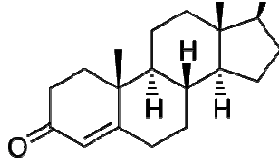
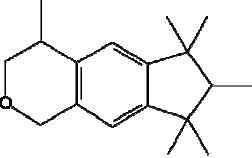
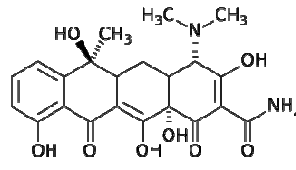
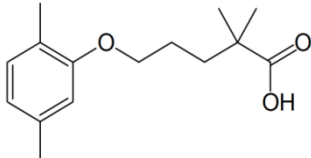
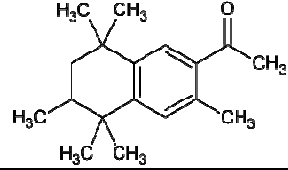
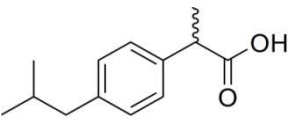
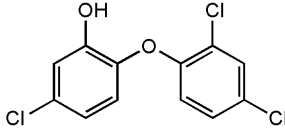
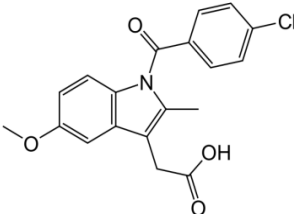
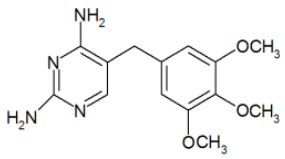
CEC General Class	Structure	CEC General Class	Structure
Diclofenac Pharmaceutical		Roxithromycin Pharmaceutical	
Erythromycin Pharmaceutical		Sulfamerazine Pharmaceutical	
Estriol (E3) Hormone		Sulfamethoxazole Pharmaceutical	
Estrone (E1) Hormone		Testosterone Hormone	
Galaxolide (HHCB) Synthetic Musk		Tetracycline Pharmaceutical	
Gemfibrozil Pharmaceutical		Tonalide (AHTN) Synthetic Musk	

Table A-1. Continued.

CEC General Class	Structure	CEC General Class	Structure
Ibuprofen Pharmaceutical		Triclosan Personal Care Product	
Indomethacin Pharmaceutical		Trimethoprim Pharmaceutical	

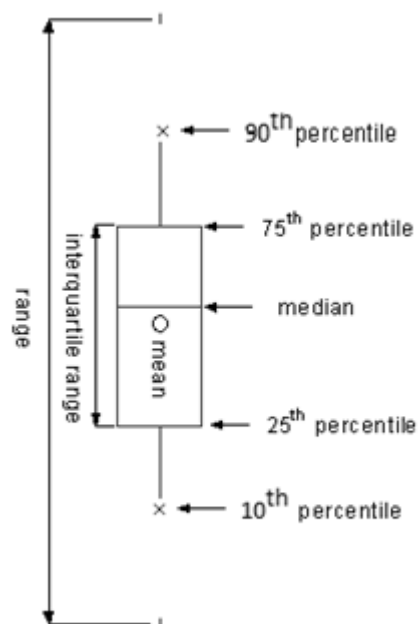


Figure A-1. Box-plot characteristics.

Table A-2. References used to build the box plots and cumulative distribution functions.

CEC	References from database
17 α -Ethinyl estradiol (EE2)	1, 8, 10, 41, 107, 116, 153, 155, 165, 202, 222, 262, 309, 315, 323, 335, 341, 342, 359, 397, 416, 421, 430, 487, 492, 627, 632, 641
17 β -Estradiol (E2)	8, 14, 24, 35, 41, 107, 116, 143, 146, 153, 155, 165, 172, 189, 202, 211, 212, 213, 229, 236, 262, 273, 280, 309, 315, 323, 335, 337, 342, 359, 397, 406, 416, 421, 487, 492, 622, 623, 626, 635, 637, 641, 644
Acetaminophen	57, 123, 193, 200, 224, 287, 313, 334, 377, 437, 616, 627, 480
Atrazine	101, 233, 369, 447, 640
Benzophenone	323, 437, 637, 640, 646
Bezafibrate	8, 10, 28, 29, 44, 168, 222, 313, 437, 632
Bisphenol A	14, 127, 143, 170, 210, 215, 222, 227, 317, 323, 334, 349, 395, 409, 416, 419, 492, 611, 640
Caffeine	44, 132, 224, 298, 334, 377, 416, 467, 490, 637, 646
Carbamazepine	7, 8, 10, 31, 36, 44, 92, 107, 132, 133, 136, 143, 153, 170, 200, 203, 222, 224, 226, 227, 233, 248, 249, 262, 264, 291, 298, 311, 313, 317, 319, 334, 341, 363, 364, 376, 377, 385, 416, 430, 437, 438, 467, 620, 627, 632, 635, 637
Ciprofloxacin	22, 102, 109, 118, 140, 177, 199, 224, 292, 344, 368, 376, 378, 383, 417, 437, 480, 601, 632, 637
Clofibrac acid	44, 73, 145, 195, 200, 224, 264, 277, 288, 291, 298, 341, 367, 378, 437, 627, 632, 635
Di (2-ethylhexyl) adipate (DEHA)	3, 14, 21, 458
Di (2-ethylhexyl) phthalate (DEHP)	5, 14, 21, 78, 139, 355, 356, 458, 606
Diclofenac	7, 8, 10, 28, 31, 36, 41, 73, 92, 107, 133, 145, 153, 164, 193, 195, 200, 222, 224, 226, 235, 249, 277, 288, 298, 313, 317, 319, 323, 334, 341, 364, 367, 369, 376, 378, 385, 416, 430, 437, 447, 467, 480, 490, 603, 616, 620, 627, 628, 631, 632, 635, 636
Erythromycin	41, 118, 143, 177, 187, 199, 200, 222, 224, 291, 298, 313, 317, 364, 368, 416, 423, 437, 616, 632, 637
Estriol (E3)	8, 116, 143, 155, 165, 170, 189, 211, 229, 236, 269, 335, 359, 416, 451, 482, 623, 626, 630, 632, 641, 644
Estrone (E1)	8, 24, 35, 107, 116, 153, 155, 165, 172, 189, 202, 222, 229, 236, 262, 269, 273, 280, 291, 315, 323, 337, 342, 349, 397, 406, 416, 421, 482, 487, 492, 622, 623, 626, 632, 637, 641, 644
Galaxolide (HHCb)	29, 43, 107, 112, 114, 133, 205, 341, 386, 396, 416, 450, 488, 636, 637, 646
Gemfibrozil	7, 44, 168, 200, 224, 226, 264, 226, 264, 313, 323, 364, 364, 369, 376, 385, 437, 438, 467, 480, 603, 616, 632, 636

Table A-2. Continued

CEC	References from database
Ibuprofen	123, 132, 133, 138, 143, 145, 153, 168, 170, 195, 222, 224, 226, 248, 249, 277, 288, 291, 298, 313, 317, 319, 323, 334, 341, 364, 367, 369, 378, 385, 388, 430, 437, 467, 480, 488, 490, 603, 616, 627, 628, 631, 632, 635, 636, 646
Indomethacin	31, 200, 313, 323, 437, 603
Ketoprofen	28, 73, 123, 132, 143, 145, 164, 170, 193, 195, 200, 224, 226, 248, 249, 288, 313, 317, 319, 323, 369, 416, 437, 467, 480, 490, 616, 628, 632, 636
Musk Ketone	43, 272, 450, 627, 646
N,N-Diethyl-toluamide (DEET)	44, 416, 637, 640, 646
Naproxen	7, 28, 36, 41, 73, 121, 132, 133, 143, 153, 170, 193, 195, 200, 216, 217, 224, 226, 248, 288, 313, 317, 319, 323, 364, 369, 378, 385, 430, 437, 467, 480, 488, 490, 603, 616, 627, 628, 631, 632, 635, 636
Nonylphenol	29, 38, 100, 106, 127, 143, 218, 222, 251, 267, 309, 348, 349, 355, 380, 381, 395, 409, 415, 416, 419, 431, 451, 470, 482, 483, 484, 485, 486, 492, 630, 636, 637, 638
NPEs	14, 29, 38, 100, 106, 127, 142, 218, 222, 309, 355, 380, 381, 382, 415, 419, 431, 458, 470, 482, 484, 485, 486, 492
Norfloxacin	22, 102, 140, 187, 199, 292, 344, 368, 378, 417, 437, 442, 480, 632
Octylphenol	14, 24, 29, 106, 127, 142, 143, 170, 218, 222, 309, 395, 409, 416, 458, 486, 492, 630, 637, 646
Perfluorooctanoic acid (PFOA)	51, 125, 239, 305, 387, 418, 440
Perfluorooctyl sulfonate (PFOS)	51, 125, 228, 239, 305, 387, 418, 440
Pyrene	33, 90, 190, 267, 408
Ranitidine	200, 226, 291, 313, 317, 437, 438, 471, 480
Roxithromycin	8, 22, 29, 41, 133, 143, 153, 199, 222, 368, 417, 423, 430, 616, 627, 632
Sulfamerazine	22, 368, 371, 400, 463
Sulfamethoxazole	8, 22, 29, 31, 41, 87, 107, 109, 133, 143, 153, 177, 199, 200, 222, 224, 225, 291, 298, 313, 368, 371, 376, 377, 383, 385, 395, 400, 423, 430, 437, 442, 447, 480, 488, 601, 616, 631, 632, 636, 637
Testosterone	335, 349, 451, 482, 641, 644
Tetracycline	22, 109, 118, 187, 196, 197, 199, 290, 292, 298, 344, 368, 376, 383, 480, 627, 632, 637
Tonalide (AHTN)	8, 10, 43, 107, 112, 114, 133, 341, 386, 396, 416, 450, 488, 636, 637
Triclosan	29, 43, 107, 112, 114, 133, 205, 317, 334, 386, 396, 416, 450, 467, 488, 636, 637, 646
Trimethoprim	7, 22, 41, 44, 104, 109, 123, 143, 187, 199, 222, 298, 313, 317, 367, 368, 377, 383, 395, 416, 417, 423, 437, 616, 627, 637

Table A-3. References used to build the MS Access Database

Ref	Authors	Journal/Publisher	Volume	Year	Pages
1	J.S. Vader, C.G. van Ginkel, F.M.G.M. Sperling, J. de Jong, W. de Boer, J.S. de Graaf, M. van der Most, P.G.W. Stokman	Chemosphere	41	2000	1239-1243
3	H.N. Gavala, F. Alatrisme-Mondragon, R. Iranpour, B.K. Ahring	Chemosphere	52	2003	673–682
4	M. Hijosa-Valsero, V. Matamoros, R. Sidrach-Cardona, J. Martin-Villacorta, E. Becares, J.M. Bayona	Water Research	44	2010	3669-3678
5	M. Huang, Y. Li, G.	Bioresource Technology	99	2008	8107-8111
7	N. Paxéus	Water Science and Technology	50	2004	253–260
8	N. Kreuzinger, M. Clara, B. Strenn, H. Kroiss	Water Science and Technology	50	2004	149–156
9	Lenz, V. Beck, M. Fuerhacker	Water Science and Technology	50	2004	141–147
10	M. Clara, B. Strenn, M. Ausserleitner, N. Kreuzinger	Water Science and Technology	50	2004	29–36
12	G. Park, J.H. Lee, I.S. Kim, J. Cho	Water Science and Technology	50	2004	239–244
14	M. Nasu, M. Goto, H. Kato, Y. Oshima, H. Tanaka	Water Science and Technology	43	2001	101–108
17	S. Beier, S. Koster, K. Veltmann, H. Fr. Schroder, J. Pinnekamp	Water Science and Technology	61	2010	1691–1698
18	L. Flyborg, B. Bjorlenius, K.M. Persson	Water Science and Technology	61	2010	1103–1120
21	A. Llop, F. Borrull, E. Pocurull	Water Science and Technology	60	2006	2425–2437
22	G.C. Ghosh, T. Okuda, N. Yamashita, H. Tanaka	Water Science and Technology	59	2009	779–786
24	L. Balest, G. Mascolo, C. Di Iaconi, A. Lopez	Water Science and Technology	58	2008	953–956
25	T. Z. D. des Mes, K. Kujawa-Roeleveld, G. Zeeman, G. Lettinga	Water Science and Technology	57	2008	1177–1182
28	N. Lindqvist, T. Tuhkanen, L. Kronberg	Water Research	39	2005	2219–2228
29	M. Clara, B. Strenn, O. Gans, E. Martinez, N. Kreuzinger, H. Kroiss	Water Research	39	2005	4797–4807

Table A-3. Continued.

Ref	Authors	Journal/Publisher	Volume	Year	Pages
31	J.L. Zhou, Z.L. Zhang, E. Banks, D. Grover, J.Q. Jiang	Journal of Hazardous Materials	166	2009	655–661
33	T. Benabdallah El-Hadj, J. Dosta, J. Mata-Alvarez	Water Science & Technology	53	2006	99–107
34	T. Okuda, Y. Kobayashi, R. Nagao, N. Yamashita, H. Tanaka, S. Tanaka, S. Fujii, C. Konishi, I. Houwa	Water Science & Technology	57	2008	65–71
35	O. Braga, G.A. Smythe, A.I. Schafer, A.J. Feitz	Water Science & Technology	52	2005	273–278
36	S. Suarez, M. Ramil, F. Omil, J.M. Lema	Water Science & Technology	52	2005	9–14
38	S. Terzic, M. Matosic, M. Ahel, I. Mijatovic	Water Science & Technology	51	2005	447–453
41	S. Suarez, J.M. Lema, F. Omil	Water Research	44	2010	3214–3224
42	J. Gasperi, V. Rocher, S. Gilbert, S. Azimi, G. Chebbo	Water Research	44	2010	3065–3076
43	I.S. Lee, S-H. Lee, J-E. Oh	Water Research	44	2010	214–222
44	Q. Sui, J. Huang, S. Deng, G. Yu, Q. Fan	Water Research	44	2010	417–426
46	Y. Lee, U. von Gunten	Water Research	44	2010	555–566
48	F.L. Rosario-Ortiz, E.C. Wert, S.A. Snyder	Water Research	44	2010	1440–1448
51	A.Y. Lin, S.C. Panchangam, P. Ciou	Chemosphere	80	2010	1167–1174
52	D. Reinhold, S. Vishwanathan, J.J. Park, D. Oh, F.M. Saunders	Chemosphere	80	2010	687–692
56	J.L. Tambosi, R.F. de Sena, M. Favier, W. Gebhardt, H.J. José, H.F. Schröder, R. de Fátima P. Muniz Moreira	Desalination	261	2010	148–156
57	F.P. Shariati, M. Reza Mehrnia, B.M. Salmasi, M. Heran, C. Wisniewski, M.H. Sarrafzadeh	Desalination	250	2010	798–800
66	R. Reif, S. Suárez, F. Omil, J.M. Lema	Desalination	221	2008	511–517
71	M. Bodzek, M. Dudziak	Desalination	198	2006	24–32

Table A-3. Continued.

Ref	Authors	Journal/Publisher	Volume	Year	Pages
72	J. Zhang, L. Giorno, E. Drioli	Desalination	194	2006	101–107
73	T.K. Kimura, H. Hara, Y. Watanabe	Desalination	178	2005	135–140
74	T. Urase, C. Kagawa, T. Kikuta	Desalination	178	2005	107–113
75	S. Lyko, T. Wintgens, T. Melin	Desalination	178	2005	95–105
77	B. De Witte, H. Van Langenhove, K. Demeestere, K. Saerens, P. De Wispelaere, J. Dewulf	Chemosphere	78	2010	1142–1147
78	M. Clara, G. Windhofer, W. Hartl, K. Braun, M. Simon, O. Gans, C. Scheffknecht b, A. Chovanec	Chemosphere	78	2010	1078–1084
80	I. Kim, N. Yamashita, H. Tanaka	Chemosphere	77	2009	518–525
85	S.K. Marttinen, M. Ruissalo, J.A. Rintala	Journal of Environmental Management	73	2004	103–109
86	J. Heidler, R.U. Halden	Journal of Environmental Monitoring	11	2009	2207–2215
87	S. Yang, J. Cha, K. Carlson	Journal of Chromatography A	1097	2005	40–53
88	W. Gebhardt, H.F. Schröder.	Journal of Chromatography A	1160	2007	34–43
89	E.C. Catalkaya, F. Kargi	Journal of Environmental Science and Health Part A	44	2009	630–638
90	K.Y. Maillacheruvu, I.A. Pathan	Journal of Environmental Science and Health Part A	44	2009	1315–1326
92	T. Heberer, D. Feldmann	Journal of Hazardous Materials	122	2005	211–218
95	A.L. Ahmad, L.S. Tan, S.R.A. Shukor	Journal of Hazardous Materials	151	2008	71–77
99	R. Molinari, P. Argurio, T. Poerio	Journal of Membrane Science	340	2009	26–34
100	D. Patureau, N. Delgenes, J.-P. Delgenes	Chemosphere	72	2008	586–591

Table A-3. Continued.

Ref	Authors	Journal/Publisher	Volume	Year	Pages
101	X.-J. Kong, D. Li, L.-Q. Cao, X.-Mei Zhang, Yan Zhao, Y. Lv, J. Zhang	Chemosphere	72	2008	59–66
102	H.A. Duong, N.H. Pham, H.T. Nguyen, T.T. Hoang, H.V. Pham, V.C Pham, M. Berg, W. Giger, A.C. Alder	Chemosphere	72	2008	968–973
104	S. Perez, P. Eichhorn, D.S. Aga	Environmental Toxicology and Chemistry	24	2005	1361–1367
106	S. Gonzalez, M. Petrovic, D. Barcelo.	Chemosphere	67	2007	335–343
107	M. Carballa, G. Manterola, L. Larrea, T. Ternes, F. Omil, J.M. Lema.	Chemosphere	67	2007	1444–1452
108	A.S. Stasinakis, A.V. Petalas, D. Mamais, N.S. Thomaidis, G. Gatidou, T.D. Lekkas	Chemosphere	68	2007	375–381
109	A.L. Batt, S. Kim, D.S. Aga	Chemosphere	68	2007	428–435
112	Y. Horii, J.L. Reiner, B.G. Loganathan, K.S. Kumar, K. Sajwan, K. Kannan	Chemosphere	68	2007	2011–2020
114	X. Zeng, G. Sheng, H. Gui, D. Chen, W. Shao, J. Fu	Chemosphere	69	2007	1305–1311
115	V. Matamoros, J. Puigagut, J. Garcia, J.M. Bayona	Chemosphere	69	2007	1374–1380
116	M. Auriol, Y. Filali-Meknassi, C. D. Adams, R. D. Tyagi, T. Noguerol, B. Pina	Chemosphere	70	2008	445–452
118	W. Chenxi, A.L. Spongberg, J.D. Witter	Chemosphere	73	2008	511–518
119	Y. Zhang, J.L. Zhou	Chemosphere	73	2008	848–853
121	V. Matamoros, M. Hijosa, J.M. Bayona	Chemosphere	75	2009	200–205
122	R. Hao, J. Li, Y. Zhou, S. Cheng, Y. Zhang	Chemosphere	75	2009	987–994
123	T. Yu, A. Y. Lin, S.K. Lateef, C. Lin, P. Yang	Chemosphere	77	2009	175–181
125	M. Murakami, H. Shinohara, H. Takada	Chemosphere	74	2009	487–493
126	J.L. Conkle, J.R. White, C.D. Metcalfe	Chemosphere	73	2008	1741–1748

Table A-3. Continued.

Ref	Authors	Journal/Publisher	Volume	Year	Pages
127	P. Pothitou, D. Voutsas	Chemosphere	73	2008	1716–1723
128	N. Cottin, G. Merlin	Chemosphere	73	2008	711–716
129	M.H. Plumlee, J. Larabee, M. Reinhard	Chemosphere	72	2008	1541–1547
132	J.L. Santos, I. Aparicio, M. Callejón, E. Alonso	Journal of Hazardous Materials	164	2009	1509–1516
133	A. Joss, E. Keller, A.C. Alder, A. Göbel, C.S. McArdell, T. Ternes, H. Siegrist	Water Research	39	2005	3139–3152
134	I. Kim, N. Yamashita, H. Tanaka.	Journal of Hazardous Materials	166	2009	1134–1140
136	Marta Carball, Francisco Omil, Juan M. Lema	Water Research	39	2005	4790–4796
138	R. Kanda, P. Griffin, H.A. James, J. Fothergill.	J. Environ. Monit.	5	2003	823–830
139	Peter Roslev, Katrin Vorkamp, Jakob Aarup, Klavs Frederiksen, Per Halkjær Nielsen	Water Research	41	2007	969 – 976
140	N. Vieno, T. Tuhkanen, L. Kronberg	Water Research	41	2007	1001 – 1012
141	M.A. Belmont, M. Ikonomidou, C.D. Metcalfe	Environmental Toxicology and Chemistry	25	2006	29–35
142	M. Clara, S. Scharf, C. Scheffknecht, O. Gans	Water Research	41	2007	4339 – 4348
143	Norihide Nakadaa, Hiroyuki Shinoharaa, Ayako Murata, Kentaro Kiri, Satoshi Managaki, Nobuyuki Sato, Hideshige Takada,	Water Research	41	2007	4373 – 4382
145	A. Tauxe-Wuersch, L.F. De Alencastro, D. Grandjean, J. Tarradellas	Water Research	39	2005	1761–1772
146	Fusheng Li, Akira Yuasab Aya Obara, Alexander P. Mathews	Water Research	39	2005	2065–2075
148	Roly Oliver, Eric May, John Williams	Water Research	39	2005	4436–4444
153	M. Carballa, G. Fink, F. Omil, J.M. Lema, T. Ternes	Water Research	42	2008	287 – 295
154	V. Matamoros, J. Garcia, J.M. Bayona,	Water Research	42	2008	653 – 660

Table A-3. Continued.

Ref	Authors	Journal/Publisher	Volume	Year	Pages
155	E.J. McAdam, J.P. Bagnall, Y.K.K. Koh, T.Y. Chiu, S. Pollard, M.D. Scrimshaw, J.N. Lester, E. Cartmell	Chemosphere	81	2010	1-6
157	L.A. Kirk, C.R. Tyler, C.M. Lye, J.P. Sumpter	Environmental Toxicology and Chemistry	21	2002	972-979
164	J.B. Quintana, S. Weiss, T. Reemtsm	Water Research	39	2005	2654-2664
165	M. Muller, S. Combalbert, N. Delgenès, V. Bergheaud, V. Rocher, P. Benoit, J.-P. Delgenès, D. Patureau, G. Hernandez-Raquet	Chemosphere	81	2010	65-71
168	A. Joss, S. Zabczynski, A. Gobel, B. Hoffmann, D. Loffler, C.S. McArdell, T.A. Ternes, A. Thomsen, H. Siegrist	Water Research	40	2006	1686 – 1696
169	A.L. Filby, J.A. Shears, B.E. Drage, J.H. Churchley, C.R. Tyler	Environ. Sci. Technology	44	2010	4348-4354
170	N. Nakada, Toshikatsu Tanishima, Hiroyuki Shinohara, Kentaro Kiri, Hideshige Takada	Water Research	40	2006	3297 – 3303
172	Y. Suzuki, T. Maruyama	Water Research	40	2006	1061 – 1069
176	V. Yangali-Quintanilla, S.K. Maeng, T. Fujioka, M. Kennedy, G. Amy	Journal of Membrane Science	362	2010	334-345
177	C. Accinelli, M.L. Sacca, I. Batisson, J. Fick, M. Mencarelli, R. Grabic	Chemosphere	81	2010	436-443
178	S. Deng, Q. Yu, J. Huang, G. Yu	Water Research	44	2010	5188-5195
180	A.M. Comerton, R.C. Andrews, D.M. Bagley, C. Hao	Journal of Membrane Science	313	2008	323-335
183	J. Lu, Q. Jin, Y. He, J. Wu, W. Zhang, J. Zhao	Water Research	44	2008	1075-1082
187	A. Gulkowska, H.W. Leung, M.K. So, S. Taniyasu, N. Yamashita, L.W.Y. Yeung, Bruce J. Richardson, A.P. Lei, J.P. Giesy, P.K.S. Lam	Water Research	42	2008	395-403
188	L. Kim, H. Tanaka	Water Environment Research	82	2010	294-301
189	R.F. Chimchirian, R.P.S. Suri, H. Fu	Water Environment Research	79	2007	969-974

Table A-3. Continued.

Ref	Authors	Journal/Publisher	Volume	Year	Pages
190	H. Carrere, A. Bernal-Martinez, D. Patureau, J. Delgenes	Environmental and Energy Engineering/ AIChE Journal	52	2006	3612-3620
193	Jim T. Yu, Edward J. Bouwer, Mehmet Coelhan	Agricultural Water Management	86	2006	72-80
194	S.J Rooklidge, J.R. Miner, T.A. Kassim, P.O. Nelson	American Water Works Association. Journal	97	2005	92-100
195	Kosjek, E. Heath, B. Kompare	Analytical and Bioanalytical Chemistry	387	2007	1379-1387
196	A. Pena, M. Paulo, L. J. G. Silva, M. Seifrtová, C. M. Lino, P. Solich	Analytical and Bioanalytical Chemistry	396	2010	2929-2936
197	N. Prado, J.Ochoa, A. Amrane	Bioresource Technology	100	2009	3769-3774
198	M. Mezcuca, M.J. Gomez, I. Ferrer, A. Aguera, M.D. Hernando, A.R. Fernandez-Alba	Analytica Chimica Acta	524	2004	241-247
199	B. Li, T. Zhang, Z. Xu, H.H.P. Fang	Analytica Chimica Acta	645	2009	64-72
200	J. Radjenovic, M. Petrovic; D. Barcelo	Anal Bioanal Chem	387	2007	1365-1377
202	T. Yoshimoto, F. Nagai, J. Fujimoto, K. Watanabe, H. Mizukoshi, T. Makino, K. Kimura, H. Saino, H. Sawada, H. Omura	Applied and Environmental Microbiology	70	2004	5283-5289
203	M. Leclercq, O. Mathieu, E. Gomez, C. Casellas, H. Fenet, D. Hillaire-Buys	Arch Environ Contam Toxicol	56	2009	408-415
204	H. Song, K. Nakano, T. Taniguchi, M. Nomura, O. Nishimura	Bioresource Technology	100	2009	2945-2951
205	K. Bester	Chemosphere	57	2004	863-870
206	S. Barnabé, I. Beauchesne, D.G. Cooper, J.A. Nicell	Water Research	42	2008	153-162
209	J.Y. Kim, K. Ryu, E.J. Kim, W.S. Choe, G.C. Cha, I. Yoo	Process Biochemistry	42	2007	1470-1474
210	J. Chen, X. Huang, D. Lee	Process Biochemistry	43	2008	451-456
211	V. Gabet-Giraud, C. Miega, J.M. Choubert, S.M. Ruel, M. Coquery	Science of the Total Environment	408	2010	4257-4269

Table A-3. Continued.

Ref	Authors	Journal/Publisher	Volume	Year	Pages
212	X. Chen, J. Hu	Process Biochemistry	44	2009	1330–1334
213	V. Ivanov, J.J. Lim, O. Stabnikova, K.Y. Gin	Process Biochemistry	45	2010	284–287
215	A.S. Stasinakis, C.I. Kordoutis, V.C. Tsiouma, G. Gatidou, N.S. Thomaidis	Bioresource Technology	101	2010	2090–2095
216	C.E. Rodríguez-Rodríguez, E. Marco-Urrea, G. Caminal	Bioresource Technology	101	2010	2259–2266
217	G. Mascolo *, L. Balest, D. Cassano, G. Laera, A. Lopez, A. Pollice, C. Salerno	Bioresource Technology	101	2010	2585–2591
218	R. Cespedes, S. Lacorte, A. Ginebreda, D. Barcelo	Environmental Pollution	153	2008	384–392
220	Ana Dordio, A.J. Palace Carvalho, Dora Martins Teixeira, Cristina Barrocas Dias, Ana Paula Pinto	Bioresource Technology	101	2010	886–892
221	L. Clouzot, P. Doumenq, N. Roche, B. Marrot	Bioresource Technology	101	2010	6425–6431
222	Heidemarie Schaar, Manfred Clara, Oliver Gans, Norbert Kreuzinger	Environmental Pollution	158	2010	1399–1404
224	W Sim, J. Lee, J. Oh	Environmental Pollution	158	2010	1938–1947
225	X. Chang, M.T. Meyer, X. Liu, Q. Zhao, H. Chen, J. Chen, Z. Qiu, L. Yang, J. Cao, W. Shu	Environmental Pollution	158	2010	1444–1450
226	M. Gros, M. Petrovic, D. Barcelo	Environmental Toxicology and Chemistry	26	2007	1553–1562
227	A. Musolff, S. Leschik, M. Möder, G. Strauch, F. Reinstorf, M. Schirmer	Environmental Pollution	157	2009	3069–3077
228	R. Ma, K. Shih	Environmental Pollution	158	2010	1354–1362
229	M. Muller, F. Rabenoelina, P. Balaguer, D. Patureau, K. Lemenach, H. Budzinski, D. Barcelo, M. Lopez De Alda, M. Kuster, J. Delgenes, G. Hernandez-Raquet	Environmental Toxicology and Chemistry	27	2008	1649–1658
230	Q. Sun, S. Deng, J. Huang, G. Shen, G. Yu	Environmental Toxicology and Pharmacology	25	2008	20–26
231	E. Chamberlain, C. Adams	Water Research	40	2006	2517–2526

Table A-3. Continued.

Ref	Authors	Journal/Publisher	Volume	Year	Pages
232	T. Kupper, C. Plagellat, R.C. Brandli, L.F. de Alencastro, D. Grandjean, J. Tarradellas	Water Research	40	2006	2603-2612
233	M. Bernhard, J. Muller, T.P. Knepper	Water Research	40	2006	3419-3428
235	H. De Wever, S. Weiss, T. Reemtsma, J. Vereecken, J. Muller, T. Knepper, O. Rorden, S. Gonzalez, D. Barcelo, M.D. Hernando	Water Research	41	2007	935-945
236	T. Hashimotoa, K. Onda, Y. Nakamura, K. Tada, A. Miya, T. Murakami	Water Research	41	2007	2117-2126
239	B. Boulanger, J.D. Vargo, J.L. Schnoor, K.C. Hornbuckle	Environ. Sci. Technol	39	2005	5524-5530
240	A.V. Dordio, A.J.E. Candeias, A.P. Pinto, C. T. da Costa, A.J.P. Carvalho	Ecological Engineering	35	2009	290-302
243	P. Pholchan, M. Jones, T. Donnelly, P.J. Sallis	Environ. Sci. Technol	42	2008	6141-6147
247	Guang-Guo Ying , Rai S. Kookana	Environment International	33	2007	199-205
248	J.L. Santos, I. Aparicio, E. Alonso	Environment International	33	2007	596-601
249	Katherine H. Langford, Kevin V. Thomas	Environment International	35	2009	766-770
251	S. Gonzalez, M. Petrovic, D. Barcelo	Journal of Hydrology	356	2008	46- 55
253	J.L. Tambosi, R.F. de Sena, W. Gebhardt, R.F.P.M. Moreira, H.J. Jose, H. Fr. Schröder	Ozone: Science & Engineering	31	2009	428-435
254	Giorgio Bertanza, Roberta Pedrazzani, Matteo Papa, Giovanna Mazzoleni, Nathalie Steimberg, Luigi Caimi, Claudia Montani, Diego Dilorenzo	Ozone: Science & Engineering	32	2010	204-208
255	S.A. Snyder, E.C. Wert, D.J. Rexing, R.E. Zegers, D.D. Drury	Ozone: Science & Engineering	28	2006	445-460
256	C. Gagnon, A. Lajeunesse, P. Cejka, F. Gagne , R. Hausler	Ozone: Science & Engineering	30	2008	387-392
257	Y. Kim, M. Osako, D. Lee	Waste Management & Research	20	2002	341-349
258	Cicek N, Londry K, Oleszkiewicz JA, Wong D, Lee Y.	Water Environmental Research	79	2007	795-800

Table A-3. Continued.

Ref	Authors	Journal/Publisher	Volume	Year	Pages
261	Pei Xu, J.E. Drewes, Christopher Bellona, Gary Amy, Tae-Uk Kim, Marc Adam, Thomas Heberer	Water Environmental Research	77	2005	40-48
262	S. Zuehlke, U. Duennbier, B. Lesjean, R. Gnirss, H. Buisson	Environment Research	78	2006	2480-2486
263	S. Suarez, M.C. Dodd, F. Omil, U. von Gunten	Water Research	41	2007	2481-2490
264	M.A. Soliman, J.A. Pedersen, H. Park, A. Castaneda-Jimenez, M.K. Stenstrom, I.H. (Mel) Suffet	Water Environment Research	79	2007	156-167
265	X. Jin, J. Hu, S. Leong Ong	Water Research	41	2007	3077-3088
266	D.M. Fuerhacker, S. Scharf, W. Pichler, T. Ertl, R. Haberl	The Science of the Total Environment	277	2001	95-100
267	M. Barret, G. Cea Barcia, A. Guillon, H. Carrère*, D. Patureau	Journal of Hazardous Materials	181	2010	241-247
269	G.D'Ascenzo, A. Di Corcia, A.Gentili, R.Mancini, R.Mastropasqua, M.Nazzari, R Samperi	The Science of the Total Environment	302	2003	199-209
271	B.D. Stanford, H.S. Weinberg	Environmental Science Technology	44	2010	2994-3001
272	Y. Lv, T. Yuan, J. Hu, W. Wang	Science of the Total Environment	408	2010	4170-4176
273	Y.K.K. Koh, T.Y. Chiu, A.R. Boobis, M.D. Scrimshaw, J.P. Bagnall, A. Soares, S. Pollard, E. Cartmell, J.N. Lester	Environmental Science Technology	43	2009	6646-6654
277	C. Zwiener, F.H. Frimmel	The Science of the Total Environment	309	2003	201-211
280	M.R. Servos, D.T. Bennie, B.K. Burnison, A. Jurkovic, R. McInnis, T. Neheli, A. Schnell, P. Seto, S.A. Smyth, T.A. Ternes.	Science of the Total Environment	336	2005	155-170
281	H. Zhang, H. Yamada, H. Tsuno	Journal of Hazardous Materials	42	2008	3375-3380
283	J.E. Loyo-Rosales, C.P. Rice, A. Torrents	Journal of Hazardous Materials	41	2007	6815-6821
284	A.L. Batt, S. Kim, D.S. Aga	Journal of Hazardous Materials	40	2006	7367-7373
286	Angela Rodayan, Ranjan Roy, Viviane Yargeau	Journal of Hazardous Materials	177	2010	237-243
287	A. Rodayan, R. Roy, V. Yargeau	Environmental Science Technology	44	2010	284-289

Table A-3. Continued.

Ref	Authors	Journal/Publisher	Volume	Year	Pages
288	K. Kimura, H. Hara, Y. Watanabe	Environmental Science Technology	41	2007	3708- 3714
289	V. Matamoros, C. Arias, H. Brix, J.M. Bayona	Environmental Science Technology	41	2007	8171- 8177
290	S. Kim, P. Eichhorn, J.N. Jensen, A.S. Weber, D.S. Aga	Environmental Science Technology	39	2005	5816- 5823
291	S. Castiglioni, R. Bagnati, R. Fanelli, F. Pomati, D. Calamari, E. Zuccato	Environmental Science Technology	40	2006	357-363
292	B. Li, T. Zhang	Environment and Science Technology	44	2010	3468- 3473
294	K.E. Conn, L.B. Barber, G.K. Brown, R.L. Siegrist	Environmental Science Technology	40	2006	7358- 7366
295	E.C. Wert, F.L. Rosario-Ortiz, S.A. Snyder	Environmental Science Technology	43	2009	4858- 4863
296	T. Kosjek, H.R. Andersen, B. Kompare, A. Ledin, E. Heath	Environmental Science Technology	43	2009	6256- 6261
298	A.Y. Lin, T.Yu, S.K. Lateef	Journal of Hazardous Materials	167	2009	1163- 1169
302	F. Alatrliste-Mondragon, R. Iranpour, B.K. Ahring	Water Research	37	2003	1260- 1269
304	D. Di Gioia, L. Sciubba, L. Bertin, C. Barberio, L. Salvadori, S. Frassinetti, F. Fava	Water Research	43	2009	2977- 2988
305	J. Yu, J. Hu, S. Tanaka, S. Fujii	Water Research	43	2009	2399- 2408
306	O. González, M. Esplugas, C. Sans, A. Torres, S. Esplugas	Water Research	43	2009	2149- 2158
307	C. Abegglen, A. Joss, C. S. McArdell, G. Fink, M. P. Schläsener, T. A. Ternes, H. Siegrist	Water Research	43	2009	2036- 2046
309	M-L. Janex-Habibi, A. Huyard, M. Esperanza, A. Bruchet	Water Research	43	2009	1565- 1576
310	A. S. Stasinaskis, S. Kotsifa, G. Gatidou, D. Mamais	Water Research	43	2009	1471- 1479
311	A. Wick, G. Fink, A. Joss, H. Siegrist, T. A. Ternes	Water Research	43	2009	1060- 1074
312	E. C. Wert, F. L. Rosario-Ortiz, S. A. Snyder	Water Research	43	2009	1005- 1014

Table A-3. Continued.

Ref	Authors	Journal/Publisher	Volume	Year	Pages
313	J. Radjenović, M. Petrović, D. Barceló	Water Research	43	2009	831-841
314	A. M. Comerton, R. C. Andrews, D. M. Bagley	Water Research	43	2009	613-622
315	T. Hashimoto, T. Murakami	Water Research	43	2009	573-582
317	B. Kasprzyk-Hordern, R. M. Dinsdale, A. J. Guwy	Water Research	43	2009	363-380
319	V. Matamoros, C. Arias, H. Brix, J. M. Bayona	Water Research	43	2009	55-62
323	T. Urase, T. Kikuta	Water Research	39	2005	1289-1300
324	G. R. Boyd, S. Zhange, D. A. Grimm	Water Research	39	2008	668-676
325	M. Clara, N. Kreuzinger, B. Strenn, O. Gans, H. Kroiss	Water Research	39	2005	97-106
326	A. C. Johnson, H. -R. Aerni, A. Gerritsen, M. Gibert, W. Giger, K. Hylland, M. Jürgens, T. Nakari, A. Pickering, M. J. -F. Suter, A. Svenson, F. E. Wettstein	Water Research	39	2005	47-58
327	B. Guieysse, G. Viklund	Chemosphere	59	2005	369-376
328	M. T. Rose, F. Sanchez-Bayo, A. N. Crossan, I. R. Kennedy	Chemosphere	63	2006	1849-1858
329	L. Sanchez-Prado, M. Llompарт, M. Lores, C. García-Jares, J. M. Bayona, R. Cela	Chemosphere	65	2006	1338-1347
333	J. Heidler, R. U. Halden	Chemosphere	66	2007	362-369
334	M. J. Gómez, M. J. Martínez Bueno, S. Lacorte, A. R. Fernández-Alba, A. Agüera	Chemosphere	66	2007	993-1002
335	M. Esperanza, M. T. Suidan, R. Marfil-Vega, C. Gonzalez, G. A. Sorial, P. McCauley, R. Brenner	Chemosphere	66	2007	1535-1544
336	J. Lee, B. C. Lee, J. S. Ra, J. Cho, I. S. Kim, N. I. Change, H. K. Kim, S. D. Kim	Chemosphere	71	2008	1582-1592
337	H. Zhang, H. Yamada, S.-E. Kim; H.-S. Kim, H. Tsuno	Water Science and Technology	54	2006	123-132
338	M. Clara, B. Strenn, N. Kreuzinger	Water Research	38	2004	947-954

Table A-3. Continued.

Ref	Authors	Journal/Publisher	Volume	Year	Pages
341	T. A. Ternes, N. Herrmann, M. Bonerz, T. Knacker, H. Siegrist, A. Joss	Water Research	38	2004	4075-4084
342	R. Kanda, J. Churchley	Environmental Technology	29	2008	315-323
344	B. Shao, D. Chen, J. Zhang, Y. Wu, C. Sun	Journal of Chromatography A	1216	2009	8312-8318
348	J. Zhange, M. Yang, Y. Zhang, M. Chen	Journal of Environmental Sciences	20	2008	135-141
349	Z-h. Liu, M. Ito, Y. Kanjo, A. Yamamoto	Journal of Environmental Sciences	21	2009	900-906
352	L. D. Nghiem, A. Manis, K. Soldenhoff, A. I. Schäfer	Journal of Membrane Science	242	2004	37-45
355	P. Fauser, J. Vikelsøe, P. B. Sørensen, L. Carlsen	Water Research	37	2003	1288-1295
356	S. K. Marttinen, R. H. Kettunen, K. M. Sormunen, J. A. Rintala	Water Research	37	2003	1385-1393
357	T. A. Ternes, J. Stüber, N. Herrmann, D. McDowell, A. Ried, M. Kampmann, B. Teiser	Water Research	37	2003	1976-1982
358	K. Bester	Water Research	37	2003	3891-3896
359	A. Svenson, A-S. Allard, M. Ek	Water Research	37	2003	4433-4443
363	J. Hollender, S.G. Zimmermann, S. Koepke, M. Krauss, C.S Mcardell, C. Ort, H. Singer, U.V. Gunten, H. Siegrist	Journal of Hazardous Materials	43	2009	7862–7869
364	C.I. Kosma, D.A. Lambropoulou, T.A. Albanis	Journal of Hazardous Materials	179	2010	804–817
365	A.Y Lin, C. Lin, J. Chiou, P.K.A. Hong	Journal of Hazardous Materials	171	2009	452–458
366	L.S. Gaulke, S.E. Strand, T.F. Kalhorn, H.D. Stensel	Environmental Science Technology	43	2009	7111–7116
367	P.H. Roberts, K.V. Thomas	Science of the Total Environment	356	2006	143-153
368	K.G. Karthikeyan, Michael T. Meyer	Science of the Total Environment	361	2006	196-207
369	L. Lishman, S.A. Smyth, K. Sarafin, S. Kleywegt, J. Toito, T. Peart, B. Lee, M. Servos, M. Beland, P. Seto	Science of the Total Environment	367	2006	544-558

Table A-3. Continued.

Ref	Authors	Journal/Publisher	Volume	Year	Pages
371	X. Peng, Z. Wang, W. Kuang, J. Tan, K. Li	Science of the Total Environment	371	2006	314-322
372	A.Göbel, C.S. McArdell, A.Joss, H. Siegrist, W. Giger	Science of the Total Environment	372	2007	361-371
373	V. Matamoros, J. Garcia; J.M. Bayona	Environment Science & Technology	39	2005	5449-5454
374	A.V. Dordio, J.T, Idália Ramalho, A.J. Palace Carvalho, A.J. Estêvão Candeias	Science of the Total Environment	380	2007	237-246
375	V. Matamoros, A. Caselles-Osorio, J. García, J.M. Bayona.	Science of the Total Environment	394	2008	171–176
376	A.L. Spongberg, J.D. Witter	Science of the Total Environment	397	2008	148-157
377	K. Choi, Y. Kim, J. Park, C. Koo Park, M.Y. Kim., H.S. Kim, P. Kim	Science of the Total Environment	405	2008	120-128
378	Saioa Zorita, Lennart Mårtensson, Lennart Mathiasson	Science of the Total Environment	407	2009	2760-2770
379	A.D. Coelho, C. Sans, A. Agüera, M.J. Gómez, S. Esplugas, M. Dezotti	Science of the Total Environment	407	2009	3572–3578
380	J. Lian, J.X. Liu, Y.S. Wei	Science of the Total Environment	407	2009	4261-4268
381	M.M. González, J. Martín, J.L. Santos, I. Aparicio, E. Alonso	Science of the Total Environment	408	2010	563-570
382	M Guang-Guo Ying, Rai S. Kookana, Anu Kumar, Munro Mortimer	Science of the Total Environment	407	2009	5147-5155
383	Gy. Plósz, H. Leknes, H. Liltved, K.V. Thomas	Science of the Total Environment	408	2010	1915–1924
385	G. Teijon, L. Candela, K. Tamoh, A. Molina-Díaz, A.R. Fernández-Alba	Science of the Total Environment	408	2010	3584–3595
387	R. Bossi, J. Strand, O. Sortkjær, M.M. Larsen	Environment International	34	2008	443–450
388	O.A.H. Jones, N. Voulvoulis, J.N. Lester	Environmental Pollution	145	2007	738-744
391	M.P. Schlusener, K. Bester	Clean	36	2008	25 – 33
395	L.B. Barber, K.E. Lee, D.L. Swackhamer, H.L. Schoenfuss	Aquatic Toxicology	82	2007	36–46
396	J. L. Reiner, J. D. Berset, K. Kannan	Arch. Environ. Contam. Toxicol.	52	2007	451–457

Table A-3. Continued.

Ref	Authors	Journal/Publisher	Volume	Year	Pages
397	L. Balest, A. Lopez, G. Mascolo, C. Di Iaconi	Biochemical Engineering Journal	41	2008	288–294
398	S. Suarez, J.M. Lema, F. Omil	Bioresource Technology	100	2009	2138–2146
400	C. Hong, H. JianYing, W. LeZheng, S. Bing	Chinese Science Bulletin	53	2008	514–520
405	T. Wintgens, M. Gallenkemper, T. Melin	Desalination	146	2002	387–391
406	A.I. Schäfel, M. Mastrup, R. Lund Jensen	Desalination	147	2002	243–250
408	E. Trably, D. Patureau	Environ Sci & Pollut Research	13	2006	170 – 176
409	C. Höhne, W. Püttmann	Environ Sci Pollut Research	15	2008	405–416
411	L.S. Gaulke, S.E. Strand, T.F. Kalhorn, H.D. Stensel	Water Environment Research	81	2009	772–778
415	C.Planas, J.M. Guadayol, M.Droguet, A.Escalas, J.Rivera, J.Caixach	Water Research	36	2002	982–988
416	W. Xue, C. Wu, K. Xiao, X. Huang, H. Zhou, H. Tsuno, H. Tanaka	Water Research		2010	
417	A.J. Watkinson, E.J. Murby, S.D. Costanzo	Water Research	41	2007	4164–4176
418	B.G. Loganathan, K.S. Sajwan, E. Sinclair, K.S Kumar, K. Kannan	Water Research	41	2007	4611–4620
419	A.S. Stasinakis, G. Gatidou, D. Mamais, N.S. Thomaidis, T.D. Lekkas	Water Research	42	2008	1796–1804
421	A. Joss, H. Andersen, T. Ternes, P.R. Richle, H. Siegrist	Environ. Sci. Technol	38	2004	3047–3055
422	M.M. Huber, T.A. Ternes, U. Gunten	Environ. Sci. Technol.	38	2004	5177–5186
423	A. Oobel, A. Thomsen, C.S. Mcardell, A. Joss, W. Giger	Environ. Sci. Technol.	39	2005	3981–3989
424	M.M. Huber, S. Korhonen, T.A. Ternes, U. Gunten	Water Research	39	2005	4290–4299
426	J.Y. Hu, X. Chen, G. Tao, K. Kekred	Environ. Sci. Technol.	41	2007	4097–4102
428	M.H. Plumlee, K. Mcneill, M. Reinhard	Environ. Sci. Technol.	43	2009	3662–3668

Table A-3. Continued.

Ref	Authors	Journal/Publisher	Volume	Year	Pages
430	M. Carballa, F. Omil, T. Ternes, J.M. Lema	Water Research	41	2007	2139-2150
431	G. Hernandez-Raquet, A. Soef, N. Delgenes, Patrick Balaguer	Water Research	41	2007	2643-2651
435	K. Kimura, T. Iwase, S. Kita, Y. Watanabe	Water Research	43	2009	3751-3758
437	R. Rosal, A. Rodriguez, J.A Perdigon-Melon, A. Petre, E. Garcia-Calvo, M.J. Gomez, A. Aguera, A.R. Fernandez-Alba	Water Research	44	2010	578-588
438	J. Reungoat, M. Macova, B.I. Escher, S. Carswell, J.F. Mueller, J. Keller	Water Research	44	2010	625-637
439	Y. Qu, C. Zhang, F. Li, J. Chen, Q. Zhou	Water Research	44	2010	2939-2947
440	R. Guo, W-J. Sim, E-S. Lee, J-H. Lee, J-E. Oh	Water Research	44	2010	3476-3486
442	Weihai Xu, Gan Zhang, Xiangdong Li, Shichun Zou, Ping Li, Zhaohui Hu, Jun Li	Water Research	41	2007	4526 – 4534
445	Y. He, G. Chen, Z. Ji, S. Li	Separation and Purification Technology	66	2009	390-396
446	S. González, J. Müller, M. Petrovic, D. Barceló, T. P. Knepper	Environmental Pollution	144	2006	926-932
447	H. Singer, S. Jaus, I. Hanke, A. Lück, J. Hollender, A. C. Alder	Environmental Pollution	158	2010	3054-3064
448	J. E. Drewes, C. Bellona, M. Oedekoven, P. Xu, T-U. Kim, G. Amy	Environmental Progress	24	2005	400-409
450	J-J. Yang, C. D. Metcalfe	Science of the Total Environment	363	2006	149-165
451	M. P. Fernandez, M. G. Ikonou, I. Buchanan	Science of the Total Environment	373	2007	250-269
458	J. Sánchez-Avila, J. Bonet, G. Velasco, S. Lacorte	Science of the Total Environment	407	2009	4157-4167
463	D. T. Sponza, P. Demirden	Separation and Purification Technology	56	2007	108-117
467	G.-G. Ying, R.S. Kookana, D.W. Kolpin	Journal of Environmental Monitoring	11	2009	1498–1505
470	S. Gonzalez, M. Petrovic, D. Barcelo	Journal of Chromatography	1052	2004	111–120

Table A-3. Continued.

Ref	Authors	Journal/Publisher	Volume	Year	Pages
471	A. Caruccia; Giovanna Cappaia; Martina Pireddaa a DIGITA, University of Cagliari, Cagliari, Italy	Journal of Environmental Science and Health	41	2006	1831 — 1842
478	L. Bo, T. Urase, X. Wang	Front. Environ. Sci. Engin. China	3	2009	236–240
479	V. Matamoros, J.M. Bayona	Environment Science & Technology	40	2006	5811-5816
480	M. Gros, M. Petrović, Antoni Ginebreda, D. Barceló	Environmental International	36	2010	15-26
482	M. Esperanza, M.T. Suidan, F. Nishimura, Z. Wang, G. Sorial, A. Zaffiro, P. McCauley, R. Brenner, G. Sayles	Environ. Sci. & Technol.	38	2004	3028-3035
483	M. Sole, M.J. Lopez de Alda, M. Castillo, C. Porte, K. Ladegaard-Pedersen, D. Barcelo	Environ. Sci. & Technol.	34	2000	5076-5083
484	M. Petrovic, M. Sole, M.J. Lopez de Alda, D. Barcelo	Environ. Toxicol. Chem	21	2002	2146-2156
485	B. Shao, J. Hu, M. Yang	Bull. Environ. Contam. Toxicol	70	2003	527-532
486	C.Y. Cheng, C.Y. Wu, C.H. Wang, W.H. Ding	Environ. Toxicol. Chem.	23	2004	599-605
487	Anderson, Henrik; Hansruedi Siegrist; Bent Halling-Sorensen; Thomas A. Ternes	Environmental Science & Technology	37	2003	4021-4026
488	Carballa, M; F. Omil; JM Lema; M Llompart; C Garcia-Jares; I Rodriguez; M Gomez; T Ternes	Water Research	38	2004	2918-2926
489	S.A Snyder, A. Samer, A.M. Redding; F.S. Cannon; J. DeCarolis; J. Oppenheimer; E.C. Wert, Y. Yoon	Desalination	202	2007	156-181
490	P. Thomas, Gregory Foster	Environmental Toxicology and Chemistry	24	2005	25-30
491	G. Winkler, R. Fischer, P. Krebs; A. Thompson; E. Cartmell, P. Griffin	Engineering in Life Sciences	7	2007	42-51
492	G.G. Ying, R. Kookana, A. Kumar	Environmental Toxicology and Chemistry	27	2008	87-94
493	T. Yi, S. Mackintosh, Diana S. Aga, W.F. Harper, Jr	Water Research	25	2011	1369-1377

Table A-3. Continued.

Ref	Authors	Journal/Publisher	Volume	Year	Pages
494	D. O'Grady, S. Evangelista, V. Yargeau	Environmental Engineering Science	26	2009	1393-1400
601	N. Le-Minh, S.J. Khan, J.E. Drewes, R.M. Stuetz	Water Research	44	2010	4295-4323
603	O. A. H. Jones, N. Voulvoulis, J. N. Lester	Critical Reviews in Environmental Science and Technology	35	2005	401-427
604	Z. Liu, Y. Kanjo, S. Mizutani	Science of the Total Environment	407	2009	731-748
606	C. Dargnat, M.-J. Teil, M. Chevreuil, M. Blanchard	Science of the Total Environment	407	2009	1235-1244
611	D.P. Mohapatra, S.K. Brar, R.D. Tyagi, R.Y. Surampalli	Chemosphere	78	2010	923-941
616	J. Sipma, B. Osuna, N. Collado, H. Monclús, G. Ferrero, J. Comas, I. Rodriguez-Roda	Desalination	250	2010	653-659
618	V. Belgiorno, L. Rizzo, D. Fatta, C. Della Rocca, G. Lofrano, A. Nikolaou, V. Naddeo, S. Meric	Desalination	215	2007	166-176
620	Y. Zhang, S.-U Geißen, C. Gal	Chemosphere	73	2008	1151-1161
621	S. K. Khanal, B. Xie, M. L. Thompson, S. Sung, S-K. Ong, J. (H.) V. Leeuwen	Environmental Science & Technology	40	2006	6537-6546
622	A.C. Johnson, J.P. Sumpter	Environmental Science & Technology	35	2001	4697-4703
623	S.S. Teske, R.G. Arnold	Rev Environ Sci Biotechnol	7	2008	107-124
625	Y. M. Lee, J. A. Oleszkiewicz, N. Cicek, K. Londry	Environmental Technology	25	2004	635-645
626	Y. K. K. Koh, T. Y. Chiu, A. Boobis, E. Cartmell, M. D. Scrimshaw, J. N. Lester	Environmental Technology	29	2008	245-267
627	K.M. Onesios, J.T. Yu, E.J. Bouwer	Biodegradation	20	2009	441-466
630	M. Auriol, Y. Filali-Meknassi, R. D. Tyagi, C.D. Adams, R.Y. Surampalli	Process Biochemistry	41	2006	525-539
631	J.L. Tambosi, L.Y. Yamanaka, H.J.J.R.F.P.M. Moreira	Quim. Nova	33	2010	411-420

Table A-3. Continued.

Ref	Authors	Journal/Publisher	Volume	Year	Pages
632	Miege, J.M. Choubert, L. Ribeiro, M. Eusebe, M. Coquery	Environmental Pollution	157	2009	1721–1726
635	M.D. Hernando, M. Petrovic, J. Radjenovic, A.R. Fernandez-Alba, D. Barcelo	Comprehensive Analytical Chemistry	50	2007	451-474
636	J. Kagle, A.W. Porter, R.W. Murdoch, G. Rivera-Cancel, A.G. Hay	Advances in Applied Microbiology	67	2009	65-108
637	A.C. Lietz and Michael T. Meyer	USDI and USGS		2006	
638	Canadian Environmental Protection Act	Environment Canada/Health Canada		2001	
639	J.E. Drewes, D. Sedlak, S. Snyder, E. Dickenson	WERF – 04-HHE-1CO		2009	
640	J.E. Drewes, E.R.V. Dickenson, S. Snyder	WERF – 03-CTS-21UR		2009	
641	J.E. Drewes, J.D.C. Hemming, J. Schauer, W.C. Sonzogni	WERF – 01-HHE-20T		2006	
644	E. Furlong, J.L. Gray, D.M. Quanrud, S. Teske, K. Esposito, J. Marine, W.P. Ela, B. Stinson, D.W. Kolpin, P.J. Phillips	WERF – 04-HHE-6		2010	
645	E.R.V. Dickenson, J.E. Drewes, J. Stevens-Garmon, S. Khan, J. McDonald	WERF – U2R07		2010	
646	R. Stephenson and J. Oppenheimer	WERF - 03-CTS-22UR		2007	

APPENDIX B

SUPPLEMENTARY MATERIAL FOR THE UV/H₂O₂ AND FENTON'S KINETIC MODELS

In this section, we present the full system of equations that were solved for each of the models described in the Chapter 3.

The models are presented for a generic target, T (T=PC or NP in our calculations) and a generic scavenger, Sc (Sc=ethanol or isopropanol).

B1. UV/H₂O₂ Model

$$\frac{d[T]}{dt} = -k_T[T] \langle [\bullet\text{OH}] \rangle - \phi_T I_0 f_T (1 - e^{-2.303A_T}) \quad (\text{B-1})$$

$$\begin{aligned} \frac{d[\text{H}_2\text{O}_2]}{dt} = & -\phi_{\text{H}_2\text{O}_2} I_0 f_{\text{H}_2\text{O}_2} (1 - e^{-2.303A}) - k_2[\text{H}_2\text{O}_2] \langle [\bullet\text{OH}] \rangle - k_3[\text{HO}_2^-] \langle [\bullet\text{OH}] \rangle \\ & - k_{10}[\text{H}_2\text{O}_2] \langle [\text{O}_2^{\bullet-}] \rangle - k_{14}[\text{H}_2\text{O}_2] \langle [\text{HO}_2^{\bullet}] \rangle - k_{15}[\text{H}_2\text{O}_2] \langle [\text{CO}_3^{\bullet-}] \rangle \\ & - k_{16} \langle [\text{CO}_3^{\bullet-}] \rangle [\text{HO}_2^-] + k_8 \langle [\bullet\text{OH}] \rangle^2 + k_{12} \langle [\text{HO}_2^{\bullet}] \rangle [\text{O}_2^{\bullet-}] + k_{13} \langle [\text{HO}_2^{\bullet}] \rangle^2 \end{aligned} \quad (\text{B-2})$$

$$\frac{d\langle[\bullet\text{OH}]\rangle}{dt} = 2\phi_{\text{H}_2\text{O}_2} I_0 f_{\text{H}_2\text{O}_2} (1 - e^{-2.303A}) - k_2[\text{H}_2\text{O}_2]\langle[\bullet\text{OH}]\rangle - k_3[\text{HO}_2^-]\langle[\bullet\text{OH}]\rangle \quad (\text{B-3})$$

$$\begin{aligned} & -k_4[\text{HCO}_3^-]\langle[\bullet\text{OH}]\rangle - k_5[\text{CO}_3^{2-}]\langle[\bullet\text{OH}]\rangle - k_6\langle[\text{HO}_2^\bullet]\rangle\langle[\bullet\text{OH}]\rangle - k_7\langle[\text{O}_2^\bullet]\rangle\langle[\bullet\text{OH}]\rangle \\ & - 2k_8\langle[\bullet\text{OH}]^2\rangle - k_9\langle[\text{CO}_3^{\bullet-}]\rangle\langle[\bullet\text{OH}]\rangle + k_{10}\langle[\text{O}_2^\bullet]\rangle[\text{H}_2\text{O}_2] + k_{14}\langle[\text{HO}_2^\bullet]\rangle[\text{H}_2\text{O}_2] \\ & - k_T[\text{T}]\langle[\bullet\text{OH}]\rangle - k_{\text{Sc}}[\text{Sc}]\langle[\bullet\text{OH}]\rangle \end{aligned}$$

$$\frac{d\langle[\text{O}_2^\bullet]\rangle}{dt} \left(1 + \frac{[\text{H}^+]}{K_{a2}}\right) = k_2[\text{H}_2\text{O}_2]\langle[\bullet\text{OH}]\rangle + k_3[\text{HO}_2^-]\langle[\bullet\text{OH}]\rangle - k_6\langle[\text{HO}_2^\bullet]\rangle\langle[\bullet\text{OH}]\rangle \quad (\text{B-4})$$

$$\begin{aligned} & - k_7\langle[\text{O}_2^\bullet]\rangle\langle[\bullet\text{OH}]\rangle - k_{10}[\text{H}_2\text{O}_2]\langle[\text{O}_2^\bullet]\rangle - k_{11}\langle[\text{CO}_3^{\bullet-}]\rangle\langle[\text{O}_2^\bullet]\rangle - k_{12}\langle[\text{HO}_2^\bullet]\rangle\langle[\text{O}_2^\bullet]\rangle \\ & - 2k_{13}\langle[\text{HO}_2^\bullet]\rangle^2 - k_{14}[\text{H}_2\text{O}_2]\langle[\text{HO}_2^\bullet]\rangle + k_{15}[\text{H}_2\text{O}_2]\langle[\text{CO}_3^{\bullet-}]\rangle + k_{16}[\text{HO}_2^-]\langle[\text{CO}_3^{\bullet-}]\rangle \end{aligned}$$

$$\frac{d\langle[\text{CO}_3^{\bullet-}]\rangle}{dt} = k_4[\text{HCO}_3^-]\langle[\bullet\text{OH}]\rangle + k_5[\text{CO}_3^{2-}]\langle[\bullet\text{OH}]\rangle - k_9\langle[\text{CO}_3^{\bullet-}]\rangle\langle[\bullet\text{OH}]\rangle \quad (\text{B-5})$$

$$- k_{11}\langle[\text{CO}_3^{\bullet-}]\rangle\langle[\text{O}_2^\bullet]\rangle - k_{15}[\text{H}_2\text{O}_2]\langle[\text{CO}_3^{\bullet-}]\rangle - k_{16}[\text{HO}_2^-]\langle[\text{CO}_3^{\bullet-}]\rangle - 2k_{17}\langle[\text{CO}_3^{\bullet-}]\rangle^2$$

$$\frac{d[\text{TotCO}_3]}{dt} = -k_4\langle[\bullet\text{OH}]\rangle[\text{HCO}_3^-] - k_5\langle[\bullet\text{OH}]\rangle[\text{CO}_3^{2-}] + k_{11}\langle[\text{O}_2^\bullet]\rangle\langle[\text{CO}_3^{\bullet-}]\rangle \quad (\text{B-6})$$

$$+ k_{15}\langle[\text{CO}_3^{\bullet-}]\rangle[\text{H}_2\text{O}_2] + k_{16}\langle[\text{CO}_3^{\bullet-}]\rangle[\text{HO}_2^-] + N\left(-\frac{d[\text{T}]}{dt}\right)$$

$$\frac{d[\text{Sc}]}{dt} = -k_{\text{Sc}}[\text{Sc}]\langle[\bullet\text{OH}]\rangle \quad (\text{B-7})$$

$$[\text{HCO}_3^-] = \frac{[\text{TotCO}_3]}{\left\{1 + \frac{[\text{H}^+]}{K_{a3}} + \frac{K_{a4}}{[\text{H}^+]}\right\}} \quad (\text{B-8})$$

$$[\text{CO}_3^{2-}] = \frac{K_{a4}[\text{HCO}_3^-]}{[\text{H}^+]} \quad (\text{B-9})$$

$$[\text{H}^+] = [\text{OH}^-] + [\text{HCO}_3^-] + 2[\text{CO}_3^{2-}] + \langle [\text{O}_2^\bullet] \rangle + [\text{HO}_2^-] + \langle [\text{CO}_3^\bullet] \rangle \quad (\text{B-10})$$

In equation (B-6), N is the total number of carbon atoms in the target molecule.

Model calculations yield concentration of all species as a function of time. For radicals, the concentration found is a volume-averaged concentration. As discussed in the manuscript, radical/radical reactions, such as reactions 8, 12 and 13 in B-2 are neglected in the calculations, but are included here for completeness. It was verified that all terms involving this type of reaction were negligible by performing calculations under the assumption $\langle [\text{R1}][\text{R2}] \rangle \approx \langle [\text{R1}] \rangle \langle [\text{R2}] \rangle$.

Direct photolysis of the target is included in equation (B-1) (second term on the right-hand side), but it was negligible in our calculations.

B2. Fenton's Model

$$\frac{d[T]}{dt} = -k_T[T][\bullet\text{OH}] \quad (\text{B-11})$$

$$\frac{d[\text{Fe}^{2+}]}{dt} = -k_4[\text{Fe}^{2+}] + k_{-4}[\text{FeOH}^+][\text{H}^+] - k_8[\text{Fe}^{2+}][\text{H}_2\text{O}_2] - k_{10}[\text{I}_a] - k_{11}[\text{I}_b] - k_{12}[\text{Fe}^{2+}][\bullet\text{OH}] \quad (\text{B-12})$$

$$\begin{aligned} & -k_{14}[\text{Fe}^{2+}][\text{HO}_2\bullet] - k_{15}[\text{Fe}^{2+}][\text{O}_2^{\bullet-}] + k_{16}[\text{Fe(III)}][\text{HO}_2\bullet] + k_{17}[\text{Fe(III)}][\text{O}_2^{\bullet-}] \\ & -k_{28}[\text{Fe}^{2+}][\text{SO}_4^{2-}] + k_{-28}[\text{FeSO}_4] - k_{34}[\text{Fe}^{2+}][\text{SO}_4^{\bullet-}] + k_{37}[\text{FeSO}_4^+][\text{HO}_2\bullet] \\ & + k_{38}[\text{FeSO}_4^+][\text{O}_2^{\bullet-}] + k_{39}[\text{Fe}(\text{SO}_4)_2^-][\text{HO}_2\bullet] + k_{40}[\text{Fe}(\text{SO}_4)_2^-][\text{O}_2^{\bullet-}] \end{aligned}$$

$$\begin{aligned} \frac{d[\text{H}_2\text{O}_2]}{dt} = & -k_8[\text{Fe}^{2+}][\text{H}_2\text{O}_2] - k_9[\text{FeOH}^+][\text{H}_2\text{O}_2] - k_{18}[\text{H}_2\text{O}_2][\bullet\text{OH}] + k_{21}[\bullet\text{OH}]^2 - k_{22}[\text{H}_2\text{O}_2][\text{HO}_2\bullet] \\ & + k_{23}[\text{HO}_2\bullet]^2 + k_{24}[\text{O}_2^{\bullet-}][\text{HO}_2\bullet] - k_{30}[\text{FeSO}_4][\text{H}_2\text{O}_2] \end{aligned} \quad (\text{B-13})$$

$$\begin{aligned} \frac{d[\bullet\text{OH}]}{dt} = & -k_8[\text{Fe}^{2+}][\text{H}_2\text{O}_2] - k_{12}[\text{Fe}^{2+}][\bullet\text{OH}] - k_{13}[\text{FeOH}^+][\bullet\text{OH}] - k_{18}[\text{H}_2\text{O}_2][\bullet\text{OH}] - k_{19}[\text{HO}_2\bullet][\bullet\text{OH}] \\ & - k_{20}[\text{O}_2^{\bullet-}][\bullet\text{OH}] - 2k_{21}[\bullet\text{OH}]^2 - k_{29}[\text{HSO}_4^-][\bullet\text{OH}] + k_{30}[\text{FeSO}_4][\text{H}_2\text{O}_2] - k_{31}[\text{FeSO}_4][\bullet\text{OH}] \\ & - k_T[T][\bullet\text{OH}] - k_{Sc}[\text{Sc}][\bullet\text{OH}] \end{aligned} \quad (\text{B-14})$$

$$\frac{d[\text{HO}_2^{\bullet-}]}{dt} = -k_5[\text{HO}_2^{\bullet-}] + k_{-5}[\text{O}_2^{\bullet-}][\text{H}^+] + k_{10}[\text{I}_a] + k_{11}[\text{I}_b] - k_{14}[\text{Fe}^{2+}][\text{HO}_2^{\bullet-}] - k_{14}[\text{FeOH}^+][\text{HO}_2^{\bullet-}] \quad (\text{B-15})$$

$$- k_{16}[\text{Fe(III)}][\text{HO}_2^{\bullet-}] + k_{18}[\text{H}_2\text{O}_2][\text{HO}_2^{\bullet-}] - k_{19}[\text{HO}_2^{\bullet-}][\text{HO}_2^{\bullet-}] - 2k_{23}[\text{HO}_2^{\bullet-}]^2 - k_{24}[\text{O}_2^{\bullet-}][\text{HO}_2^{\bullet-}]$$

$$- k_{32}[\text{FeSO}_4][\text{HO}_2^{\bullet-}] - k_{37}[\text{FeSO}_4^+][\text{HO}_2^{\bullet-}] - k_{39}[\text{Fe}(\text{SO}_4)_2^-][\text{HO}_2^{\bullet-}] - k_{40}[\text{Fe}(\text{SO}_4)_2^-][\text{O}_2^{\bullet-}]$$

$$\frac{d[\text{O}_2^{\bullet-}]}{dt} = k_5[\text{HO}_2^{\bullet-}] - k_{-5}[\text{O}_2^{\bullet-}][\text{H}^+] - k_{15}[\text{Fe}^{2+}][\text{O}_2^{\bullet-}] - k_{15}[\text{FeOH}^+][\text{O}_2^{\bullet-}] - k_{17}[\text{Fe(III)}][\text{O}_2^{\bullet-}] \quad (\text{B-16})$$

$$- k_{20}[\text{O}_2^{\bullet-}][\text{HO}_2^{\bullet-}] - k_{24}[\text{O}_2^{\bullet-}][\text{HO}_2^{\bullet-}] - k_{33}[\text{FeSO}_4][\text{O}_2^{\bullet-}] - k_{38}[\text{FeSO}_4^+][\text{O}_2^{\bullet-}]$$

$$\frac{d[\text{FeOH}^+]}{dt} = +k_4[\text{Fe}^{2+}] - k_{-4}[\text{FeOH}^+][\text{H}^+] - k_9[\text{FeOH}^+][\text{H}_2\text{O}_2] - k_{13}[\text{FeOH}^+][\text{HO}_2^{\bullet-}] \quad (\text{B-17})$$

$$- k_{14}[\text{FeOH}^+][\text{HO}_2^{\bullet-}] - k_{15}[\text{FeOH}^+][\text{O}_2^{\bullet-}] - k_{35}[\text{FeOH}^+][\text{SO}_4^{\bullet-}]$$

$$\frac{d[\text{SO}_4^{\bullet-}]}{dt} = k_{29}[\text{HSO}_4^-][\text{HO}_2^{\bullet-}] - k_{34}[\text{Fe}^{2+}][\text{SO}_4^{\bullet-}] - k_{35}[\text{FeOH}^+][\text{SO}_4^{\bullet-}] - k_{36}[\text{FeSO}_4][\text{SO}_4^{\bullet-}] \quad (\text{B-18})$$

$$\frac{d[\text{FeSO}_4]}{dt} = k_{28}[\text{Fe}^{2+}][\text{SO}_4^{\bullet-}] - k_{28}[\text{FeSO}_4] - k_{30}[\text{FeSO}_4][\text{H}_2\text{O}_2] - k_{31}[\text{FeSO}_4][\text{HO}_2^{\bullet-}] \quad (\text{B-19})$$

$$- k_{32}[\text{FeSO}_4][\text{HO}_2^{\bullet-}] - k_{33}[\text{FeSO}_4][\text{O}_2^{\bullet-}] - k_{36}[\text{FeSO}_4][\text{SO}_4^{\bullet-}]$$

$$\frac{d[\text{Fe(III)}]}{dt} = -\frac{d[\text{Fe}^{2+}]}{dt} - \frac{d[\text{FeOH}^+]}{dt} \quad (\text{B-20})$$

$$\frac{d[\text{Sc}]}{dt} = -k_{\text{Sc}}[\text{Sc}][\text{HO}_2^{\bullet-}] \quad (\text{B-21})$$

$$[\text{Tot}(\text{SO}_4)] = [\text{HSO}_4^-] + [\text{SO}_4^{2-}] + [\text{FeSO}_4^+] + 2[\text{Fe}(\text{SO}_4)_2^-] + [\text{FeSO}_4] + [\text{SO}_4^{\bullet-}] \quad (\text{B-22})$$

$$[\text{Fe}(\text{III})] = [\text{Fe}^{3+}] + [\text{FeOH}^{2+}] + [\text{Fe}(\text{OH})_2^+] + 2[\text{Fe}_2(\text{OH})_2^{4+}] + [\text{I}_a] + [\text{I}_b] \quad (\text{B-23})$$

$$[\text{FeOH}^{2+}] = \frac{K_1[\text{Fe}^{3+}]}{[\text{H}^+]} \quad (\text{B-24})$$

$$[\text{Fe}(\text{OH})_2^+] = \frac{K_2[\text{Fe}^{3+}]}{[\text{H}^+]^2} \quad (\text{B-25})$$

$$[\text{Fe}_2(\text{OH})_2^{4+}] = \frac{K_3[\text{Fe}^{3+}]^2}{[\text{H}^+]^2} \quad (\text{B-26})$$

$$[\text{I}_a] = \frac{K_{\text{Ia}}[\text{Fe}^{3+}][\text{H}_2\text{O}_2]}{[\text{H}^+]} \quad (\text{B-27})$$

$$[\text{I}_b] = \frac{K_{\text{Ib}}K_1[\text{Fe}^{3+}][\text{H}_2\text{O}_2]}{[\text{H}^+]^2} \quad (\text{B-28})$$

$$[\text{HSO}_4^-] = K_{25}[\text{SO}_4^{2-}][\text{H}^+] \quad (\text{B-29})$$

$$[\text{FeSO}_4^+] = K_{26}[\text{Fe}^{3+}][\text{SO}_4^{2-}] \quad (\text{B-30})$$

$$[\text{Fe}(\text{SO}_4)_2^-] = K_{27}[\text{Fe}^{3+}][\text{SO}_4^{2-}]^2 \quad (\text{B-31})$$

Peroxy-iron complexes are $I_a=(Fe(HO_2)^{2+})$ and $I_b=(Fe(OH)(HO_2)^+)$. Their contribution to the H_2O_2 balance is negligible under the pH conditions employed in this work.

The equilibrium constants reported in Tables 3-2 and 3-3 correspond to a solution with ionic strength of 0.1 M, as reported by De Laat and Le.²¹ Changes in ionic strength of the solution will result in changes of the activity coefficients of charged species. Corrections to the equilibrium constants can be calculated in terms of estimates of activity coefficients. To illustrate this calculation, consider the reaction FE27 (Table 3-3). Let K_{27} be the equilibrium constant used in the calculations (as it appears in equation B-31, corresponding to an ionic strength S) and $K_{27,0.1}$ be the reported value at ionic strength 0.1 M. We can state that

$$K_{27} = K_{27,0.1} \frac{\{\gamma\}_{S=0.1M}}{\{\gamma\}_S} \quad (B-32)$$

where the activity coefficient product is given by

$$\{\gamma\} = \frac{\gamma_{Fe(SO_4)_2^-}}{\gamma_{Fe^{3+}} \gamma_{SO_4^{2-}}^2} \quad (B-33)$$

The ionic strength of the solution can be calculated from the concentration of all ionic species in terms of the charge number for each species, z_i , by

$$S = \frac{1}{2} \sum [C_i] z_i^2 \quad (\text{B-34})$$

Activity coefficients are calculated for species with various charges from the correlations

$$\ln(\gamma_{1\pm}) = -0.5 \left(\frac{\sqrt{S}}{1+1.5\sqrt{S}} - 0.3S \right) \quad (\text{B-35})$$

$$\ln(\gamma_{2\pm}) = -2 \left(\frac{\sqrt{S}}{1+1.5\sqrt{S}} - 0.3S \right) \quad (\text{B-36})$$

$$\ln(\gamma_{3\pm}) = -4.5 \left(\frac{\sqrt{S}}{1+1.5\sqrt{S}} - 0.3S \right) \quad (\text{B-37})$$

B3. Giovanni-NASA Data for the Calculation of Solar Spectral Irradiance using SMARTS (Chapter 3).

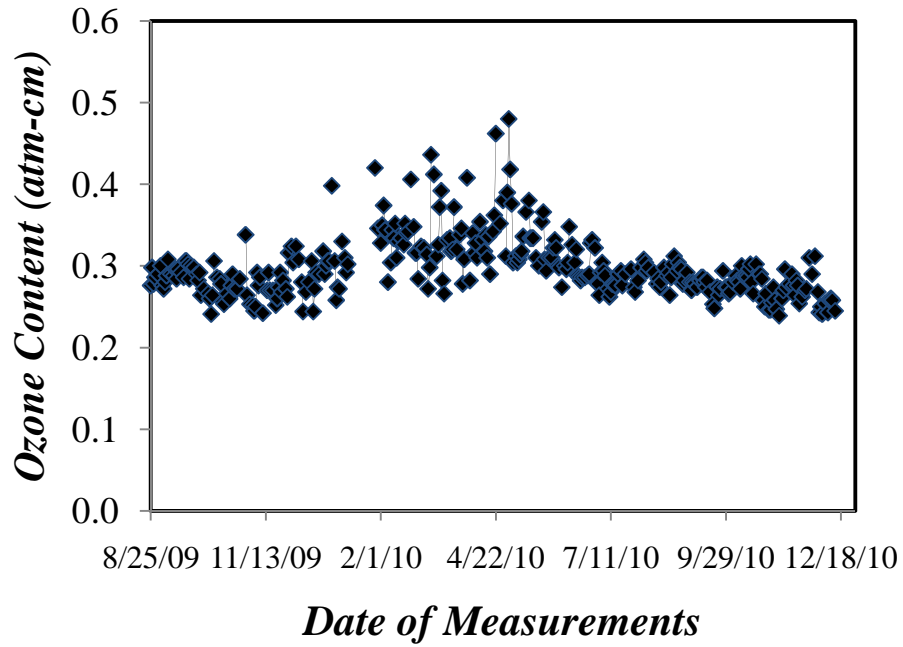


Figure B1. Ozone content in the atmosphere at Tucson AZ, from August 2009 to December 2010.

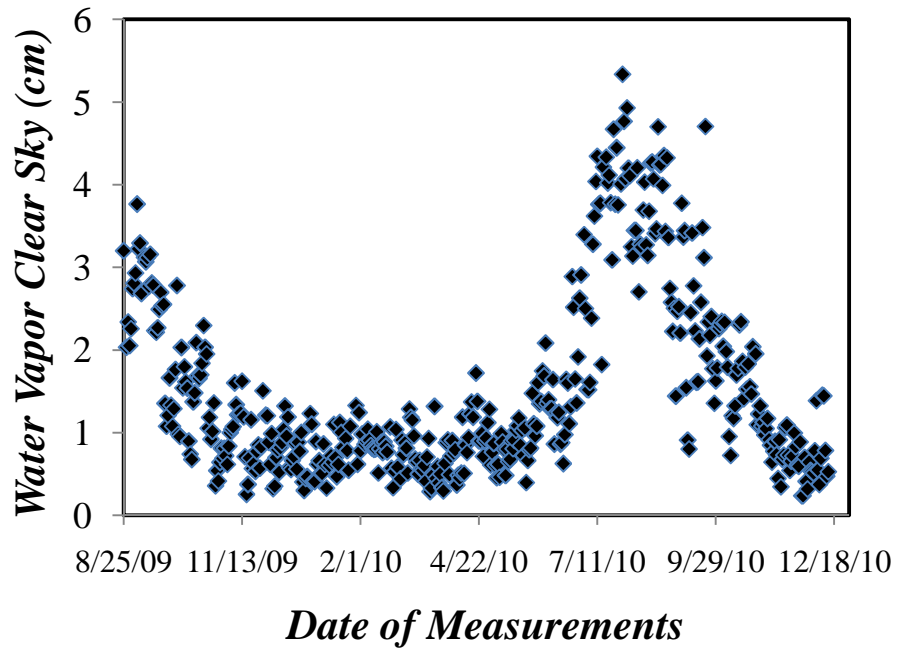


Figure B2. Water vapor content in the atmosphere at Tucson AZ, from August 2009 to December 2010.

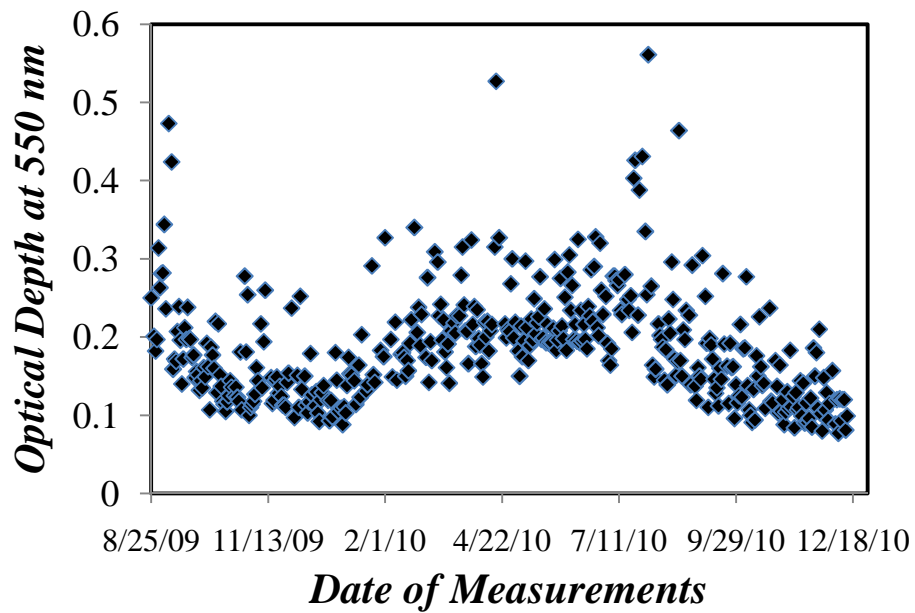


Figure B3. Water vapor content in the atmosphere at Tucson AZ, from August 2009 to December 2010.

APPENDIX C

ADDITIONAL RESEARCH ON FLOW OF NON-NEWTONIAN WASTE SLURRIES
WITH APPLICATION TO TRANSPORT OF NUCLEAR WASTE**Analysis of the Horizontal Pipeline Flow of Non-Newtonian Settling Dense Slurries**

Mario R. Rojas and A. Eduardo Sáez

Department of Chemical and Environmental Engineering, The University of Arizona, Tucson, AZ 85721,
USAmrojas@email.arizona.edu and esaez@email.arizona.edu

C.1. Abstract

The steady-state flow of dense aqueous slurries in horizontal pipes with Newtonian and non-Newtonian (Casson) carrier fluids has been analyzed using a two-layer model consisting of a top layer of flowing suspension and a settled bed of particles. The coarse solids used have a wide range of particle density, average size and particle size distributions, and the fluids studied were designed to simulate U.S. Department of Energy Hanford site waste slurries. The Doron and Barnea (1987) two-layer model was modified and extended to the quantification of slurries containing wide particle size distributions, including high-density particles, as well as non-Newtonian fluids. The most important changes from previous models include an independent settling analysis for different particle size fractions, effects of the shape of the particles on the settling velocity calculations, and a new correlation to represent the turbulent particle dispersivity. To incorporate the rheological properties of the fluids, the Wilson-Thomas turbulent flow equation for a Casson fluid (Wilson and Thomas 1985) was used. The results indicate that the turbulent dispersivity of settling particles is sensitive to particle size and density. A

new correlation is proposed to relate particle dispersivity to Archimedes number (Ar). The model also gives good estimation of the critical deposition velocity as the minimum of the pressure drop vs. superficial slurry velocity relation. The existence of a stationary layer can be observed and predicted by the model under laminar and turbulent flow conditions.

Keywords: Non-Newtonian Slurries, Two-layer Model, Horizontal Pipeline Flow, Solids Transport

C.2. Introduction

The transport of slurries in horizontal pipes is a process with widespread application in practice. Even though it is generally desirable to operate at velocities that ensure complete suspension of solids, some processes operate under conditions at which a granular deposit occupies part of the cross section of the pipe. In fact, for slurries composed of dense particles, it might be economically attractive to operate in a regime in which a granular deposit exists. Typically, these processes involve suspension of particles with wide particle size distributions in turbulent flows.

Gillies *et al.* (1991) proposed a two-layer model to predict the head losses for coarse-particle or settling slurries in horizontal pipes as a modification of the Wilson (1970) model. Gillies *et al.*'s model is capable of representing solids concentration profiles over the cross section, and their relation to the mean flow velocity and the settling particle velocity. The same research group has used the two-layer model in different applications, such as the study of frictional losses in concentrated slurry flows (Gillies and Shook

2000) and the modeling of heterogeneous slurries at relatively high fluid velocities (Gillies *et al.* 2004), with successful results.

Doron and Barnea (1993) proposed a three-layer model as an extension of their own two-layer model (Doron *et al.* 1987) and other published models. They proposed that the main limitation of the two-layer model is its inability to predict accurately the existence of a stationary bed at low flow rates: in some cases when a stationary bed was observed, model results indicated flow with a moving bed. This also leads to reduced reliability of the pressure drop calculations for low flow rates, at which a stationary bed can be expected. Using the three-layer model, the authors were able to quantify the critical deposition velocity as the limit when the stationary bed height approaches zero. The value obtained can be viewed as an upper limit for the critical velocity since, in practice, a bed layer can be considered to vanish when its height is of the order of the particle size. According to their results, model predictions are in fairly close agreement with the Turian *et al.* (1987) expression and the correlation proposed by Gillies *et al.* (1991a) for critical velocity, which were derived from semi-empirical analyses.

The Doron and Barnea model incorporates a cross-sectional solids mass balance to quantify the solid distribution in the pipe under steady-state conditions. The balance leads to a one-dimensional version of the sedimentation-dispersion equation, whose solution yields the vertical solids concentration profile in the cross section of the moving layer. The solids settling velocities and dispersion coefficients are vital for the accurate performance of this prediction.

Similar two- and three-layer models have been developed and extended to other applications (Gorji and Ghorbani, 2008). Ramadan *et al.* (2005) proposed an extension of the three-layer to non-Newtonian (power-law) fluids to predict solids transport in horizontal and inclined wellbore drilling applications. The model is focused on the prediction of transport rates for drilling applications.

In this work, we modify the two-layer model to characterize the flow of dense/concentrated Newtonian and non-Newtonian slurries with broad particle size distributions in flow through horizontal pipes, in an attempt to represent real waste slurries of the US DOE's Hanford site. For the case of Newtonian fluids, the most important changes from previous models include independent settling analysis for different particle size fractions, effects of the shape of the particles on the settling velocity calculation, and a new correlation to represent turbulent particle dispersivities. To extend the model to non-Newtonian fluids, a new approach has been developed and tested. The Wilson-Thomas Turbulent flow equation for Casson fluids has been coupled with the two-layer model. The transition between laminar and turbulent flow has been studied using the Wasp criterion (Bingham fluids) adapted by Poloski *et al.* (2008) to Casson fluids.

C.3. Experimental

Materials. The suspensions (simulants) used were designed to match specific physical properties, such as rheology and particle size distribution (PSD), of actual waste slurries of the Hanford site. The carrier fluid was water and all experiments were performed at

20°C. Glass (Spherglass, Potters Industry), alumina (Washington Mills) and stainless steel 316 (Aemtek), were selected to represent the coarse particles in the experiments. These materials have densities of 2500, 3770 and 7950 kg/m³, respectively, and were qualified as “low”, “medium” and “high” particle density.

Particle size distributions range from 1 to 200 μm. Other properties of the simulants are listed in Tables C-1 and C-2. Simulants are identified by a two-letter code: the first letter identifies the particle density (low, medium or high as stated above), and the second letter refers to relative particle size. Examples of particle morphologies are shown in Figure C-1. The glass particles are spherical but the alumina and stainless steel particles have irregular shapes. In order to include the effect of shape in drag coefficient calculations, we followed the analysis presented by Tran-Cong *et al.* (2004). Since their correlation for particle drag coefficient is based on the definition of circularity and surface-equivalent sphere to nominal diameter ratio, these have been included in Table C-1. The definition of surface-equivalent sphere to nominal diameter ratio (d_A/d_n), is the ratio between d_A , the particle diameter defined in terms of projected area of the sphere (A_p)

$$d_A = \sqrt{4A_p / \pi} \quad (\text{C-1})$$

and the volume-equivalent-sphere diameter or nominal diameter, calculated from the particle volume (V),

$$d_n = \sqrt[3]{6V/\pi} \quad (\text{C-2})$$

Experimental Setup. The slurries were prepared in a 400-gal mixing tank connected to a flow loop system. During the experiment, the slurry is transported through the system by a 15-hp/1800 rpm centrifugal pump (Georgia Iron Works). The main section of the flow-loop consists of 3 in schedule 40 stainless steel straight horizontal pipeline on which different pressure ports were installed. Pressure drops were measured with a differential pressure transducer over a pipe length of 5.7 m.

Table C-1. Properties of the Newtonian simulants.

Acronym	LL	LH	HL	HH
Particle hydraulic diameter (μm) dp_h	10.9	138.0	25.0	150.0
Solids content (vol %)	9.8	7.4	9.3	3.0
Particle density (kg/m^3)	2500	2500	7950	7950
Particle circularity (c)	1.000	1.000	0.901	0.901
d_A/d_n	1.000	1.000	1.151	1.151
Bed layer solids concentration C_b (vol %)	60	60	60	40

Table C-2. Properties of the non-Newtonian simulants.

Acronym	LH1	LH2	MM1	MM2
Particle hydraulic diameter (μm) dp_h	116.0	152.7	83.3	85.5
Solid vol fraction (%)	8.4	10.7	9.5	9.7
Fines vol fraction (%)	7.7	9.6	8.9	10.7
Particle density (kg/m^3)	2500	2500	3770	3770
Fines particles density (kg/m^3)	2500	2500	2500	2500
Infinite shear rate viscosity (Pa s)	0.0018	0.0026	0.0023	0.0024
Casson yield stress (Pa)	2.4	4.4	2.4	4.7
Particle Circularity (c)	1.000	1.000	0.4472	0.4472
Surface-equiv-sphere diameter (d_A/d_n)	1.000	1.000	1.1689	1.1689
Bed Layer solids concentration C_b (%)	60	60	50	50

The slurry is recirculated through the system until the flow reaches steady state (approximately 30-60 min). Before it enters the main horizontal measurement section, the slurry flows through a Coriolis flow meter (Micro-Motion, F-series). A chiller connected to the mixing-tank was used to keep the temperature constant during the experiment (20 °C).

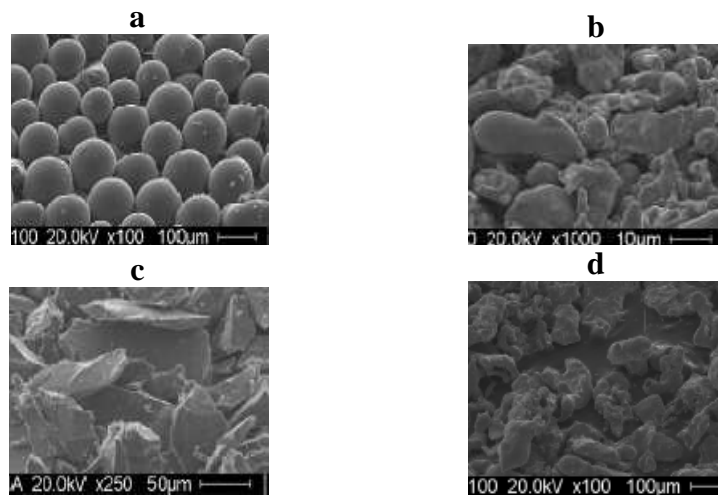


Figure C-1. Micrographs of (a) LH, (b) HL, (c) MM and (d) HH simulant particles.

All the tests were conducted starting with a relatively high superficial velocity of 3-4 m/s, and then the velocity was decreased in 0.15 m/s steps until a rise in differential pressure was detected, indicating the presence of a settled bed of particles; this point was considered as the experimental critical deposition velocity.

After the Coriolis flow meters, the slurry entered an electrical resistance tomography (ERT) probe (Industrial Tomography Systems) that recorded cross-sectional maps of the slurry electrical conductivity in real time. Since conductivity is a function of solids

concentration, these maps yield a representation of the solids distribution over the cross section, including observation of the deposited bed layer.

C.4. Model Description and Modifications

The model is based on the distribution of forces along the flow direction over a cross-sectional area of the pipe, and mass balances. The contribution of each layer to the force balance consists of shear stresses at the pipe wall and at the interface, which can be calculated by means of friction factors. More details about the formulation of the two-layer model are provided by Doron and Barnea (1993). Figure C-2 shows the general scheme for the two-layer model, identifying the stress distribution in the pipe cross-sectional area.

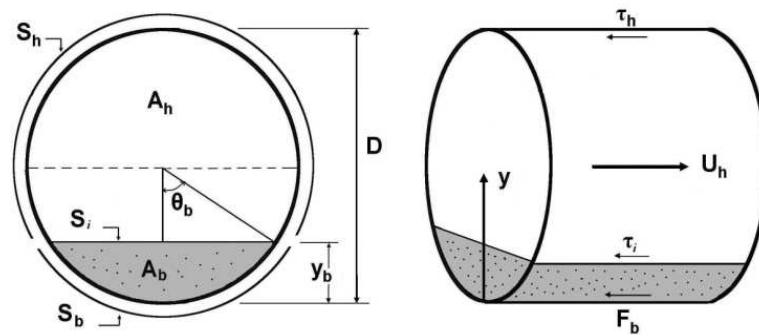


Figure C-2. Geometry and stress distribution in the two-layer model.

The model assumes that vertical (y) particle transport is governed by the convection-dispersion equation, which balances the settling flux of particles with a turbulent dispersion flux,

$$\varepsilon \frac{d^2 C}{dy^2} + w \frac{dC}{dy} = 0 \quad (\text{C-3})$$

where w is the terminal settling velocity of the particles, ε is the turbulent dispersivity, and C is the solids concentration (solids volume fraction). This equation was applied to different particle size ranges within the particle size distribution of the solid. Details are presented in the Discussion section below. Integrating equation (3) over the cross-section of the upper layer yields the mean solids concentration in the upper layer,

$$C_h = \frac{C_b D^2}{2A_h} \int_{\theta_b}^{\pi/2} \exp\left(-\frac{wD}{2\varepsilon} [\sin \gamma - \sin(\theta_b)]\right) \cos^2 \gamma d\gamma \quad (\text{C-4})$$

where D is the pipe diameter, A_h is the cross-sectional area of moving layer, θ_b is the angle associated with the stationary bed location (Figure C-2), and C_b is the concentration of solids in the stationary bed, used as boundary condition in the integration of equation (3). Mass balances in solid and liquid phases yield

$$U_h C_h A_h + U_b C_b A_b = U_s C_s A \quad (\text{C-5})$$

$$U_h (1 - C_h) A_h + U_b (1 - C_b) A_b = U_s (1 - C_s) A \quad (\text{C-6})$$

where U_s is the superficial velocity of the slurry, U_b is the velocity of liquid moving through the stationary bed, and A_b is the cross-sectional area of stationary bed. The value

of C_h obtained from equation (4) must equal the value obtained from the mass balances.

A force balance in the flow direction can be expressed as

$$\frac{\tau_h S_h + \tau_i S_i}{A_h} = \frac{F_{mb} + \tau_b S_b - \tau_i S_i}{A_b} \quad (\text{C-7})$$

where τ represents the shear stress acting on the surfaces of each layer at the pipe surface (h and b subscripts) or at the interface (i) between layers (Figure C-2), S represents perimeter, F_{mb} is the dry friction force exerted by the bed layer, which includes the effect of the submerged weight of particles and the transmission of stresses from the interface, and is given by

$$F_{mb} = \eta \left\{ 2C_b \left(\frac{D}{2} \right)^2 (\rho_s - \rho_l) g \left[\left(\frac{2y_b}{D} - 1 \right) \left(\theta_b + \frac{\pi}{2} \right) + \cos \theta_b \right] + \frac{\tau_i S_i}{\tan \phi} \right\} \quad (\text{C-8})$$

where ρ_s and ρ_l are the densities of solid and carrier fluid, respectively, η is the dry friction coefficient, y_b is the bed height, ϕ is the internal friction angle and g is the acceleration of gravity.

The angle and perimeters (θ_b , S_h , S_b , S_i) can be expressed as functions of y_b and, therefore, for a given flow condition, it is possible to solve the preceding set of equations having y_b , C_h , U_h and U_b as unknowns. If the system exhibits a stationary bed (our case), the static dry friction force is no longer equal to the maximum dry friction force. In this case, the

equations to solve are the mass balance (equation 4), and the pressure gradient per unit length is then obtained from

$$A_h \frac{dP}{dx} = -\tau_h S_h - \tau_i S_i \quad (\text{C-9})$$

The shear stresses are expressed in terms of friction factors as follows

$$\tau_i = \frac{1}{2} \rho_i U_i^2 f_i \quad (\text{C-10})$$

where the subscript i represents the interface between the two layers. Similar definitions apply to the two layers (h and b). The densities of each layer are given by

$$\rho_h = \rho_s C_h + \rho_l (1 - C_h) \quad (\text{C-11})$$

And the friction coefficient (f) for each layer can be calculated using the following correlation

$$f_h = \alpha \text{Re}_h^\beta \quad (\text{C-12})$$

where α and β are constants that depend of the flow regime: turbulent ($\alpha=0.046$, $\beta=0.2$) and laminar ($\alpha=16$, $\beta=1$). The Reynolds numbers are based on the velocity and density of each layer. Furthermore, the friction factor in the moving layer is given by the Colebrook correlation, using the particle size as an equivalent roughness,

$$\frac{1}{\sqrt{2f_i}} = -0.86 \ln \left(\frac{d_p}{3.7D_h} + \frac{2.51}{\text{Re}_i \sqrt{2f_i}} \right) \quad (\text{C-13})$$

The set of equations described above were used to model the Newtonian simulants. The non-Newtonian simulants used in this work were simulated using a new approach. The Wilson and Thomas (1985) theory for turbulent flow has been adapted and coupled to the two-layer model. This theory considers the effect of variable fluid viscosity on the velocity profiles of the viscous sub-layers in turbulent flow.

Through the analysis of viscosity effects at the time and length scales of dissipative micro eddies, the theory predicts a thickening of the viscous sub-layer, which tends to increase throughput velocity and thus promotes drag reduction. The Wilson-Thomas theory has been adapted to different rheological behaviors, including Casson fluids, for which it has been shown that the superficial velocity achieved by a Casson fluid for a given shear stress is related to the velocity of an equivalent Newtonian fluid by

$$U = U_n + 2.5u^* \ln \left(\frac{1 - \xi}{1 + \frac{2}{3}\sqrt{\xi} + \frac{1}{3}\xi} \right) + u^* \left[\xi(2.5 + 1.25\xi) + 11.6 \left(\frac{2}{3}\sqrt{\xi} + \frac{1}{3}\xi \right) \right] \quad (\text{C-14})$$

where ξ is the ratio of the yield stress to the wall shear stress (τ_c/τ_w), U_n is the superficial velocity for an equivalent Newtonian fluid at the same shear stress, and u^* is the shear velocity, calculated from

$$u^* = \sqrt{\frac{\tau_w}{\rho_h}} \quad (\text{C-15})$$

Calculation of the pressure drop of a Casson fluid for homogeneous turbulent flow requires the use of this last equation. For laminar flow, the equivalent expression is

$$\frac{8U}{D} = \left(\frac{\tau_w}{\mu_c} \right) \left[1 - \frac{16}{7} \sqrt{\xi} + \frac{4}{3} \xi - \frac{1}{21} \xi^4 \right] \quad (\text{C-16})$$

where μ_c is the viscosity of a Casson fluid, whose constitutive equation in shear flow relating shear stress, τ , to shear rate, $\dot{\gamma}$, is given by

$$\tau^{1/2} = \tau_c^{1/2} + (\mu_c \dot{\gamma})^{1/2} \quad (\text{C-17})$$

We have adapted these equations to the two-layer model to simulate the upper layer. The process starts by relating the wall shear stress in equations (14) or (16) (depending on the flow regime) to the shear stress in the upper flow region (τ_h and τ_i), assuming that the lower layer is stationary. The wall shear leads to a pressure gradient given by

$$A_h \frac{dP}{dx} = -\tau_w (S_h + S_i) \quad (\text{C-18})$$

For a given bed height, all the geometric parameters can be calculated. If the pressure gradient is given, the effective wall shear stress can be obtained from equation (18),

which allows for calculation of ξ . At this point, the effective viscosity of the Casson fluid can be calculated from

$$\mu = \frac{\mu_c}{(1 - \sqrt{\xi})^2} \quad (\text{C-19})$$

To calculate the Newtonian superficial velocity (U_n), we solve Colebrook's equation for the friction coefficient at the interface simultaneously with equation (9), using the friction factors and Reynolds numbers of a Newtonian fluid. Once the mean Newtonian fluid velocity is known, equation (14) can be used to calculate the velocity in the upper layer (U_h), the Reynolds number of the fluid, and the corresponding superficial fluid velocity,

$$U_s = \frac{U_h A_h}{A} \quad (\text{C-20})$$

After these calculations, the no-slip condition should be checked to insure the existence of a stationary layer, followed by the calculation of settling velocity, dispersivity and verification of the mass balance (equation 4). The calculation proceeds iteratively until the concentration in the upper layer (C_h) is the actual inlet concentration (C_s).

The calculation of the dispersion coefficient used in equation (4) and the modifications made to Taylor's equation will be addressed in the discussion. All calculations were performed using an iterative program developed in MATLAB[®].

C.5. Results and Discussion

The two-layer model, as described above, can be used, in principle, to predict the non-homogeneous flow behaviour of slurries. Given the scenario of a stable stationary bed without a moving bed above it, according to the model equations, one of the most important factors that control the actual upper layer solids concentration is the balance between particle turbulent dispersion and settling. At this point, it is considered that the particles have a specified particle size distribution that can be discretized into narrow ranges, each characterized by its own dispersivity and settling velocity. The calculation of settling velocity is one of the most important modifications proposed here. It includes effects of the solids concentration, turbulence intensity and particle shape, which affect the estimation of the drag coefficient for the particles. Settling velocities were calculated considering narrow portions of the PSD separately, as follows,

$$w_{oi} = \sqrt{\frac{4(s-1)d_{pi}g}{3C_{Di}}} \quad (C-21)$$

where C_{Di} is the drag coefficient for particle size range I, calculated using the particle Reynolds number based on w_{oi} , and $s = \rho_s / \rho_l$. In order to account for the PSD, values of drag coefficient were obtained using the modified form of the Clift *et al.* (1978) correlation provided by Tran-Cong *et al.* (2004), which takes into consideration the shape of the particles. In addition, to account for turbulence effects in the drag coefficient calculations, the correlation proposed by Brucato *et al.* (1998) is used, which considers the Kolmogorov scale of dissipative eddies.

Once the drag coefficients are known and values of w_{oi} were calculated for each fraction of the PSD, we calculated a particle hindered settling velocity into the cluster for each of the fractions using the equation developed by Cheng (1997). Finally, the effective settling velocity of the particles to be used in the integration of equation (4) is calculated as follows,

$$w = \frac{\sum_i (w_i C_{hi})}{C_h} \quad (\text{C-22})$$

Calculations have shown that this approach gives a settling velocity lower than that obtained using a simple average particle size.

The turbulent dispersivity in the original Doron and Barnea model is calculated from the original Taylor's equation (Taylor 1954),

$$\varepsilon = aD_h u^* \quad (\text{C-23})$$

where $a=0.026$. However, this approach does not appropriately take into account particle characteristics (density, size, shape, PSD), which become more relevant in this work due to the relatively large particle size and density of some of the simulants. Analysis of our data suggested that the coefficient in Taylor's equation is related to particles properties, and that there is a stronger dependence of the dispersivity on fluid velocity for our slurries.

It is important to recall that Taylor's correlation applies to solutes in turbulent flow and not to settling particles. Our results indicate that turbulent transport of particles is slower than transport of molecular species, which could be a consequence of increase of energy dissipation in smaller eddies (of size comparable to the solid particles).

Figure C-3 shows the dependence of the dispersion coefficient calculated by fitting our model to experimental data with hydraulic diameter and shear velocity (u^*). Different correlations were obtained depending on particle properties, so using preliminary data for Newtonian fluids, and based on these results, we have postulated that the coefficient “ a ” depends on Reynolds number and the Archimedes number of the particles through an empirical correlation given by

$$a = kAr^n Re^m \quad (\text{C-24})$$

where n and m were found to be 0.411 and 0.75, respectively, k is a constant and Ar is the Archimedes number of the particles present in the slurry, defined by

$$Ar = \frac{gd_p^3(s-1)\rho_h^2}{\mu_h^2} \quad (\text{C-25})$$

We extended the correlation to include both Newtonian and non-Newtonian simulants data. The results are shown in Figure C-4. Note that the new correlation is applicable to all simulants. It is important to point out that particles with very different densities and

PSDs but with similar Archimedes numbers possess similar values of a , which supports the mathematical form of the proposed correlation.

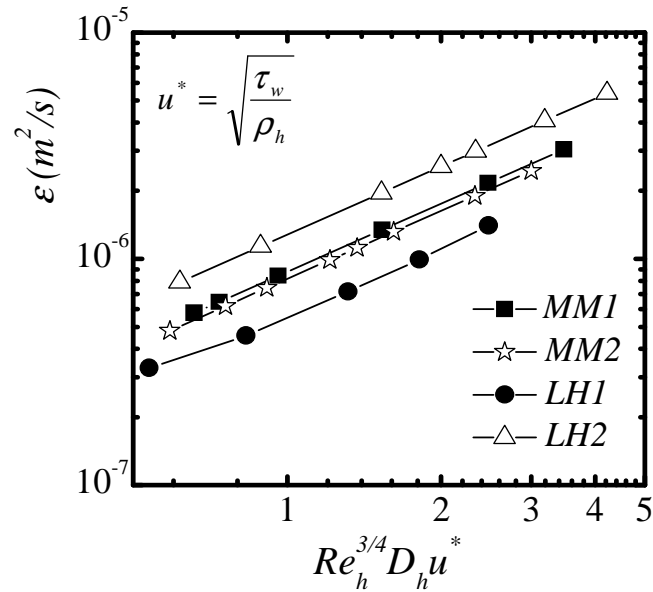


Figure C-3. Particle dispersivity as fitted to experimental data. The slopes of these curves represent the different a values that depend on Ar .

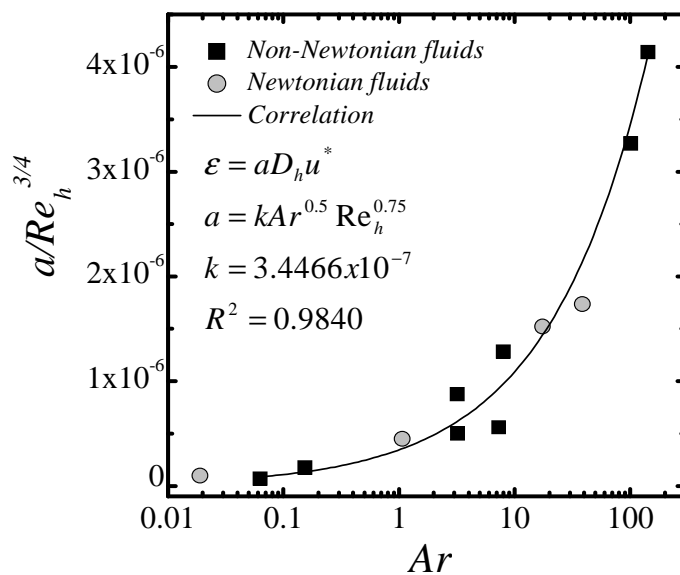


Figure C-4. Particle dispersivity correlation.

Turbulent dispersivities have been found to be correlated in previous works (albeit in different applications) with Ar and Re . For instance, Wen and Yu (1966) and Reganathan *et al.* (2004) used such a correlation to represent solids dispersion coefficients in liquid-solid fluidized beds.

The two-layer model was used to predict the pressure drop over the 5.71 m of straight horizontal pipe for different simulants using the proposed correlation for particle dispersivity. Figure C-5 shows pressured drop vs. superficial velocity for the low-density Newtonian simulants (LL, LH), including the predictions of the modified two-layer model.

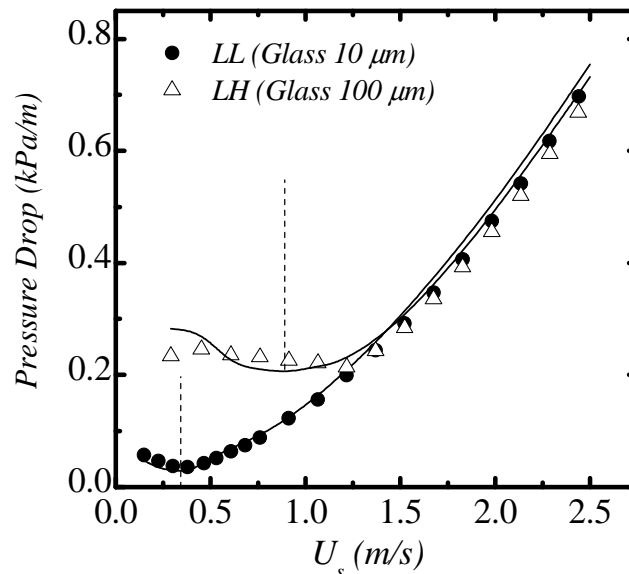


Figure C-5. Pressure drop as a function of superficial velocity for the low density/small particle size Newtonian simulants. Solid lines represent the model.

The results in Figure C-5 follow the typical trends observed in flow of concentrated slurries: at high fluid velocities, when the solid is fully suspended, the pressure drop decreases monotonically with a reduction in velocity. Additional decreases in fluid velocity lead to the formation of a stationary (or moving) layer in the bottom of the pipe, whose growth as the velocity is reduced causes a decrease in suspension flow area and a consequent increase in the pressure drop. At very low fluid superficial velocities, the pressure drop continues to rise as the bed thickness increases uniformly.

The minimum observed in the pressure drop curves yields the critical deposition velocity of the suspension. All the experimental data analyzed in this work present a stable stationary layer at low fluid velocities except the HH stimulant, which exhibited a transition from moving bed to stationary bed at high velocities. Figure C-5 shows that, for low particle densities, the modified model proposed here predicts the pressure drops satisfactorily in the whole velocity range evaluated. For both simulants, the modified model predicts accurately the critical velocity (dashed lines). The minimum in the predicted curves is close to the point at which the model predicts that the stationary bed disappears with any additional increment in fluid velocity.

Figure C-6 shows results for the non-Newtonian simulants with intermediate particle density and size (MM). The fluid with the higher yield stress (MM2) exhibits a higher pressure drop at low fluid velocities. Although there is an important difference in the rheological properties of these two fluids, the critical velocities are quite similar. In this

case, the flow is always turbulent, and the model once again gives an accurate representation of the experimental data.

Figure C-7 shows the thickness of the stationary bed layer height predicted by the model as a function of superficial velocity. For practical purposes, it can be considered that the bed disappears when its height approaches the particle diameter, which usually happens at velocities in the range 0.3-1.5 m/s. However, for the very dense/large particle size slurry (HH), the experimental observations and the ERT images suggest that the stagnant bottom layer only disappears at the maximum velocity used.

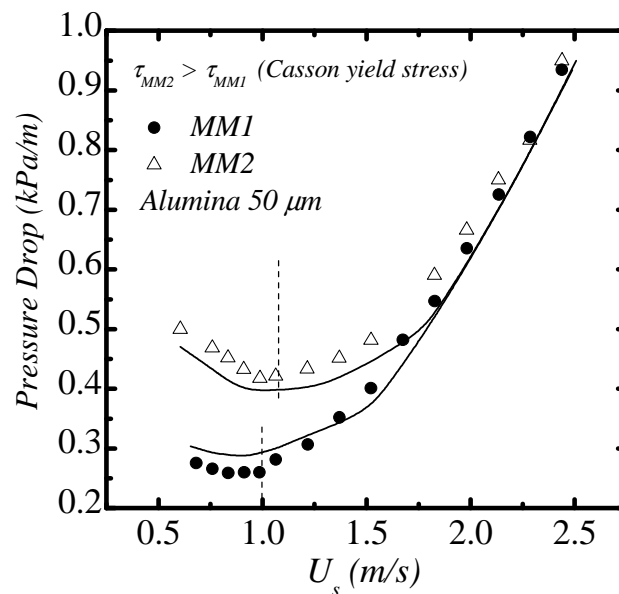


Figure C-6. Pressure as a function of superficial velocity for medium density/medium particle size fluids. Solid lines represent the model.

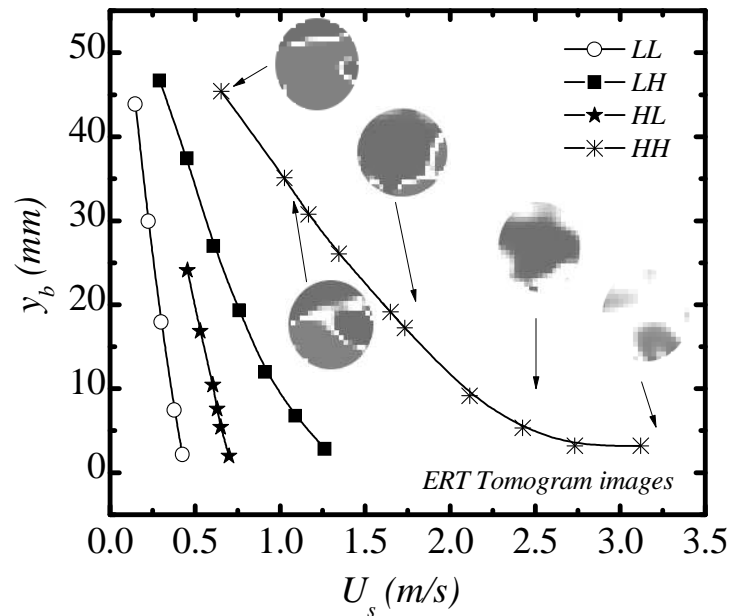


Figure C-7. Stationary bed height predicted by the model as a function of superficial velocity for studied simulants. ERT images for HH qualitatively follow the trends predicted by the model.

For HH, the model also predicts a high critical velocity compared with all other simulants. There is a solids layer in the bottom of the pipe even at velocities above the critical velocity, which is due to a transition between a stationary layer and a moving layer at high fluid velocities. However, this moving layer is so small that it exists only in a narrow range of velocity preceding the total disappearance of the bed at high velocities. Figure C-7 also shows the tomography images (ERT) obtained for the HH simulant for different superficial fluid velocities. These images provide a way to study the evolution of the bed layer at the bottom of the pipe. The images show a presence of a stationary bed over practically all the range of fluid velocity studied. For all the other fluids, the disappearance of the bed layer predicted by the model matches the experimental results and the ERT images (results not shown).

C.6. Conclusions

The two-layer model of Doron and Barnea has been modified to study slurries made up by Newtonian and non-Newtonian fluids composed of dense particles with broad particle size distributions and irregular shapes. To include the non-Newtonian properties of the simulants and their effects on the flow, the two-layer model has been coupled with the Wilson-Thomas turbulence equation for Casson fluids. The model predicts accurately pressure drops, critical deposition velocities and the thickness of the stationary bed when it is present.

The changes introduced in the model include a novel way to calculate the effective settling velocity of the whole PSD, taking into account the effect of turbulence and irregular shape of particles in the drag coefficient calculation. A new correlation for the solids dispersion coefficient was developed to improve model predictions. The dispersion coefficient depends on the particle Archimedes and Reynolds numbers. Pressure drops, critical deposition velocities, and thickness of the bed layers have been successfully predicted for all the slurries, demonstrating the potential applicability of this model to simulate the hydrodynamics of complex slurries at the U.S. Department of Energy's Hanford site.

C.7. Acknowledgements

This work was supported by Battelle. The authors are grateful to Adam Poloski and Harold Adkins of Pacific Northwest National Laboratory in Richland, WA, for helpful discussions and for providing experimental results.

C.8. Literature Cited

Brucato, A., Grisafi, F., Montante, G. Particle Drag Coefficients in Turbulent Flow. *Chemical Engineering Science*, 53, 3295-3314 (1998).

Cheng, N-S. J. Effects of Concentration on Settling Velocity of Sediment Particles. *Hydraulic Engineering*, 123, 728-731 (1997).

Clift, R., Grace, J.R., Weber M.E. *Bubbles, Drops and Particles*. Academic Press, New York, (1978).

Doron, P., Granica, D. and Barnea, D. Slurry Flow in Horizontal Pipes-Experimental and Modeling. *International Journal of Multiphase Flow*, 13, 535-547 (1987).

Doron, P. and Barnea, D. A Three-Layer Model for Solid-Liquid Flow in Horizontal Pipes. *International Journal of Multiphase Flow*, 19, 1029-1043 (1993).

Gillies, R.G., Shook, C.A., Wilson K.C. An Improved Two Layer Model for Horizontal Slurry Pipeline Flow. *Canadian Journal of Chemical Engineering*, 69, 173-178 (1991a).

Gillies, R.G., Shook, C.A. A Deposition Velocity Correlation for Water Slurries. *Canadian Journal of Chemical Engineering*, 69, 1225-1227 (1991b).

Gillies R.G., Shook C.A. Modelling High Concentration Settling Slurry Flows. *Canadian Journal of Chemical Engineering*, 78, 709-716 (2000).

Gillies, R.G., Shook, C.A., Xu J. Modelling Heterogeneous Slurry Flows at High Velocities. *Canadian Journal of Chemical Engineering*, 82, 1060-1065 (2004).

Gorji, M., Ghorbani, N. The Influences of Velocity on Pressure Losses in Hydrated Slurries. *International Journal of Numerical Methods for Heat & Fluid Flow*, 18, 5-13 (2008).

Poloski, A.P., Adkins, H.E., Abreah, J., Casella, A.M., Hohimer, R.E., Nigl, F., Minette, M.J., Toth, J.J., Tingey, J.M., Yokuda S.T. DOE Publication No. WTP-RPT-175. Deposition Velocities of Newtonian and Non-Newtonian Slurries in Pipelines. Pacific Northwest National Laboratory, Richland, WA, (2008).

Ramadan, A., Skalle, P., Saasen, A. Application of a Three-Layer Modeling Approach for Solids Transport in Horizontal and Inclined Channels. *Chemical Engineering Science*, 60, 2557-2570 (2005).

Renganathan, T. and Krishnaiah, K. Liquid Phase Mixing in 2-Phase Liquid–Solid Inverse Fluidized Bed. *Chemical Engineering Journal*, 98, 213-218 (2004).

Taylor, G. The Dispersion of Matter in Turbulent Flow Through a Pipe. *Proceedings of the Royal Society of London*, A223, 446-468 (1954).

Tran-Cong, S., Gay, M., Michaelides, E. Drag Coefficients of Irregularly Shaped Particles. *Powder Technology*, 139, 21-32 (2004).

Turian, R.M., Hsu, F.L. Estimation of the Critical Velocity in Pipeline Flow of Slurries, *Powder Technology*, 51, 35-47 (1987).

Wen, C.Y. and Yu, Y.H. Mechanics of Fluidization. *Chemical Engineering Progress Symposium Series*, 66, 101-111 (1966).

Wilson, K.C. Stationary Deposits and Sliding Beds in Pipes Transporting Solids. *Proceedings of the 1st International Conference on the Hydraulic Transport of Solids in Pipes*. BHRA Fluid Engineering, Cranfield, UK. C3, 28. (1970).

Wilson, K.C. and Thomas, A. A New Analysis of the Turbulent Flow of Non-Newtonian Fluids. *The Canadian Journal of Chemical Engineering*, 63, 539-546 (1985).

Wilson, K.C. and Thomas, A. New Analysis of Non-Newtonian Turbulent Flow Yield-Power-Law Fluids. *The Canadian Journal of Chemical Engineering*, 65, 335-338 (1987).

C.9. Nomenclature

a	coefficient in the modified Taylor equation
A	surface area (m ²)
Ar	Archimedes number
c	particle circularity
C	solid volume concentration (vol %)
C_D	drag Coefficient
C_s	slurry input volume concentration (vol %)
D	pipe diameter (m)
d_A/d_n	surface-equivalent sphere to nominal diameter ratio
d_p	particle diameter (m)
dP/dx	pressure gradient (Pa/m)
ERT	Electrical Resistance Tomography
f	friction coefficient
F_{mb}	dry friction force - moving bed (N)
g	acceleration of gravity (m/s ²)
LL	low density/small particle size/Newtonian slurry
LH	low density/large particle size/Newtonian slurry
$LH1$	low density/large particle size/non-Newtonian, low yield stress slurry
$LH2$	low density/large particle size/non-Newtonian, high yield stress slurry
HL	high density/small particle size/Newtonian slurry
HH	high density/large particle size/Newtonian slurry
m, n	adjustable parameters in the modified Taylor equation
$MM1$	medium density/medium particle size/non-Newtonian, low yield stress slurry
$MM2$	medium density/medium particle size/non-Newtonian, high yield stress slurry

and

Acronyms

P	pressure (Pa)
PSD	particle size distribution
Re	Reynolds number
s	ratio of density of the particle and carrier fluid
S	perimeter of layer or interface (m)
U	superficial fluid velocity (m/s)
U_n	mean velocity for an equivalent Newtonian fluid (m/s)
u^*	shear velocity (m/s)
w	terminal settling velocity of particles (m/s)
y_b	bed height (m)

Greek symbols

α, β	constants for friction coefficient calculation
ε	solids dispersivity (m ² /s)
ϕ	internal friction angle
$\dot{\gamma}$	Shear rate (s ⁻¹)
μ_c	Casson fluid viscosity (Pa s)
η	dry friction coefficient
ρ	density of layers (kg/m ³)
ρ_p	particle density (kg/m ³)
θ	angle associated with bed height
τ	shear stress of layers or interface (Pa)
τ_c	Casson yield stress (Pa)
τ_w	wall shear stress (Pa)
ξ	ratio of Casson yield stress to wall shear stress

Subscripts

b	bed layer
h	upper (moving) layer
i	interface between layers
s	mixture or slurry